LAWRENCE
LIVERMORE
NATIONAL
LABORATORY

LLNL-TH-653594

Two Contemporary Problems in Magnetized Plasmas: the ion-ion hybrid resonator and MHD stability in a snowflake divertor

W. A. Farmer

April 23, 2014

Disclaimer

This work performed under the auspices of the U.S. Department of Energy by Lawrence Livermore National Laboratory under Contract DE-AC52-07NA27344.

University of California
Los Angeles

Two Contemporary Problems in Magnetized Plasmas: the ion-ion hybrid resonator and MHD stability in a snowflake divertor

A dissertation submitted in partial satisfaction
of the requirements for the degree
Doctor of Philosophy in Physics

by

William Anthony Farmer

2014

Abstract of the Dissertation

Two Contemporary Problems in Magnetized Plasmas: the ion-ion hybrid resonator and MHD stability in a snowflake divertor

by

William Anthony Farmer

Doctor of Philosophy in Physics

University of California, Los Angeles, 2014

Professor George J. Morales, Chair

The first part of the dissertation investigates the effects of multiple-ions on the propagation of shear Alfvén waves. It is shown that the presence of a second ion-species allows for the formation of an ion-ion hybrid resonator in the presence of a magnetic well. A full-wave description is shown to explain the measured eigenfrequencies and spatial form of the resonator modes identified in experiments in the Large Plasma Device (LAPD) at UCLA. However, it is determined that neither electron collisions or radial convection of the mode due to coupling to either the compressional or ion-Bernstein wave can explain the observed dissipation.

Ray tracing studies for shear Alfvén waves are performed in various magnetic geometries of contemporary interest. In a tokamak, it is found that the hybrid resonator can exist in the cold-plasma regime, but that ion-temperature effects combined with curvature effects cause the wave reflection point to shift towards the cyclotron frequency of the heavier ion. A one-dimensional WKB model is applied to a tokamak geometry for conditions corresponding to a burning fusion plasma to characterize the resonator. Instability due to fusion-born alpha particles is assessed. An approximate form of the global eigenmode is considered. It is identified that magnetic field shear combined with large ion temperature can cause coupling to an ion-Bernstein wave, which can limit the instability. Finally, the radiation pattern of shear Alfvén waves generated by a burst of charged particles in the presence of two-ion

species is considered. The spectral content and spatial patterns of the radiated waves are determined.

The second part of the dissertation considers the MHD stability of the plasma near a divertor in a tokamak. Two types of modes are considered: a ballooning mode and an axisymmetric, quasi-flute mode. Instability thresholds are derived for both modes and numerically evaluated for parameters relevant to recent experiments. This is done to determine whether these modes could be responsible for convection of the plasma in the vicinity of the poloidal null point. It is determined that MHD instability about a standard equilibrium is unlikely to explain the experimental results observed on the tokamak, TCV [Reimerdes *et al.*, Plasma Phys. Contr. Fusion **55**, 124027 (2013)]. From these results, it is concluded that the most likely explanation for the discrepancy is that the underlying equilibrium assumed in the calculation does not contain all the complexities present in the experiments.

LLNL-TH-653594

The dissertation of William Anthony Farmer is approved.

Dmitri D. Ryutov

Christopher T. Russell

Troy A. Carter

Walter N. Gekelman

George J. Morales, Committee Chair

University of California, Los Angeles

2014

To the memory of my grandfather, Harry Paige Farmer. Because of his participation in the American nuclear program, both his health and mental state declined painfully over the last several decades of his life. Both his country and his posterity owe him a great debt.

Table of Contents

List of Figures

List of Tables

Acknowledgments

The author is deeply grateful to G. J. Morales and D. D. Ryutov for the mentoring that they have provided. They are, indeed, true gentlemen. The author would also like to acknowledge J. E. Maggs and S. T. Vincena for collecting the experimental data presented here, and for valuable guidance in analyzing the data. The work was partially sponsored by DOE grant DE-SC0007791, and a portion of the work was performed under the auspices of the U.S. Department of Energy by Lawrence Livermore National Laboratory under Contract DE-AC52-07NA27344.

Vita

2006–2007	Teaching Assistant, Physics and Astronomy Department, BYU. Graded homework and exams for introductory physics courses and upper division, Math Methods class.
2007	Intern, Lawrence Livermore National Lab, assisted in development of neutrino detector deployed at San Onofre Nuclear Reactor
2008	B.S. (Physics), Magna Cum Laude, Brigham Young University
2008–2010	Teaching Assistant, Physics and Astronomy Department, UCLA. Taught introductory lab classes and theory discussion sections. Assisted in teaching upper division quantum classical mechanics. Graded homework and exams, wrote solutions, and held office hours.
2010–2012	Research Assistant, Physics and Astronomy Department, UCLA.
2011	Summer Intern, Lawrence Livermore National Lab. Used particle-in-cell code and analytic models to investigate filamentation in fast-ignition scenarios.
2012–present	Lawrence Scholar, Lawrence Livermore National Lab.

Publications

W. A. Farmer and G. J. Morales. "The ion-ion hybrid resonator in a fusion environment", submitted to Phys. Plasmas on 17 March 2014.

D. D. Ryutov, R. H. Cohen, W. A. Farmer, T. D. Rognlien, M. V. Umansky. "The 'Churning mode' of plasma convection in the tokamak divertor region", Physica Scripta, in press.

W. A. Farmer. "Ballooning modes localized near the null point of a divertor", Phys. Plasmas, 21, 042114 (2014).

W. A. Farmer and D. D. Ryutov. "Axisymmetric curvature-driven instability in a model toroidal geometry". Phys. Plasmas, 20, 092117 (2013).

W. A. Farmer and G. J. Morales. "Propagation of Shear Alfvén waves in two-ion species plasmas confined by a nonuniform magnetic field". Phys. Plasmas, 20, 082132 (2013).

S. T. Vincena, W. A. Farmer, J. E. Maggs, G. J. Morales. "Investigation of an ion-ion hybrid Alfvén wave resonator", Phys. Plasmas, 20, 012111 (2013).

W. A. Farmer and G. J. Morales. "Cherenkov radiation of shear Alfvén wave in plasmas with two ion species", Phys. Plasmas, 19, 092109 (2012).

W. A. Farmer, G. J. Morales, S. T. Vincena, and J. E. Maggs. "The ion-ion hybrid Alfvén resonator in a fusion environment", in Proc. of the 39th European Conference on Plasma Physics and 16th Int. Congress on Plasma Physics, Stockholm, 2012.

S. T. Vincena, W. A. Farmer, J. E. Maggs, G. J. Morales. "Laboratory realization of an ion-ion hybrid Alfvén wave resonator", Geophys. Res. Lett., 38, L11101 (2011).

CHAPTER 1

Introduction

1.1 Historical Perspective

This dissertation examines two contemporary problems in magnetically confined plasmas. The first is an examination of the properties of shear Alfvén waves in a plasma consisting of two ion species of differing charge to mass ratios. The second is an examination of magnetohydrodynamic (MHD) instability in the presence of a poloidal null in a tokamak divertor.

The impact of multiple ion species on wave propagation in a magnetized plasma has been investigated for more than a half-century. It was first observed by Buchsbaum that a plasma with two ion species exhibits a unique frequency, the ion-ion hybrid frequency, that acts as a collective resonance for waves propagating across the magnetic field [1]. This observation was also made by Smith and Brice and applied to an ionospheric plasma [2]. This resonance is primarily due to the vanishing of the perpendicular component of the cold plasma dielectric tensor, which takes the form

$$\varepsilon_{\perp} = \frac{c^2}{v_A^2} \frac{1 - \omega^2/\omega_{ii}^2}{\left(1 - \omega^2/\Omega_1^2\right)\left(1 - \omega^2/\Omega_2^2\right)}. \tag{1.1}$$

In the above expression, c is the speed of light, v_A, the Alfvén velocity, ω, the wave frequency, Ω_j is the cyclotron frequency for ion species, j, with plasma frequency, ω_{pj}, and ω_{ii} is the ion-ion hybrid frequency, given by,

$$\omega_{ii}^2 = \frac{\omega_{p1}^2 \Omega_2^2 + \omega_{p2}^2 \Omega_1^2}{\omega_{p1}^2 + \omega_{p2}^2}. \tag{1.2}$$

This resonance was later verified experimentally by Ono [3] among others. The shear Alfvén wave propagates predominantly along the magnetic field, with wave energy falling inside

a cone, for electrons in both the inertial and adiabatic regimes. This property has also been verified by experiments [4, 5] and simulations [6]. Because the wave propagates predominantly along the confining magnetic field, the ion-ion hybrid frequency acts as cutoff for the wave. This property can be seen from the simplified dispersion relation, valid for perpendicular scales that are much smaller than the ion skin-depth,

$$k_{||}^2 = k_0^2 \varepsilon_\perp \left(1 - \frac{k_\perp^2}{k_0^2 \varepsilon_{||}}\right). \tag{1.3}$$

Here, $k_{||}$ and $k_\perp$ are the parallel and perpendicular wave numbers, respectively, $k_0 = \omega/c$ is the vacuum wave number, and $\varepsilon_{||}$ is the parallel component of the dielectric tensor. Because of this wave cut-off, the shear wave can reflect upon propagating into a magnetic field gradient. This reflection occurs when the wave frequency matches the local value of the ion-ion hybrid frequency, $\omega = \omega_{ii}$.

The important role played by this wave cut-off has long been recognized by the space physics community. Young et al. [7] observed that ULF wave spectra could be qualitatively explained by the inclusion of a minority of helium in a background of protons. Motivated by these observations, Rauch and Roux [8] performed raytracing studies in which multiple reflections of ULF waves occur at conjugate points where $\omega = \omega_{ii}$ in the earth's dipole field. Further observations compared magnetic field measurements of GEOS 1 and 2 to ground-based magnetometers at the magnetic footprints of the satellites [9]. These results were consistent with wave reflection at the ion-ion hybrid layer in the magnetosphere. Other observations indicated that narrow-banded waves localized to the auroral region and generated by an energetic electron beam could be explained by the presence of a two-ion, $H^+ - He^+$ plasma [10]. The presence of two, conjugate reflection points in the magnetosphere motivated Guglielmi et al. [11] to conclude that a wave resonator would naturally exist in planetary magnetospheres. This dissertation refers to this resonator as the ion-ion hybrid resonator, though it has been referred to by other names. The characteristic resonator spectrum was computed and compared to data from the ISEE-1 and 2 satellites, but the observed data did not have sufficient resolution to verify the existence of the resonator. Further understanding of the ion-ion hybrid resonator was developed in a detailed theoretical study by Mithaiwala

et al. [12]. This work considered the excitation of the mode as a consequence of man-made neutral gas release. It concluded that the wave energy could be trapped for several reflections, and would ultimately dissipate by radial convection and collisional effects. Apart from playing a key role in magnetospheric resonators, the shear Alfvén wave is also of interest, because the waves can be driven unstable by energetic ion distributions [13] and pitch-angle scatter energetic electrons [14].

Experimental evidence of shear wave reflection at the ion-ion hybrid frequency has been found in both linear devices [15] and tokamaks [16]. Further, experiments in which the shear wave was indirectly excited through mode conversion processes in a tokamak detected a discrete frequency spectrum at the plasma edge [17]. This suggests the possibility of an ion-ion hybrid resonator in a tokamak due to variations in magnetic field strength along a field line from the outboard to the inboard side.

Excitation of the resonator in a tokamak environment could occur by either mode conversion from an incident compressional wave or excitation by energetic particles introduced into the plasma either by neutral beams or naturally by alpha particles under fusion conditions. In current ion-cyclotron frequency (ICRF) heating scenarios, an incident compressional wave experiences a resonance as it propagates across the magnetic field, resulting in heating of the minority ion species [18, 19, 20, 21, 22]. Lee et al. [23] reported excitation of ion Bernstein waves (IBW) through linear mode conversion of an incident compressional wave. This is relevant to the ion-ion hybrid resonator, because, quoting Intrator et al. [17], "the distinction between IBW and [kinetic Alfvén wave] may be more semantic than real." More recently on Alcator C-Mod, minority heating was accomplished by injecting fast waves into deuterium plasmas with a minority of helium-3 [24]. Toroidal rotation occurred and was shown to correlate with the radio-frequency (RF) power injected. Further, a mode converted shear Alfvén wave was observed, approximately on the same flux surface where the RF flow occurred. These experimental results suggest that it is possible to excite the resonator indirectly by mode conversion of the incident compressional wave. Excitation by an energetic ion population is supported by a theoretical study performed by Lashmore-Davies and Russell [25], in which they considered instability of the shear wave by a fusion-born alpha population. They

showed that instability does indeed occur in a narrow frequency band close to the ion-ion hybrid frequency and for certain perpendicular wavelengths.

Study of the resonator in a tokamak geometry has been limited. Shear Alfvén waves are well understood for frequencies much smaller than the ion cyclotron frequencies [26]. Due to toroidicity effects, marginally stable eigenmodes exist within frequency gaps and can be excited by energetic ion populations. This feature is supported by experimental evidence [27], and theoretical studies are able to qualitatively reproduce the observed behavior [28]. Moiseenko and Tennfors [29] attempted to extend the theory to frequencies above the ion-ion hybrid in two-ion species plasmas. They identified a new class of modes that can exist at these frequencies, but they did not consider the possibility of a resonator.

These theoretical and experimental results suggest that the shear wave may be relevant to the "alpha channeling" concept. Alpha channeling was originally proposed by Fisch and Rax [30] because the Landau damping of lower hybrid waves by alpha particles was thought to interfere with current drive in a tokamak reactor. However, as Fisch and Rax showed, by judicious choice of the diffusion path, the alpha particle diffusion in velocity can be effectively coupled to diffusion in space, thereby giving growth rather than damping of the lower hybrid wave. In the process of releasing the alpha particle energy, there is necessarily diffusion of the alpha particles towards the periphery, which not only releases energy to power the current drive but also promptly removes the fusion ash and purifies the plasma fuel. During mode-converted ion Bernstein wave experiments on the Tokamak Fusion Test Reactor (TFTR), energetic deuterium beam ions were used as surrogate particles in order to examine the interactions of these energetic particles with the ion Bernstein waves. Anomalously high loss rates for energetic particles were observed [31, 32]. The high loss rate, in principle, could be due to either an effect that amplifies the wave field or one that accelerates the diffusion process. The most plausible explanation was an internal eigenmode excited by the ion Bernstein wave (IBW) and that interacts with the beam ions [33]. Because of these many results, it is appropriate to study the ion-ion hybrid resonator in a fusion environment.

The second topic of study in this dissertation, MHD stability near a poloidal null in a tokamak divertor, is of interest due to the recently proposed snowflake divertor [34, 35]. The

snowflake divertor was proposed as a method for reducing heat loads on the divertor plates. This is necessary because the expected heat loads in a reactor are well beyond the limits of existing materials. In a standard divertor configuration, the poloidal field strength, B_p, increases linearly with distance from the null point, $B_p \propto d$, and the separatrices dividing the core plasma from the scrape-off-layer (SOL) and private flux region form a characteristic 'X' shape. In contrast, the snowflake divertor possesses a quadratic dependence, $B_p \propto d^2$, causing the separatrices to possess a characteristic hexagonal structure, which resembles a snowflake. The quadratic dependence of the poloidal field strength leads to an increased flux expansion at the target plates, increased shear in the pedestal region, and stronger squeezing of magnetic flux-tubes passing near the null-point [36]. The flux expansion reduces heat loads directly by increasing the area over which the heat is deposited. The increased shear and stronger squeezing of magnetic flux-tubes will impact plasma instabilities common to the edge region: edge-localized modes (ELMs) and blobs. Further theoretical investigation concluded that the magnetic geometry of the snowflake divertor will lead to increased divertor radiation leading to plasma detachment from the divertor plates, alleviation of the divertor target heat load, and better control of ELMs [37].

The snowflake divertor has been realized experimentally on the tokamaks, NSTX [38, 39], TCV [40, 41, 42], and DIII-D [43]. These results demonstrated that a snowflake divertor can be realized in an H-mode plasma. A reduction in heat loads was observed and ELM properties were altered. The experiments on NSTX observed impurity screening and partial detachment as a result of increased radiative losses by the SOL plasma [39], while the experiments on TCV observed that the snowflake divertor would redistribute the edge power onto additional strike points, allowing for further reductions in heat flux [42, 44]. This redistribution cannot be explained by standard transport processes alone [45] and suggests that enhanced plasma convection is occurring in the vicinity of the poloidal null. Three possible sources of the enhanced convection have been proposed: a loss of equilibrium, instability of an axisymmetric, curvature-driven mode which leaves the toroidal field unperturbed, and a ballooning instability occurring in the vicinity of the null point [46]. While simple scaling arguments of these mechanisms have been employed [47, 48], more detailed investigation is

necessary to elucidate the cause of the enhanced transport. Further, a detailed understanding of the precise mechanism which is driving this convective process is necessary in order to optimize the reduction in heat loads. The second portion of this dissertation aims to do just that by performing a detailed theoretical analysis of both the axisymmetric and ballooning instabilities.

1.2 Major Results

Chapter 2 presents both experimental data and theoretical modeling of experiments performed on the Large Plasma Device (LAPD) at UCLA. In the experiment, an antenna launches shear Alfvén waves. The background plasma consists of various mixtures of hydrogen and helium, and the background magnetic field is shaped to form a magnetic well centered on the antenna. The antenna is driven in both monochromatic and pulsed configurations. A full-wave description is developed based on a cold-plasma treatment. Electron collisions are included in the parallel component of the dielectric tensor. Radial density gradients and coupling to the compressional wave are neglected. Figure 1.1 shows a wavelet transform of a magnetic field measurement when the antenna is pulsed. The probe is located inside the magnetic well. Trapped, resonator modes exist between the two ion-ion hybrid frequencies marked by the red lines labeled ω_{ii}(750 G) and ω_{ii}(1250 G). The long-lived signals are identified as the eigenmodes of the cavity. In the bottom panel, cuts are made at various times, showing the temporal decay of the peaks. The predicted eigenfrequencies are given by the vertical dash-dotted lines. The quality factors of the observed peaks is found to be on the order of 20. If dissipation were due to electron collisions alone, the theory predicts quality factors an order of magnitude greater than that which is observed. In Chapter 3, ray tracing is used to assess whether radial convection of the mode caused by coupling to the compressional and ion-Bernstein waves could account for the observed quality factors. While this is an important dissipation mechanism, even with the radial spreading of the mode, the predicted quality factor is still too large by a factor of five. It is also determined that ion-neutral collisions, ion-cyclotron damping, and electron Landau damping are unlikely

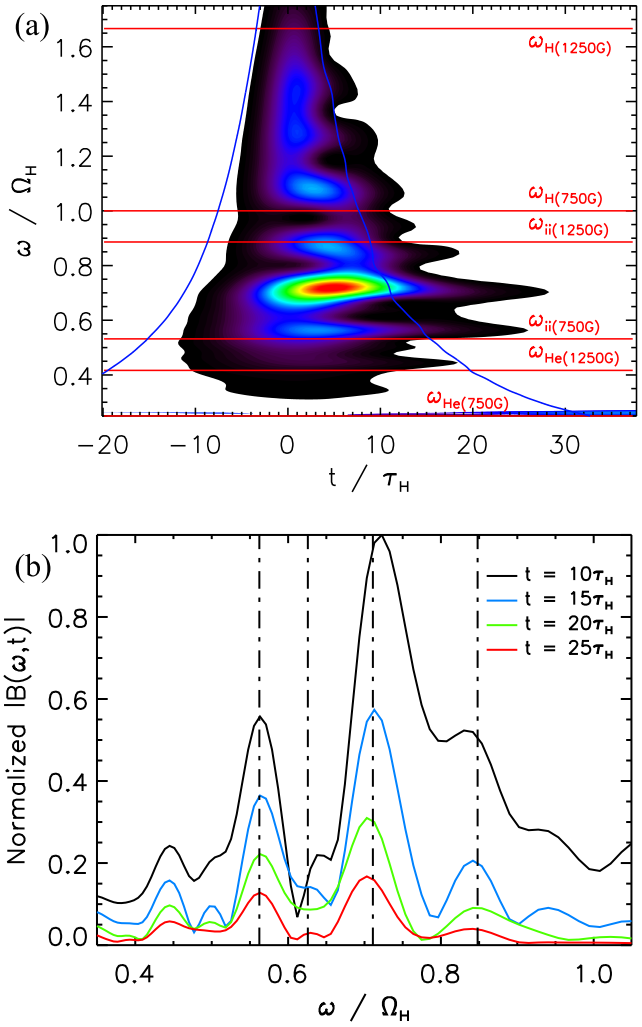

Figure 1.1: (a) Color contours of Morlet wavelet amplitude of magnetic field fluctuations show the response of the H^+ - He^+ resonator after excitation with a current impulse of width $\Delta t = \tau_H$ at $t = 0$. The plasma is 45% hydrogen and the probe is at z = +128 cm, r = +17.5 cm. (b) Instantaneous wavelet spectra obtained from vertical cuts in (a) at four different times. Vertical dashed lines are the predicted resonator eigenfrequencies.

to provide the necessary dissipation. Future investigation should explore the role of radial density gradients on mode conversion processes, and transit time acceleration of electrons in the reflection region. However, these effects are beyond the scope of this dissertation.

Chapter 3 uses ray-tracing to explore the propagation of shear Alfvén waves in the presence of two-ion species in three magnetic geometries of contemporary interest: a linear device relevant to studies on LAPD, a pure toroidal field relevant to studies on the Enormous Toroidal Device (ETPD) at UCLA, and a tokamak. The studies on LAPD and ETPD both illustrate the presence of radial reflections due to coupling to the compressional and ion-Bernstein wave. In the presence of a pure toroidal field, the curvature of the field line is shown to preferentially increase $k_\perp$ in the direction opposite the field line curvature. This causes several radial reflections to occur over the trajectory of the ray. In a tokamak, these radial reflections could be used to focus the ray, prolonging the time for which the wave energy is radially confined. Figure 1.2 illustrates ray propagation in a tokamak with ITER-like parameters. A poloidal cross-section of the ray trajectories is displayed with the rays undergoing large toroidal displacements over the trajectories shown. The blue curve illustrates ray propagation when ion-temperature effects are negligible. The ray is launched from the position $r = 50$ cm, $z = 20$ cm. Initially, it propagates outward across the nested flux surfaces until it experiences a radial reflection, at which point, it wanders inward towards the magnetic axis. Because ion-temperature effects are negligible, the ray reflects at roughly the same location in r, where the wave frequency matches the local ion-ion hybrid frequency. The red dashed curve illustrates the ray trajectory when finite ion temperature effects are included. For this ray, parallel reflection no longer occurs when the wave frequency matches the local ion-ion hybrid frequency. Instead, the reflection point becomes dependent on the value of $k_\perp$. Since the curvature of the field line preferentially increases $k_\perp$ in the direction opposite to the field-line curvature, the reflection point recedes towards the tritium cyclotron frequency as the ray propagates. The red dashed curve shown in the figure is not a trapped mode, because the size of the well expands to such a degree that kinetic damping processes would dissipate the mode before reflection could occur.

To better understand under what conditions trapped modes can exist in a burning plasma,

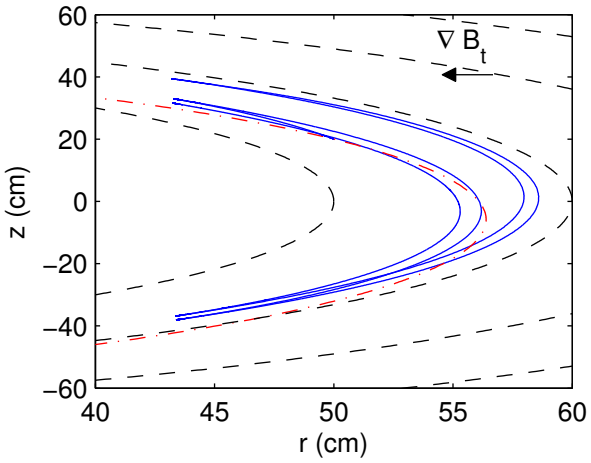

Figure 1.2: Poloidal projection of ray trajectories in ITER. Vertical axis represents vertical displacement of a ray from the magnetic axis, and the horizontal axis represents the radial displacement from the magnetic axis. The black dashed lines represent the nested flux surfaces. The solid (blue) curve is a ray for which the cold plasma dispersion relation is used, and the dashed-dotted (red) curve uses the hot-ion dispersion relation. Both rays have an initial perpendicular wave number that points towards the magnetic axis. The direction of the gradient of the toroidal field strength is shown; the perpendicular wave number preferentially increases in the opposite direction of this gradient. The cold ray is trapped within the magnetic well. It wanders outward across magnetic flux surfaces before propagating inward due to the perpendicular reflection examined earlier for ETPD. The hot ion result is not confined due to the reflection point moving towards the inboard side of the device as the perpendicular wave number increases.

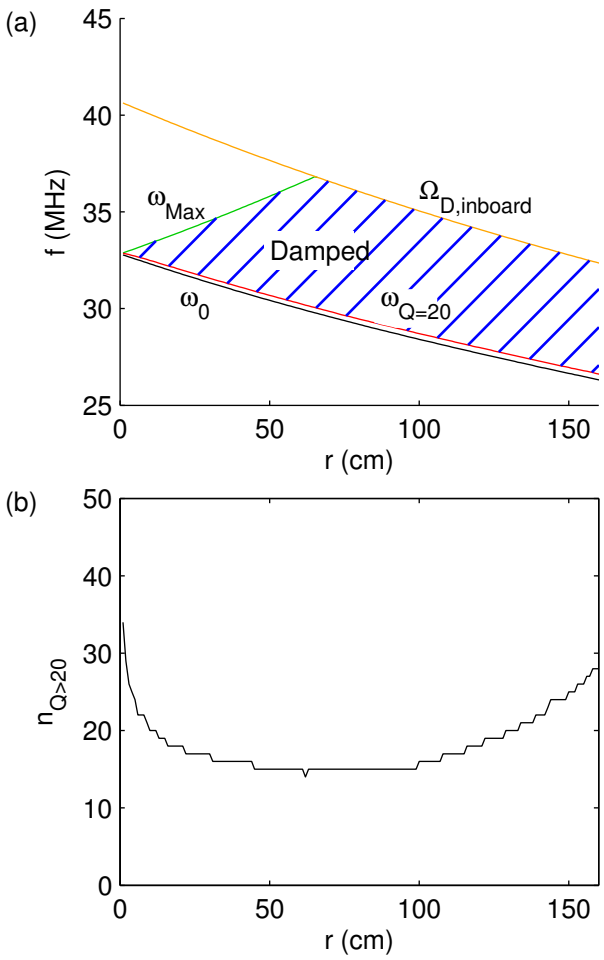

Figure 1.3: Radial dependence of resonator parameters. Horizontal axes correspond to radius from magnetic axis. Plasma parameters and safety factor are given in Fig. 4.6. Magnetic field strength is given by Eq. (4.45) with $B_0 = 53$ kG and $R = 621$ cm; perpendicular wavelength is $\lambda_\perp = 10$ cm, corresponding to $k_\perp \delta_e = 0.043$ at the magnetic axis. (a) Radial dependence of relevant frequencies. Vertical axis corresponds to frequency in MHz. Bottom black curve corresponds to the fundamental eigenfrequency in the resonator, ω_0; red curve to frequency of modes having $Q = 20$, $\omega_{Q=20}$. The slanted green line, labeled ω_{Max}, corresponds to the cut-off frequency on the inboard side; waves in the blank region to its left are not trapped. This frequency terminates when the deuterium cyclotron frequency on the inboard side, represented by the top orange curve labeled $\Omega_{\mathrm{D,inboard}}$, because of heavy cyclotron damping. The blue hatched region, labeled "Damped", corresponds to strongly damped modes with $Q < 20$. (b) Vertical axis corresponds to the number of long-lived modes with $Q > 20$.

Chapter 4 uses a one-dimensional WKB model with a fully kinetic dispersion relation. Radial profiles of plasma parameters determined by simulations are used to model the plasma [49], and the geometry is described in the cylindrical approximation. Figure 1.3 displays parameters associated with the trapped modes as a function of the radius of the flux surface, r. The top panel illustrates the fundamental frequency, the black curve labeled ω_0, and the frequency for which a mode has a quality factor of $Q = 20$ due to kinetic damping, the red curve labeled $\omega_{Q=20}$. Above $\omega_{Q=20}$, heavy damping occurs as illustrated by the blue hatched region. The reference frequency, ω_{Max} indicated by the green line, represents the reflection frequency on the inboard side of the flux surface. Above this frequency, the wave propagates along the entire flux surface and is not trapped. The green line terminates at the cyclotron frequency of deuterium on the inboard side, $\Omega_{D,\mathrm{inboard}}$ indicated by the orange line, because heavy cyclotron damping is expected to occur. From this display, it is clear that trapped modes will exist in a narrow frequency band close to the reflection frequency on the outboard side. The bottom panel displays the number of modes with quality factors greater than 20 as a function of radius, showing that many modes exist over the radius of the plasma. Beyond characterizing the modes, an assessment of plasma instability due to a ring-distribution of fusion born alpha particles is also made. From this assessment, it is determined that a bandwidth of roughly 600 kHz will be unstable over most of the flux surfaces. This instability is shown to depend on the value of $k_\perp$, and for this reason, if the effects of magnetic curvature and magnetic shear are included, this instability can be detuned for a given mode. Since many values of $k_\perp$ will be excited, it is unclear from this model what the ultimate nature of this instability will be, and state of the art simulation tools would be needed to fully assess the consequences of the wave-particle interaction.

Chapter 5 details an investigation of Cherenkov radiation due to a charged particle burst in the presence of a two-ion species plasma. The wake pattern is obtained for the inertial and kinetic regimes of wave propagation. Due to the presence of two ion-species, the Alfvén waves propagate within two different frequency bands separated by a gap. One band is restricted to frequencies below the cyclotron frequency of the heavier species and the other to frequencies between the ion-ion hybrid frequency and the cyclotron frequency of the lighter

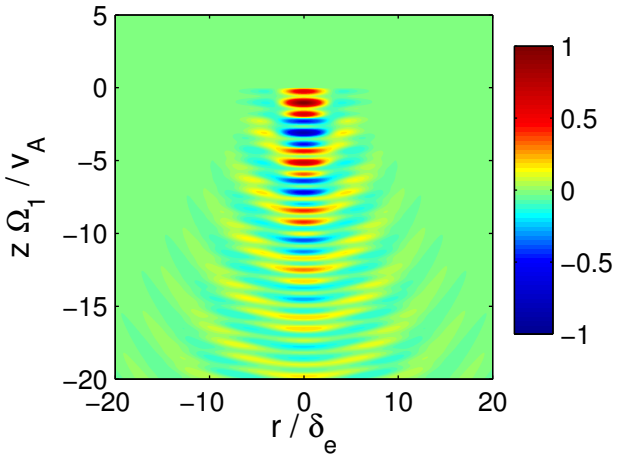

Figure 1.4: Wake radiated by a particle burst in the inertial regime. Spatial pattern of parallel current density $j_z/|j_z|_{\mathrm{Max}}$ in the inertial regime for a hydrogen-helium plasma. Color contours represent the current wake at $t = 0$ with the charge burst centered at the origin and moving upwards. Two separate patterns are clearly visible. The broader, longer wavelength pattern corresponds to the lower frequency branch and the narrower, shorter wavelength pattern, to the upper branch.

species. The radiation pattern in the slower frequency band is found to exhibit essentially the same properties reported in a previous study [50] of a single species plasma. However, the upper frequency band differs from the lower one in that it always allows for the Cherenkov radiation condition to be met. The methodology is extended to examine the Alfvénic wake of point-charges in the inertial and adiabatic regimes. The adiabatic regime is illustrated for conditions applicable to fusion-born alpha particles in ITER. Figure 1.4 illustrates the wake for a charged-particle burst for conditions relevant to LAPD and in the inertial regime. In the figure, the two patterns are clearly visible, and the inverted-V structure due to the backward-traveling nature of the shear wave is evident.

Chapters 6 and 7 detail an investigation of MHD plasma stability for the plasma in the divertor of a tokamak. Analysis is performed for both a standard divertor and a snowflake. The plasma is assumed to have an equilibrium in which confinement is achieved by the interaction of the poloidal current with the toroidal field. However, since the plasma pressure

in this region is small, $\beta_t = 8\pi p/B_t^2 \ll 1$, and the toroidal field is well described by its vacuum field. The poloidal field is assumed to be curl free, reflecting the neglect of toroidal current. Flux coordinates are used to describe the complex geometry present in the vicinity of the poloidal null of a divertor. In Chapter 6, instability of ballooning modes is considered. It is shown that this threshold depends on the orientation of the flux surfaces with respect to the major radius with a critical angle appearing due to the convergence of the field lines away from the null point. When the angle that the major radius forms with respect to the flux surfaces exceeds this critical angle, the system is stabilized. Further, the scaling of the instability threshold with the aspect ratio and the ratio of the scrape-off-layer width to the major radius is shown. The instability threshold is evaluated for parameters of existing devices, and it is concluded that this instability should not be active. For this reason, it is not likely to explain current experimental results [44] which suggest that a mechanism is present that enhances transport in the divertor [45]. Chapter 7 uses much of the machinery developed in the preceding chapter to investigate instability of an axisymmetric, quasi-flute mode. The instability thresholds for the axisymmetric mode are shown to possess the same scalings as those for the ballooning mode. For this reason, the axisymmetric mode is also not likely to explain the experimental results reported to date.

CHAPTER 2

Resonator in LAPD

This chapter outlines both theoretical modeling and experimental results obtained from an investigation of the ion-ion hybrid resonator in the Large Plasma Device (LAPD) [51] at UCLA. Section 2.1 outlines the theoretical model used to compare to the experimental data. Section 2.2 applies the model and approximates the magnetic profile as a simple square well. This simple model allows for concise predictions to guide and plan experiments. Section 2.3 extends the square well model to include gradient effects due to the gradual transition that occurs from the low field to high field regions. Section 2.4 presents the experimental results. Two types of experiments are performed. In the first, the antenna is driven monochromatically, and the response is measured as a function of frequency. In the second, the antenna is pulsed, launching many frequencies at once. In this latter experiment, a wavelet analysis is performed of the data to determine the long-lived frequencies and their associated quality factors. Finally, a comparison of the theoretical model to the experimental predictions is made in section 2.5, and major conclusions are presented.

2.1 Model

The theory presented here assumes a cold plasma model. This is a good approximation for the plasma parameters encountered in the LAPD experiments. Starting from Maxwell's equations, and including a source current, $\mathbf{j}$, oscillating with frequency, ω, the resulting equation is

$$\nabla \times (\nabla \times \mathbf{E}) - \frac{\omega^2}{c^2} \boldsymbol{\varepsilon} \cdot \mathbf{E} = \frac{4\pi i \omega}{c^2} \mathbf{j}. \tag{2.1}$$

Here, $\mathbf{E}$ is the electric field, c, the speed of light, and $\boldsymbol{\varepsilon}$ is the cold plasma dielectric tensor. Cylindrical coordinates are the natural choice for the LAPD, so the coordinate system (r, ϕ, z) is employed with the origin located at the center of the plasma column. The antenna is modeled by an axial current channel of radius R and length $2a$ located at the center of a magnetic well. The azimuthally symmetric Fourier component of the radial feeds is included by requiring that $\nabla \cdot \mathbf{j} = 0$. This preserves azimuthal symmetry for the system, and derivatives with respect to ϕ can be neglected as a result.

The background magnetic field takes the form $\mathbf{B} = B_r(r, z)\hat{\mathbf{r}} + B_z(z)\hat{\mathbf{z}}$. The function, $B_z(z)$, is determined from the experimental magnetic profile. The condition, $\nabla \cdot \mathbf{B} = 0$, implies that

$$B_r = -\frac{r}{2}\frac{dB_z(z)}{dz}. \tag{2.2}$$

If the characteristic length scale of B_z is large compared to the radius of the device, B_r can be neglected. For typical magnetic profiles, the magnetic length scale is 270 cm with the radius of the LAPD, 50 cm. Thus, for this model, the background magnetic field is assumed to be along the z-axis and to depend only on z. Additionally, the densities of all plasma species (both ions and electrons) are assumed to be uniform. In reality, a radial density profile exists in the plasma, and this gradient modifies the radial eigenfunctions from the uniform case. A further simplification exists through neglecting the off-diagonal components of the dielectric tensor, ε_{xy}, removing the coupling between the shear and compressional Alfvén waves. This approximation is appropriate when the largest transverse scale in the system is smaller than the ion-skin depth, as is the case in LAPD. This last approximation is postponed for now, but it will be made later in this section.

Equation (2.1) now becomes

$$\frac{\partial}{\partial z}\left(\frac{\partial E_z}{\partial r} - \frac{\partial E_r}{\partial z}\right) - k_0^2\varepsilon_\perp E_r - k_0^2\varepsilon_{xy}E_\phi = \frac{4\pi i\omega}{c^2}j_r, \tag{2.3}$$

$$\frac{\partial^2 E_\phi}{\partial z^2} + \frac{\partial}{\partial r}\left[\frac{1}{r}\frac{\partial}{\partial r}\left(rE_\phi\right)\right] + k_0^2\varepsilon_\perp E_\phi - k_0^2\varepsilon_{xy}E_r = 0, \tag{2.4}$$

$$\frac{1}{r}\frac{\partial}{\partial r}\left[r\left(\frac{\partial E_r}{\partial z} - \frac{\partial E_z}{\partial r}\right)\right] - k_0^2\varepsilon_{||}E_z = \frac{4\pi i k_0}{c}j_z, \tag{2.5}$$

where $k_0 = \omega/c$. Because the coefficients appearing in the above three equations do not

depend on r, all quantities can be expanded through a Fourier-Bessel transform. The azimuthal magnetic field is easily measured with the use of B-dot magnetic probes, and so it is included in the expressions below.

$$E_z(r,z) = \int_0^\infty J_0(k_\perp r)\tilde{E}_z(k_\perp,z)k_\perp dk_\perp, \tag{2.6}$$

$$E_r(r,z) = \int_0^\infty J_1(k_\perp r)\tilde{E}_r(k_\perp,z)k_\perp dk_\perp, \tag{2.7}$$

$$E_\phi(r,z) = \int_0^\infty J_1(k_\perp r)\tilde{E}_\phi(k_\perp,z)k_\perp dk_\perp, \tag{2.8}$$

$$j_r(r,z) = \int_0^\infty J_1(k_\perp r)\tilde{j}_r(k_\perp,z)k_\perp dk_\perp, \tag{2.9}$$

$$j_z(r,z) = \int_0^\infty J_0(k_\perp r)\tilde{j}_z(k_\perp,z)k_\perp dk_\perp, \tag{2.10}$$

$$B_\phi(r,z) = \int_0^\infty J_1(k_\perp r)\tilde{B}_\phi(k_\perp,z)k_\perp dk_\perp. \tag{2.11}$$

Requiring that the current density of the source satisfy $\nabla \cdot \mathbf{j} = 0$ results in

$$\frac{\partial \tilde{j_z}}{\partial z} + k_\perp \tilde{j}_r = 0. \tag{2.12}$$

This allows for the elimination of $\tilde{j}_r$ in the equations that follow. With these transformations, Eqs. (2.3)-(2.5) can be reduced to two coupled equations,

$$\frac{\partial^2 \tilde{E}_r}{\partial z^2} + k_0^2\varepsilon_\perp\left(1 - \frac{k_\perp^2}{k_0^2\varepsilon_{||}}\right)\tilde{E}_r + k_0^2\varepsilon_{xy}\left(1 - \frac{k_\perp^2}{k_0^2\varepsilon_{||}}\right)\tilde{E}_\phi = \frac{4\pi i k_0}{ck_\perp}\frac{\partial \tilde{j}_z}{\partial z}, \tag{2.13}$$

$$\frac{\partial^2 \tilde{E}_\phi}{\partial z^2} + \left(k_0^2\varepsilon_\perp - k_\perp^2\right)\tilde{E}_\phi - k_0^2\varepsilon_{xy}\tilde{E}_r = 0, \tag{2.14}$$

and the algebraic expressions

$$\tilde{E}_z = \frac{1}{k_\perp^2 - k_0^2\varepsilon_{||}}\left(\frac{4\pi i k_0}{c}\tilde{j}_z - k_\perp\frac{\partial \tilde{E}_r}{\partial z}\right), \tag{2.15}$$

$$\tilde{B}_\phi = \frac{1}{k_\perp^2 - k_0^2\varepsilon_{||}}\left(\frac{4\pi k_\perp}{c}\tilde{j}_z + ik_0\varepsilon_{||}\frac{\partial \tilde{E}_r}{\partial z}\right). \tag{2.16}$$

In this form, the role of ε_{xy} is clear as it provides the coupling between the two components, $\tilde{E}_r$ and $\tilde{E}_\phi$. In the limit of small transverse scale, a single, uncoupled equation results,

$$\frac{\partial^2 \tilde{E}_r}{\partial z^2} + k_0^2\varepsilon_\perp\left(1 - \frac{k_\perp^2}{k_0^2\varepsilon_{||}}\right)\tilde{E}_r = \frac{4\pi i k_0}{ck_\perp}\frac{\partial \tilde{j}_z}{\partial z}, \tag{2.17}$$

Equation (2.17) contains an effective potential and a source term on the right hand side. To understand the form of the potential, expressions for $\varepsilon_\perp$ and $\varepsilon_{||}$ are needed. For frequencies on the order of the ion-cyclotron frequencies, and including two ion species in the formulation,

$$\varepsilon_{||} = -\frac{\omega^2}{\omega_{pe}^2}, \tag{2.18}$$

$$\varepsilon_\perp = \left(\frac{c}{v_A}\right)^2 \frac{1-\frac{\omega^2}{\omega_{ii}^2}}{\left(1-\frac{\omega^2}{\Omega_1^2}\right)\left(1-\frac{\omega^2}{\Omega_2^2}\right)}, \tag{2.19}$$

where the frequencies, Ω_1 and Ω_2, are the ion cyclotron frequencies and ω_{pe} is the electron plasma frequency, ω_{ii} is the ion-ion hybrid frequency, and v_A is the Alfvén speed. The Alfvén speed and the ion-ion hybrid frequency are related to the ion plasma and cyclotron frequencies as follows,

$$v_A = \frac{\Omega_1\Omega_2}{\sqrt{\omega_{p1}^2\Omega_2^2 + \omega_{p2}^2\Omega_1^2}}c, \tag{2.20}$$

$$\omega_{ii}^2 = \frac{\omega_{p1}^2\Omega_2^2 + \omega_{p2}^2\Omega_1^2}{\omega_{p1}^2 + \omega_{p2}^2}. \tag{2.21}$$

To better understand the resonator, the constant magnetic field case with no source is considered in the context of Eq. (2.17). A constant field would allow for a Fourier transform in the z coordinate and would lead to the dispersion relation,

$$k_{||}^2 = \frac{\omega^2}{v_A^2}\frac{1-\frac{\omega^2}{\omega_{ii}^2}}{\left(1-\frac{\omega^2}{\Omega_1^2}\right)\left(1-\frac{\omega^2}{\Omega_2^2}\right)}\left(1+k_\perp^2\delta_e^2\right), \tag{2.22}$$

where $\delta_e = c/\omega_{pe}$ is the electron skin depth. For a fixed value of $k_\perp$, it is clear from the form of the dispersion relation that two wave-particle resonances exist at the cyclotron frequencies of the respective ions, while a cutoff exists at the ion-ion hybrid frequency which has a value between the two cyclotron frequencies. Figure 2.1 illustrates this relation by showing the separation of wave solutions into two distinct bands separated by an evanescent region. A cutoff exists in the upper band. It is this cutoff that gives rise to the possibility of a resonator.

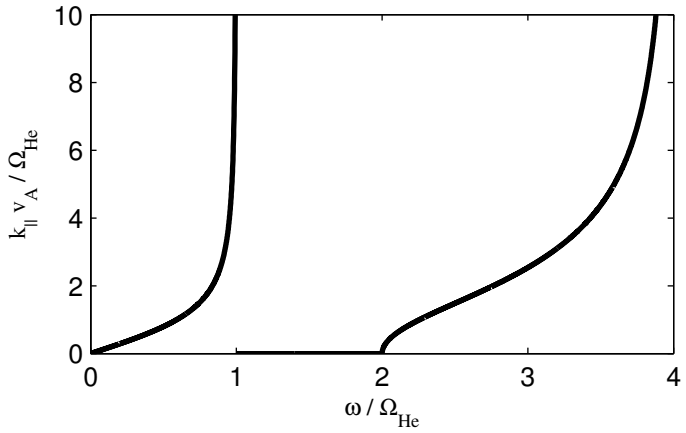

Figure 2.1: Plot of Eq. (2.22). Vertical axis is the scaled parallel wave number, and horizontal axis is the scaled frequency. Plots are made for $k_\perp \delta_e = 1$ and equal concentrations of H-He. Resonances are present at cyclotron frequencies of hydrogen and helium. A cutoff is present at the ion-ion hybrid frequency at $\omega/\Omega_{He} = 2$. An evanescent region exists between the helium cyclotron frequency and the ion-ion hybrid frequency.

Since the density is assumed constant, it is clear that the only spatial variations in the potential term of equation (2.17) is through $\varepsilon_\perp$ which depends on the magnetic field strength through the cyclotron frequencies. If the background magnetic field strength has the form of a magnetic well, it is possible to create two conjugate reflection points and trap the waves. Thus, in order to solve equation (2.17), a magnetic profile must first be specified. The next two sections discuss solutions to this equation when certain approximations for the magnetic profile are made.

2.2 Square well model

The simplest model for a magnetic profile that still retains the necessary features to create a resonator is a square well. In this case, the differential equation can be solved in a piecewise fashion. The source term is neglected in what follows, but a simple relation is derived to give a rough estimate of the eigenfrequencies based on the length of the well.

Let the magnetic well have length $2L$, with $z = 0$ chosen to be the center of the well.

The frequency, ω, and magnetic field strength inside the well, B_l, are assumed to give a propagating solution, k_l, which falls in the upper frequency band illustrated in Fig. 2.1. Similarly, the magnetic field strength outside the well, B_h, is assumed to give rise to an evanescent solution, k_h, which would fall in the gap shown in the same figure. Both k_l and k_h are assumed to be both real valued and positive, and they are given by the modulus of the solution to equation (2.22) evaluated at the appropriate magnetic field strength. With these definitions, the piecewise solution for equation (2.17) can be written as

$$\tilde{E}_r(z, k_\perp) = \begin{cases} C_1 e^{-k_h z} & z > L \\ C_2 \left(e^{ik_l z} \pm e^{-ik_l z} \right) & |z| < L \\ \pm C_1 e^{k_h z} & z < -L \end{cases} . \tag{2.23}$$

The solution has been written in a form such that it is inherently either even or odd. This is a required property of the solution due to the symmetry of the magnetic well.

In order to find the eigenfrequencies associated with the eigenfunctions, the boundary conditions must be specified. These conditions are that E_r and $\varepsilon_{||} E_z$ must be continuous across the boundary. From Eq. (2.15), this can be shown to be equivalent to the continuity of E_r and $(\varepsilon_\perp / k_{||}) E_r$. Applying these conditions results in the equations,

$$C_2 \left(e^{ik_l L} \pm e^{-ik_l L} \right) = C_1 e^{-k_h L}, \tag{2.24}$$

$$\frac{\varepsilon_{\perp l}}{k_l} C_2 \left(e^{ik_l L} \mp e^{-ik_l L} \right) = -i \frac{\varepsilon_{\perp h}}{k_h} C_1 e^{-k_h L}. \tag{2.25}$$

Eliminating C_1 and C_2 from the two equations and applying the dispersion relation yields the equations

$$\cot(k_l L) = \sqrt{-\frac{\varepsilon_{\perp l}}{\varepsilon_{\perp h}}}, \tag{2.26}$$

$$\tan(k_l L) = -\sqrt{-\frac{\varepsilon_{\perp l}}{\varepsilon_{\perp h}}}, \tag{2.27}$$

where the solutions to the first equation are the eigenfrequencies of the even solutions and the solutions to the second equation, of the odd.

From this simple model, the eigenfrequencies can be calculated. For comparison to a possible experiment in the LAPD, the eigenfrequencies are computed for a hydrogen-helium plasma with an electron density, $n_e = 1.3 \times 10^{12}$ cm^{-3}, $n_H / n_e = 0.45$, $L = 200$ cm,

$B_l = 750$ G, $B_h = 1250$ G, and $k_\perp \delta_e = 1$ with the plasma assumed to satisfy quasi-neutrality. Under these conditions, six eigenfrequencies exist in the interval between the ion-ion hybrid frequency inside the well ($\omega_{ii}/\Omega_{H,l} = 0.5310$) and the ion-ion hybrid frequency outside the well ($\omega_{ii}/\Omega_{H,l} = 0.8849$). The scaled frequencies are $\omega/\Omega_{H,l} = 0.5571$, 0.6216, 0.6644, 0.7543, 0.8214, and 0.8677.

2.3 Inclusion of gradient effects

In reality, the transition between the interior of the well and the exterior of the well is not so sharp. To include the effects of the magnetic gradient, the well is now approximated by three spatial regions instead of two. In addition to the low magnetic field region (the bottom of the well) and the high magnetic field region (the top of the well), a linear gradient region is included. In the linear gradient region, the dielectric can be expanded as follows,

$$\varepsilon_\perp(z,\omega) \approx \left.\frac{\partial \varepsilon_\perp^R}{\partial z}\right|_{z_0} (z - z_0) + i\varepsilon_\perp^I. \tag{2.28}$$

The imaginary part of the dielectric in the above equation is introduced in order to provide an ad hoc dissipation channel to account for additional dissipation mechanisms that are not presently considered. Collisions by the electrons can be included in the parallel dielectric through the relation

$$\varepsilon_{||} = -\frac{\omega_{pe}^2}{\omega\,(\omega + i\nu_e)}, \tag{2.29}$$

where ν_e represents the collision frequency of the electrons. This frequency is given, for example, in the NRL Plasma Formulary [52], and is

$$\nu_e = 2.91 \times 10^{-6}\, n_e \Lambda T_e^{-3/2}, \tag{2.30}$$

where n_e is the electron number density measured in cgs units, T_e is the electron temperature measured in eV, and Λ is the Coulomb logarithm. For the parameters in LAPD, the Coulomb logarithm is given by $\Lambda = 23 - \ln\left(n_e^{1/2} Z T_e^{-3/2}\right)$, where Z is the average ionization state of the ions. For a typical LAPD plasma, $n_e \sim 10^{12}$ cm^{-3} and $T_e \sim 5$ eV, giving a Coulomb logarithm of $\Lambda = 11.6$ and a collision rate of $\nu_e = 3.0$ MHz, which is a factor of four

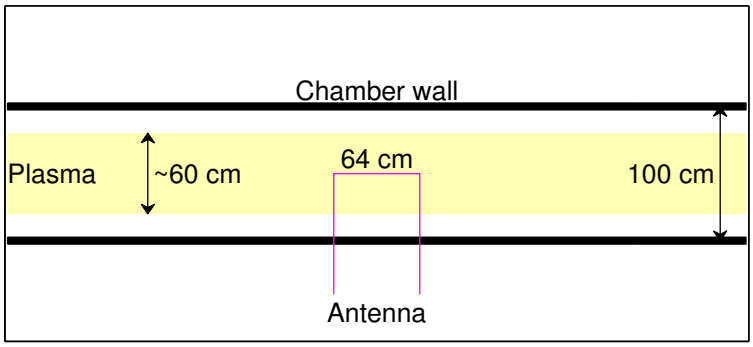

Figure 2.2: Schematic of the experiment. Chamber wall is black, plasma is yellow, and antenna is represented by magenta line.

to five greater than the typical eigenfrequency encountered in the experiments. However, uncertainties in both the electron density and temperature allow for variation of this collision frequency by roughly a factor of two.

The antenna used in the experiment consists of a bare copper rod (R =0.48 cm = 0.96 δ_e in radius) bent into three legs of a rectangle and placed in the chamber as shown in Fig. 2.2. The axial leg extends along the confinement magnetic field at the center of the plasma column. The perpendicular legs extend out of the chamber via electrically isolated, vacuum feed-throughs. In the theoretical model, the antenna current is Fourier decomposed in the azimuthal angle, ϕ, and only the azimuthally symmetric component is retained. This includes all of the axial current but only a portion of the current in the perpendicular legs. Further, the current channel is centered inside the constant magnetic field region at the bottom of the well. The source term in Eq. (2.17) takes the form,

$$\frac{\partial \tilde{j}_z}{\partial z} = \frac{R j_0}{k_\perp} J_1(k_\perp R) \left[\delta(z-a) - \delta(z+a)\right]. \tag{2.31}$$

In the above equation, δ represents the Dirac-delta function, and the length of the antenna is $2a$.

Figure 2.3 shows an example of a fit that approximates the magnetic field profile. The parameters used to generate the figure are similar to those found in the experiment. The solid black line represents the experimental profile, while the dashed red line corresponds

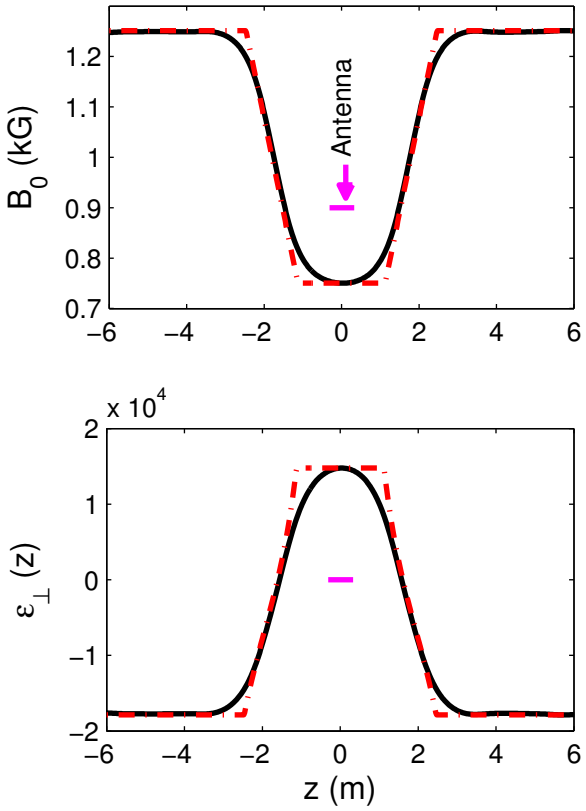

Figure 2.3: Linear fit to shape well. Top panel shows the experimental profile as a function of axial position (solid black line) and a fit with two constant B-field regions are connected by a linear ramp (dashed red line). Bottom panel shows the corresponding perpendicular dielectric as a function of axial position. The bottom plot corresponds to a 60% hydrogen, 40% helium plasma with an electron density of 1×10^{12} cm^{-3} and a frequency of 633 kHz.

to the fit. The magenta line in the center of the well represents the spatial extent of the antenna. The top panel illustrates the magnetic profile, and the bottom, the perpendicular dielectric.

The total solution to Eq. (2.17) consists of seven unknown constants, C_i, whose values are determined by matching both the value of the function and its gradient at each boundary with the additional jump condition of the antenna. These conditions in conjunction with the appropriate parity of the solution (in this case, odd parity) allow for the evaluation of

the driven solution to the problem. For $z > 0$, the solution takes the form,

$$\tilde{E}_r = \begin{cases} C_1 e^{ik_l z} + C_2 e^{-ik_l z} & z < a \\ C_3 e^{ik_l (z-a)} + C_4 e^{-ik_l (z-a)} & a < z < L_1 \\ C_5 Ai\left[\alpha(z - z_0) + i\mu\right] + C_6 Bi\left[\alpha(z - z_0) + i\mu\right] & L_1 < z < L_2 \\ C_7 e^{-k_h (z - L_2)} & L_2 < z \end{cases}, \tag{2.32}$$

where

$$\alpha = \left[-k_0^2 \left. \frac{\partial \varepsilon_\perp^R}{\partial z} \right|_{z_0} \left(1 - \frac{k_\perp^2}{k_0^2 \varepsilon_{||}} \right) \right]^{1/3}, \tag{2.33}$$

and

$$\mu = \left(\varepsilon_\perp^I / \left. \frac{\partial \varepsilon_\perp^R}{\partial z} \right|_{z_0} \right) \alpha. \tag{2.34}$$

In Eq. (2.32), L_1 and L_2 denote the beginning and end of the linear gradient region. The functions, Ai and Bi, are the two linearly independent solutions to the Airy differential equation.

The resulting boundary conditions can be represented by a matrix equation of the form $Ax = b$, where x is a vector whose components are the seven constants, b is a vector representing the inhomogeneous source, and A is a matrix determined by the piecewise boundary conditions. This matrix equation can be inverted, and a frequency spectrum can be generated as a function of axial position and $k_\perp$. As mentioned before, dissipation is included in $\varepsilon_\perp$ through the value of μ, and in $\epsilon_{||}$ through an electron collision frequency. These mechanisms keep the spectrum finite in the vicinity of the resonant frequencies, preventing the determinant of A from vanishing. The specific dissipation mechanisms represented by μ should depend on the frequency of the driver, and so μ should depend on frequency. Without modeling the specific dissipation mechanisms in more detail, it is impossible to predict the specific frequency dependence of μ. As a result, μ is assumed constant, and this assumption accounts for some of the discrepancies between the theory and the experimental data. Once the Fourier-Bessel representation of the field is determined, this transform can be inverted to compute the field at position r and z for a given drive frequency. This integral is performed numerically with care taken to ensure numerical convergence. The lower limit of the integral is taken to be $k_{\perp,\min}$ which is determined from the first zero of the equation, $J_0(k_{\perp,\min} R_p) = 0$,

where R_p is the radius of the plasma and is taken to be 30 cm for definiteness. This has the effect of excluding small values of $k_\perp$ from the driven response, which is necessary because of the finite radial extent of the plasma.

If all dissipation is ignored, the eigenfrequencies and eigenfunctions of the well can be generated in the undriven case. This amounts to using the real values for both $\varepsilon_\perp$ and $\varepsilon_{||}$ and removing the source. Further, since the eigenfrequencies and eigenfunctions will exhibit a weak dependence on $k_\perp$, a discrete radial Bessel representation is employed, as opposed to the continuous representation used in Eqs. (2.6) - (2.11). This takes the form

$$E_r(r,z) = \sum_\nu \tilde{E}_{z,\nu}(z) J_1(k_{0\nu} r), \tag{2.35}$$

$$E_z(r,z) = \sum_\nu \tilde{E}_{r,\nu}(z) J_0(k_{0\nu} r), \tag{2.36}$$

$$B_\phi(r,z) = \sum_\nu \tilde{B}_{\phi,\nu}(z) J_1(k_{0\nu} r). \tag{2.37}$$

Here, the role of $k_\perp$ is replaced by $k_{0\nu}$ where $J_0(k_{0\nu} R_p) = 0$. This description removes the need to match the jump condition provided by the end of the antenna, and the eigenfrequencies are determined by means of requiring the resulting function to be either even or odd and to be continuous and differentiable at each boundary. Mathematically, this corresponds to finding the frequency for which the determinant of A is zero.

Figure 2.4 illustrates the driven spectrum and the undriven eigenfrequencies generated by the methods described previously. This spectrum corresponds to axial position $z = 0$ cm and $r = 5$ cm for a plasma consisting of a 60% H^+, 40% He^+ ion mixture. In generating the curve, an electron temperature and density of $T_e = 5$ eV and $n_e = 1 \times 10^{12}$ cm^{-3} is used, which corresponds to an electron collision frequency of $\nu_e = 3.02$ MHz. Additionally, a value of $\mu = -0.2$ is used in order to obtain a spectrum with damping comparable to what is observed in the experiment. The horizontal arrows bounded by the dashed black lines illustrate the range of trapped frequencies in the well. The vertical, blue lines illustrate the eigenfrequencies in the undriven case for a perpendicular wave number, $k_\perp \delta_e = 0.25$. The blue lines located at $\omega/\Omega_H = 0.48$ and 0.65 have axially anti-symmetric B_ϕ eigenfunctions. The eigenfunction located at $\omega/\Omega_H = 0.55$ is symmetric. The first peak in the driven spectrum corresponds

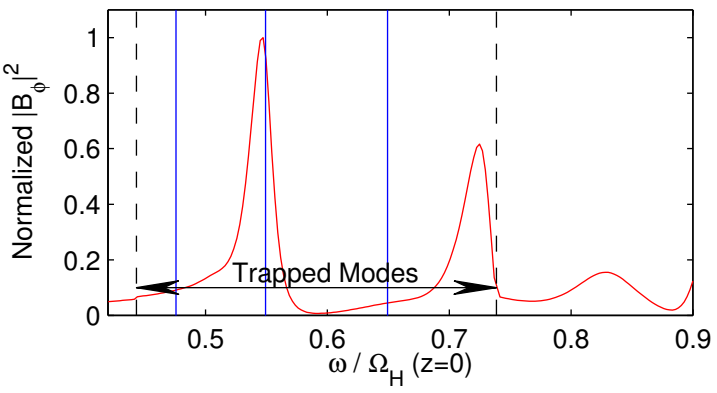

Figure 2.4: Driven spectrum at axial position, $z = 0$ cm and radial position, $r = 5$ cm, for a 60% hydrogen, 40% helium plasma with an electron density of 1×10^{12} cm^{-3}. Horizontal axis is the frequency scaled to the hydrogen cyclotron frequency. Vertical axis is the normalized $|B_\phi|^2$ response. Solid red line illustrates the driven spectrum while the vertical blue lines illustrate the undriven eigenfrequencies.

to this symmetric mode and agrees well with the corresponding undriven eigenfrequency. This reflects the fact that the eigenfrequency depends weakly on $k_\perp$, and so the driven peak does not shift much even though it is a superposition of many different perpendicular wave numbers. The peak located at $\omega/\Omega_H = 0.73$ is also symmetric and does not have a corresponding undriven eigenfrequency because it would fall outside of the frequency range spanned by the trapped modes. The effects of dissipation allow the peak to begin to form even though the well is not long enough for the undriven eigenfrequency to appear. The anti-symmetric peaks are not present in the driven spectrum for two reasons: first, the spectrum is calculated at $z = 0$ cm, and second, because the perfect symmetry of the model and the parity of the antenna prevents the source from coupling to these modes.

Figure 2.5 illustrates the axial shape of the driven mode at frequency $\omega/\Omega_H = 0.55$ line, which corresponds to the first peak of the driven spectrum in Fig. 2.4. The response is normalized to its peak value and is illustrated by the blue line. The magnetic profile fit is shown by the red dashed line. For this case, the bottom of the well is at 750 G and the top, 1250 G. The antenna position is illustrated by the magenta line, and the vertical black lines illustrate the axial positions of Probes 1 and 2 which will be referred to later when discussing

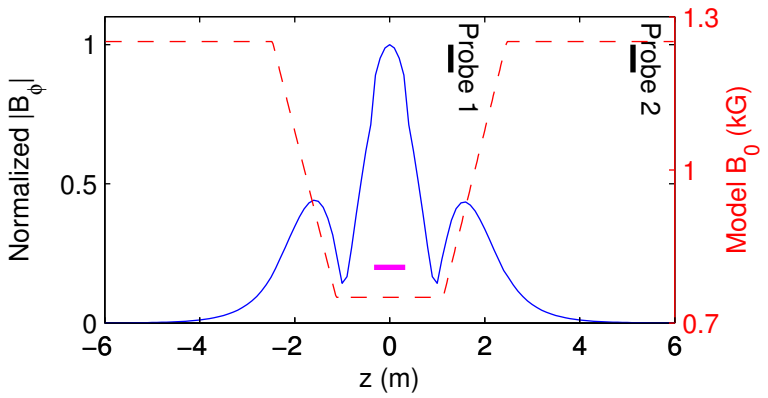

Figure 2.5: Blue line is the amplitude of $|B_\phi|$ as a function of axial position at radial position $r = 5$ cm and frequency $\omega/\Omega_H = 0.55$. Same plasma parameters are used as in Fig. 2.4. Red dashed line shows magnetic field profile; magenta line, the antenna location; and the solid black lines illustrate experimental probe positions.

the experimental results.

2.4 Experimental results

In the experiment, the antenna, centered in the magnetic well, is driven using tone bursts of 20 cycles. The same magnetic well configuration is explored for three different concentration ratios of hydrogen and helium ions as shown in Fig. 2.6. For the resonator, it is within the upper (hydrogen) propagation band that the trapped eigenmodes are formed. Therefore, the experimental results are presented with the frequencies scaled to the hydrogen cyclotron frequency Ω_H; due to the axial field variation, this scaling is performed using the values of Ω_H at $z = 0$, that is, at the bottom of the well. Figures 2.6(a)-2.6(c) display the spatial variation of the ion cyclotron frequencies and ion-ion hybrid frequencies for the following concentration ratios, $\eta_H = n_H/n_e$: (a) $\eta_H = 0.25$, (b) $\eta_H = 0.38$, and (c) $\eta_H = 0.61$. The lower propagation bands ($\omega < \Omega_{He}$) are shaded in yellow; the propagation gaps ($\Omega_{He} < \omega < \omega_{ii}$) are white; the upper propagation bands are shaded in cyan; and overlaid with a third color within the upper bands (matching the color of the subplot to the immediate right (d-f)) are the wave trapping regions. In the trapping regions, the waves satisfy two criteria: (1) They can be launched by

the antenna, i.e., $\omega < \Omega_H$ at the center of the well, and (2) their frequency can match the reflection condition, $\omega = \omega_{ii}(z)$, at a location within the plasma column. For all three cases, tunneling between potential eigenmodes in the resonator and the lower propagation bands is prevented since the minimum ω_{ii} in the system is chosen to be everywhere greater than the maximum value of Ω_{He}. Further, for $\eta_H = 0.25$, the upper boundary of the trapping region is determined by the $\omega < \Omega_H(z = 0)$ criterion, while a substantial propagating upper band exists for the $\eta_H = 0.61$ case.

The resulting wave amplitude spectra $|B_y(\omega)|$ (measured with Probe 1, a B-dot probe, located at $r = 5$ cm and at an axial position as shown in Fig. 2.5) are presented in Figs. 2.6(d)-2.6(f). Each of these sub-figures corresponds to the case to its immediate left (a-c). The data displayed are obtained after the antenna current is switched off, so that a comparison to the theoretical predictions of the un-driven eigenmode case is appropriate. Specifically, the displayed spectra are obtained from FFTs of a 10-cycle, Hanning-windowed time series starting immediately after termination of the antenna current. For this linear study, each spectrum is normalized to its maximum value. For reference, within each subplot, a semi-transparent horizontal bar is drawn arbitrarily at the normalized height of 0.5 and covers the frequency range of potential resonator eigenfrequencies. Within these bands, individual spectral peaks are manually identified and marked with vertical arrows to indicate the experimentally observed eigenfrequencies for each case. The upper propagation band in Fig. 2.6(f) is clearly visible between $0.7 < \omega/\Omega_H < 1$ and should not be interpreted as evidence of a fourth eigenfrequency for that case.

Next, an experiment is considered in which the antenna is pulsed using a waveform with a width of one cyclotron period of hydrogen at 750 Gauss (the center of the well). The signal is measured by Probe 1. A plane of data is taken with a B-dot probe, and is averaged over two to eight shots at each point to reduce noise through statistical averaging. In analyzing the data, it is important to determine the frequency content of the signal as a function of time. This is best accomplished by using a continuous wavelet transform [53]. In order to perform this transform, the DC component of the signal is removed, and the resulting signal is numerically integrated to compute the oscillating magnetic field as a function of time. A

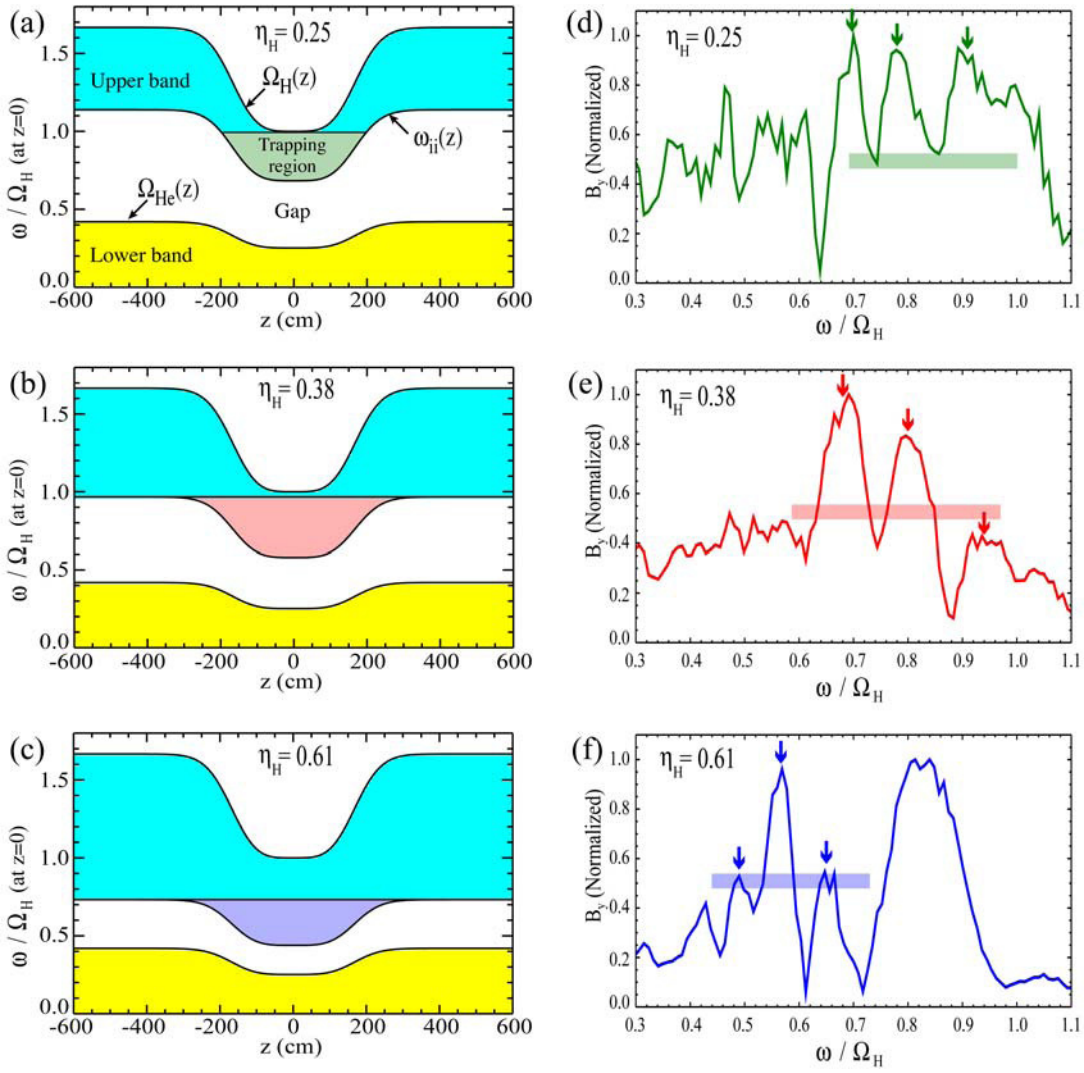

Figure 2.6: ((a)-(c)) Axial variation of the upper (cyan) and lower (yellow) propagation bands; the cold plasma propagation gap (middle, white); and the trapping regions (color–coded) for three concentrations of hydrogen ($\eta_H = n_H/n_e$) in a H^+-He^+ plasma. ((d)-(f)) Normalized wave magnetic field amplitude spectra measured by Probe 1 at $r = 5$ cm as launched in the resonator by the antenna. Each of these three subplots corresponds to the case to its immediate left. The semi-transparent horizontal bars delineate the trapping regions, and the arrows mark the manually identified modes. The broad "peak" in (f) for $0.7 < \omega/\Omega_H < 1$ is a continuum of a freely propagating modes, not another resonance.

wavelet transform of the resulting signal is then performed using a Morlet wavelet function which takes the form,

$$\psi = \frac{1}{\pi^{\frac{1}{4}} s^{\frac{1}{2}}} \exp\left(\frac{ipt}{s} - \frac{t^2}{2s^2}\right). \tag{2.38}$$

Here, p is the order of the Morlet Wavelet, taken to be 24, and s is the scale of the wavelet. One can relate the scale of the wavelet to a frequency by the equation $\omega = p/sdt$ where dt is the temporal spacing between sampling points in the signal.

The top panel of Fig. 2.7 illustrates a wavelet transform of the data. This data is taken at a radial position of $r = 17.4$ cm. The horizontal axis is time scaled to the cyclotron period of hydrogen, τ_H, at the bottom of the well, and the vertical axis is the frequency scaled to the cyclotron frequency of hydrogen, again, at the bottom of the well. Time $t = 0$ corresponds to the maximum current in the the antenna pulse, which lasts for roughly one τ_H. The red, horizontal lines show the various reference frequencies: the ion cyclotron and ion-ion hybrid frequencies both inside and outside of the well. The blue contour is a confidence measure which outlines when the antenna amplitude has decayed to 10% of its peak value. Although the antenna pulse is only τ_H long, it is artificially broadened due to the width of the Morlet wavelet. When looking in the trapped band between $\omega_{ii}(750\ G)$ and $\omega_{ii}(1250\ G)$, it is clear that there are at least two frequencies that extend well beyond the envelope of the pulse. These frequencies are candidate eigenmodes. The bottom panel illustrates a frequency cut at various times to show the slow decay of the signal and to more clearly distinguish the extended signals present in the top panel. The vertical dashed lines give the theoretical, undriven eigenfrequencies for a 45% H^+, 55% He^+ plasma with an electron density of $n_e = 1.3 \times 10^{12}$ cm^{-3}.

In order to determine the quality factor, Q, of the resonator, a temporal cut is plotted as a function of time as shown in Fig. 2.8. The logarithm of the amplitude is plotted on the vertical scale with the scaled time on the horizontal scale. The temporal cuts are made for the two prominent frequencies in Fig. 2.7, $\omega/\Omega_H = 0.56$ and $\omega/\Omega_H = 0.71$, and are illustrated by the solid, red line and the dashed, blue line, respectively. Assuming an exponential decay of the signal, $\left|\tilde{B}(\omega, t)\right| \propto \exp(-t/2\tau)$ with τ being the characteristic decay time, the decay time can be determined by a linear fit to the signals during their decay. For the two peaks,

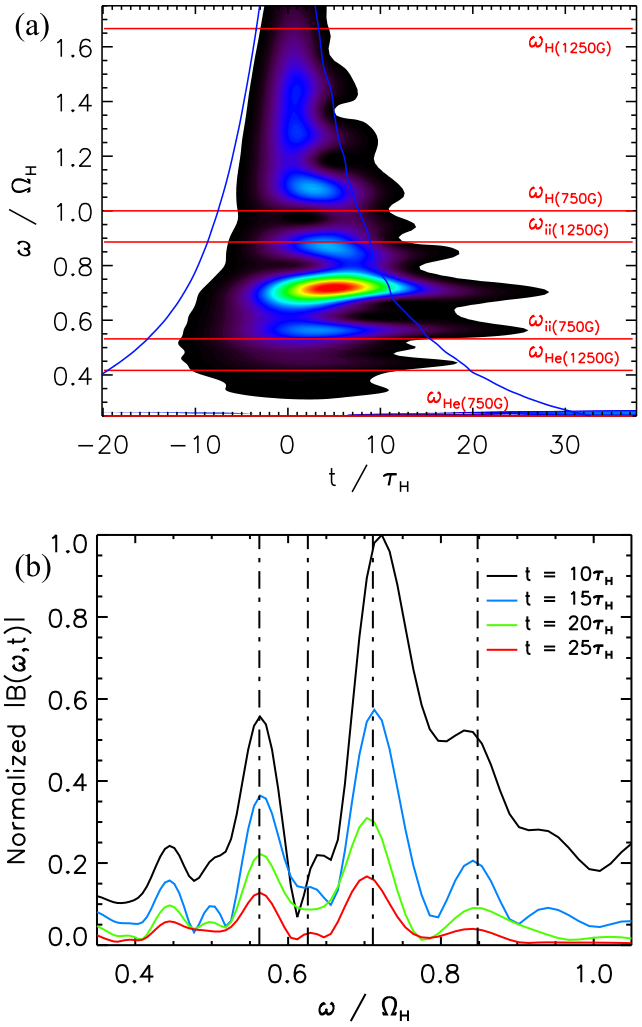

Figure 2.7: (a) Color contours of Morlet wavelet amplitude of magnetic field fluctuations show the response of the H^+ - He^+ resonator after excitation with a current impulse of width $\Delta t = \tau_H$ at $t = 0$. The plasma is 45% hydrogen and the probe is at z = +128 cm, r = +17.5 cm. (b) Instantaneous wavelet spectra obtained from vertical cuts in (a) at four different times. Vertical dashed lines are the predicted resonator eigenfrequencies.

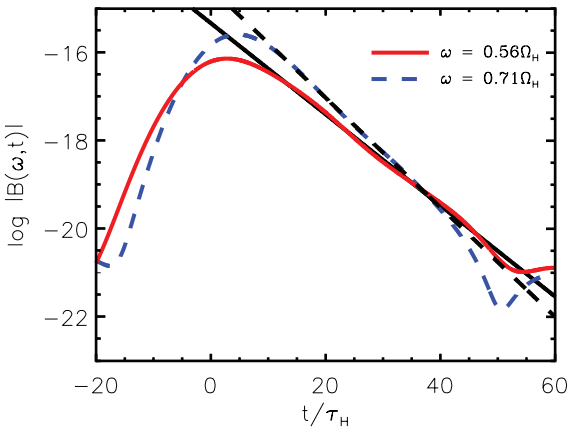

Figure 2.8: Exponential fits to the temporal decay of the wavelet amplitude for the two prominent spectral peaks ($\omega/\Omega_H = 0.56$ and 0.71) in Fig. 2.7. Solid red and dashed blue line correspond to the wavelet amplitude, and solid and dashed black lines, to the corresponding exponential fit. Fits give a characteristic decay time of $\tau = 4.23$ μs and $\tau = 3.52$ μs for the red and blue lines, corresponding to a quality factor of $Q = 17.3$ and 18.0, respectively.

$\omega/\Omega_H = 0.56$ and 0.71, the decay times are $\tau = 4.23$ and 3.52 μs, respectively. Thus, the quality factors, $Q = \tau\omega$, of the resonances are $Q = 17.3$ and 18.0.

To show the global nature of the eigenmodes, a survey of radial position and axial position is made. The results are shown in Fig. 2.9. The top panel shows the wavelet spectra at $t/\tau_H = 25$ measured with Probe 1 for various positions in the plane perpendicular to the confinement field. The radial positions sampled are color coded with the asterisks present in the grid to give an idea of where the measurements are performed. The grid is 40×40 cm. The four curves are normalized to their peak value in the plot so they are easily compared. The bottom panel shows the signal at $t/\tau_H = 25$ and the radial position indicated by the black asterisk in the top panel, but varying the axial position. The positions of Probes 1 and 2 are illustrated in Fig. 2.5, and Probe 0 is located at the center of the well at axial position, $z = 0$ cm. The absolute magnitude of Probe 2 is suppressed by several orders of magnitude relative to the signals in Probes 0 and 1, but they are, again, normalized to their peak values in the plot for easy comparison. It is clear from these plots that the structure of these resonances is indeed a global one.

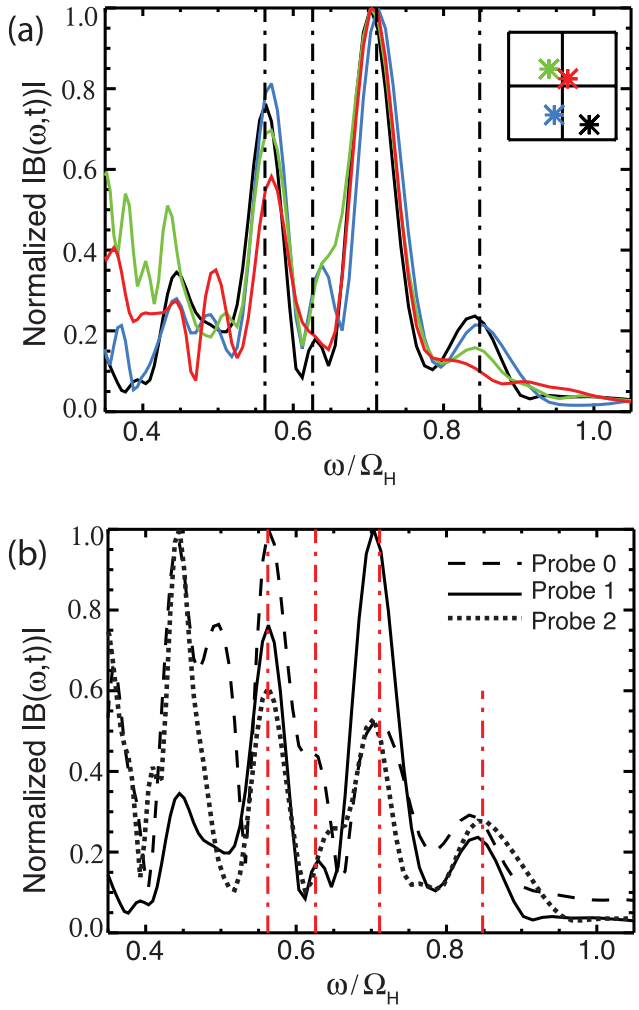

Figure 2.9: Sampling of the pulsed wave form at various positions. (a) Wavelet spectra taken at $t/\tau_H = 25$ from Probe 1 at various locations in a plane. The spectra are normalized to peak value. The grid in the upper right is color coded with the line plots to show where in the plane the spectrum is measured. The grid is 40 cm x 40 cm. The dashed lines corresponds to the theoretical eigenfrequencies. (b) Wavelet spectra taken at the same time and position as the black curve in (a), but at different axial positions. Again, the curves are normalized to peak value and the red dashed lines are theoretical resonances. Probe 0 is located at z = 0 cm, and, Probes 1 and 2 are at positions shown in Fig. 2.5

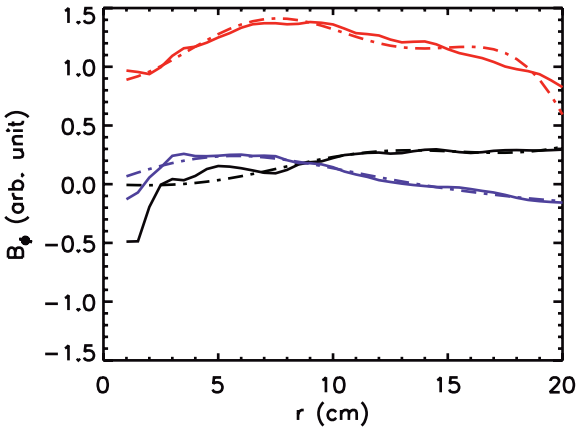

Figure 2.10: A plot of $\tilde{B}_{\phi,m}(r)$ for $\omega/\Omega_{He} = 0.56$. Solid lines represent experimental data and dashed lines represent a least-squares fit to the radial functions shown in Eq. (2.39). The black line is for $m = 0$; the red line, $m = 1$; and the blue line, $m = 2$.

Next, an analysis of the azimuthal mode number and radial structure of the fields is performed on the experimental data. To do this, a plane of data taken by Probe 1 is considered. A wavelet transform of the data is performed and attention is confined to the time $t/\tau_H = 20$ for both candidate resonance frequencies, $\omega/\Omega_{He} = 0.56$ and 0.71. Since the wavelet has an inherent $e^{-i\omega t}$ dependence, this is removed by multiplying each wavelet signal by $e^{i\omega t}$. Further, the resulting data set, $\{B_x, B_y\}$, is converted into a polar coordinate system, $\{B_r, B_\phi\}$. In performing this transformation, an assumption must be made as to the true center of the plasma. This is taken to be the center of the plane of data, which should be approximately the true center of the plasma, though error on the order of one centimeter is possible. The data is then interpolated onto concentric circles centered at the assumed center of the plasma, possessing 64 azimuthal angle grid points. The smallest circle has a radius of 1 cm, with radial spacings of 1/2 cm extending to a maximum radius of 20 cm.

Upon performing the above steps, the magnetic field is now given as a function of both the radius and the azimuthal angle. It can now be decomposed into both radial and azimuthal

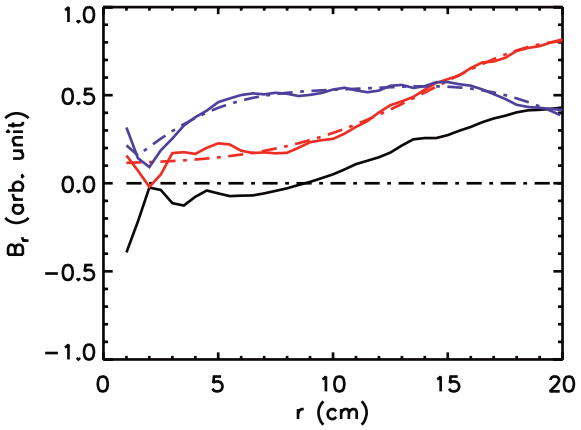

Figure 2.11: A plot of $\tilde{B}_{r,m}(r)$ for $\omega/\Omega_{He} = 0.56$. Solid lines represent experimental data and dashed lines represent a least-squares fit to the radial functions shown in Eq. (2.40). The black line is for $m = 0$; the red line, $m = 1$; and the blue line, $m = 2$.

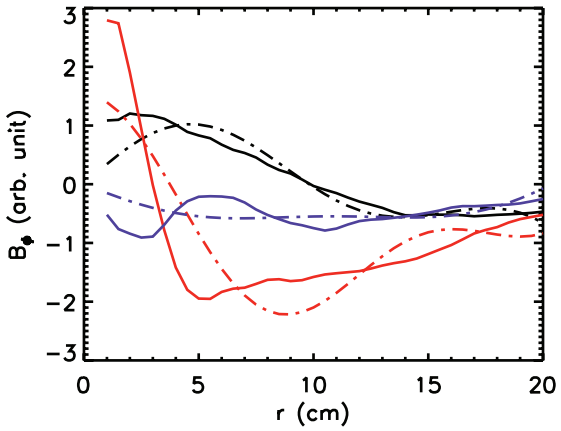

Figure 2.12: A plot of $\tilde{B}_{\phi,m}(r)$ for $\omega/\Omega_{He} = 0.71$. Solid lines represent experimental data and dashed lines represent a least-squares fit to the radial functions shown in Eq. (2.39). The black line is for $m = 0$; the red line, $m = 1$; and the blue line, $m = 2$.

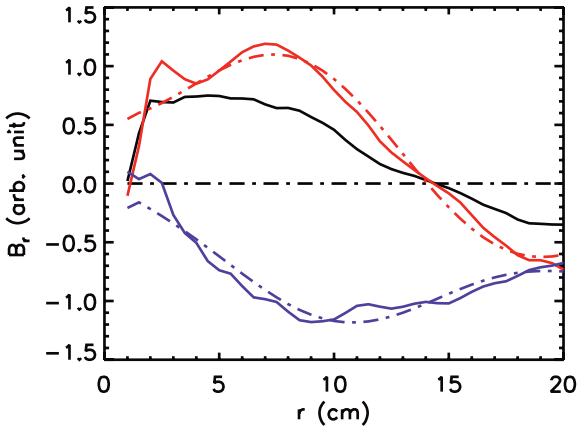

Figure 2.13: A plot of $\tilde{B}_{r,m}(r)$ for $\omega/\Omega_{He} = 0.71$. Solid lines represent experimental data and dashed lines represent a least-squares fit to the radial functions shown in Eq. (2.40). The black line is for $m = 0$; the red line, $m = 1$; and the blue line, $m = 2$.

eigenfunctions as

$$B_\phi(r,\phi) = \sum_m \tilde{B}_{\phi,m}(r)e^{im\phi} = \sum_{m,\nu} C_{\nu,m} J'_m\left(x_{\nu,m}\frac{r}{R_p}\right)e^{im\phi}, \tag{2.39}$$

$$B_r(r,\phi) = \sum_m \tilde{B}_{r,m}(r)e^{im\phi} = \sum D_{\nu,m}\frac{m}{r}J_m\left(x_{\nu,m}\frac{r}{R_p}\right)e^{im\phi}. \tag{2.40}$$

Here, the quantity, $x_{\nu,m}$, represents the zeros of the bessel function, J_m, ensuring that the field quantity, B_r vanishes at the radius, $r = R_p$. This corresponds to an assumed conducting boundary at the edge of the plasma, which is again taken to be $R_p = 30$ cm. In order to compare with the above theoretical curves, a fast Fourier transform (FFT) is performed at each radial location, decomposing the data into the azimuthal eigenfunctions, $e^{im\phi}$. Next, a least squares fit is made between the candidate radial eigenfunctions and the observed radial pattern for each azimuthal mode number, m. This amounts to varying the constants, $C_{\nu,m}$ and $D_{\nu,m}$, to get the best fit between the theoretical curves and the data. For a given m value, four radial functions are included in the fit.

The results are displayed in Figs. 2.10 - 2.13. The first two plots are for $\omega/\Omega_{He} = 0.56$ and the second two, for $\omega/\Omega_{He} = 0.71$. Further, Figs. 2.10 and 2.12 plot the azimuthal magnetic field, B_ϕ, and Figs. 2.11 and 2.13 plot the radial magnetic field, B_r. In order to capture

both positive and negative m numbers, for $m \neq 0$, the real part of $\tilde{B}_m + \tilde{B}_{-m}$ is plotted. This is done to convert to a sinusoidal representation instead of a complex exponential representation, and the corresponding plots are for the $\cos m\phi$ part of the expansion. In the figures, the solid lines represent experimental data while the dashed lines represent the fits to the radial basis functions. The black lines correspond to $m = 0$; red, $m = 1$; and blue, $m = 2$. Discrepancies between the fits and the data are most likely due to error in the choice of the center. Further, the plane of data did not possess the symmetry that would have been expected around the antenna. A likely explanation of this is due to interference by the probe as it moved deeper into the plasma. Regardless, it is clear that this is affecting the results. Finally, the theoretical curves assume no radial gradients.

2.5 Comparison of theory to experiment and summary

First a comparison between the experimental data and the undriven eigenfrequencies is performed. This is done by overlaying the observed resonator eigenfrequencies from the three cases of Figs. 2.6(d)-2.6(f) with the theoretically predicted undriven eigenfrequencies displayed as functions of a continuous variation in η_H as shown in Fig. 2.14. The range of possible eigenfrequencies is bounded on the lower end by ω_{ii} at $z = 0$ (lower red curve) and the continuum of waves propagating above ω_{ii} at the high-field end of the well (upper red curve). Again, for the frequencies used, the antenna does not launch shear waves above the hydrogen cyclotron frequency at $z = 0$ (marked by the orange horizontal line). The theoretical values of the resonant frequencies are determined by the model described in section 2.3. The predicted eigenfrequencies of undriven modes are shown as dashed lines. Both even and odd parity modes are represented, as the undriven case does not have the strict symmetry requirement inherent in the idealized driven-case, and the exact form of the source is removed from consideration. For the highest concentration of hydrogen ($\eta_H = 0.61$), both the number and frequency of the observed spectral peaks match well with the theoretical prediction. For lower hydrogen concentrations, the agreement is not as good, which is primarily attributed to the larger width of the observed peaks in comparison to the predicted frequency spacing.

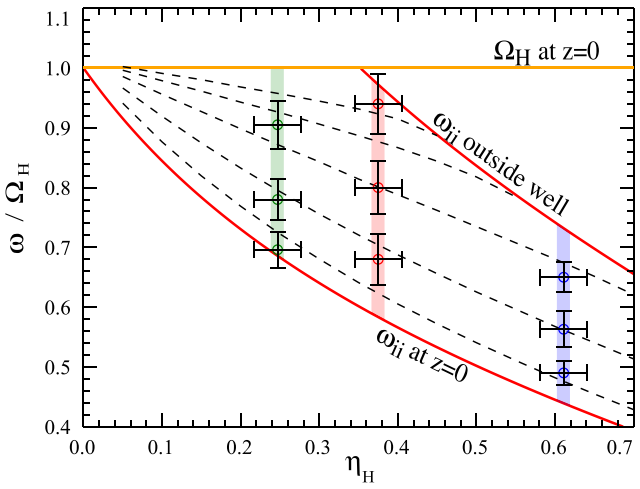

Figure 2.14: Comparison of measured eigenfrequencies to theoretical predictions for three ratios of hydrogen-to-electron densities, η_H, in the helium-hydrogen resonator. Frequencies are scaled to the hydrogen cyclotron frequenty at the center of the resonator ($z = 0$). The dashed black lines are the theoretical predictions and the data points are color coded to the marked peaks in the spectra shown in Figs. 2.6(d)-2.6(f). The vertical semi-transparent frequency bands correspond to the horizontal bands of the same color in Figs. 2.6(d)-2.6(f). The solid red and orange lines bound the range of possible eigenfrequencies, as explained in the text.

This feature makes it difficult to discern individual peaks from broader, merged peaks.

An attempt is now made to determine the source of the damping observed in the experiments. An examination of the quality factors due to electron collisions alone is first performed. To remove all ad hoc dissipation from the theoretical model, $\mu = 0$ is chosen. The frequency of the electron collisions is varied by changing the electron temperature. Figure 2.15 displays the two peaks present in Fig. 2.4 at the same plasma conditions but with the electron temperature varied. The top panel, Fig. 2.15(a), corresponds to the first peak, and the bottom panel, Fig. 2.15(b), to the second. The horizontal axes corresponds to the frequency scaled to the hydrogen cyclotron frequency at the bottom of the well, and the vertical axes, to $|B_\phi|^2$. The spectra have been normalized to their peak value. The solid, dashed, and dash-dotted curves correspond to electron temperatures of $T_e = 5,\ 2,$ and 1 eV, respectively. Using Eq. (2.30), these temperature values correspond to a scaled collision

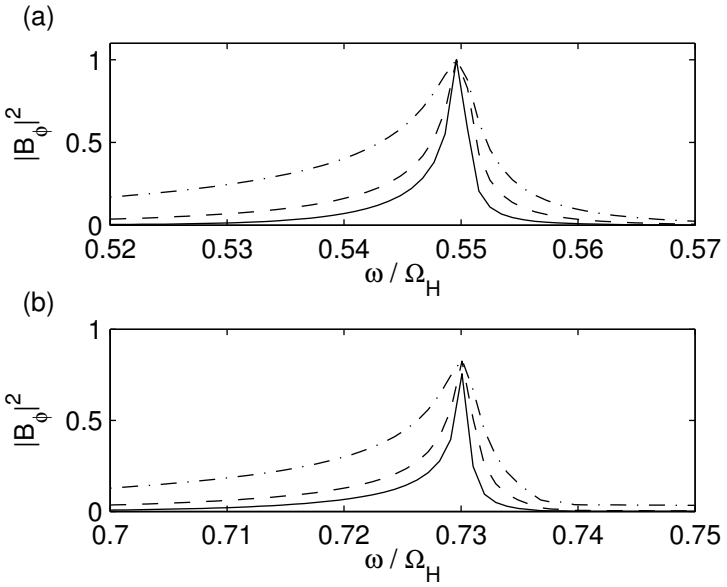

Figure 2.15: Power spectra with $\mu = 0$ at three different electron temperatures. Solid, dashed, and dash-dotted curves correspond to electron temperatures, $T_e = 5, 2,$ and 1 eV, respectively. All other parameters are the same as in Fig. 2.4 (a) First peak. Quality factors are 229, 145, and 60, respectively. (b) Second peak. Quality factors are 406, 228, and 95, respectively.

frequency of $2\pi\nu_e/\Omega_H = 2.6$, 9.1, and 23, with quality factors for the first peak, $Q = 229$, 145, and 60; and for the second peak, $Q = 406$, 228 and 95, respectively.

Experimentally, LAPD discharges typically have electron temperatures of 5-8 eV. For the electron temperatures surveyed in Fig. 2.15, even at 1 eV, the collisions are not sufficient to explain the experimental results, giving quality factors that are roughly 3-5 times greater than those observed in the experiment. If the value of $k_{\perp,\min}$, the lower bound of the Fourier integral, is artificially increased at electron temperatures of 5 eV, the quality factors of the observed peaks decline to realistic values obtained in the experiment. This is because electron collisions are able to dissipate energy due to interaction with the parallel electric field. At small values of $k_\perp$, the parallel electric field decreases in relative amplitude, and the electron collisions are unable to dissipate the energy. For this reason, electron collisions are unable to explain the quality factors associated with the long-lived, small $k_\perp$ modes. An additional

source of damping is required that must be included in the perpendicular component of the dielectric tensor. If an ad hoc damping mechanism is included, Fig. 2.4 is obtained. The quality factors for the peaks in this plot are 25 and 27. These values are much closer to the observed values, and this suggests an additional damping mechanism beyond what is included in the model is required.

One physical mechanism that could introduce an imaginary part in the perpendicular dielectric tensor is the presence of ion-neutral collisions. If the interaction is modeled by the collision of two solid spheres, then the corresponding cross section is

$$\sigma = \pi \left(r_i + r_n\right)^2, \tag{2.41}$$

where r_i and r_n are the effective radius of the ion and neutral, respectively. From this cross-section, the collision frequency of an ion with the background neutrals can be determined. This calculation results in [54]

$$\nu_{in} = n_n \sigma \left(\frac{8T_i}{\pi m_{in}}\right)^{1/2}, \tag{2.42}$$

where m_{in} is the reduced mass of the colliding particles. Taking the neutral density to be $n_n = 10^{12}$ cm^{-3}, the ion temperature to be $T_i = 1$ eV, and the collision to be ionized hydrogen colliding with neutral hydrogen, with $r_i = r_n = 0.5 \times 10^{-8}$ cm, the Bohr radius, then the collision frequency is 696 Hz. Scaling this collision frequency to the cyclotron frequency of hydrogen, $2\pi\nu_{in}/\Omega_H = 6 \times 10^{-4}$, far below the frequencies observed in the experiment. For this reason, ion-neutral collisions are unlikely to explain the observed quality factors.

Cyclotron damping is also unlikely to explain the observed quality factors. Large cyclotron damping occurs when $(\omega - n\Omega_i)/k_{||}\bar{v}_i \sim 1$. Taking $\omega = n\Omega_i + \Delta\omega$ and $\omega/k_{||} \sim v_A$, the condition for cyclotron resonance is

$$\frac{\Delta\omega}{\omega} \sim \frac{\bar{v}_i}{v_A}. \tag{2.43}$$

For parameters relevant to the experiment, the right hand side of the above equation evaluates to roughly 0.01. This means that cyclotron damping is only relevant over a bandwidth of roughly 1% of the cyclotron harmonic. For this reason, it is not an adequate mechanism

to explain the observations. In considering Landau damping, a generalization of the parallel dielectric must be made which includes both electron collisions and kinetic damping [55]. It is possible that Landau damping contributes, but it suffers from the same deficiency as electron collisions; it will not damp modes with small values of $k_\perp$. Another possible mechanism to explain the observed quality factors is enhanced radial convection of the mode in the reflection layer due to coupling to the compressional and ion-Bernstein waves. To include this effect in a full-wave description, Eqs. (2.13) and (2.14) must be solved with finite-Larmor-radius terms included in the formulations of $\varepsilon_\perp$ and ε_{xy}. In the absence of this investigation, these effects are explored from a ray-tracing stand point in the next chapter, where it is concluded that they are also unlikely to explain the observed damping. This ray-tracing investigation will include the effects of magnetic-field line curvature which would influence the refraction of the waves. Other possible effects that could lead to the low observed quality factors are radial density gradients, mode conversion to an ion-Bernstein wave near the position at which the wave frequency matches the second cyclotron harmonic of helium, and transit time acceleration in the reflection region. These effects are not considered in this dissertation.

In summary, cavity modes have been observed in a magnetic well that have eigenfrequencies consistent with theoretical predictions describing an ion-ion hybrid resonator. The eigenfrequencies are predicted within reasonable accuracy, considering the approximations in the theory and the uncertainties in the plasma parameters. From the experimental data, it is clear that non-axisymmetric modes are also present in the device. This suggests that the eigenfrequencies are largely independent of azimuthal mode number. The quality factors observed in the experiment are an order of magnitude smaller than those which would be predicted by electron collisions alone. Further, ion-neutral collisions, ion-cyclotron damping, and Landau damping are also unlikely to explain the observed quality factors.

CHAPTER 3

Effects due to a nonuniform magnetic field

For a specific magnetic well geometry, ray tracing studies are useful in determining the degree to which the wave energy can be trapped. Several studies have investigated the propagation of shear Alfvén waves in the presence of multiple ion species in a dipole magnetic geometry [8, 12] and in mirror machines [56, 57]. This chapter builds on the previous ray tracing studies to assess the properties of possible ion-ion hybrid resonators in other geometries relevant to contemporary laboratory experiments, and with differing plasma parameters. Specifically, ray tracing studies are performed in a geometry relevant to LAPD to assess the degree to which radial convection of the wave energy influences the quality factors determined in Chapter 2. Ray tracing studies are also performed in toroidal geometries to understand more clearly whether a resonator could exist within a burning plasma. Because of the large ion temperatures that would exist in such a plasma, finite Larmor radius (FLR) effects for the ions must be included in the dispersion relation. The introduction of finite ion temperature into the problem allows the possibility of coupling between the shear wave and the IBW. While this chapter does not address the mode conversion problem, it illustrates the effect of ion temperature on the ray trajectories for burning plasma conditions in ITER.

The chapter is organized as follows. Section 3.1 reviews the ray tracing formulation and details the numerical method used to solve the resulting equations, paralleling the method used by Rauch and Roux [8]. The section also presents expressions for the group velocity that are used in analyzing the results for different plasma devices. Section 3.2 examines group velocity contours and ray trajectories relevant to the experiments detailed in Chapter 2, and estimates the quality factors expected for the resonator due to radial spreading of the wave energy alone. Section 3.3 examines the ray trajectories of waves launched in the Enormous

Toroidal Plasma Device (ETPD) [58] and discusses the effects of field-line curvature on the ray. Section 3.4 considers ray trajectories of waves in ITER and discusses the implications of finite temperature effects. Section 3.5 discusses the validity of the ray tracing approach in the geometries considered and summarizes the results.

3.1 Formulation

3.1.1 Ray Tracing Equations

In formulating the ray tracing equations, the dispersion relation is used to determine the frequency as a function of the wave vector and the plasma parameters (which presumably vary with position but are assumed constant in time in this dissertation). This frequency then becomes the effective Hamiltonian for the ray trajectory with the wave vector playing the role of the canonical momentum [59]. However, the ray tracing equations for the position of the ray, $\mathbf{r}$, can alternatively be formulated in terms of the index of refraction [60], n, and the scaled wave vector, $\mathbf{v} = \mathbf{k}/k_0$. In this approach, the ray tracing equations take the form

$$\frac{d\mathbf{r}}{ds} = \frac{1}{n^2}\left(\mathbf{v} - n\frac{\partial n}{\partial \mathbf{v}}\right), \tag{3.1}$$

$$\frac{d\mathbf{v}}{ds} = \frac{1}{n}\frac{\partial n}{\partial \mathbf{r}}. \tag{3.2}$$

In Eqs. (3.1) and (3.2), s is a measure of the path length and is related to the time variable through $s = ct$.

To apply the previous equations to the situations of interest here, the expression for the index of refraction must be obtained for the shear Alfvén wave. The dispersion relation is extracted from Maxwell's equations with the plasma dielectric included. This leads to the expression,

$$\left(\varepsilon_\perp - n^2\right)\left(\varepsilon_\perp\varepsilon_{||} - \varepsilon_\perp n^2\sin^2\psi - \varepsilon_{||}\cos^2\psi\right) - \varepsilon_{xy}^2\left(\varepsilon_{||} - n^2\sin^2\psi\right) = 0, \tag{3.3}$$

where ψ is defined as the angle between the confinement magnetic field and the scaled wave vector. It obeys the relation,

$$\mathbf{v}\cdot\mathbf{B}_0 = nB_0\cos\psi. \tag{3.4}$$

In Eq. (3.3), the role of the off-diagonal term of the dielectric tensor is clear; it leads to coupling between the shear and the compressional roots. This is seen by the fact that upon neglecting it, the dispersion relations for the shear wave and the compressional wave are recovered independently for any ψ. Including this term leads to the expression,

$$n^2 = \frac{b \pm |b|\sqrt{1 - 4ad/b^2}}{2a}, \tag{3.5}$$

with,

$$a = \varepsilon_\perp \sin^2\psi + \varepsilon_{||} \cos^2\psi, \tag{3.6}$$

$$b = \left(\varepsilon_\perp^2 - \varepsilon_{xy}^2\right) \sin^2\psi + \varepsilon_\perp \varepsilon_{||} \left(1 + \cos^2\psi\right), \tag{3.7}$$

$$d = \varepsilon_{||} \left(\varepsilon_\perp^2 - \varepsilon_{xy}^2\right). \tag{3.8}$$

The appropriate sign must be chosen for the shear root. It is not specified here as the choice depends on the value of the wave frequency relative to the cyclotron frequencies of the individual species. From Eq. (3.5), it is clear that n only depends on $\mathbf{v}$ through the angle, ψ. Differentiating Eq. (3.4) with respect to $\mathbf{v}$ results in the expression

$$\frac{\partial\psi}{\partial\mathbf{v}} = \frac{\mathbf{v}B_0 \cos\psi - n\mathbf{B}_0}{n^2 B_0 \sin\psi}. \tag{3.9}$$

In all the following work, the other derivatives are evaluated numerically due to the complexity of the resulting analytic expressions. These numerical derivatives are computed via a centered difference with the difference size chosen such that any error introduced through this approximation is of the same order as other sources of error inherent in the calculation.

In this system, it is apparent that there are seven equations that must be satisfied (six from the differential equations, and the seventh, from the dispersion relation requirement that $|\mathbf{v}| = n$) with six unknowns. In this sense, the system is over-determined. Rigorously, the dispersion relation property simply reflects that the Hamiltonian for this system is conserved, and a correct solution of the differential equations must have this property. In practice, however, due to numerical errors, this condition can be violated after a few computational steps are implemented. In order to address this problem, a technique proposed by Yabroff [61] is adopted in which $\mathbf{v}$ is renormalized after each numerical update so that it maintains the proper length, n.

In choosing a numerical scheme, due to the computational expense of each function evaluation, a multi-step method is preferred. For the implementation in this study, a fourth order Runge-Kutta scheme is used for the first four time steps, and following that, a fourth order, Adams-Moulton predictor corrector method is applied. This enables the time step to be halved or doubled depending on the relative error present in the calculation.

In evaluating the index of refraction, Eq. (3.5) is sufficient for the cold plasma case as the dielectric components only depend on the frequency, the densities of the relevant species, and the local value of the magnetic field. When ion temperature effects are included, $\varepsilon_\perp$ and ε_{xy} become functions of $k_\perp = k_0 n \sin\psi$ (see Eqs. (3.13) and (3.14) in subsection 3.1.2). It naively appears that Eq. (3.5) can be solved by fixed point iteration. However, this method fails to converge quickly near reflection points. Because of this behavior, Newton's method is used to solve the implicit equation numerically.

3.1.2 Group Velocity

Regardless of how the ray tracing equations are handled, the ray moves along a path determined by the local group velocity. Thus, it is useful to understand the behavior of the group velocity when interpreting the ray tracing results. The parallel and perpendicular group velocities are expressed as

$$v_{g||} = \frac{\partial \omega}{\partial k_{||}}, \tag{3.10}$$

$$v_{g\perp} = -\frac{\partial k_{||}}{\partial k_\perp} v_{g||}. \tag{3.11}$$

In evaluating these expressions, the cold plasma approximation for the parallel dielectric is used as given in Eq. (2.18). For the perpendicular dielectric and off-diagonal components, both the cold and warm plasma expressions are considered in order to determine the relative effects of finite ion temperature on the rays. The cold plasma expression for $\varepsilon_\perp$ is given in Eq. (2.19), and the off-diagonal component, ε_{xy} by the expression,

$$\varepsilon_{xy} = \sum_{j=1,2} \frac{\omega_{pj}^2}{\Omega_j^2} \frac{\frac{\omega}{\Omega_j}}{1 - \frac{\omega^2}{\Omega_j^2}}. \tag{3.12}$$

While the displacement current and the electron contribution can be neglected in $\varepsilon_\perp$, the electron contribution must be included in ε_{xy}. For this reason, the electron contribution has been partitioned to match each ion contribution in order to yield the compact expression in Eq. (3.12). When ion temperature effects are included, the expressions are

$$\varepsilon_\perp = \sum_{j=1,2}\sum_{l=1}^{\infty}\frac{\omega_{pj}^2}{\Omega_j^2}\frac{1}{1-\left(\frac{\omega}{l\Omega_j}\right)^2}\frac{I_l(k_\perp^2\rho_j^2)e^{-k_\perp^2\rho_j^2}}{\frac{1}{2}k_\perp^2\rho_j^2}, \tag{3.13}$$

$$\varepsilon_{xy} = -\frac{\omega_{pe}^2}{\omega\Omega_e} + \sum_{j=1,2}\sum_{l=1}^{\infty}\frac{\omega_{pj}^2}{\omega\Omega_j}\frac{2}{1-\left(\frac{\omega}{l\Omega_j}\right)^2}\left(I_l'(k_\perp^2\rho_j^2) - I_l(k_\perp^2\rho_j^2)\right)e^{-k_\perp^2\rho_j^2}, \tag{3.14}$$

where ρ_j is the thermal Larmor radius of the j-th ion species, and I_l is the modified Bessel function of order l. From these expressions, it is seen that in this approximation, $\bar{v}_i/v_A \ll 1$, the dielectric does not depend on $k_{||}$, which makes it straightforward to solve the dispersion relation for $k_{||}$. The resulting expression is

$$k_{||}^2 = k_0^2\varepsilon_\perp + \frac{1}{2}\left[k_\perp^2\left(k_0^2\delta_e^2\varepsilon_\perp - 1\right) \pm D\right], \tag{3.15}$$

$$D = \sqrt{k_\perp^4\left(1+k_0^2\delta_e^2\varepsilon_\perp\right)^2 + 4k_0^4\varepsilon_{xy}^2\left(1+k_\perp^2\delta_e^2\right)}, \tag{3.16}$$

with $\delta_e = c/\omega_{pe}$ the electron skin depth. This expression can be used to evaluate the parallel and perpendicular group velocities leading to

$$v_{g||} = \frac{4k_{||}}{\left[2+k_\perp^2\delta_e^2 \pm k_\perp^4\delta_e^2\left(1+k_0^2\delta_e^2\varepsilon_\perp\right)/D\right]\frac{\partial}{\partial\omega}\left(k_0^2\varepsilon_\perp\right) \pm \left[4k_0^2\varepsilon_{xy}\left(1+k_\perp^2\delta_e^2\right)/D\right]\frac{\partial}{\partial\omega}\left(k_0^2\varepsilon_{xy}\right)}, \tag{3.17}$$

$$v_{g\perp} = G + \frac{2k_0^4\left(1+k_\perp^2\delta_e^2\right)\left(\varepsilon_\perp\frac{\partial\varepsilon_\perp}{\partial k_\perp} - \varepsilon_{xy}\frac{\partial\varepsilon_{xy}}{\partial k_\perp}\right) - k_0^2\frac{\partial\varepsilon_\perp}{\partial k_\perp}\left[2k_{||}^2 + k_\perp^2\left(1+k_\perp^2\delta_e^2\right)\right]}{2k_{||}\left[2k_{||}^2 + k_\perp^2 - k_0^2\varepsilon_\perp\left(2+k_\perp^2\delta_e^2\right)\right]}, \tag{3.18}$$

$$G = \frac{k_\perp\left[k_{||}^2\left(1-k_0^2\delta_e^2\varepsilon_\perp\right) - 2k_\perp^2k_0^2\delta_e^2\varepsilon_\perp - k_0^2\varepsilon_\perp - k_0^4\delta_e^2\left(\varepsilon_{xy}^2 - \varepsilon_\perp^2\right)\right]}{k_{||}\left[2k_{||}^2 + k_\perp^2 - k_0^2\varepsilon_\perp\left(2+k_\perp^2\delta_e^2\right)\right]}. \tag{3.19}$$

In the following sections these expressions are evaluated for the relevant machine parameters.

3.2 Propagation in LAPD

To better understand the ray trajectories to be presented, it is useful to first consider the behavior of the group velocity for the relevant plasma conditions. Figure 3.1 shows color contours of the dependence of the group velocity on perpendicular wave number and scaled frequency, using the cold ion dielectrics in Eqs. (2.19) and (3.12). The parameters correspond to the experiments reported in Chapter 2. A hydrogen-helium plasma is considered with concentration ratio $n_H/n_e = 0.45$ and satisfying charge quasi-neutrality. The electron density is $n_e = 1.3 \times 10^{12}\,\mathrm{cm}^{-3}$, the magnetic field, $B = 750$ G, giving an Alfvén speed of $v_A = 8.85 \times 10^7\,\mathrm{cm/s}$. Figure 3.1 displays the components of the group velocity vector as color contours over a relevant range of values of the scaled perpendicular wave number and scaled wave frequency. The top panel, Fig. 3.1(a), illustrates the dependencies of the parallel group velocity, and the bottom panel, Fig. 3.1(b), those of the perpendicular group velocity. On the horizontal axis, the wave frequency is scaled to the cyclotron frequency of helium. In the LAPD resonator experiment this would be equivalent, for a fixed wave frequency, to the axial coordinate along which the strength of the magnetic field varies. On the vertical axis, the perpendicular wave number is scaled to the electron skin depth and shown over a positive range of values. Note that the color scale for the bottom panel, Fig. 3.1(b), is two orders of magnitude smaller than in Fig. 3.1(a), and also, that it includes positive and negative values since the waves can have a backward character in the perpendicular direction. From these displays, it is clear that for $k_\perp \delta_e > 0.1$ (indicated by the white dashed line), the parallel group velocity is much larger than the perpendicular group velocity resulting in essentially field-aligned propagation. There is a parallel cutoff for the wave at the ion-ion hybrid frequency, $\omega/\Omega_{He} \approx 2.12$, represented by the vertical, dashed red line. For larger scaled-frequencies the wave is backward-traveling with the perpendicular phase velocity and the perpendicular group velocity having opposite sign. These are all typical characteristics of the shear wave. As $k_\perp$ decreases towards zero, the perpendicular group velocity switches sign, becoming a forward-propagating wave. In this region the ion-ion hybrid frequency ceases to act as a cutoff, and the wave is no longer field-aligned, having a significant perpendicular

component to the group velocity, as is more typical of a compressional mode. However, in LAPD the finite radial dimension of the plasma does not allow these compressional features to play a role, i.e., the window of propagation lies above the white dashed line indicated in Fig. 3.1. Lastly, the peculiar feature at $\omega/\Omega_{He} = 3.04$ deserves mention. At this frequency the off-diagonal component of the dielectric tensor, ε_{xy}, vanishes; since no coupling to the compressional mode exists, the mode remains backward- traveling for all values of $k_\perp$. For a general two-ion species plasma this behavior occurs at the cross-over frequency,

$$\omega_X^2 = \frac{\omega_{p1}^2\Omega_2^3 + \omega_{p2}^2\Omega_1^3}{\omega_{p1}^2\Omega_2 + \omega_{p2}^2\Omega_1}. \tag{3.20}$$

Figure 3.2 presents horizontal line-cuts of Fig. 3.1, illustrating the variation of the group velocity components at selected values of the scaled perpendicular wave number. The top panel, Fig. 3.2(a), again corresponds to the parallel group velocity, and the bottom panel, Fig. 3.2(b), to the perpendicular group velocity. The horizontal axis in both plots corresponds to the scaled frequency as in the contour plots of Fig. 3.1. The four selected curves in each panel use values of $k_\perp\delta_e = 0.086$ (solid), 0.11 (dashed), 0.16 (dashed-dotted), and 0.34 (solid with dotted markers) that correspond to the ray trajectories described in Figs. 3.6-3.9, respectively, shown later in this section. For comparison, the white dashed line in Fig. 3.1, corresponding to the smallest possible perpendicular wave number in LAPD, has the value of $k_\perp\delta_e = 0.098$. Thus, the perpendicular wave numbers represented in Figs. 3.6-3.9 are representative of those which would be found in the LAPD resonator. From the top panel of Fig. 3.2, it is apparent that there is very little change in the parallel group velocity as $k_\perp$ increases over this parameter range. The cutoff is located at roughly the ion-ion hybrid frequency, and the wave continuously slows down as it approaches the hydrogen cyclotron resonance (i.e., $\omega = 4\Omega_{He}$). The lower panel shows a much more drastic change in the perpendicular group velocity. Due to the inclusion of ε_{xy} in the dispersion relation, the perpendicular group velocity is always slightly positive near the ion-ion hybrid frequency, although this effect decreases in importance as $k_\perp$ increases. As $k_\perp$ increases, the line-cuts exhibit the backward-traveling property of the shear Alfvén wave over a larger portion of

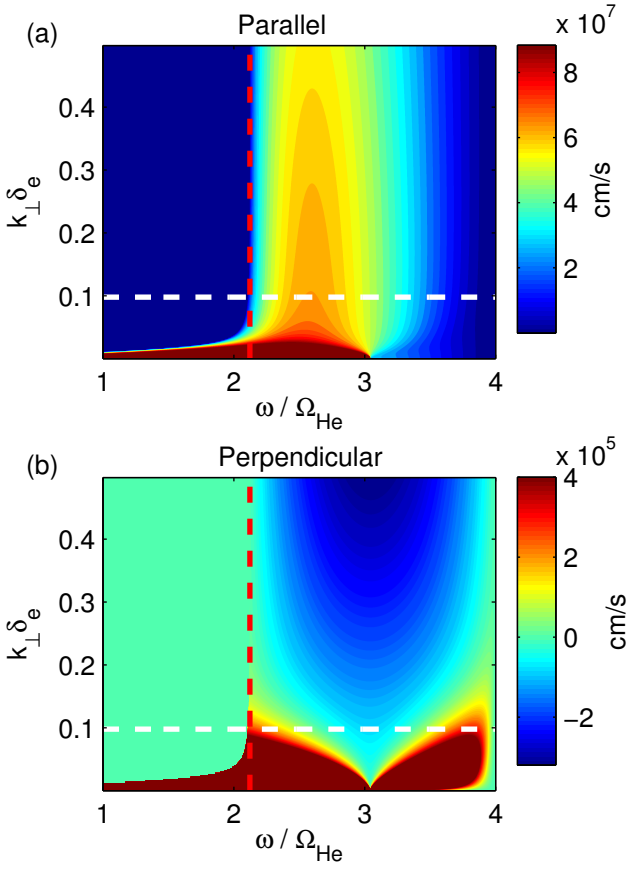

Figure 3.1: Contour displays of components of group velocity for upper branch of shear Alfvén wave obtained from cold plasma dispersion relation for LAPD parameters. Ion mixture is 45% H+, 55% He+, magnetic field strength is 750 G and the electron density is $1.3 \times 10^{12}\text{cm}^{-3}$. Vertical axis is the scaled perpendicular wave number, $k_\perp \delta_e$, and the horizontal axis, the scaled frequency, ω/Ω_{He}. (a) Parallel group velocity, (b) perpendicular group velocity. White dashed line represents lower limit on perpendicular wave numbers allowed in LAPD due to finite radial size. Red dashed line represents the ion-ion hybrid frequency. Note that contour scales in panels (a) and (b) differ by two orders of magnitude.

the frequency range. But at small values of $k_\perp$, the wave becomes forward-traveling, as the coupling to the compressional mode increases.

Figure 3.3 illustrates the behavior of the shear-mode dispersion relation when finite ion temperature is included for LAPD conditions. Shown are color contours of the scaled parallel wave number $k_{||}v_A/\Omega_{He}$ as a function of scaled perpendicular wave number and frequency. The calculation uses Eqs. (3.13) and (3.14) in place of Eqs. (2.19) and (3.12). The base plasma parameters are the same as in Figs. 3.1 and 3.2, but now the ion temperature is set to $T_i = 1$ eV for both ion species. This results in a ratio of $\rho_{He}/\delta_e = 0.6$. The vertical axis is the scaled perpendicular wave number, and the horizontal axis is the scaled frequency. The same scaling factors as in Fig. 3.1 are used for both quantities. At small values of $k_\perp\delta_e$, the wave propagates for all frequencies, and exhibits compressional-mode behavior. As $k_\perp\delta_e$ increases, a parallel cutoff appears. Its value starts close to the ion-ion hybrid frequency ($\omega_{ii}/\Omega_{He} = 2.12$), but due to temperature effects it deviates slightly from this value, as indicated by the thick white lines, which correspond to the $k_{||} = 0$ condition. Two kinetic features appear at the cyclotron harmonics of helium, but they are small effects due to the small temperature considered. An important feature illustrated near the top right quadrant of Fig. 3.3 is that, for large $k_\perp$, and frequencies above the third helium harmonic, the contours exhibit a leftward tilt. Because the perpendicular group velocity can be expressed as $v_{g\perp} = (\partial\omega/\partial k_\perp)$ with $k_{||}$ fixed in this partial derivative, the direction of this component of the group velocity can be deduced from the direction that a contour of constant $k_{||}$ takes in this display format. If the contour moves right (left) for increasing $k_\perp$, then the wave is forward (backward) traveling.

Figure 3.4 uses the same display format and color scale as Fig. 3.1. It illustrates the effects caused by the inclusion of a finite ion temperature to shear-mode propagation in the LAPD plasma, for the plasma parameters of Fig. 3.3. Again, the red dashed line represents the ion-ion hybrid frequency. The first four harmonics of the helium ion are included in the expressions for $\varepsilon_\perp$ and ε_{xy} as they fall in the frequency range displayed. The general features are as before with the addition of enhanced perpendicular propagation, indicating ion-Bernstein wave (IBW) features, especially for frequencies close to the cyclotron harmonics

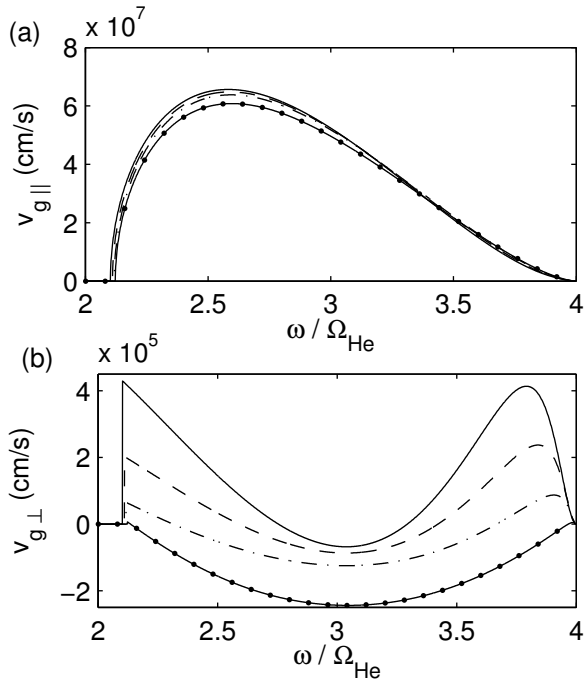

Figure 3.2: Line cuts of contour displays in Fig. 3.1 for selected values of $k_\perp \delta_e$. (a) Parallel group velocity, (b) perpendicular group velocity. Vertical axis is the corresponding component of the group velocity and horizontal axis, the scaled frequency. The solid, dashed, dash-dotted, and dotted curves correspond to values of $k_\perp \delta_e = 0.086$, 0.11, 0.16, and 0.34, respectively. The parallel group velocity is largely unchanged over this parameter range while the perpendicular group velocity indicates reflections in the perpendicular direction due to the inclusion of ε_{xy} in the dispersion relation. At small values of $k_\perp$, these reflections are close to ω_X given by Eq. (3.20). As $k_\perp$ increases, the reflections move towards ω_{ii} and Ω_H. The wave is forward-traveling for frequencies close to ω_{ii} indicating a reversal in perpendicular direction as the wave approaches the parallel reflection point.

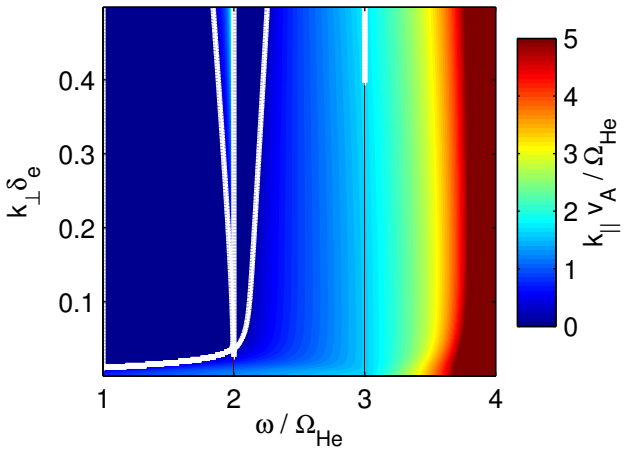

Figure 3.3: Contour display of dispersion relation for the same LAPD base parameters used in Fig. 3.1, but now both ion species have a finite temperature of $T_i = 1$ eV. The vertical axis is the scaled perpendicular wave number, the horizontal axis the scaled frequency, and the contours correspond to the scaled parallel wave number. The $k_{||} = 0$ contour is given by the white curves. Finite ion- temperature effects appear at the second harmonic of helium where coupling to IBWs occurs. A similar feature exists at the third harmonic but is less pronounced. Due to FLR effects, the $k_{||} = 0$ contour no longer converges to ω_{ii} asymptotically as $k_\perp \to \infty$.

and to the ion-ion hybrid frequency. Also, at larger $k_\perp$ the cutoff-frequency differs from the value of the ion-ion hybrid frequency. The large perpendicular group velocity near the cutoff can be explained by the departure of the cutoff from the ion-ion hybrid. Figure 3.5 shows line-cuts of Fig. 3.4, similar to those in Fig. 3.2 associated with Fig. 3.1. The line styles correspond to the same values of $k_\perp \delta_e$ as in Fig. 3.2. Comparing Fig. 3.5 to Fig. 3.2, it can be seen that the perpendicular group velocity is larger near the cutoff when finite ion temperature is included than in the cold ion case; the parallel group velocity is essentially unchanged. Further, a bite-out at $\omega/\Omega_{He} = 3$ exists due to the cyclotron harmonic response.

With this background, the ray tracing results are now examined. The magnetic field is defined as in Chapter 2 in both Eq. (2.2) and the preceding discussion. The axial (z-dependence) of the magnetic well is approximated by the expression

$$B_z(z) = B_{\min} + (B_{\max} - B_{\min}) \tanh^2 \left(\frac{z^2}{L^2} \right), \tag{3.21}$$

where, $B_{\min} = 750$ G, $B_{\max} = 1250$ G, and $L = 182.6$ cm. For the ray trajectories presented in this section, the frequency is $f = 818$ kHz or $\omega/\Omega_H = 0.71$ at $B = B_{\min}$, corresponding to the largest peak shown in Fig. 2.7. Each ray trajectory begins at the origin of the cylindrical coordinate system. The initial angle, ψ, between the z-axis and the initial scaled wave vector, $\mathbf{v}$, is varied for each ray with the magnitude of $\mathbf{v}$ determined by the dispersion relation. This initial choice of ψ sets the value of the perpendicular wavelength, which is mostly invariant along the trajectory; small variations arise due to the radial component of the magnetic field whose magnitude increases with radius.

In determining the resonator quality factor, Q, due solely to radial spreading of the associated ray, it is useful to start from the definition

$$Q = \omega \frac{U}{P}, \tag{3.22}$$

where U is the energy stored and P is the power lost. The stored energy can be written as $U = \bar{u}\pi R^2 d$ where R is the transverse dimension of the device, d is the spatial extent of the well in the longitudinal direction, and $\bar{u}$ is an average energy density stored in the wave

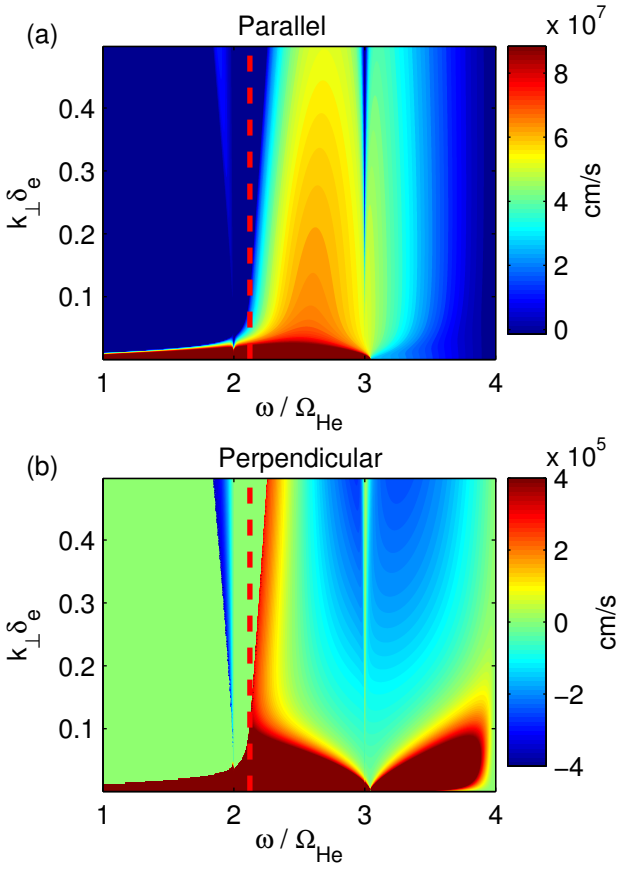

Figure 3.4: Contours of group velocity including finite ion temperature corresponding to conditions used in Fig. 3.3. To be contrasted to the cold ion case of Fig. 3.1. Vertical axis is the scaled perpendicular wave number and horizontal axis is the scaled frequency. (a) Parallel group velocity, (b) perpendicular group velocity. Red dashed line represents ω_{ii}. Finite ion temperature generates features near harmonics of Ω_{He} and causes the parallel cutoff to deviate from ω_{ii} at large values of $k_\perp$. A large, perpendicular group velocity is now present near the parallel cutoff. Note that contour scales in panels (a) and (b) differ by two orders of magnitude.

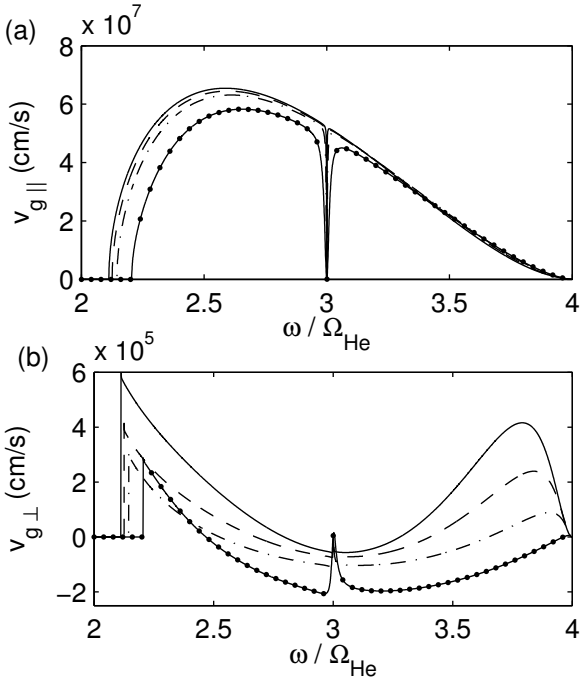

Figure 3.5: Line cuts of contour displays in Fig. 3.4 for selected values of $k_\perp \delta_e$. (a) Parallel group velocity, (b) perpendicular group velocity. Vertical axis is the corresponding component of the group velocity and horizontal axis, the scaled frequency. Line styles correspond to the same values of $k_\perp$ in Fig. 3.2. Overall, the qualitative behavior is similar to the cold ion case of Fig. 3.2 except that a bite-out appears in both components of the group velocity at $\omega/\Omega_{He} = 3$, the parallel cutoff moves to higher frequencies as $k_\perp$ increases, and the perpendicular group velocity is much larger near the parallel cutoff.

across the column of the plasma. The expression for the power lost is $P = v_{g\perp} 2\pi R d u_{r=R}$ with $u_{r=R}$, the energy density at the edge of the plasma and $v_{g\perp}$, the average perpendicular group velocity over the trajectory of the ray. This can be computed by $v_{g\perp} = \Delta r/\Delta t$ where Δr is the radial displacement that a ray experiences upon traveling from the center to the reflection point and Δt is the time it takes for the ray to travel this distance. Implicit in this expression is the assumption that all wave energy that reaches the plasma edge escapes. Substituting these expressions into Eq. (3.22) gives the expression

$$Q = \left[\frac{\bar{u}}{u_{r=R}}\right] \frac{R}{\Delta r} \omega \Delta t. \tag{3.23}$$

The factor contained in square brackets is a geometric factor and depends on the radial eigenmode of the system. Taking this factor to be of order unity, an estimate for the quality factor can be extracted from the ray tracing studies. The radius, R, is taken to be the width of the plasma column which is roughly 20 cm. The remaining parameters can be determined by examining the specific ray in question.

In Figs. 3.6-3.9, various ray trajectories in the (z, r) plane are shown. In each figure, the vertical axis is the z-axis of the plasma column, and the horizontal axis represents the transverse, radial direction r. No motion for the rays in the azimuthal direction is considered. The solid curves represent rays calculated using the cold ion dielectric as given in Eqs. (2.18), (2.19) and (3.12). The dashed line uses the warm ion dielectric as given in Eqs. (2.18), (3.13), and (3.14) with an ion temperature $T_i = 1$ eV for both species. The initial angles are $\psi_0 = 81.5°$, $83.4°$, $85.4°$,and $87.7°$ for Figs. 3.6, 3.7, 3.8, and 3.9 respectively, resulting in a higher $k_\perp$ value for each successive figure ($k_\perp \delta_e = 0.086$, 0.11, 0.16, and 0.34, respectively). As mentioned previously, these values correspond respectively to the solid, dashed, dash-dotted, and dotted lines in both Figs. 3.2 and 3.5. Note that the length-scale used for the axial direction in Figs. 3.6-3.9 is a factor of 100 larger than in the transverse direction because wave propagation is essentially along the magnetic field. Also, Figs. 3.6-3.9 display the behavior on small radial scales on the order of centimeters; this is done to aid the reader in understanding the plots. The features of the ray trajectories displayed extrapolate well to larger radii, except that the curvature of the mirror magnetic field causes a slight bowing

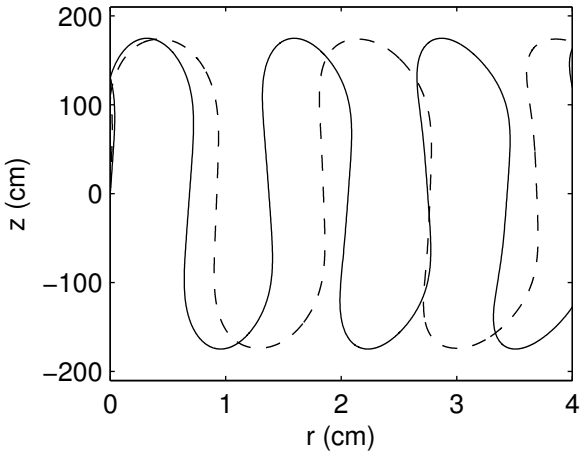

Figure 3.6: Ray trajectories for LAPD. Vertical axis is the axial displacement of the ray, and the horizontal axis, the radial displacement. The rays are launched from the center of the magnetic well ($r = 0, z = 0$) with the initial value of $k_\perp$ corresponding to the value associated with the solid curves in Figs. 3.2 and 3.5. Note that the axial scale (z) is two orders of magnitude larger than transverse scale (r) to accommodate the highly field-aligned propagation. The solid curve uses cold ions, and the dashed curve includes finite ion temperature effects. Both rays are predominantly field-aligned exhibiting only slight transverse displacements close to the reflection layer. The transverse propagation near the reflection layer is dominant and causes the rays to wander towards the edge of the plasma.

as the ray propagates between reflection points.

From Fig. 3.6, it is seen that the perpendicular group velocity reverses direction in both the cold and hot rays as they approach the reflection point. This is in agreement with the contour plots of the group velocity, as shown in Figs. 3.1 and 3.4. This feature follows from the fact that, near the midplane (z = 0), the wave is a backward wave, hence it focuses radially, while near the reflection layer radial-spreading results because the wave becomes a forward wave. In order for the wave energy to be lost (or not) out of the column, one effect must dominate over the other. In this case, it is clear that the transverse motion near the reflection point is dominant and causes net wave propagation towards the edge of the plasma. It is also apparent that finite ion temperature leads to enhanced transverse motion

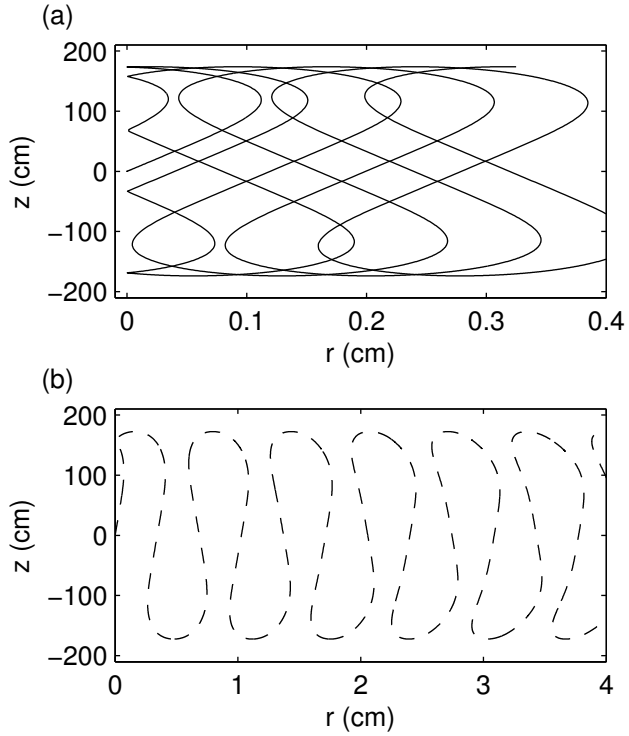

Figure 3.7: Ray trajectories for LAPD with initial value of $k_\perp$ corresponding to the value associated with the dashed curves in Figs. 3.2 and 3.5. Top panel (a) uses cold ions, and bottom panel (b) includes finite ion temperature. The top panel shows that the backward-traveling nature of the ray at the center of the well ($z = 0$) is counterbalanced by the forward-traveling nature of the wave near the reflection points resulting in little net transverse motion of the ray even after many transits. This effect is not present in the bottom panel as the inclusion of ion temperature causes increased transverse motion near the reflection point.

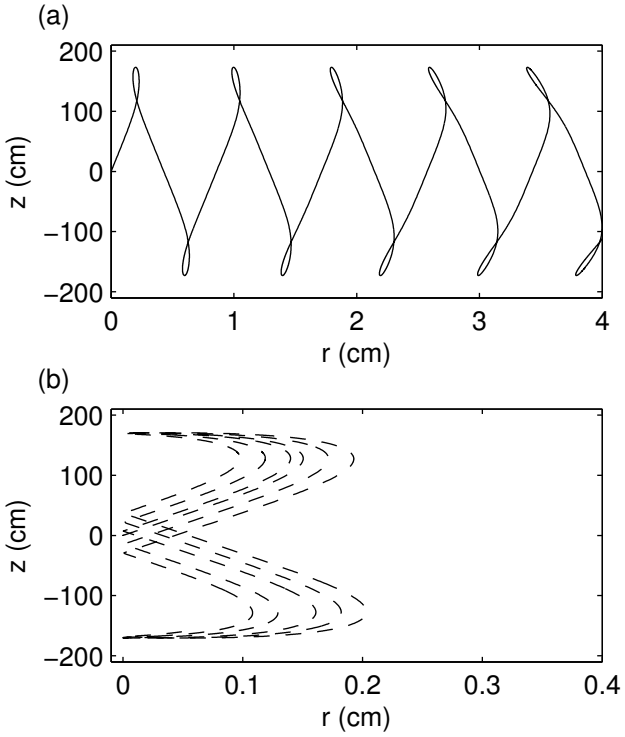

Figure 3.8: Ray trajectories for LAPD with initial value of $k_\perp$ corresponding to the value associated with the dashed-dotted lines in Figs. 3.2 and 3.5. Top panel (a) uses cold ions, and bottom panel (b) includes finite ion temperature. For the top panel, the backward-traveling nature of the ray near the center of the well (z = 0) dominates and the ray wanders to the plasma edge. In the bottom panel, the backward-traveling nature of the wave towards the center is balanced by the forward-traveling nature at the reflection point. The resulting ray almost retraces itself.

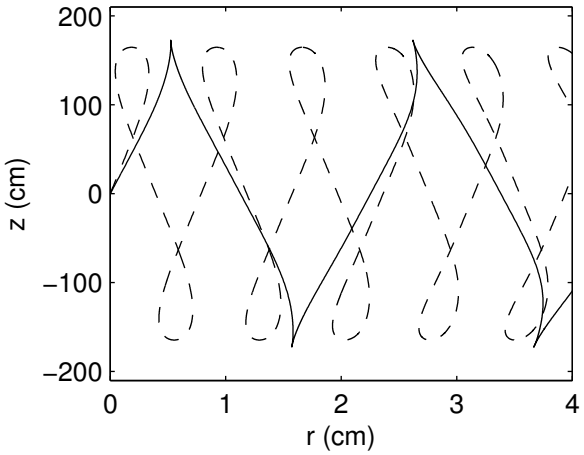

Figure 3.9: Ray trajectories for LAPD with initial value of $k_\perp$ corresponding to the value associated with the solid curve with dotted markers in Figs. 3.2 and 3.5. Here the solid curve uses cold ions, and dashed curve includes finite ion temperature. For this wave number the backward-traveling nature of the wave dominates the transverse motion of the ray in both cold and warm ion cases causing the rays to move to the plasma edge.

near the reflection layer over the cold ion result, as expected from Figs. 3.1 and 3.4. In computing the quality factor, Eq. (3.23) is used here and in all subsequent calculations. It is determined that Q = 230 for the cold ion ray and Q = 160 when ion temperature is included.

It is not necessarily the case that the inclusion of finite ion temperature leads to smaller Q-values. In the top panel of Fig. 3.7 and the bottom panel of Fig. 3.8, it can clearly be seen that little radial wandering occurs due to the balance of the transverse motion near the midplane ($z = 0$) and near the reflection layer. This occurs at different initial angles for the cold-ion and warm-ion trajectories due to the increase in the perpendicular group velocity for the warm ions. It is conceivable that, if properly tuned, a ray would perfectly retrace itself and the quality factor due to radial spreading would be infinite, as no radial motion would take place. The quality factors for Fig. 3.7 are Q = 2500 for the cold-ion ray and Q = 430 for the warm-ion case, while for Fig. 3.8 these values become Q = 130 and Q = 14,000, respectively.

For Fig. 3.9, it is clear that the backward-traveling motion at the midplane ($z = 0$)

is dominant and leads to the ray quickly traveling to the edge of the plasma. Again, the perpendicular motion of the ray near the reflection layer is more pronounced when ion temperature is included. In this case the quality factors are Q = 130 for the cold ions and Q = 360 for warm ions.

Finally, it must be noted that the assumptions underlying the ray tracing equations are not rigorously satisfied as applied to the LAPD resonator in the axial direction, because the axial gradient scale length of the confinement magnetic field in the resonator configuration used in LAPD is comparable to the axial wavelength of the candidate eigenmodes. However, there is no such deficiency in the radial direction. The present ray tracing results can, however, be used to obtain an estimate of the qualitative features that would be present in a full wave treatment that includes both the effects of ε_{xy} and finite ion temperature. Specifically, coupling to the IBW in the reflection layer is not expected to enhance the loss of wave energy for the parameters present in the experiment. Additionally, these features are useful in understanding the remainder of the chapter, as well as in illustrating properties expected in future discussions of resonator phenomena.

3.3 Propagation in ETPD

The background magnetic field in the Enormous Toroidal Plasma Device (ETPD) at UCLA [58] is well-described in zeroth-order by a toroidal field. Adopting different notation in this section, a cylindrical coordinate system is defined to be (ρ, ϕ, z). In this coordinate system, the magnetic field takes the form,

$$\mathbf{B} = \frac{B_0}{1 + \frac{r}{R}\cos\theta}\hat{\boldsymbol{\phi}}. \tag{3.24}$$

For the present configuration of ETPD, $B_0 = 200$ G is the magnetic field strength on axis, $R = 500$ cm is the major radius, r is the radial distance from the magnetic axis, and θ is the poloidal angle. In the actual operation of the device, a small vertical field (z-component) is applied to create a helical field-line geometry consisting of multiple plasma rings. In this manuscript, the z-component is neglected in order to gain an understanding of the pure

effects of field-line curvature on the ray path. The plasma considered consists of two ion species, hydrogen and helium, of equal concentrations with a generic electron density of $n_e = 1 \times 10^{12}\,\mathrm{cm}^{-3}$, and equal ion temperatures of $T_i = 10$ eV. Because of the significantly lower magnetic field and much larger ion temperature than is achieved in LAPD, finite ion Larmor radius effects play an important role in the ray trajectories in ETPD.

In the purely toroidal field, two wave propagation invariants exist. The first is the z-component of the wave vector, k_z. The second invariant, m, is related to the toroidal component of the scaled wave vector, $k_\phi = m/\rho$. For simplicity, k_z is set to zero, and due to the nature of the magnetic field, $k_{||} = k_\phi$ and $k_\perp = k_\rho$. Due to the invariant nature of the parallel wave number, $k_{||}$ cannot vanish except when it is zero from the outset. This precludes the possibility of a resonator in this environment, but the rays, in principle, can sample the ion-ion hybrid layer due to cross-field propagation. Using the simplified dispersion relation, Eq. (1.3), which neglects coupling to the compressional wave, and solving for k_ρ gives

$$k_\rho^2 \delta_e^2 = \frac{m^2}{k_0^2 \rho^2 \varepsilon_\perp} - 1. \tag{3.25}$$

It is clear from this expression that a radial reflection point exists at $\rho = m/k_0\sqrt{\varepsilon_\perp}$ preventing the ray from traveling to larger radii. As this radial reflection point is approached, $k_\perp$ becomes small, and the wave starts to exhibit compressional features. This alters the predominantly field-aligned propagation characteristic of the shear mode

Figure 3.10 illustrates two ray trajectories in ETPD, each corresponding to a frequency of $\omega/\Omega_{He} = 2.6$ at the starting radius, $r = 0$ cm. The vertical axis indicates the distance of the ray from the minor axis. The horizontal axis is the time (in μs) that is required for the ray to travel from the starting position ($r = 0$) to a given value of r. The solid curve is a ray calculated with the cold ion dispersion relation, and the dashed curve, a ray that is found from the warm ion expressions. The two dash-dotted lines represent the positions at which the frequency matches the local ion-ion hybrid frequency, $\omega_{ii}/\Omega_{He} = 2$, at $r = -116$ cm, and the third cyclotron harmonic of helium at $r = 77$ cm, as labeled in the figure. The direction of the gradient of the magnetic field strength is also shown, increasing for negative values of r. The ray is launched from an initial position where the x-axis intersects the

minor axis, $\mathbf{r}_0 = R\hat{\mathbf{x}}$. The initial wave vector is placed in the plane defined by the vectors $\hat{\boldsymbol{\rho}}$ and $\hat{\boldsymbol{\phi}}$ with the angle between the wave vector and the magnetic field set to $\psi_0 = 88.9°$ and set to a negative value for both the solid line and the dashed line (which, for the dashed line, gives a value of $k_\perp \delta_e = 0.5$ with $\rho_{He}/\delta_e = 6.1$ initially). The solid curve illustrates the backward-traveling nature of the shear mode as it initially propagates towards positive values of r. As it approaches the radial reflection point, at roughly t = 120 μs, the group velocity switches direction due to transitioning from a backward-traveling wave with high $k_\perp$ to a forward traveling wave with small $k_\perp$. This is due to the coupling associated with the ε_{xy} term included in the dispersion relation. As $k_\perp$ continues to decrease, eventually k_ρ flips sign, and the wave experiences another, more abrupt, radial reflection. The process then occurs in reverse order, but now with a positive k_ρ. From the ray trajectory, it can be deduced that the toroidal field preferentially increases the value of k_ρ. This can be understood from Eq. (3.2). If $\partial n/\partial \mathbf{r}$ is expanded in terms of the parameters on which it depends,

$$\frac{\partial n}{\partial \mathbf{r}} = \frac{\partial n}{\partial \psi}\frac{\partial \psi}{\partial \mathbf{r}} + \frac{\partial n}{\partial B}\frac{\partial B}{\partial \mathbf{r}}. \tag{3.26}$$

The first term on the right is a pure curvature effect, and the second term is due to the magnetic field gradient. It is clear from Eq. (3.25) that the effect of curvature causes $|k_\rho|$ to decrease from its initial negative value towards zero as the ray travels radially outward (towards positive r). Upon reflection, k_ρ becomes positive, and its value increases as it travels radially inward (towards negative r). The result is that the curvature tends to increase k_ρ as the ray propagates. Similarly, $\partial n/\partial B < 0$ and $\partial B/\partial \mathbf{r}$ points radially inward leading to the same effect due to the magnetic gradient. Thus, for the cold ray, k_ρ is always increasing as it propagates. This curvature effect is not exclusively a two-ion effect, but is present also in a single-ion species plasma when ion temperature effects are negligible. Finally, a comment should be made regarding the two-dimensional representation of the three-dimensional ray trajectory. Because the parallel group velocity is much larger than the perpendicular group velocity over a majority of the ray trajectory, the ray completes several toroidal transits during the course of its motion. For example, at $t = 120\,\mu$s, the cold ray experiences roughly three toroidal transits.

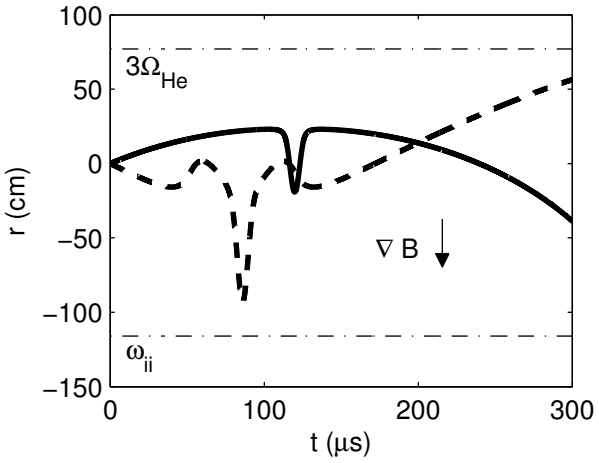

Figure 3.10: Ray trajectories for ETPD. The plasma is comprised of 50% H+, 50% He+ ions with an electron density of $10^{12}\,\mathrm{cm}^{-3}$. Vertical axis represents radial displacement from the center of the plasma with positive (negative) values representing outboard (inboard) propagation. The horizontal axis is time of propagation. The direction of the magnetic field gradient is shown. This gradient causes the perpendicular wave number to increase in the opposite direction. The two dashed-dotted lines represent the positions where the wave frequency matches the local values of ω_{ii} and the third harmonic of Ω_{He}, as indicated. The solid curve illustrates a ray trajectory using cold ions and the dashed curve uses hot ions with $T_i = 10$ eV. Both rays start with $k_\perp$ initially pointing radially inward.

The finite ion temperature result for this magnetic configuration contains some features present in the cold result, but to better understand the kinetic effects, the dispersion relation is considered in Fig. 3.11 and the group velocity, in Fig. 3.12. Figure 3.11 illustrates the dispersion relation using the display format of Fig. 3.3. Again, the scaled frequency is on the horizontal axis, and the scaled perpendicular wave number is on the vertical axis; the color contours represent the scaled parallel wave number. The $k_{||} = 0$ boundary is outlined as a thick white line, as before. Figure 3.12 is the analog of Figs. 3.1 and 3.4, using similar axes, with the contours representing the parallel group velocity shown in the top panel and those for the perpendicular group velocity in the bottom panel. The red dashed line represents the ion-ion hybrid frequency and would be the cold cutoff in the absence of temperature effects. From Figs. 3.11 and 3.12 it is apparent that the inclusion of temperature effects creates a complex structure between each cyclotron harmonic. The wave properties can be separated into three distinct regions based on the relative values of $k_\perp$ and ω. At small values of $k_\perp$, the dispersion relation resembles that of the compressional mode, i.e., it propagates isotropically in the direction of the wave vector and does not resonate strongly with the cyclotron harmonics of helium. At intermediate values of $k_\perp$ (roughly in the range of $k_\perp \delta_e = 0.15 - 0.3$) and values of ω close to the first and second cutoffs, the wave begins to exhibit more of the shear mode characteristics. This is evident by the regions over which the wave is backward-traveling, and by the small value of the perpendicular group velocity relative to the parallel component. Finally, at larger values of $k_\perp$ and for values of ω away from the first and second cutoff, the wave becomes increasingly forward- propagating with increasing perpendicular group velocity. The inclusion of ion temperature introduces new cutoffs (propagation bands) at various frequencies that depend strongly on $k_\perp$. The nature of the wave at these cutoffs, whether it is forward or backward-traveling, corresponds to the direction of the $k_{||} = 0$ contour in Fig. 3.11 as before. These properties are useful in interpreting the ray trajectory represented by the dashed line in Fig. 3.10. For that ray, the initial parameters are chosen such that $k_\perp \delta_e = 0.5$ and $\omega/\Omega_{He} = 2.6$, so that the wave starts as forward- traveling. Because k_ρ has a negative value, this leads to inward (negative r) propagation. Due to magnetic gradient and curvature effects, the value of k_ρ increases

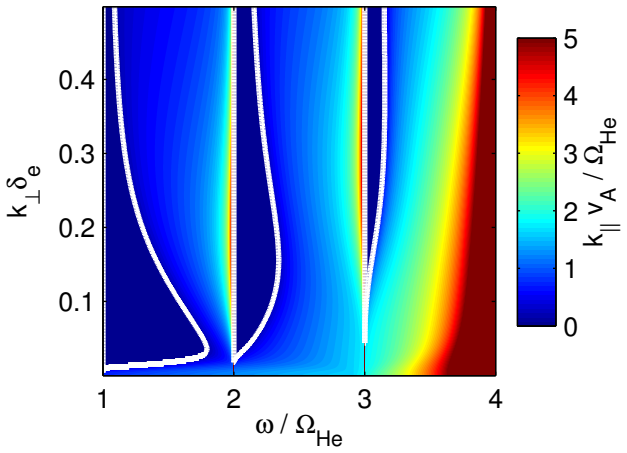

Figure 3.11: Contour display of dispersion relation for ETPD conditions given in Fig. 3.10 with magnetic field strength of $B = 200$ Gauss and hot ions. Vertical axis is the scaled perpendicular wave number, the horizontal axis is the scaled frequency, and the contours are the scaled parallel wave number. The $k_{||}$ contour is illustrated by the thick white lines. The 'S' shape of the contours between helium cyclotron harmonics shows regions with a backward-traveling wave sandwiched between two forward-traveling regions.

from its negative value towards zero, decreasing the value of $k_\perp \delta_e$. From Fig. 3.12(b), it can be seen that there are three distinct regions that the wave must travel through in parameter space as $k_\perp$ approaches zero. In transitioning from one region to the next, the ray changes its direction of radial propagation. It is for this reason that there are five total radial reflections observed in the figure. The radial reflection at $t = 90\,\mu$s corresponds to the reversal of k_ρ from negative to positive. The two reflections adjacent to this $k_\perp = 0$ point represent that transition from a forward traveling wave to a backward traveling wave at intermediate values of $k_\perp$. The last two radial reflection points represent the transition from intermediate values of $k_\perp$ to large values where the wave is again forward-traveling. At large values of t, the wave approaches the third cyclotron harmonic of helium, located at $r = 77$ cm.

Figure 3.13 illustrates the trajectories of a bundle of rays launched from the same position and with the same plasma conditions as the ray described in Fig. 3.10. The rays are all launched at the same frequency ($\omega/\Omega_{He} = 2.6$), but differ with respect to the initial angle, ψ,

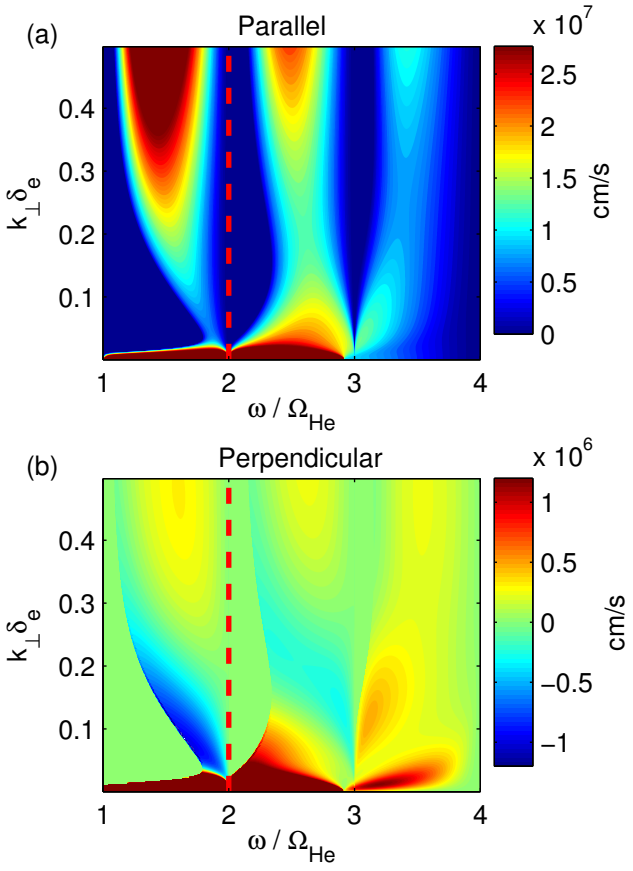

Figure 3.12: Contour displays of components of group velocity for conditions given in Fig. 3.11. Vertical axis is the scaled perpendicular wave number and horizontal axis is the scaled frequency. (a) Parallel group velocity, (b) perpendicular group velocity. The red dashed line is the ion-ion hybrid frequency. Regions of forward and backward-traveling waves are seen in the bottom panel.

between the magnetic field and the wave vector. These angles are both positive and negative 11.25°, 22.5°, 33.75°, 45°, 56.25°, 67.5°, 78.75°, 84.38°, 84.6°, 85.5°, 86.4°, 87.3°, 88.2°, and 89.1°. The survey of opening angles is roughly equivalent to starting each of the rays at a different point along the lines in Fig. 3.10. The top panel of Fig. 3.13 corresponds to the cold ion result (the solid curve in Fig. 3.10), and the bottom panel, to the warm ion result (the dashed curve in Fig. 3.10). In both panels, time (in μs) is displayed along the horizontal axis with 150 microseconds corresponding, roughly, to one toroidal transit. The vertical axis on the left side indicates radial displacement from the initial position, with positive values corresponding to the outboard side and negative values to the inboard side of the torus. The vertical axis on the right side shows the corresponding change in the ratio of the frequency to the local value of the cyclotron frequency of helium. In the top panel, it is seen that some of the rays at lower values of positive ψ are quickly refracted out of the plasma column, in both the positive and negative radial directions. These correspond to low perpendicular wave number and possess compressional wave features. Those with more oblique initial angles are more field-aligned and thus propagate farther before refracting out of the plasma column. Rays whose perpendicular wave vector initially point inward, propagate outward (due to the backward-traveling nature of the wave). As they do so, $k_\perp$ increases towards positive values until they experience a radial reflection. Thus, the wave energy is predominantly deposited on the inboard side. When ion temperature is included in the analysis, this picture changes. As seen in the lower panel (note that time axis is compressed relative to that of top panel), many rays experience multiple radial reflections as mentioned in the discussion of Fig. 3.10. Those rays that start with $k_\perp$ initially pointing outward ultimately arrive at the outboard side of the device, regardless of how many radial reflections occur. Those rays that start with $k_\perp$ pointing inward are carried to the inboard side of the device due to the large inward radial excursion shown in Fig. 3.10 near the zero of $k_\perp$.

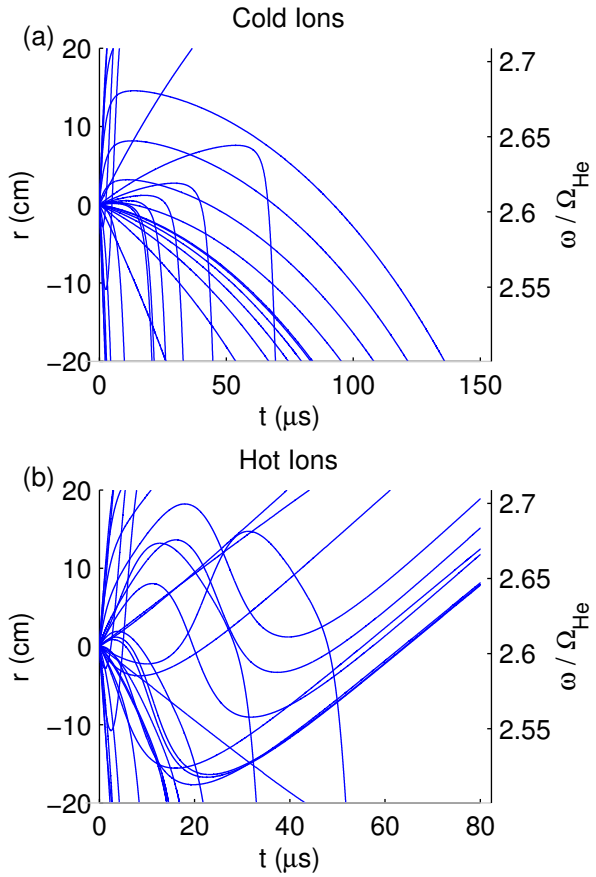

Figure 3.13: A bundle of rays propagating in ETPD. The vertical axis on the left represents radial displacement from the center of the plasma with positive (negative) values representing outboard (inboard) motion. The vertical axis on the right represents the scaled frequency associated with the radial position of the ray. The horizontal axis is the time of propagation for the ray. (a) Cold ions. Rays with low perpendicular wave number have compressional characteristics and are quickly lost out of the plasma. More oblique rays stay within the plasma column for a greater length of time. Radial reflections cause wave propagation towards the inboard side. (b) Hot ions. Rays with an initial perpendicular wave number pointing towards the inboard side are turned towards the inboard side when $k_\perp$ becomes small enough that compressional features dominate. Rays with perpendicular wave number pointing towards the outboard side propagate towards the third cyclotron harmonic of helium.

3.4 Propagation in ITER

Next, the dispersion relation and group velocity for ITER [62] burning plasma parameters are considered. Figure 3.14 is the equivalent of Figs. 3.4 and 3.12, but now evaluated for characteristic parameters expected for the ITER device. Accordingly, the frequency is scaled to the tritium cyclotron frequency, Ω_T. A deuterium-tritium plasma is considered with equal concentrations of each species. The total electron density is set to $n_e = 1.0 \times 10^{14}\,\mathrm{cm}^{-3}$, the magnetic field, $B = 53$ kG, giving an Alfvén speed of $v_A = 7.34 \times 10^8\,\mathrm{cm/s}$. The ion temperature is $T_i = 10$ keV for both ion species. This results in a ratio of $\rho_T/\delta_e = 6$. Only two harmonics are included in the expressions for $\varepsilon_\perp$ and ε_{xy} in this case. For these constant parameters, the cold ion-ion hybrid frequency is $\omega_{ii}/\Omega_T = \sqrt{1.5} \approx 1.22$, and is represented by the red dashed line in Fig. 3.14. As before, the top panel, Fig. 3.14(a), corresponds to the parallel group velocity and the bottom panel, Fig. 3.14(b), to the perpendicular group velocity. Note that now the color scales in the top and bottom panels have been increased each by roughly an order of magnitude from those used in Fig. 3.4 for LAPD. As was seen in the analysis of the ETPD device, three distinct regions of $k_\perp$ and ω exist, corresponding to the three different wave properties this mode can have. The $k_{||} = 0$ contour, indicated by the leading left edge of the contour plot, shows that the wave is backward-traveling near the reflection point, but as this contour approaches its asymptotic limit at large $k_\perp$, it becomes nearly vertical in the plane and the magnitude of the perpendicular group velocity vanishes. Figure 3.15 illustrates this property by displaying line-cuts of the group velocity at various values of $k_\perp$. The horizontal axis corresponds to the scaled frequency, and the vertical axis is the appropriate group velocity. The top panel corresponds to the parallel group velocity, and the bottom panel, the perpendicular group velocity. The values of $k_\perp\delta_e = 0.1$, 0.2, 0.3, and 0.4 correspond to the solid line, the dashed line, the dot-dashed line, and the solid line with dotted markers, respectively. In both panels, the thick tick mark on the horizontal axis indicates the value of the ion-ion hybrid frequency. In the top panel, Fig. 3.15(a), it is clear that the parallel group velocity increases and the wave cutoff moves to lower frequencies with increasing perpendicular wave number. Both effects are attributed to the increasing

importance of finite ion Larmor radius effects. The lower panel shows the corresponding perpendicular group velocity. At higher frequencies, the perpendicular group velocity also increases. Near the cutoff, the wave is backward-traveling, but with a smaller perpendicular group velocity as $k_\perp$ increases. The abrupt change in value displayed at the cutoff simply indicates that the perpendicular group velocity does not vanish near the reflection point, a feature previously shown in Fig. 3.5 for LAPD conditions.

With this understanding, the ray trajectories are now explored in a simplified magnetic geometry representative of a tokamak device. The magnetic field consists of a toroidal field component, B_t, and a poloidal field, B_p. In the cylindrical approximation, these fields are

$$B_t = B_0 \left(1 - \frac{r}{R}\cos\theta\right), \tag{3.27}$$

$$B_p = \frac{rB_0}{Rq(r)}, \tag{3.28}$$

where $B_0 = 53$ kG is the magnetic field at the magnetic axis, r is the radius from the magnetic axis, $R = 621$ cm is the major radius, θ is the poloidal angle, and $q(r)$ is the safety factor. For ease of computation, the safety factor is assumed to have a profile of the form

$$q(r) = 1 + 3\left(\frac{r}{a}\right)^2, \tag{3.29}$$

where $a = 200$ cm is the minor radius of the device. In the numerical ray tracing code used for this case, it is easier to solve the differential equations in Cartesian coordinates, but to write the previous expressions in toroidal coordinates. Because of this, a mapping between the two is helpful, i.e., $(\phi, \theta, r) \rightarrow (x, y, z)$ is the toroidal position. These coordinates are connected through the relations

$$\theta = \tan^{-1}\frac{z}{\rho}, \tag{3.30}$$

$$\phi = \tan^{-1}\frac{y}{x}, \tag{3.31}$$

$$r = \sqrt{\rho^2 + z^2 + R^2 - 2R\rho}, \tag{3.32}$$

$$\rho = \sqrt{x^2 + y^2}. \tag{3.33}$$

The representative burning plasma in ITER is assumed to be an equal mixture of deuterium and tritium with a total electron density of $n_e = 10^{14}\,\mathrm{cm}^{-3}$. When temperature effects are

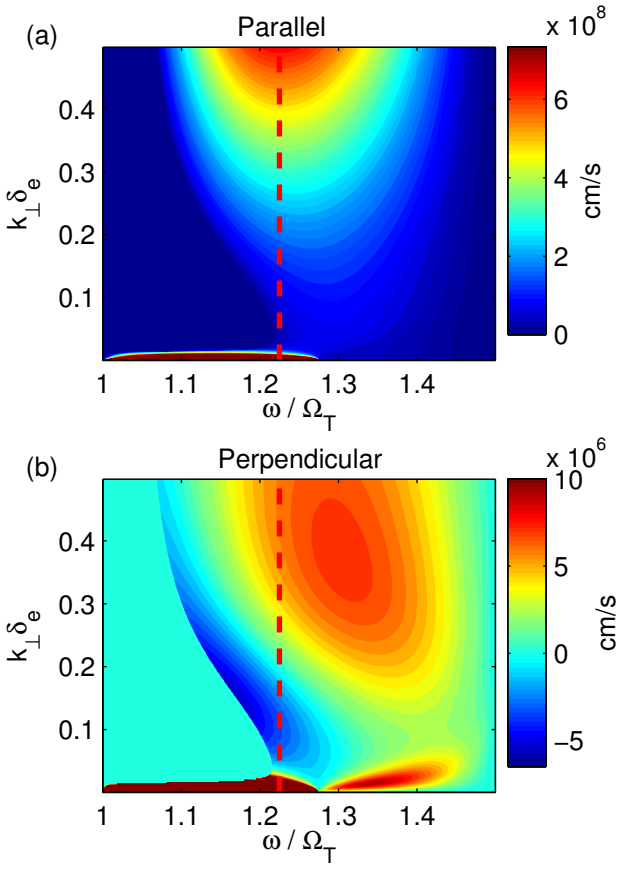

Figure 3.14: Contour displays of components of group velocity for ITER conditions. The plasma is comprised of 50% D+, 50% T+ with an electron density of $10^{14}\,\mathrm{cm}^{-3}$, equal ion temperatures of 10 keV and a toroidal magnetic field strength of 53 kG. Vertical axis is the scaled perpendicular wave number and horizontal axis is the scaled frequency. (a) Parallel group velocity, (b) perpendicular group velocity. Red dashed line is ion-ion hybrid frequency. Several of the qualitative features of the group velocity seen in Figs. 3.4 and 3.12 are also present. Note that contour scales in panels (a) and (b) differ by two orders of magnitude.

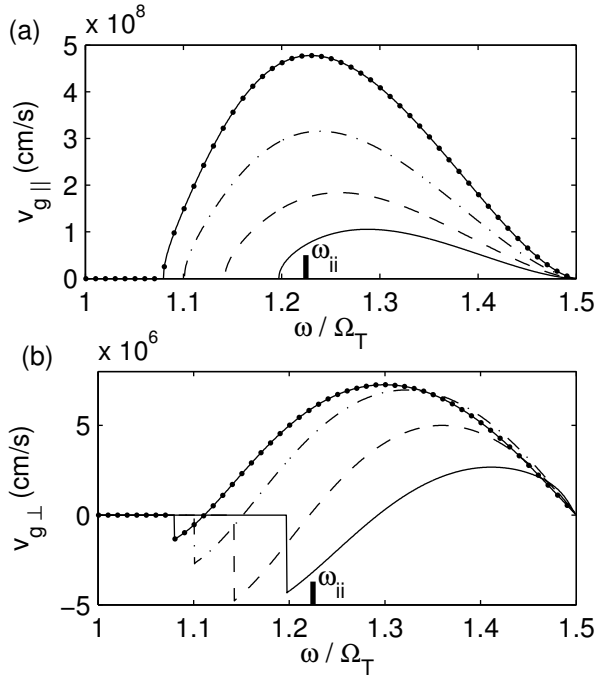

Figure 3.15: Line cuts of the contour displays in Fig. 3.14 for selected values of $k_\perp$. The values of $k_\perp \delta_e = 0.1$, 0.2, 0.3, and 0.4 are represented by the solid curve, dashed curve, dashed-dotted curve, and solid curve with dotted markers, respectively. The small, thick vertical lines at the bottom of each panel represent the ion-ion hybrid frequency. (a) The parallel group velocity. Greater variation between cuts is seen with the rays having larger speed as $k_\perp$ increases. (b) The perpendicular group velocity. The frequency interval over which the wave is backward-traveling shifts to lower frequencies, together with the reflection point, as $k_\perp$ increases.

considered, the ion temperature is taken to be $T_i = 10$ keV for both ion species. But at this stage, to limit complicating effects, the electron response is taken to be in the inertial regime.

Figure 3.16 illustrates two ray trajectories in ITER, each at a frequency of $f = 31$ MHz. This frequency, again, lies within the band in which trapping occurs in a cold plasma. The plane represented is that of a poloidal cross section where the horizontal axis is the radial position as measured from the magnetic axis, and the vertical axis corresponds to the z-coordinate in Eq. (3.30). The black dashed curves indicate the toroidal magnetic flux surfaces. The solid blue curve represents a ray calculated with the cold ion dispersion relation, and the dashed-dotted red curve, with ion temperature included. Both rays are launched from an initial position of $x - R = 50$ cm, $y = 0$ cm, and $z = 20$ cm. The initial wave vector is oriented so that it lies in a plane formed by $\hat{\mathbf{B}}$, a unit vector pointing in the direction of the total magnetic field and $\hat{\mathbf{r}}$, a unit vector pointing normal to the magnetic flux surface. The angle formed between the magnetic field and the initial wave vector is $\psi = 89.6°$ for the cold ion ray, and $\psi_0 = 85.7°$ for the warm ion ray. The initial k_r points towards the magnetic axis, and the initial $k_{||}$ in the direction of the magnetic field. The direction of the gradient of the toroidal field is illustrated in the upper, right-hand side of the figure. The field gradient causes the wave vector to increase preferentially in the direction opposite to the gradient; the effect exists for both cold and hot ions. The reason for this is presented in the discussion following Eq. (3.26) in section 3.3. As in the ETPD case, the quantity, $k_\phi = m/\rho$, is an invariant of the motion. However, the presence of a poloidal field in a tokamak allows for $k_{||}$ to vanish at conjugate points, thus creating a resonator configuration.

The cold ray, as illustrated by the solid blue curve in Fig. 3.16, displays the backward-traveling nature of the wave. The ray, initially with a negative k_r, travels radially outward. As it does so, the effects of both curvature and magnetic gradient as described in section 3.3, cause the value of k_r to preferentially increase towards positive values. This causes a radial reflection, which then causes the ray to reverse direction and to move inward across the magnetic flux surfaces. The ray can be seen to wander outward for three bounces before

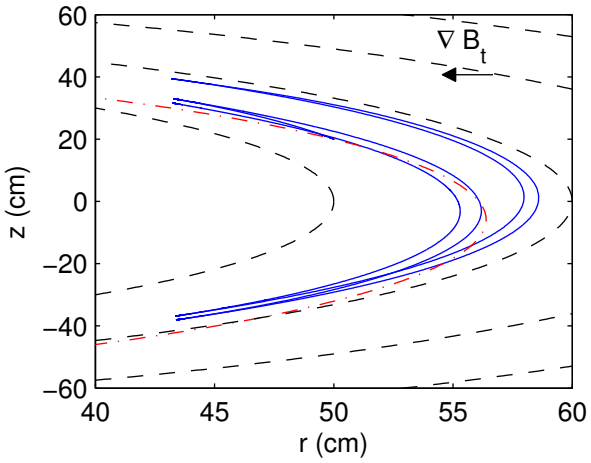

Figure 3.16: Poloidal projection of ray trajectories in ITER. Vertical axis represents vertical displacement of a ray from the magnetic axis, and the horizontal axis represents the radial displacement from the magnetic axis. The black dashed lines represent the nested flux surfaces. The solid (blue) curve is a ray for which the cold plasma dispersion relation is used, and the dashed-dotted (red) curve uses the hot-ion dispersion relation. Both rays have an initial perpendicular wave number that points towards the magnetic axis. The direction of the gradient of the toroidal field strength is shown; the perpendicular wave number preferentially increases in the opposite direction of this gradient. The cold ray is trapped within the magnetic well. It wanders outward across magnetic flux surfaces before propagating inward due to the perpendicular reflection examined earlier for ETPD. The hot ion result is not confined due to the reflection point moving towards the inboard side of the device as the perpendicular wave number increases.

it starts to move inward. The trajectory, and the fact that it retraces itself due to the radial reflection, indicates that the effects of field line curvature and magnetic gradient, in and of themselves, do not destroy the resonator. In fact, due to the induced radial reflections, they serve to focus the energy allowing for constructive reinforcement over the course of multiple transits. It is worth mentioning that at the reflection points along the field line, the conditions for ray tracing break down even though they are well satisfied away from these reflection points. This is in agreement with the study by Rauch and Roux [8]. In their study, they verified that close to the reflection point, the wave equation reduces to Airy's differential equation which confirms that reflection indeed happens. Their same analysis also applies in the case presented here. Further, this suggests that a WKB analysis would be appropriate for this situation. The distance traveled by a ray between conjugate reflection points is on the order of 10 meters with the parallel wavelength being on the order of 30 cm at z = 0. The fact that the effective wave potential becomes small near the reflection points indicates that the connection formulas must be used and a quantization condition would result from a WKB analysis. Such an analysis is performed in Chapter 4.

The dashed-dotted red curve in Fig. 3.16 illustrates a ray trajectory in which ion temperature effects are included. In order to obtain a complete ray trajectory, an additional ray is launched from the same starting position but with the direction of the wave vector reversed, giving a complete passing through the region. Because of the effects of field line curvature and magnetic gradient, the value of k_r preferentially increases as in the previous cases. From Figs. 3.13 and 3.14, it can be seen that the inclusion of hot ion effects causes the reflection point of the wave to decrease below the traditional, cold ion-ion hybrid frequency as $k_\perp$ increases. This causes the reflection point to continuously recede away from the ray as the ray propagates towards the reflection point. Thus, as the ray propagates, it achieves increasing values of $k_\perp$ causing the reflection point to approach the cyclotron frequency of tritium.

To illustrate the expected electron behavior to be encountered, Fig. 3.17 displays the value of the scaled phase-velocity parameter usually entering in the plasma dispersion function, $\zeta = \omega/\sqrt{2}k_{||}\bar{v}_e$, where $\bar{v}_e$ is the electron thermal velocity. The electron temperature is

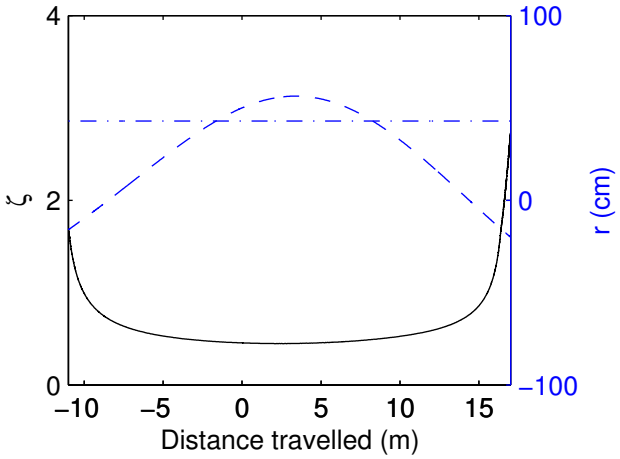

Figure 3.17: Scaled phase velocity parameter associated with the hot-ion ray in Fig. 3.16. The horizontal axis is the distance traveled by the ray, which includes toroidal motion. The vertical axis on the left represents the value of the kinetic electron parameter $\zeta = \omega/\sqrt{2}k_{||}\bar{v}_e$ and corresponds to the solid black curve. The electron temperature is 10 keV. The numerical values attained indicate that the electron response is in the adiabatic regime. The vertical axis on the right is the value of the radial displacement of the ray from the magnetic axis and corresponds to the dashed (blue) curve. The dashed-dotted horizontal line represents the position at which the wave frequency matches the local value of the ion-ion hybrid frequency.

taken to be 10 keV, and $k_{||}$ is extracted from the hot-ion ray trajectory shown in Fig. 3.16. The horizontal axis in Fig. 3.17 corresponds to the distance the ray has traveled (in meters). The values of the solid black curve are given by the left vertical scale, which represents the value of ζ as the ray evolves. The dashed (blue) curve displays the radial position of the ray as it moves along its trajectory and its value is displayed in the vertical scale on the right of the figure. The dash-dotted line shows the position at which the wave frequency matches the local value of the ion-ion hybrid frequency, where the reflection would occur if ion temperature effects were negligible. As can be seen from Fig. 3.17, the ray travels well past the point where it would traditionally reflect in a cold plasma. The values of ζ found in Fig. 3.17 indicate that the electron response is not in the inertial regime. Instead of using Eq. (2.18), the electrons would better be treated by the adiabatic approximation, i.e., Eq. (2.18) should be replaced with

$$\varepsilon_{||} \rightarrow \frac{k_D^2}{k_{||}^2}, \tag{3.34}$$

where $k_D = \omega_{pe}/\bar{v}_e$ is the Debye wave number. To gain a qualitative understanding of the change expected, the dispersion relation with adiabatic electrons is considered. It is a relatively straightforward calculation to show that the dispersion relation in this case can be solved for $k_{||}^2$ resulting in the expression

$$\frac{k_{||}^2}{k_0^2} = \varepsilon_\perp + \frac{\pm\left[b^2 + 4ad\right]^{1/2} - b}{2a}, \tag{3.35}$$

where the definitions of a, b, and d now become

$$a = \frac{k_D^2}{k_0^2} + \frac{k_\perp^2}{k_0^2}\varepsilon_\perp, \tag{3.36}$$

$$b = \frac{k_D^2}{k_0^2}\left[\varepsilon_\perp\left(\frac{k_\perp^2}{k_0^2} + \varepsilon_\perp\right) + \varepsilon_{xy}^2 + \frac{k_D^2}{k_0^2}\right], \tag{3.37}$$

$$d = \frac{k_D^2}{k_0^2}\varepsilon_{xy}^2 - \frac{k_\perp^2}{k_0^2}\left(\frac{k_\perp^2}{k_0^2}\varepsilon_\perp^2 + \varepsilon_\perp\varepsilon_{xy}^2\right). \tag{3.38}$$

Figure 3.18 shows a contour display of Eq. (3.35) using Eqs. (3.13) and (3.14) for the dielectric tensor components, which include ion temperature effects. The plasma parameters are for ITER values as specified previously. From the display, it is seen that many of the same features present in the dispersion relation in the inertial case are also present in the adiabatic

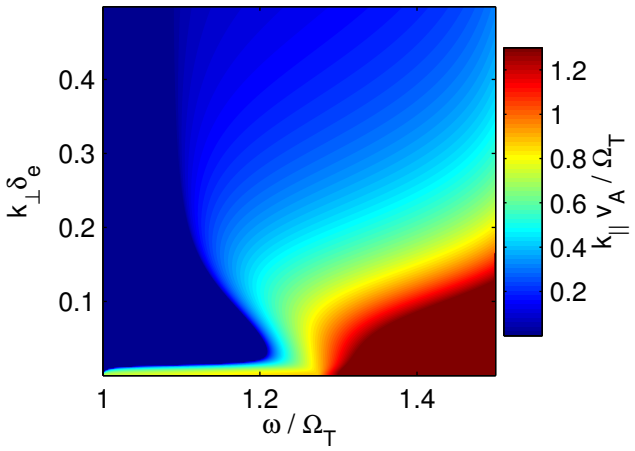

Figure 3.18: Contour display of the dispersion relation of a shear Alfvén wave in the upper branch with adiabatic electron behavior for ITER. The vertical axis is the scaled perpendicular wave number, the horizontal axis is the scaled frequency, and the contours are the scaled parallel wave number. The general features that are present in the inertial dispersion relation are also exhibited here.

case: coupling to the compressional wave occurs at small values of $k_\perp$, as $k_\perp$ increases; the wave is initially forward, then backward, then forward traveling again; etc. This suggests that consideration of adiabatic electrons may not greatly alter the general conclusions extracted from the inertial results. However, kinetic damping has not been considered, and this is an important consideration to determine whether the wave energy can be long-lived. Such an analysis is performed in Chapter 4.

3.5 Discussion

It is appropriate to emphasize the degree of extrapolation made in applying the eikonal approximation to the various cases considered in this survey. The condition for the applicability of the eikonal approximation is $R = (\lambda/n)\, dn/ds$ where λ is the wavelength, n is the index of refraction, and ds is a differential element of path length. This condition is equivalent to the statement that the wavelength is much smaller than the characteristic length-scale over which the index of refraction changes. For LAPD, as has been discussed at the end of section

3.2, the eikonal approximation is not rigorously satisfied. The axial gradient scale-length is roughly that of the magnetic field, which is approximately two meters. The smallest value of the parallel wavelength for the cases considered is 2 - 2.5 meters, making $R \sim 1$. Thus, the eikonal approximation does not work well in this direction. In this regard, the results reported in section 3.2 should be seen as complimentary to the results shown in Chapter 2. The new information that is extracted from the present ray tracing survey pertains to the short perpendicular wavelength effects due to finite ion temperature and transverse gradient. In the cases considered in section 3.2, the perpendicular gradient scale-length is on the order of the radius of the device or 50 cm, with the perpendicular wavelength ranging from 8 - 30 cm depending on the particular case in question. Thus, the radial transport of wave energy is well described in this picture. For ETPD, because of the toroidal symmetry of the device, the eikonal approximation is quite valid in this direction. In the transverse direction, the gradient scale-length is roughly the major radius of the device, 5 meters, and the perpendicular wavelengths are on the order of centimeters except near a radial reflection. For ITER, an analogous assessment holds in the perpendicular direction. However, with the inclusion of a poloidal field, it is important to account for the direction parallel to the magnetic field. For the cases examined in section 3.4, the parallel wavelengths are on the order of 30 cm towards the center of the well, with the gradient length-scale being on the order of meters. Thus, the eikonal approximation is valid in the cold case everywhere except near a parallel reflection point. As mentioned in section 3.4, this is in agreement with an analogous study by Rauch and Roux [8] for the Earth's magnetosphere. That study showed that reflection indeed occurs if a local, full-wave model is used, and a similar argument applies to the equivalent cold plasma cases reported in section 3.4. When hot plasma effects are included, the eikonal approximation is valid except in the neighborhood of the tritium cyclotron frequency, as is expected.

From the results of Chapter 2, it is concluded that the large theoretical quality factors are due to small values of $k_\perp$, which are least damped by the electron collisions. For this reason, the radial convection at small values of $k_\perp$ is of greatest interest. The quality factor at small $k_\perp$ is given in the discussion associated with Fig. 3.6; in the warm ion case it is

$Q = 160$, though this is accurate to a constant of order unity. If this is combined with the effect of dissipation due to electron collisions, a total quality factor is determined by

$$\frac{1}{Q_T} = \sum_i \frac{1}{Q_i}, \tag{3.39}$$

where Q_i is the quality factor due to each individual mechanism. Using the quality factor for Fig. 2.15(a) with an electron temperature of $T_e = 5$ eV results in a total quality factor of $Q \sim 90$. This is roughly a factor of five greater than that which is observed. From this, it is concluded that radial convection is a more important source of damping than that introduced by electron collisions. However, these two mechanisms alone are still unable to explain the low quality factors observed in the experiment. In order to explain this discrepancy, other processes must be considered. This requires consideration of mode conversion processes and/or particle resonances in the nonuniform wave environment to fully describe the behavior of this resonator.

It has been demonstrated that when temperature effects are negligible, and for rays propagating along a curved field line, field-line curvature effects preferentially increase the component of the wave vector in the direction opposite to the curvature of the field line. This, combined with a zero in the perpendicular group velocity, explains the radial focusing effect identified by Mithaiwala *et al.* [12] in the analysis of a magnetospheric resonator. The radial focusing of the wave enhances energy trapping in resonators that exist along a field line where the curvature is predominantly in one direction. When ion temperature effects are considered, similar propagation characteristics are found as in the cold-ion case. However, at sufficiently large temperatures, three regions of parameter space are introduced which determine the qualitative characteristics of the wave. At small values of $k_\perp \delta_e$, the wave is isotropic and strongly exhibits compressional mode characteristics. At intermediate values, the wave is backward traveling with a cutoff existing close to the ion-ion hybrid frequency, exhibiting shear mode characteristics. At large values, the wave again becomes forward-traveling. A single ray can experience all three regions of parameter space as it propagates through a plasma confined in a toroidal magnetic field, experiencing a perpendicular reflection as it transitions from one region to the next.

When ion temperature effects are negligible in a tokamak device, as may be the case for edge conditions, it is clear from the ray tracing studies that a resonator can exist in such a plasma. The effects of field line curvature cause the ray to be focused radially allowing for many reflections which largely retrace each other. However, when ion temperature effects are included, especially at the core temperatures expected in ITER burning plasmas, the ray-tracing studies make it difficult to conclude whether the resonator can still exist. This question is considered in more detail in section 4.5, where the combined effects of ion temperature and shear of the magnetic field are treated. From the ray-tracing study, it is certainly true that modes that would initially be trapped at larger frequencies in a cold plasma will no longer reflect due to both FLR effects and the influence of magnetic curvature.

CHAPTER 4

Shear Alfvén waves in ITER

In this chapter, a one-dimensional WKB model is employed in a tokamak geometry to more fully explore the properties of the ion-ion hybrid resonator in a fusion environment. In section 4.1, a WKB model is rigorously derived from the field equations with the following physical approximations. First, it is assumed that the ions do not exhibit any cyclotron or transit time damping, so that both $\varepsilon_\perp$ and ε_{xy} are only functions of $k_\perp$ and ω. The electrons are treated in both the inertial and adiabatic limits, and the compressional root is neglected. The wave equation governing the electric field is shown to reduce to the familiar, one-dimensional WKB model in both cases. The kinetic dispersion relation is then considered in section 4.2 in order to determine the degree to which kinetic damping terms are important. Using sections 4.1 and 4.2 as motivation, the one-dimensional WKB model is generalized to include both cyclotron and electron Landau damping as a small correction in section 4.3 with electron collisions neglected. Electron collisions are negligible for the plasma parameters relevant to ITER primarily due to the large electron temperatures present, with the electron collision frequency roughly four orders of magnitude smaller than the cyclotron frequencies of the ions. Properties of the eigenmodes are explored using this model. Next, instability of the resonator modes due to energetic fusion-born alpha particles is considered in section 4.4. This instability investigation parallels work done by Lashmore-Davies and Russell [25]. An investigation of the influence of shear on the resonator modes is then considered in section 4.5. Finally, the results of this chapter are summarized in section 4.6.

4.1 WKB model with no damping

A simple one dimensional model can be constructed to explore the properties of an ion-ion hybrid resonator in a tokamak. Such a model automatically neglects the effects of field line curvature, toroidicity, and magnetic shear. To properly assess these effects would necessarily require a more sophisticated description. As a preliminary step, a heuristic, analytic model is adopted in section 4.5 which does account for some of these complicated effects. Before doing this, a simple one-dimensional model is adopted to develop intuition.

It is useful to start from Eq. (2.1) without the source term. In adopting a one dimensional model, a slab geometry is assumed with

$$\nabla = ik_\perp \hat{\mathbf{x}} + \frac{\partial}{\partial z}\hat{\mathbf{z}}. \tag{4.1}$$

This results in three coupled equations for the three electric field components,

$$-\frac{\partial}{\partial z}\left(\frac{\partial E_x}{\partial z} - ik_\perp E_z\right) - k_0^2\left(\varepsilon_\perp E_x - i\varepsilon_{xy}E_y\right) = 0, \tag{4.2}$$

$$-\frac{\partial^2 E_y}{\partial z^2} + k_\perp^2 E_y - k_0^2\left(\varepsilon_\perp E_y + i\varepsilon_{xy}E_x\right) = 0, \tag{4.3}$$

$$ik_\perp\left(\frac{\partial E_x}{\partial z} - ik_\perp E_z\right) - k_0^2\varepsilon_{||}E_z = 0. \tag{4.4}$$

The third equation can be used to remove E_z from the system of equations,

$$E_z = -\frac{ik_\perp}{k_\perp^2 - k_0^2\varepsilon_{||}}\frac{\partial E_x}{\partial z}. \tag{4.5}$$

Upon substitution into the remaining two equations, the system is reduced to

$$\left[\frac{\partial^2}{\partial z^2} + k_0^2\varepsilon_\perp\left(1 - \frac{k_\perp^2}{k_0^2\varepsilon_{||}}\right)\right]E_x - ik_0^2\varepsilon_{xy}\left(1 - \frac{k_\perp^2}{k_0^2\varepsilon_{||}}\right)E_y = 0, \tag{4.6}$$

$$\left[\frac{\partial^2}{\partial z^2} + \left(k_0^2\varepsilon_\perp - k_\perp^2\right)\right]E_y + ik_0^2\varepsilon_{xy}E_x = 0, \tag{4.7}$$

which can be recast in matrix form as

$$\frac{\partial^2 \mathbf{E}_\perp}{\partial z^2} + V(z)\mathbf{E}_\perp = 0, \tag{4.8}$$

$$V(z) = \begin{pmatrix} k_0^2\varepsilon_\perp\left(1 - \frac{k_\perp^2}{k_0^2\varepsilon_{||}}\right) & -ik_0^2\varepsilon_{xy}\left(1 - \frac{k_\perp^2}{k_0^2\varepsilon_{||}}\right) \\ ik_0^2\varepsilon_{xy} & k_0^2\varepsilon_\perp - k_\perp^2 \end{pmatrix}. \tag{4.9}$$

To make progress, the form of $\varepsilon_{||}$ must be specified. The calculation can be performed in two limits: the inertial limit ($\omega/k_S \gg \bar{v}_e$) and the adiabatic limit ($\omega/k_S \ll \bar{v}_e$) where $\bar{v}_e$ is the electron thermal velocity. The choice of limit gives differing expressions for the parallel dielectric, with all other elements of the model remaining the same. In the inertial limit, the appropriate expression is given by Eq. (2.18). In the adiabatic limit, the parallel dielectric is given by

$$\frac{1}{\varepsilon_{||}} \to -\frac{1}{k_D^2}\frac{\partial^2}{\partial z^2}, \tag{4.10}$$

where $k_D = \omega_{pe}/\bar{v}_e$ is the Debye wave number. It is important to remember that as the reflection layer is approached, $k_S \to 0$ regardless of the choice for $\varepsilon_{||}$. Thus, if the electrons are in the adiabatic regime towards the interior of the well, then as the reflection point is approached, the electrons will pass from the adiabatic regime through a resonant layer to the inertial regime. It is difficult to capture the effects of this transition from adiabatic to inertial in the equations as formulated. Rigorous treatment of this transition would require an integral equation approach, though this is not done here. Instead, this damping is described in a perturbative sense in subsequent sections of this chapter. In this section, the adiabatic or inertial limit is taken and applied to the full well.

4.1.1 Inertial electrons

When Eq. (2.18) is used for the parallel component of the dielectric tensor, the form of Eqs. (4.8) and (4.9) can be used without modification. At this point, the WKB approximation can be made. It is, therefore, useful to factor the components of the electric field into a rapidly varying function multiplied by a slowly varying function. Because there are two modes present in the solutions, both should be accounted for in the formulation. Thus, the perpendicular electric field is written as

$$\mathbf{E}_\perp = \left(\mathbf{E}_S e^{i\psi_S} + \mathbf{E}_C e^{i\psi_C}\right) e^{ik_\perp x}, \tag{4.11}$$

where a subscript, S, denotes a quantity associated with the shear root and a subscript, C, with the compressional root. The two vectors, $\mathbf{E}_S$ and $\mathbf{E}_C$, are taken to be eigenvectors of the matrix, $V(z)$, with eigenvalues $k_S^2(z)$ and $k_C^2(z)$, respectively. This form of $\mathbf{E}_\perp$ can

now be substituted into the differential equation. Further, it is convenient to take an inner product of the resulting vector equation with $\mathbf{E}_S$ and $\mathbf{E}_C$. This results in two equations,

$$\begin{aligned}\left[\mathbf{E}_S \cdot \tfrac{d^2\mathbf{E}_S}{dz^2} + i\tfrac{d}{dz}\left(E_S^2 \tfrac{d\psi_S}{dz}\right) + E_S^2\left(k_S^2 - \left(\tfrac{d\psi_S}{dz}\right)^2\right)\right] e^{i\psi_S} \\ + \mathbf{E}_S \cdot \left[\tfrac{d^2\mathbf{E}_C}{dz^2} + 2i\tfrac{d\mathbf{E}_C}{dz}\tfrac{d\psi_C}{dz}\right] e^{i\psi_C} = 0,\end{aligned} \tag{4.12}$$

$$\begin{aligned}\left[\mathbf{E}_C \cdot \tfrac{d^2\mathbf{E}_C}{dz^2} + i\tfrac{d}{dz}\left(E_C^2 \tfrac{d\psi_C}{dz}\right) + E_C^2\left(k_C^2 - \left(\tfrac{d\psi_C}{dz}\right)^2\right)\right] e^{i\psi_C} \\ + \mathbf{E}_C \cdot \left[\tfrac{d^2\mathbf{E}_S}{dz^2} + 2i\tfrac{d\mathbf{E}_S}{dz}\tfrac{d\psi_S}{dz}\right] e^{i\psi_S} = 0,\end{aligned} \tag{4.13}$$

where k_S^2 and k_C^2 are both given by the expression for $k_{||}^2$ in Eq. (3.15) with the appropriate sign chosen. The eigenvectors, $\mathbf{E}_S$ and $\mathbf{E}_C$, are given by

$$\mathbf{E}_{S,C} = \frac{\mathbf{v}}{|\mathbf{v}|} E_{S,C}(z), \tag{4.14}$$

$$\mathbf{v} = \left(\left(k_\perp^2 - k_0^2\varepsilon_{||}\right)\hat{\mathbf{x}} + i\varepsilon_{xy}\frac{k_\perp^2 - k_0^2\varepsilon_{||}}{k_0^2\varepsilon_\perp - k_\perp^2 - k_{S,C}^2}\hat{\mathbf{y}}\right), \tag{4.15}$$

with the z-component of the electric field given by Eq. (4.5). Because the vectors, $\mathbf{E}_S$ and $\mathbf{E}_C$, are assumed to be slowly varying, the second order derivatives are neglected in Eqs. (4.12) and (4.13). Further, the last term in both equations represents coupling between the two modes. Since mode conversion processes are not of primary interest in this calculation, these terms are dropped. Finally, the equations can be expressed in terms of the traditional WKB approximation [63] with

$$E_S(z) = \frac{C}{\sqrt{k_S(z)}}, \tag{4.16}$$

$$\psi_S(z) = \int^z k_S(z')dz'. \tag{4.17}$$

For a magnetic well where two turning points exist, the following quantization condition results,

$$\int_{-z_0(\omega_n)}^{z_0(\omega_n)} k_S(\omega_n, z)dz = \left(n + \frac{1}{2}\right)\pi, \tag{4.18}$$

where the frequency dependence has been emphasized in the final expression. Here, z_0 is the turning point of the wave i.e. $k_S(\omega, z_0) = 0$, and the well has been assumed symmetric about the point $z = 0$. The quantity, n, takes on integer values beginning at zero, and corresponds to the quantum number of the trapped mode with frequency ω_n. Because the turning point

also depends on frequency, the above expression is an implicit equation that must be solved numerically. Eigenfunctions can similarly be constructed resulting in the expression

$$E_S(z)e^{i\psi(z)} = \begin{cases} \frac{A_1}{\sqrt{|k_S(z)|}} \exp\left(-\int_z^{-z_0} |k_S(z')|dz'\right) & z < -z_0 \\ \frac{2A_2}{\sqrt{k_S(z)}} \sin\left(\int_z^{z_0} k_S(z')dz' + \frac{\pi}{4}\right) & |z| < z_0 \\ \frac{A_2}{\sqrt{|k_S(z)|}} \exp\left(-\int_{z_0}^{z} |k_S(z')|dz'\right) & z > z_0 \end{cases} , \tag{4.19}$$

where $A_1 = \pm A_2$ with the sign being chosen by whether the eigenfunction is even or odd, the function being determined to an overall normalization. The divergence of the solution at the turning point is fixed in the traditional way by using an Airy function solution near the reflection point.

Figure 4.1 plots the three components of the electric field from such a WKB description of the trapped modes. Both the plasma parameters and the magnetic field description correspond to that which was used for the initial position of the cold ray in Fig. 3.16. The frequency is chosen to correspond to the $n = 32$ trapped mode in the resonator. The horizontal axes correspond to the distance traversed along a field line and relates to the poloidal angle through the expression, $s = Rq(r)\theta$. The top, middle, and bottom panel correspond to E_x, E_y, and E_z, respectively. Because E_y and E_z are 90 degrees out of phase with E_x, the imaginary part of these functions is plotted. Note that while the units of each plot are arbitrary, the relative magnitude of each component is different, and the vertical scalings on each plot are not the same. The amplitude of E_y reflects the degree to which coupling to the compressional mode occurs. Since $k_\perp$ is much larger than the ion-skin depth, this coupling is small, and this is reflected in the small relative amplitude of E_y. Further, because $k_S = 0$ at the reflection point, the vanishing of E_z in the vicinity of this point reflects the electrostatic nature of the field. Close to the center of the well, a nonzero electromagnetic component of the mode exists.

4.1.2 Adiabatic electrons

If the adiabatic limit, Eq. (4.10), is used for the parallel component of the dielectric tensor. Using this form creates a question as to the placement of the differential operator. If a

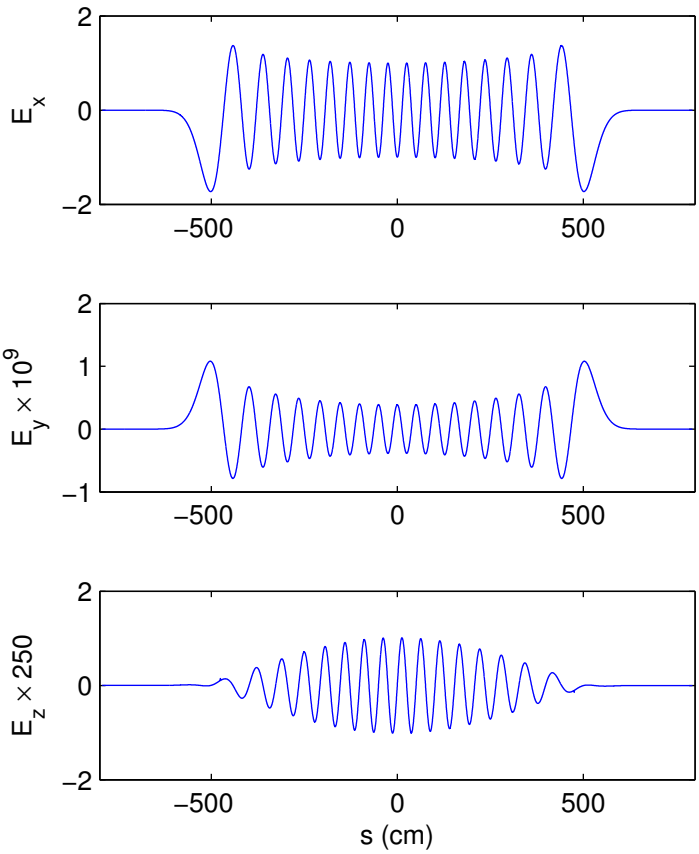

Figure 4.1: Components of the electric field for $n = 32$ inside an ITER-type well with plasma parameters and magnetic geometry corresponding to the initial position of the cold ray in Fig. 3.16. Electrons are in the inertial regime. Horizontal axes are distance traversed along a field line, and vertical axes, to electric field strength in arbitrary units. (a) E_x, (b) E_y, and (c) E_z. Note the different relative scalings on the vertical axes in each panel.

self-adjoint formulation is enforced, the matrix equation becomes

$$\frac{\partial}{\partial z}M(z)\frac{\partial}{\partial z}\mathbf{E}_\perp + A(z)\mathbf{E}_\perp = 0. \tag{4.20}$$

$$M(z) = \begin{pmatrix} 1+\frac{k_\perp^2}{k_D^2} & i\varepsilon_{xy}\frac{k_\perp^2}{k_D^2} \\ 0 & 1 \end{pmatrix}, \tag{4.21}$$

$$A(z) = \begin{pmatrix} k_0^2\epsilon_\perp & -ik_0^2\varepsilon_{xy} \\ ik_0^2\varepsilon_{xy} & k_0^2\varepsilon_\perp - k_\perp^2 \end{pmatrix}. \tag{4.22}$$

This form resembles a generalized eigenvalue problem of the form $A\mathbf{v} = \lambda B\mathbf{v}$, where A and B are matrices and $\mathbf{v}$ is the eigenvector with associated eigenvalue, λ. For a constant background magnetic field, the problem can be solved for $k_{||}$, and the result gives the solution to the Booker quartic for adiabatic electrons as given in Eq. (3.35).

Again, the WKB approximation can be made while accounting for both the shear and compressional roots. Thus, the perpendicular electric field is written as

$$\mathbf{E}_\perp = \left(\mathbf{E}_S e^{i\psi_S} + \mathbf{E}_C e^{i\psi_C}\right) e^{ik_\perp x}, \tag{4.23}$$

with the same notation used previously. The two vectors, $\mathbf{E}_S$ and $\mathbf{E}_C$ are taken to be eigenvectors of the generalized eigenvalue problem for constant magnetic field, with eigenvalues $k_S^2(z)$ and $k_C^2(z)$, respectively. In this case, $k_{S,C}(z) = d\psi_{S,C}/dz$ as before. This form of $\mathbf{E}_\perp$ can now be substituted into the differential equation. After some simplification, the following equations result:

$$\begin{aligned} &\left[\mathbf{E}_S\cdot\frac{d^2\mathbf{E}_S}{dz^2} + i\frac{d}{dz}\left(E_S^2\frac{d\psi_S}{dz}\right)\right] + \mathbf{E}_S\cdot\left[\frac{d^2\mathbf{E}_C}{dz^2} + 2i\frac{d\mathbf{E}_C}{dz}\frac{d\psi_C}{dz}\right]e^{i(\psi_C-\psi_S)} \\ &+\mathbf{E}_S\cdot M^{-1}\frac{dM}{dz}\left[\left(\frac{d\mathbf{E}_S}{dz} + i\mathbf{E}_S\frac{d\psi_S}{dz}\right) + \left(\frac{d\mathbf{E}_C}{dz} + i\mathbf{E}_C\frac{d\psi_C}{dz}\right)e^{i(\psi_C-\psi_S)}\right] = 0, \end{aligned} \tag{4.24}$$

$$\begin{aligned} &\left[\mathbf{E}_C\cdot\frac{d^2\mathbf{E}_C}{dz^2} + i\frac{d}{dz}\left(E_C^2\frac{d\psi_C}{dz}\right)\right] + \mathbf{E}_C\cdot\left[\frac{d^2\mathbf{E}_S}{dz^2} + 2i\frac{d\mathbf{E}_S}{dz}\frac{d\psi_S}{dz}\right]e^{i(\psi_S-\psi_C)} \\ &+\mathbf{E}_C\cdot M^{-1}\frac{dM}{dz}\left[\left(\frac{d\mathbf{E}_C}{dz} + i\mathbf{E}_C\frac{d\psi_C}{dz}\right) + \left(\frac{d\mathbf{E}_S}{dz} + i\mathbf{E}_S\frac{d\psi_S}{dz}\right)e^{i(\psi_S-\psi_C)}\right] = 0. \end{aligned} \tag{4.25}$$

If $\psi_{S,C}$ varies more rapidly than any other quantity in the problem. The bottom term containing M^{-1} can be dropped. Further, the second, square-bracketed term on the first line of the above two equations represents coupling, and is neglected as in the inertial treatment.

This leaves the equation for the shear mode,

$$\left[\mathbf{E}_S \cdot \frac{d^2\mathbf{E}_S}{dz^2} + i\frac{d}{dz}\left(E_S^2\frac{d\psi_S}{dz}\right)\right] = 0. \tag{4.26}$$

Finally, the second derivative term can be neglected, and the magnitude of E_S possesses the same form as in Eq. (4.16) with the appropriate definition for k_S. The polarization of the vector must be found by finding the eigenvector of the matrix equation for constant background magnetic field. The expressions for k_S^2 and k_C^2 are given by Eq. (3.35) with the appropriate sign choice. The associated eigenvectors are

$$\mathbf{E}_\perp = \frac{\mathbf{h}}{|\mathbf{h}|}E_S(z), \tag{4.27}$$

$$\mathbf{h} = \begin{pmatrix} a\left(\varepsilon_\perp - \frac{k_S^2+k_\perp^2}{k_0^2}\right) \\ -i\varepsilon_{xy} \end{pmatrix}. \tag{4.28}$$

From these equations, it is seen that the one-dimensional WKB formulation also applies in this limit. The quantization condition and the eigenfunction are given, as before, in Eqs. (4.18) and (4.19). Further, these equations coupled with Eq. (4.5) fully determine the individual components of the electric field. To use Eq. (4.5), the value of k_S is substituted into $\varepsilon_{||}$ appearing in the denominator of the expression.

Figure 4.2 is the adiabatic analog of Fig. 4.1. The same plasma parameters and magnetic geometry are used as in the previous figure, and the axes correspond to the same quantities. The frequency is chosen to again correspond to an $n = 32$ trapped mode, which results in a slightly different frequency. The same conclusions that were drawn in the previous case also apply here, and little qualitative difference exists between Figs. 4.1 and 4.2.

4.2 Kinetic dispersion relation

Now consider a warm, homogeneous plasma with two ion species: deuterium and tritium. The confining magnetic field is chosen to point along the z-direction of a Cartesian coordinate system, (x, y, z), with the wave vector lying in the x-z plane $\mathbf{k} = k_\perp\hat{\mathbf{x}} + k_{||}\hat{\mathbf{z}}$. The general

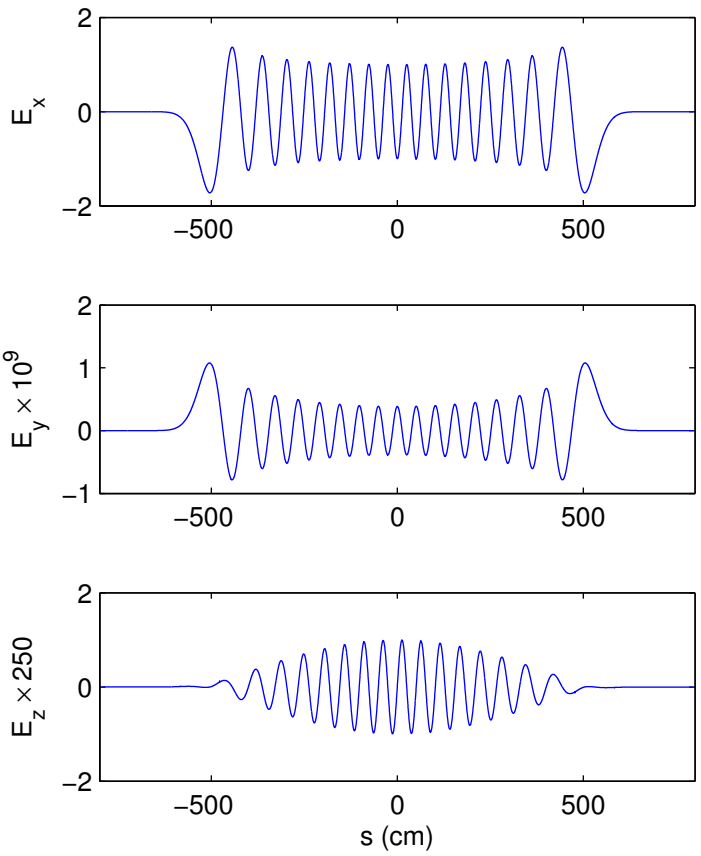

Figure 4.2: Components of the electric field for $n = 32$ inside an ITER-type well with plasma parameters and magnetic geometry corresponding to the initial position of the cold ray in Fig. 3.16. Electrons are in the adiabatic regime. Horizontal axes are distance traversed along a field line, and vertical axes, to electric field strength in arbitrary units. (a) E_x, (b) E_y, and (c) E_z. Note the different relative scalings on the vertical axes in each panel.

dispersion relation can be written as

$$\begin{aligned} &D_S D_C + D_X - 2k_\perp k_{||}\left[k_0^2\varepsilon_{yz}\varepsilon_{xy} + \varepsilon_{xz}\left(k^2 - k_0^2\varepsilon_{yy}\right)\right] \\ &- 2k_0^4\varepsilon_{xz}\varepsilon_{yz}\varepsilon_{xy} - k_0^2\varepsilon_{yz}^2\left(k_0^2\varepsilon_{xx} - k_{||}^2\right) - k_0^2\varepsilon_{xz}^2\left(k^2 - \varepsilon_{yy}\right) = 0, \end{aligned} \tag{4.29}$$

where,

$$D_C = k^2 - k_0^2\varepsilon_{yy} \tag{4.30}$$

$$D_S = k_0^2\varepsilon_{xx}\varepsilon_{zz} - k_\perp^2\varepsilon_{xx} - k_{||}^2\varepsilon_{zz}, \tag{4.31}$$

$$D_X = -k_0^2\varepsilon_{xy}^2\left(k_0^2\varepsilon_{zz} - k_\perp^2\right), \tag{4.32}$$

with $k^2 = k_\perp^2 + k_{||}^2$. In these expressions, D_C and D_S represent the individual dispersion relations of a pure compressional, and a pure shear root, respectively, with D_X representing coupling between the two modes. The other terms in Eq. (4.29) are associated with finite ion temperature and are first order or higher in the Larmor radius. To simplify, it is first assumed that the wave frequency is on the order of the ion cyclotron frequencies so that $\omega \sim \Omega_i \ll \omega_{pi} \ll \omega_{pe}, \Omega_e$. Further, the perpendicular wavelength, $\lambda_\perp$, is assumed to be much larger than the electron Larmor radius, ρ_e, so that $k_\perp\rho_e \ll 1$. This allows the electrons to be treated as cold except in the parallel dielectric tensor component, ε_{zz}. Next, it is assumed that the Alfvén speed is much larger than the ion thermal speed. This condition can be cast in the form,

$$\frac{B(\mathrm{kG})^2}{T(\mathrm{keV})n(\mathrm{cm}^{-3})} \gg 10^{-14}, \tag{4.33}$$

where B is the confining magnetic field in kiloGauss, T is the plasma temperature in keV, and n is the electron number density. For an ITER-like plasma, $B \approx 50$ kG, $T \approx 10$ keV, and $n \approx 10^{14}\mathrm{cm}^{-3}$, so that the left hand side of Eq. (4.33) is on the order of 10^{-12} and the condition is satisfied. Further, the toroidal field varies weakly compared to the rapid decreases in temperature and density near the edge, and this relation holds over the whole plasma column. Because of this condition, the off-diagonal components of the dielectric tensor, ε_{xz} and ε_{yz}, can be neglected. With these assumptions, the dispersion relation is simplified to

$$D_S D_C + D_X = 0. \tag{4.34}$$

Expressions for the components of the dielectric tensor for a warm plasma can be found in various textbooks, e.g. [64], and are given by

$$\varepsilon_{xx} = 1 + \frac{\omega_{pe}^2}{\Omega_e^2} - \sum_i \frac{\omega_{pi}^2}{\omega^2} \sum_{n=-\infty}^{\infty} \frac{n^2}{\lambda_i} \Lambda_n \left[-x_{0i} Z(x_{ni})\right], \tag{4.35}$$

$$\varepsilon_{yy} = \varepsilon_{xx} + 2 \sum_i \frac{\omega_{pi}^2}{\omega^2} \sum_{n=-\infty}^{\infty} \lambda_i \Lambda_n' \left[-x_{0i} Z(x_{ni})\right], \tag{4.36}$$

$$\varepsilon_{xy} = -i \frac{\omega_{pe}^2}{\omega \Omega_e} - i \sum_i \frac{\omega_{pi}^2}{\omega^2} \sum_{n=-\infty}^{\infty} n \Lambda_n' \left[-x_{0i} Z(x_{ni})\right], \tag{4.37}$$

$$\varepsilon_{zz} = 1 - \frac{k_{De}^2}{2k_{||}^2} Z' \left(\frac{\omega}{\sqrt{2} k_{||} \bar{v}_e} \right) - \sum_i \left[\frac{\omega_{pi}^2}{\omega^2} \Lambda_0 + \sum_{n \neq 0} \frac{k_{Di}^2}{2k_{||}^2} \frac{\omega - n\Omega_i}{\omega} \Lambda_n Z'(x_{ni}) \right]. \tag{4.38}$$

In the previous expressions, Z is the plasma dispersion function with argument $x_{nj} = (\omega - n\Omega_j) / \sqrt{2} k_{||} \bar{v}_j$, the function, Λ_n, is related to the modified Bessel function, I_n, through the relation, $\Lambda_n(\lambda_j) = I_n(\lambda_j) \exp(-\lambda_j)$ with argument $\lambda_j = k_\perp^2 \rho_j^2$, and the Larmor radius defined as $\rho_j = \bar{v}_j / \Omega_j$. The thermal velocities of the relevant species of mass m_j are related to the temperature through $\bar{v}_j = \sqrt{T_j / m_j}$, and the Debye wave number is defined by $k_{Dj} = \omega_{pj} / \bar{v}_j$. Finally, the subscript, j, can represent the electrons, e, or the ions, i, and the cyclotron frequency of the electrons is taken to be positive with the sign explicitly shown.

Equation (4.34) can be solved numerically for $k_{||}$ as a function of $k_\perp$ and ω in order to examine the field-aligned propagation properties relevant to shear waves. To do so, Newton's method is used to converge upon a solution. An initial guess is required, and this is chosen by finding the solution to Eq. (4.34) in the inertial limit, i.e., in the limit that $k_{||} \to 0$. In this limit, the components of the dielectric tensor are independent of $k_{||}$, and the plasma dispersion function can be replaced with its asymptotic expression for large argument to yield,

$$\varepsilon_{xx} \to 1 + \frac{\omega_{pe}^2}{\Omega_e^2} + \sum_i \sum_{n>0} \frac{\omega_{pi}^2 / \Omega_i^2}{1 - \omega^2 / n^2 \Omega_i^2} \frac{\Lambda_n}{\lambda_i / 2}, \tag{4.39}$$

$$\varepsilon_{yy} \to \varepsilon_{xx} - 4 \sum_i \sum_{n>0} \frac{\omega_{pi}^2 / \Omega_i^2}{1 - \omega^2 / n^2 \Omega_i^2} \lambda_i \Lambda_n', \tag{4.40}$$

$$\varepsilon_{xy} \to -i \frac{\omega_{pe}^2}{\omega \Omega_e} + 2i \sum_i \sum_{n>0} \frac{\omega_{pi}^2 / \omega \Omega_i}{1 - \omega^2 / n^2 \Omega_i^2} \Lambda_n', \tag{4.41}$$

$$\varepsilon_{zz} \to 1 - \frac{\omega_{pe}^2}{\omega^2} - \sum_i \left[\frac{\omega_{pi}^2}{\omega^2} \Lambda_0 + 2 \sum_{n>0} \frac{\omega_{pi}^2}{\omega^2 - n^2 \Omega_i^2} \Lambda_n \right] \to - \frac{\omega_{pe}^2}{\omega^2}, \tag{4.42}$$

and the solution to the dispersion relation is given by

$$\frac{k_{||}^2}{k_0^2} = \frac{\varepsilon_{xx} + \varepsilon_{yy}}{2} + \frac{1}{2} \left[\frac{k_\perp^2}{k_0^2} \left(\frac{\omega^2}{\omega_{pe}^2} \varepsilon_{xx} - 1 \right) \pm d \right], \tag{4.43}$$

$$d = \sqrt{\left[\left(\varepsilon_{yy} - \frac{k_\perp^2}{k_0^2} \right) - \varepsilon_{xx} \left(1 + k_\perp^2 \delta_e^2 \right) \right]^2 + 4 \varepsilon_{xy}^2 \left(1 + k_\perp^2 \delta_e^2 \right)}, \tag{4.44}$$

where $\delta_e = c/\omega_{pe}$ is the electron skin depth. The appropriate sign must be chosen for the shear root. When Eq. (4.43) is set to zero, it can be solved for a frequency as a function of the perpendicular wave number. This frequency is a generalization of the ion-ion hybrid frequency at which reflection of the shear wave occurs; it includes FLR effects and the coupling of the shear wave to the compressional wave. At this frequency, for moderate values of $k_\perp$, the wave propagates perpendicular to the magnetic field and is essentially electrostatic in nature, resembling an ion Bernstein wave. However, in the cold plasma limit, this mode reduces to the shear wave that has been studied in previous chapters. Thus, Eq. (4.34) can be solved using the inertial solution as an initial guess near this contour in $(k_\perp, \omega)$ space where the inertial limit is precisely valid and both cyclotron and Landau damping are negligible. Discretizing the parameter space in terms of frequency and perpendicular wave number, Eq. (4.34) can then be solved by stepping outward from this contour using the closest known solutions to extrapolate a guess for the adjacent point. In evaluating the plasma dispersion function, a technique proposed by Weideman is used [65], supplemented with the asymptotic forms for large argument.

The numerical procedure outlined above is used to generate Figs. 4.3 - 4.5. The plasma parameters are $n_e = 5.9 \times 10^{13}$ cm^{-3} and $T_e = 31.1$ keV, with the deuterium and tritium densities, $n_D = n_T = n_e/2$, and temperatures, $T_D = T_T = 27.8$ keV, and a background magnetic field of $B = 53$ kG. In Fig. 4.3, the real part of $k_{||}$ is examined. The top panel, Fig. 4.3(a), shows contours of the real part of the scaled parallel wave number, $k_{||} v_A/\Omega_T$, with the scaled frequency, ω/Ω_T, on the horizontal axis and the scaled perpendicular wave number, $k_\perp \delta_e$, on the vertical axis, where δ_e refers to the electron skin-depth, and v_A is the Alfvén speed. The portion of the parameter space for which the wave is evanescent is

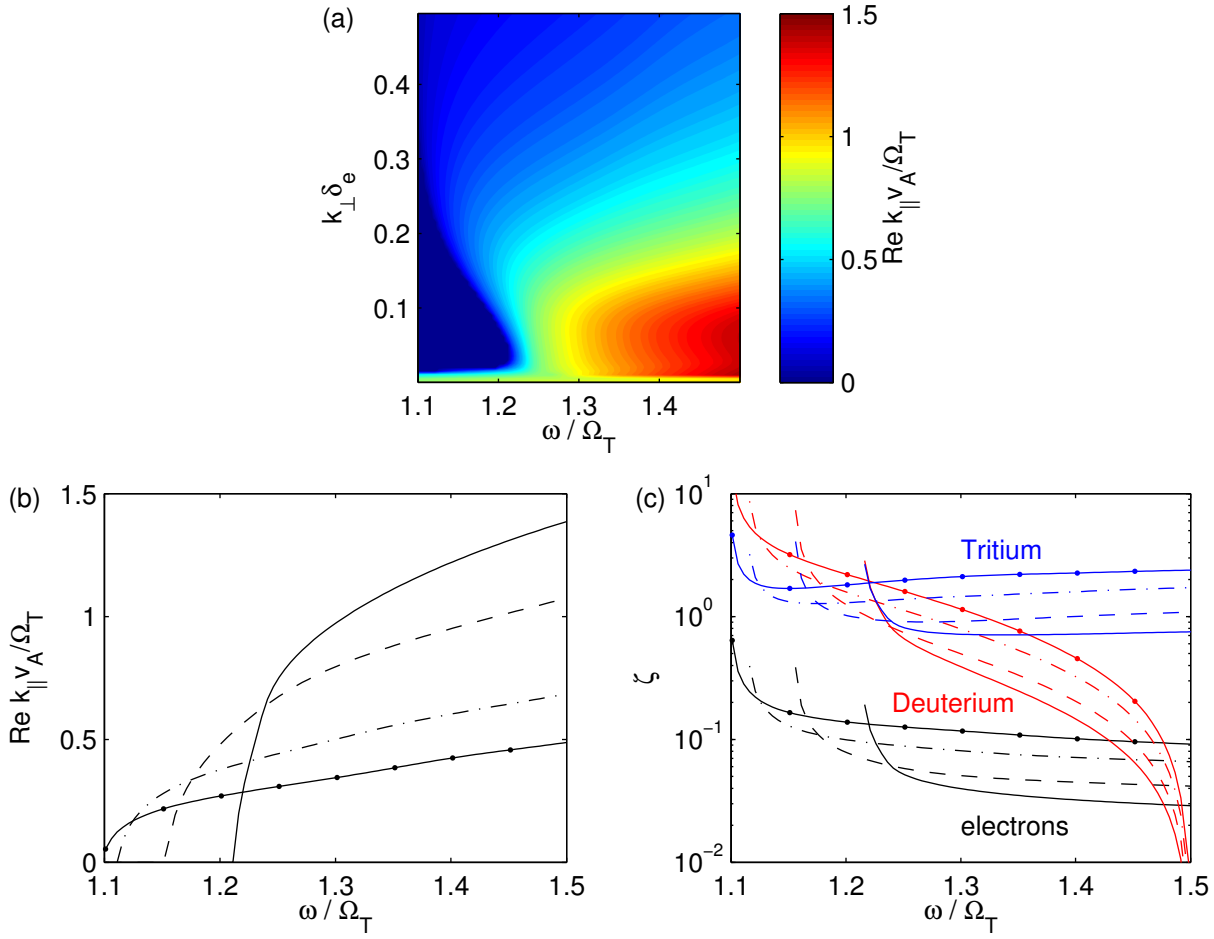

Figure 4.3: Kinetic dispersion relation of the shear Alfvén wave for burning plasmas expected in ITER. Magnetic field strength is 53 kG, electron density is 5.9×10^{13} cm^{-3}, electron temperature is 31.1 keV, with equal concentrations of deuterium and tritium with temperatures of $T_D = T_T = 27.8$ keV. Horizontal axes are the frequency scaled to the tritium gyro frequency, ω/Ω_T. (a) Contour plot of real part of scaled parallel wave number, $k_{||}v_A/\Omega_T$, with scaled perpendicular wave number, $k_\perp \delta_e$, on the vertical axis. (b) Line-cuts of panel (a) made at $k_\perp \delta_e = 0.045$ (solid), 0.145 (dashed), 0.245 (dashed-dotted), and 0.345 (solid with dotted markers). (c) Arguments of plasma dispersion functions illustrating relative importance of electron Landau and ion-cyclotron damping. Line-styles correspond to same values of $k_\perp \delta_E$ as in panel (b). Black curves, label "electrons", correspond to electron Landau damping. Red and blue curves, labeled "Deuterium" and "Tritium", correspond to deuterium and tritium cyclotron damping, respectively.

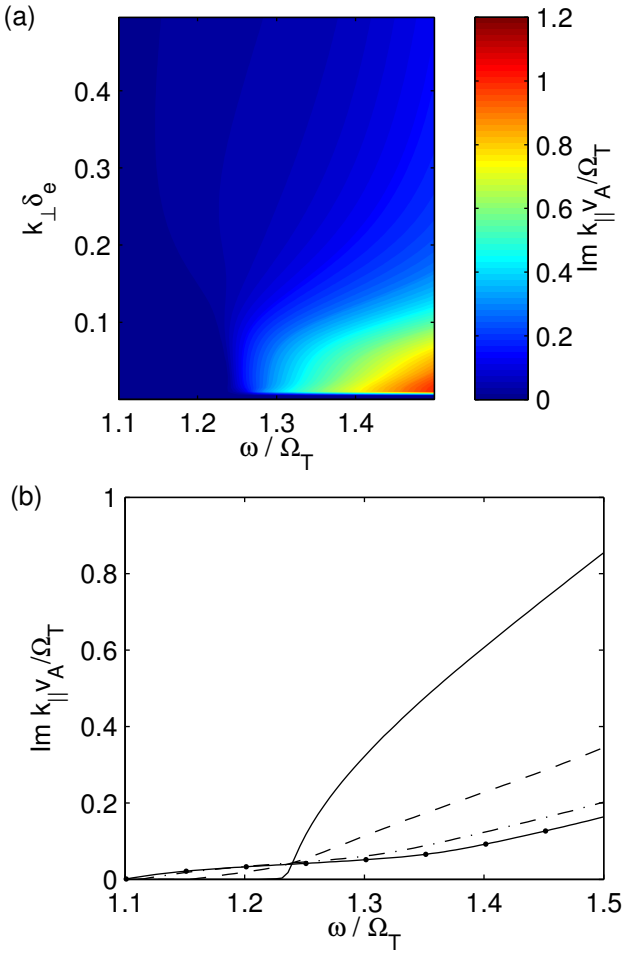

Figure 4.4: Imaginary part of the parallel wave number for parameters used in Fig. 4.3. Horizontal axes are the scaled frequency, ω/Ω_T. (a) Contour plot of imaginary part of $k_{||}v_A/\Omega_T$ with scaled perpendicular wave number, $k_\perp\delta_e$, on the vertical axis. (b) Line-cuts of panel (a). Line-styles correspond to same values of $k_\perp\delta_e$ in Fig. 4.3(b).

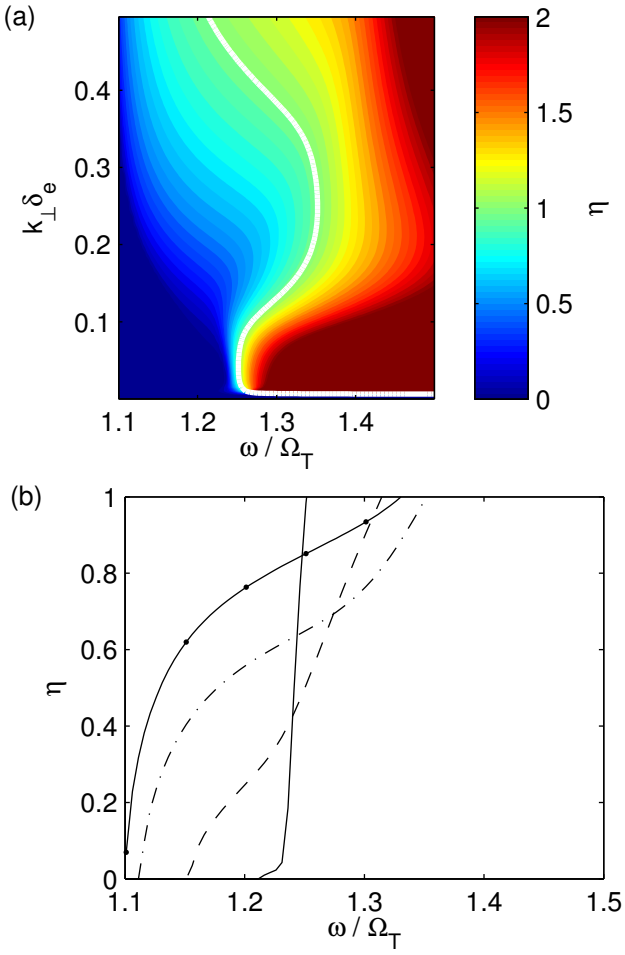

Figure 4.5: Effective damping experienced in one wavelength, $\eta = 2\pi \mathrm{Im}(k_{||})/\mathrm{Re}(k_{||})$, for parameters used in Fig. 4.3. Horizontal axes are the scaled frequency, ω/Ω_T. (a) Contour plot of η with scaled perpendicular wave number, $k_\perp \delta_e$, on the vertical axis. The value $\eta = 1$ is shown by the white contour. Regions to the right of this contour are heavily damped, and regions to the left illustrate where candidate resonator modes exist. (b) Line-cuts of panel (a). Line-styles correspond to same values of $k_\perp \delta_e$ in Fig. 4.3(b).

represented by the dark blue region; the border of this region represents the point at which a parallel cutoff occurs. At small values of $k_\perp \delta_e$, the cutoff frequency approaches the value of the ion-ion hybrid frequency, $\omega_{ii}/\Omega_T = \sqrt{3/2} \approx 1.22$. At large wave numbers, FLR effects become significant, and the cutoff frequency approaches the cyclotron frequency of tritium. In the bottom-left panel, Fig. 4.3(b), line cuts of the contour plot are made at different values of $k_\perp \delta_e$. The horizontal axis is the scaled frequency, and the vertical axis, the real part of the scaled parallel wave number. The cuts are made at the values of $k_\perp \delta_e = 0.045$ (solid), 0.145 (dashed), 0.245 (dashed-dotted), and 0.345 (solid with dotted markers). From these line-cuts, the dependence of the cutoff recency on perpendicular wave number is clear. Further, the parallel wave number rises most rapidly at smaller values of $k_\perp \delta_e$. The bottom-right panel, Fig. 4.3(c), displays the argument of the plasma dispersion function, labeled ζ, for the dominant terms that contribute to the damping. The horizontal axis corresponds to the scaled frequency, and the vertical axis, to ζ. For the electrons, represented by the black curves, Landau damping is dominant, thus the parameter, $\zeta = x_{0e}$, is shown. For the ions, damping at the fundamental cyclotron frequency is dominant; accordingly, $\zeta = |x_{1i}|$ is displayed for deuterium and tritium, the red and blue curves, respectively. The line styles correspond to the same perpendicular wave number values displayed in the middle planel. Damping is large for the electrons when the parameter, ζ, is close to unity, with the inertial and adiabatic regimes corresponding to $\zeta \gg 1$ and $\zeta \ll 1$, respectively. For the ions, cyclotron damping is greatest when $\zeta = 0$, though cyclotron damping is still significant when $\zeta \sim 1$ and becomes negligible when $\zeta \gg 1$. It is clear that the electrons are adiabatic over most of the frequency range. Strong cyclotron damping due to tritium ions takes place over most of the frequency range, with heavy damping due to deuterium also occurring, peaking at the cyclotron frequency of deuterium, $\omega/\Omega_T = 1.5$. Close to the wave cutoff, all of the damping parameters diverge to infinity due to the vanishing of the parallel wave number, indicating that the waves are undamped.

In Fig. 4.4, the imaginary part of $k_{||}$ is examined. The top panel, Fig. 2(4.4), is a contour plot of the imaginary part of the scaled parallel wave number with the scaled frequency on the horizontal axis, and the scaled perpendicular wave number on the vertical axis. In the

bottom panel, Fig. 4.4(b), line-cuts are made of the top panel at various values of the perpendicular wave number. Again, the line-styles correspond to the same values of $k_\perp \delta_e$ as in Fig. 4.3(b). At small values of $k_\perp \delta_e$, where coupling to the compressional wave is strong, the damping is weak. As the value of $k_\perp \delta_e$ increases and the wave begins to exhibit properties of the shear wave, the damping becomes significant. As $k_\perp \delta_e$ increases further, the absolute magnitude of the damping decreases. To assess the effect of damping on the resonator, the parameter, $\eta = 2\pi \mathrm{Im}(k_{||}/\mathrm{Re}(k_{||})$, is evaluated; it measures the amount of damping experienced in one parallel wavelength. This quantity is shown in Fig. 4.5. The top panel, Fig. 4.5(a), is a contour plot of the relative damping, with the scaled frequency on the horizontal axis and the scaled perpendicular wave number on the vertical axis. The white curve corresponds to the value $\eta = 1$. Signals in the region to the right of this curve damp by more than one e-folding in a wavelength. The region to the left of the white contour is weakly damped, and candidate resonator modes may occur in this portion of the parameter space. The bottom panel, Fig. 4.5(b), shows line-cuts of the top panel at different values of $k_\perp \delta_e$, with the line-styles corresponding to the same values as in Fig. 4.3(b).

4.3 WKB analysis with kinetic effects

In analyzing the resonator modes, a cylindrical approximation of the tokamak geometry is made as in section 3.4. In this approximation, the magnetic flux surfaces are concentric circles of radius, r, centered on the magnetic axis. The poloidal angle is θ, and in these coordinates, the toroidal field has the dependence,

$$B_t = \frac{B_0}{1 + \frac{r}{R}\cos\theta}, \tag{4.45}$$

where R is the major radius and B_0 is a characteristic value for the toroidal field. The safety factor is defined by

$$q(r) = \frac{rB_0}{RB_p}. \tag{4.46}$$

The total magnetic field strength is given by

$$B = B_t\sqrt{1 + \frac{B_p^2}{B_t^2}} = B_t\sqrt{1 + \left(\frac{r}{q(r)R}\right)^2} \approx B_t. \tag{4.47}$$

In this expression, the small aspect ratio approximation is made, and it is sufficient to approximate the total magnetic field strength as due to the toroidal field alone. Within this approximation, the distance traversed by a field line is related to the poloidal coordinate through the relation

$$s = \theta\sqrt{R^2 q(r)^2 + r^2} \approx Rq(r)\theta. \tag{4.48}$$

Profiles for the electron density, safety factor, and electron and ion temperatures are found from simulation results reported in Fig. 41 (c) and (d) of Gormezano et al. [49]. The profiles were originally reported as functions of the scaled variable, x, which relates to the flux coordinate, Φ, through the relation $x = (\Phi/\pi a^2 B_t)^{1/2}$. In the cylindrical approximation, this reduces to $x = r/a$. The resulting profiles are reproduced here in the cylindrical approximation as shown in Fig. 4.6 with the minor radius chosen to be $a = 200$ cm. The top panel, Fig. 4.6(a), shows the electron density (solid curve) and the safety factor (dashed curve). The vertical axis on the left corresponds to the electron density, and on the right, to the safety factor. The horizontal axis, common to both panels, is the radius from the magnetic axis. The bottom panel, Fig. 4.6(b), displays the electron (solid curve) and ion (dashed curve) temperatures, with the vertical axis corresponding to temperature and the horizontal axis to the radius from the magnetic axis. These profiles are used to extract reasonable estimates of the type of behavior expected in a burning plasma.

With these profiles specified, a WKB method is implemented. As in previous sections, the effects of magnetic shear are neglected, and the perpendicular wave number, $k_\perp$, is assumed constant. In introducing kinetic effects, the damping is assumed to be weak in this model and is treated as a higher order correction in order to determine the quality factor, Q, of the resulting modes. If, a posteriori this assumption is violated, i.e., the resulting quality factor is small, such modes cannot be considered candidate resonator modes. For this reason, the mode can be approximately described by the formalisms outlined in sections 4.1.1 and 4.1.2. This motivates a generic wave equation that will satisfy the one-dimensional WKB formalism. This equation takes the form,

$$\frac{d^2\Psi}{ds^2} + \mathrm{Re}\left[k_S^2(s, \omega_n, k_\perp)\right]\Psi = 0, \tag{4.49}$$

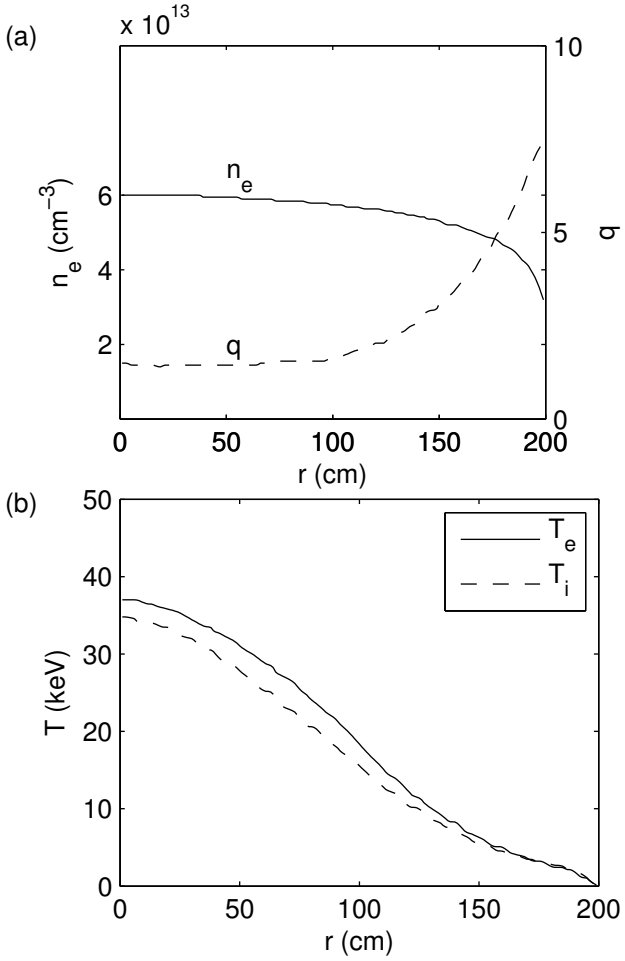

Figure 4.6: Radial profiles of plasma parameters used in analysis. Profiles determined from Fig. 41(c) and (d) of Ref. [49], adapted to a cylindrical approximation for the tokamak geometry. The horizontal axis corresponds to radius from the magnetic axis. (a) Radial dependence of electron density and safety factor. The left vertical axis corresponds to electron density (solid curve). The right vertical axis corresponds to the safety factor (dashed curve). (b) Radial dependence of electron and ion temperatures. The left vertical axis corresponds to temperature in keV. The electron and ion temperatures correspond to the solid and dashed lines, respectively. The temperatures of deuterium and tritium are assumed to be equal.

where Ψ is the characteristic amplitude of the shear wave, and k_S is the shear root for $k_{||}$ from the dispersion relation. The compressional wave is excluded in this formulation as in previous sections. The above equation gives rise to the same quantization condition as before,

$$\int_{-s_0(\omega_n)}^{s_0(\omega_n)} \mathrm{Re}\left[k_S^2(s,\omega_n,k_\perp)\right] \mathrm{d}s = \left(n+\frac{1}{2}\right)\pi, \tag{4.50}$$

where $s_0(\omega)$ is the distance along a field line, measured from the outboard side, at which the wave is expected to reflect; it corresponds to the turning points of the effective potential. The value of k_S is now determined by solving Eq. (4.34) along the field line trajectory. The WKB approximation is known to work best for modes with large quantum numbers. For modes of small quantum number, an alternative formulation can be used in which the parallel wave number is approximated locally as a parabolic potential,

$$\mathrm{Re}\left[k_S^2(s)\right] = V(s) \approx V(0) + \frac{1}{2}V''(0)s^2. \tag{4.51}$$

The well known quantization condition for such an effective potential is

$$\sqrt{-\frac{2}{V''(0)}}V(0) = 2n+1. \tag{4.52}$$

For the present application it is found that the difference between the fundamental frequencies found by the WKB method and the parabolic fit differ typically by a factor on the order of 0.1%. For this reason, in what follows the WKB method is applied. However, an advantage in the parabolic approximation is that analytic eigenfunctions result for the fundamental modes. These functions could be used in a future study to construct approximate full-wave solutions for these modes.

To determine an approximate form for the quality factor, the axial WKB-eigenfunction inside the well is first examined. This takes a form similar to Eq. (4.19), namely

$$\Psi \propto \frac{2}{\sqrt{k_S(s)}} \sin\left[\int_s^{s_0} k_S(s')\mathrm{d}s' + \frac{\pi}{4}\right]. \tag{4.53}$$

Utilizing the quantization condition given in Eq. (4.51), this can be rewritten as

$$\Psi \propto \frac{1}{k_S(s)} e^{-i\pi/4}\left[e^{i\int_{-s_0}^{s} k_S(s')\mathrm{d}s'} \pm e^{-i\int_{s_0}^{s} k_S(s')\mathrm{d}s'}\right], \tag{4.54}$$

where the sign choice depends on the evenness or oddness of the specific mode, and is unimportant for the present purposes. The form of the eigenfunction can be interpreted as an incident wave from the left superposed with a reflected wave traveling from the right. Variations in the amplitude are associated with the changes in wave velocity. Considering k_S to be complex at this point, the wave amplitude decrease is largely due to the phase factors present in the exponential functions. Upon each round trip, the wave amplitude is reduced by a factor of

$$\exp\left\{-2\int_{-s_0}^{s_0}\mathrm{Im}\left[k_S(s')\right]\mathrm{d}s'\right\}. \tag{4.55}$$

Thus, if a source is continually pumping the system with an input power of $P=\omega|\Psi_0|^2$, the stored energy in the resulting wave is

$$E=\frac{|\Psi_0|^2}{\left[1-e^{-2\int_{-s_0}^{s_0}\mathrm{Im}[k_S(s')]\mathrm{d}s'}\right]^2}. \tag{4.56}$$

The quality factor is approximated as

$$Q\sim\frac{1}{\left[1-e^{-2\int_{-s_0}^{s_0}\mathrm{Im}[k_S(s')]\mathrm{d}s'}\right]^2}. \tag{4.57}$$

Although only kinetic sources of dissipation are considered here, the actual quality factor in an experiment likely also exhibits a reduction due to radial convection of the wave and mode conversion at the reflection point.

Figure 4.7 shows the calculated eigenfrequencies as a function of radius. For these results, the magnetic field strength is given by Eq. () with the characteristic strength of the toroidal field taken to be $B_0=53$ kG, and equal concentrations of deuterium and tritium are assumed with quasi neutrality satisfied. The perpendicular wavelength is taken to be $\lambda_\perp=10$ cm, which gives a scaled perpendicular wave number of $k_\perp\delta_e=0.0431$ at the magnetic axis. This scaled value increases as the density slowly decreases towards the plasma edge. In the top panel, Fig. 4.7(a), the horizontal axis corresponds to radial distance from the magnetic axis, and the vertical axis, to frequency in MHz. The lower solid black curve, labeled by ω_0, gives the fundamental frequency of the resonator at a given value of the outboard radius of a magnetic surface. Due to the overdoing that occurs, the cutoff frequency at the outboard

position is in close proximity to this value. Immediately above this curve, the red line, labeled by $\omega_{Q=20}$, represents the frequency of modes having a quality factor $Q = 20$. Above this red dashed line there is cross-hatching (blue in color) that indicates the region of heavily damped modes. In practice, the frequency of candidate resonator modes lies in the narrow strip between the bottom solid curve and the dashed line. The slanted green line labeled by ω_{Max} corresponds to the largest frequency for which a reflection could occur on the inboard side, i.e., the cutoff frequency on the inboard side. At larger radii, this frequency is greater than the deuterium cyclotron frequency on the inboard side and loses meaning. For this reason, the line is terminated when it intersects this cyclotron frequency. For reference, the cyclotron frequency of deuterium on the inboard side is represented by the top orange curve. From this display, it is clear that within this description, long-lived resonator modes exist in a narrow frequency bandwidth, of roughly 200-300 kHz, near the cutoff frequency on the outboard side. In the bottom panel, Fig. 4.7(b), the number of trapped modes as a function of radius is shown. The horizontal axis corresponds to the distance from the magnetic axis, and the vertical axis, to the number of modes. The solid curve corresponds to the maximum number of modes, $n_{Q>20}$, having quality factors, Q, greater than 20. This number stays around 15-30 over the domain shown; modes with larger quantum numbers are heavily damped and are not expected to be excited.

The quality factors of the fundamental modes calculated for the parameters associated with Fig. 4.7 are found to be in the range of $Q > 10^6$ across the entire plasma column. Such large values of Q are, of course not realistic, and simply indicate that wave-particle damping due to electron Landau resonance and ion cyclotron resonance is negligible for these modes. To determine the realistic quality factor for these modes, a consideration of radial convection of wave energy and mode conversion processes is necessary.

Figure 4.8 displays the dependence of the quality factor on mode number. For the solid curve, the parameters are the same as in Fig. 4.7, with the calculation performed at $r = 50$ cm, which corresponds to an electron temperature of $T_e = 31.1$ keV and a scaled perpendicular wave number of $k_\perp \delta_e = 0.0433$. For the dashed curve, the same parameters are used, with the exception that the ion and electron temperatures are both decreased pro-

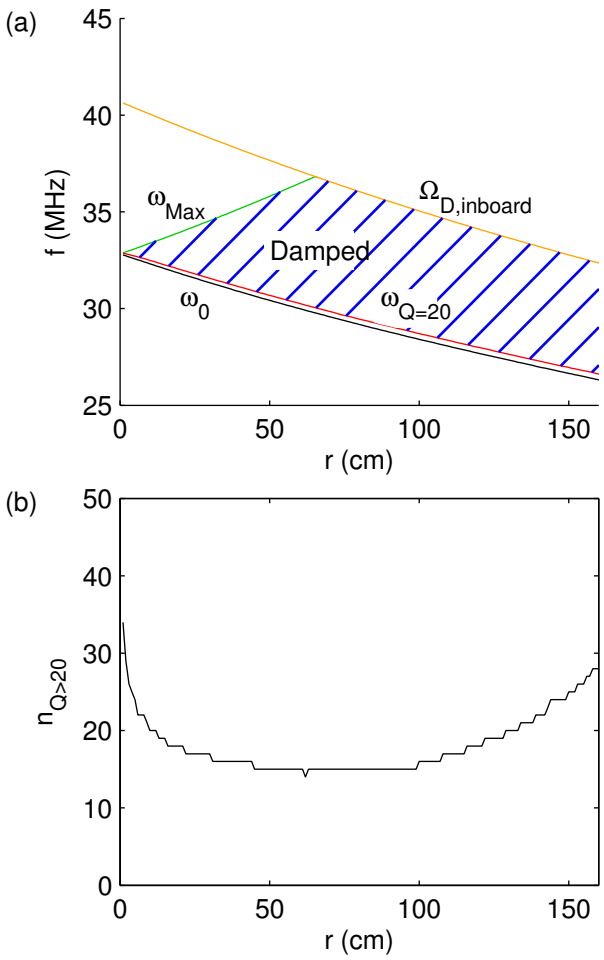

Figure 4.7: Radial dependence of resonator parameters. Horizontal axes correspond to radius from magnetic axis. Plasma parameters and safety factor are given in Fig. 4.6. Magnetic field strength is given by Eq. (4.45) with $B_0 = 53$ kG and $R = 621$ cm; perpendicular wavelength is $\lambda_\perp = 10$ cm, corresponding to $k_\perp \delta_e = 0.043$ at the magnetic axis. (a) Radial dependence of relevant frequencies. Vertical axis corresponds to frequency in MHz. Bottom black curve corresponds to the fundamental eigenfrequency in the resonator, ω_0; red curve to frequency of modes having $Q = 20$, $\omega_{Q=20}$. The slanted green line, labeled ω_{Max}, corresponds to the cut-off frequency on the inboard side; waves in the blank region to its left are not trapped. This frequency terminates when the deuterium cyclotron frequency on the inboard side, represented by the top orange curve labeled $\Omega_{\mathrm{D,inboard}}$, because of heavy cyclotron damping. The blue hatched region, labeled "Damped", corresponds to strongly damped modes with $Q < 20$. (b) Vertical axis corresponds to the number of long-lived modes with $Q > 20$.

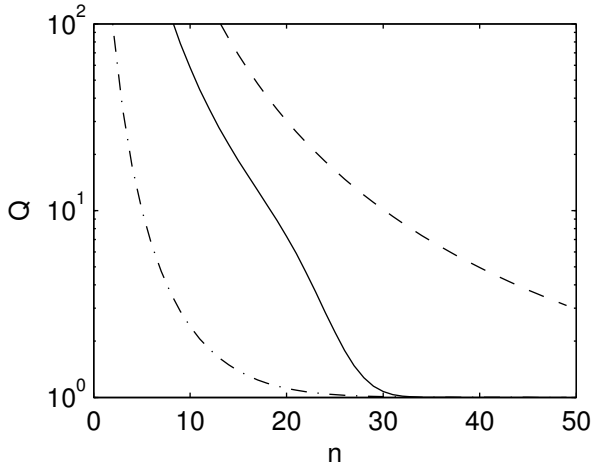

Figure 4.8: Dependence of the quality factor, Q, on resonator mode number. The horizontal axis corresponds to the mode number, and the vertical axis, to Q. The plasma parameters used for the solid curve are the same as those given in Fig. 4.7 evaluated at $r = 50$ cm; the electron temperature is $T_e = 31.1$ keV, and the scaled perpendicular wave number, $k_\perp \delta_e = 0.0433$. The dashed curve uses the same parameters, except that the electron and ion temperatures are decreased proportionally, so that $T_e = 8.39$ keV. The dash-dotted curve, similarly, uses the same parameters as the solid curve, except that $k_\perp \delta_e = 0.1433$. In reality, modes with $Q > 100$ are essentially undamped by wave-particle interactions and would be limited by some other mechanism.

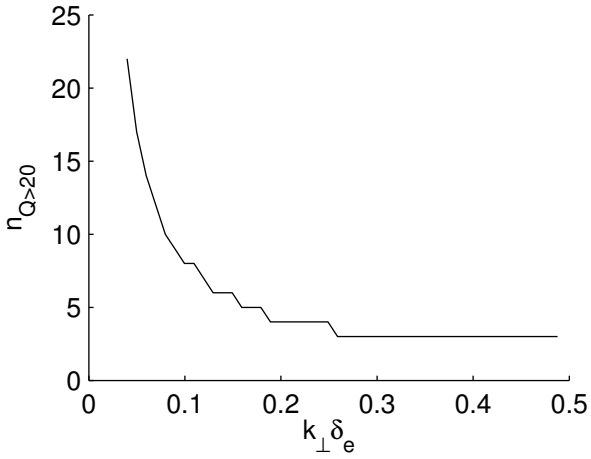

Figure 4.9: Number of long-lived modes as a function of scaled perpendicular wave number. The horizontal axis corresponds to the scaled perpendicular wave number, $k_\perp \delta_e$, and the vertical axis, to the number of modes with $Q > 20$, $n_{Q>20}$. The rapid decrease is due to increased cyclotron damping as $k_\perp$ increases.

portionally so that the peak electron temperature on axis is 10 keV. This corresponds to an electron temperature of $T_e = 8.39$ keV at $r = 50$ cm, where the calculation is performed. Finally, the dash-dotted curve is calculated with the same parameters as the solid curve, except that the perpendicular wavelength is decreased to $\lambda_\perp = 3$ cm, resulting in a scaled perpendicular wave number of $k_\perp \delta_e = 0.1443$. As mentioned previously, wave particle interactions are negligible for low mode numbers; these undamped modes will be limited in actual experiments by other processes. For definiteness, an undamped mode is considered here to be a mode for which $Q > 100$. For this reason, the vertical axis in Fig. 4.8 is scaled to have $Q = 100$ as its maximum value. The undamped modes correspond to $n \leq 8$ for the solid line, $n \leq 13$ for the dashed line, and $n \leq$ ‘ for the dash-dotted line. The curves rise rapidly towards the unrealistic large values near the fundamental mode, $n = 0$. From Fig. 4.8 it is seen that decreasing the temperature decreases the damping as expected, and that decreasing the perpendicular wavelength increases the damping. This is primarily due to the decrease in the rise of the real part of k_S, as shown in Fig. 4.4(b), which causes the eigenfrequencies to shift away from the cutoff frequency. This upshift in frequency leads to an increase in the relative damping, shown in Fig. 4.5(a). Figure 4.9 shows the number of

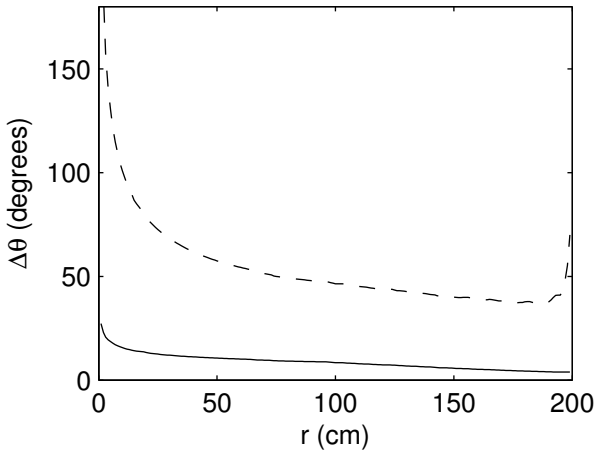

Figure 4.10: Poloidal extent of the trapped modes. Horizontal axis corresponds to the radius, r, and the vertical axis, to the size of the well measured in poloidal angle, $\Delta\theta$. The reflection points occur at $\theta_0 = \pm\Delta\theta/2$. The solid curve corresponds to the fundamental mode, and the dashed curve, to a mode for which $Q = 20$. The poloidal extent of long-lived modes falls between the two curves. The increase towards the magnetic axis is a geometrical effect, while the increase in the dashed curve towards the magnetic axis is a geometrical effect, while the increase in the dashed curve towards the edge is due to rapid decreases in plasma density and temperature.

modes that are not heavily damped at $r = 10$ cm. The vertical axis corresponds to the number of modes with $Q > 20$, and the horizontal axis, the scaled perpendicular wave number. The parameters used are the same as those used for Fig. 4.8 with the exception that the perpendicular wave number now varies.

Figure 4.10 illustrates the poloidal extent of the modes. The horizontal axis corresponds to the radius of the given flux surface at which the calculation is performed, and the vertical axis corresponds to the poloidal angular (in degrees) extent of the corresponding mode. The solid curve corresponds to the fundamental mode, and the dashed line corresponds to a mode for which $Q = 20$. The angle spanned by the fundamental mode decreases monotonically, rising sharply towards the magnetic axis. The fundamental mode is largely localized poloidally over all of the flux surfaces, except in a very narrow region near the center. The dashed line exhibits similar trends, except that it rises sharply near the edge. This is due to the rapid decrease in the density and temperature of the plasma. While this mode spans a much larger poloidal angle, it is still largely localized over most of the flux surfaces.

4.4 Instability due to fusion-born alphas

In this section, a methodology smilier to that introduced by Lashmore-Davies and Russell [25] is used to assess the possibility that fusion-born alpha particles can drive the resonator modes unstable. The difference in the present study is that spatial amplification is considered for a fixed real frequency, and medium nonuniformities are retained within a WKB description. Instability corresponds to $\mathrm{Im}[k_{||}] < 0$, with $\mathrm{Re}[k_{||}] > 0$, i.e. the wave grows in the direction of propagation.

The alpha particles are assumed to be a perturbation on the wave propagation properties, with the alpha particle density taken to be the expansion parameter. Terms that are first order in this density are retained, and higher order terms are neglected. To perform this expansion, the dielectric tensor components are separated into a zeroth order contribution, $\varepsilon_{ij}^{(0)}$, and a first order contribution, $\varepsilon_{ij}^{(1)}$. The components, xz and yz, do not have a zeroth

order contribution, because they do not enter into the zeroth-order dispersion relation, considered in section 4.2. For this reason, the last three terms on the bottom line of Eq. (4.29) are neglected. Keeping terms to first order,

$$D_C = D_C^{(0)} - k_0^2 \varepsilon_{yy}^{(1)}, \tag{4.58}$$

$$D_S = D_S^{(0)} + \left[\varepsilon_{xx}^{(1)} \left(k_0^2 \varepsilon_{zz}^{(0)} - k_\perp^2\right) + \varepsilon_{zz}^{(1)} \left(k_0^2 \varepsilon_{xx}^{(0)} - k_{||}^2\right)\right], \tag{4.59}$$

$$D_X = D_X^{(0)} - 2k_0^2 \varepsilon_{xy}^{(1)} \varepsilon_{xy}^{(0)} \left(k_0^2 \varepsilon_{zz}^{(0)} - k_\perp^2\right) - k_0^4 \varepsilon_{zz}^{(1)} \left(\varepsilon_{xy}^{(0)}\right)^2, \tag{4.60}$$

where the zeroth order terms for $D_C^{(0)}$, $D_S^{(0)}$, and $D_X^{(0)}$ are defined in Eqs. (4.30)-(4.32), with the dielectric coefficients evaluated with their zeroth order forms. With these expressions, the dispersion relation, to first order, is

$$D = D^{(0)} + D^{(1)}, \tag{4.61}$$

$$D^{(0)} = D_C^{(0)} D_S^{(0)} + D_X^{(0)}, \tag{4.62}$$

$$\begin{aligned} D^{(1)} = &-k_0^2 \varepsilon_{yy}^{(1)} + \left(k_0^2 \varepsilon_{zz}^{(0)} - k_\perp^2\right) \left[\varepsilon_{xx}^{(1)} D_C^{(0)} - 2k_0^2 \varepsilon_{xy}^{(1)} \varepsilon_{xy}^{(0)}\right] + \varepsilon_{zz}^{(1)} \left(k_0^2 \varepsilon_{xx}^{(0)} - k_{||}^2\right) D_C^{(0)} \\ &- k_0^4 \varepsilon_{zz}^{(1)} \left(\varepsilon_{xy}^{(0)}\right)^2 - 2k_\perp k_{||} \left[k_0^2 \varepsilon_{yz}^{(1)} \varepsilon_{xy}^{(0)} + \varepsilon_{xz}^{(1)} \left(k^2 - k_0^2 \varepsilon_{yy}^{(0)}\right)\right]. \end{aligned} \tag{4.63}$$

Next, $k_{||}$ is similarly expanded as $k_{||} = k_{||}^{(0)} + k_{||}^{(1)}$. Upon Taylor expanding D about $k_{||}^{(0)}$, and solving for the first order correction,

$$k_{||}^{(1)} = -\frac{D^{(1)}\left(k_{||}^{(0)}\right)}{\left.\frac{\partial D^{(0)}}{\partial k_{||}}\right|_{k_{||}^{(0)}}}. \tag{4.64}$$

This allows the first order correction to be determined for the zeroth-order mode described in section 4.2. Instbaility arises in those portions of the device where $\mathrm{Im}\left[k_{||}^{(0)} + k_{||}^{(1)}\right] < 0$, indicating that drive from the alpha particles must overcome the kinetic damping caused by the background plasma.

To model the fusion-born alpha particles, a ring-distribution is used. This could have relevance for the core plasma of a tokamak in the immediate post-birth phase before collisional relaxation can occur, and is therefore, of interest to the alpha-channeling question. It takes the form,

$$f_\alpha(v_\perp, v_{||}) = n_\alpha \left(\frac{1}{2\pi v_{\perp\alpha}} \delta(v_\perp - v_{\perp\alpha})\right) \left(\frac{1}{\sqrt{2\pi}\bar{v}_{||\alpha}} e^{-\frac{v_{||}^2}{2\bar{v}_{||\alpha}^2}}\right), \tag{4.65}$$

where n_α is the density of the alpha particles, and $v_{\perp\alpha}$ and $\bar{v}_{||\alpha}$ are characteristic velocities for the distribution. These velocities can be related to an effective temperature through $T_{\perp\alpha} = m_\alpha v_{\perp\alpha}^2/2$ and $T_{||\alpha} = m_\alpha \bar{v}_{||\alpha}^2/2$, where $T_{\perp\alpha} + T_{||\alpha} = 3.5$ MeV, the energy of an alpha particle following a DT fusion event. This distribution function is used to obtain the contribution to the dielectric tensor from the alpha particles. The form of this contribution can be cast in terms of integrals over the perpendicular and parallel velocity directions, which are already evaluated [64]. The result is

$$\varepsilon_{xx}^{(1)} = \frac{\omega_{p\alpha}^2}{\omega^2} \sum_n \left\{ \left[-1 + \frac{n\Omega_\alpha}{\sqrt{2}k_{||}\bar{v}_{||\alpha}} Z(x_{n\alpha}) \right] P_n + \left[1 + x_{n\alpha} Z(x_{n\alpha}) \right] \frac{v_{\perp\alpha}^2}{\bar{v}_{||\alpha}^2} \frac{n^2 J_n^2}{k_\perp^2 \rho_\alpha^2} \right\}, \tag{4.66}$$

$$\varepsilon_{xy}^{(1)} = i\frac{\omega_{p\alpha}^2}{\omega^2} \sum_n \left\{ \left[-1 + \frac{n\Omega_\alpha}{\sqrt{2}k_{||}\bar{v}_{||\alpha}} Z(x_{n\alpha}) \right] Q_n + \left[1 + x_{n\alpha} Z(x_{n\alpha}) \right] \frac{v_{\perp\alpha}^2}{\bar{v}_{||\alpha}^2} \frac{n J_n J_n'}{k_\perp \rho_\alpha} \right\}, \tag{4.67}$$

$$\varepsilon_{yy}^{(1)} = \frac{\omega_{p\alpha}^2}{\omega^2} \sum_n \left\{ \left[-1 + \frac{n\Omega_\alpha}{\sqrt{2}k_{||}\bar{v}_{||\alpha}} Z(x_{n\alpha}) \right] R_n + \left[1 + x_{n\alpha} Z(x_{n\alpha}) \right] \frac{v_{\perp\alpha}^2}{\bar{v}_{||\alpha}^2} J_n'^2 \right\}, \tag{4.68}$$

$$\varepsilon_{xz}^{(1)} = -\frac{1}{2}\frac{\omega_{p\alpha}^2}{\omega^2}\frac{k_\perp}{k_{||}} \sum_n Z'(x_{n\alpha}) \left[n^2 P_n + \frac{\omega - n\Omega_\alpha}{\Omega_\alpha} \frac{v_{\perp\alpha}^2}{\bar{v}_{||\alpha}^2} \frac{n J_n^2}{k_\perp^2 \rho_\alpha^2} \right], \tag{4.69}$$

$$\varepsilon_{yz}^{(1)} = -\frac{i}{2}\frac{\omega_{p\alpha}^2}{\omega^2}\frac{k_\perp}{k_{||}} \sum_n Z'(x_{n\alpha}) \left[n S_n - \frac{\omega - n\Omega_\alpha}{\Omega_\alpha} \frac{v_{\perp\alpha}^2}{\bar{v}_{||\alpha}^2} \frac{J_n J_n'}{k_\perp^2 \rho_\alpha^2} \right], \tag{4.70}$$

$$\varepsilon_{zz}^{(1)} = \frac{\omega_{p\alpha}^2}{\omega^2} + \frac{\omega_{p\alpha}^2}{\omega^2} \sum_n \left\{ \left[1 - x_{n\alpha}^2 Z'(x_{n\alpha}) \right] U_n - Z'(x_{n\alpha}) \frac{\bar{v}_{||}^2}{v_{\perp\alpha}^2} x_{0\alpha} k_\perp \rho_\alpha J_n J_n' \right\}, \tag{4.71}$$

where the notation used in Eqs. (4.35)-(4.38) has been adopted, with the definitions of $x_{n\alpha}$ and ρ_α generalized to $x_{n\alpha} = (\omega - n\Omega_\alpha)/\sqrt{2}k_{||}\bar{v}_{||\alpha}$ and $\rho_\alpha = v_{\perp\alpha}/\Omega_\alpha$, and where J_n is a Bessel function with argument $k_\perp \rho_\alpha$. The remaining undefined parameters are,

$$P_n = \frac{2}{k_\perp \rho_\alpha} J_n J_n', \tag{4.72}$$

$$Q_n = n J_n'^2 + \left(\frac{n^2}{k_\perp^2 \rho_\alpha^2} - 1 \right) J_n^2, \tag{4.73}$$

$$R_n = \frac{2n^2}{k_\perp \rho_\alpha} \left(1 - \frac{k_\perp^2 \rho_\alpha^2}{n^2} \right) J_n J_n', \tag{4.74}$$

$$S_n = J_n'^2 + \left(\frac{n^2}{k_\perp^2 \rho_\alpha^2} - 1 \right) J_n^2, \tag{4.75}$$

$$U_n = \frac{1}{2} J_n^2 - \frac{\bar{v}_{||\alpha}^2}{v_{\perp\alpha}^2} k_\perp \rho_\alpha J_n J_n'. \tag{4.76}$$

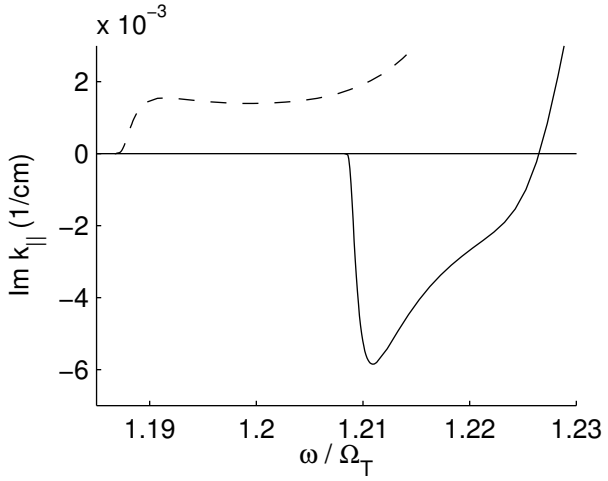

Figure 4.11: Imaginary part of $k_{||}$ due to a ring-distribution of alpha particles for different values of $k_\perp$. Calculation performed for a homogeneous plasma with parameters corresponding to Fig. 4.6 at position, $r = 50$ cm on the outboard side. The alpha particle distribution is described by Eq. (4.65), with temperatures, $T_{\perp\alpha} = 2$ MeV and $T_{||\alpha} = 1.5$ MeV, and density, $n_\alpha = 0.01 n_e$. On the horizontal axis is the scaled frequency, and on the vertical axis, the imaginary part of the parallel wave number, Im$k_{||}$. The solid and dashed curves correspond to $\lambda_\perp = 9$ and 5 cm, respectively. Instability drive is present when Im $k_{||}$ is negative, for the solid curve, and is caused by a negative value of P_1 in Eq. (4.66).

After examining the relative importance of the various terms presented in Eqs. (4.66)-(4.71), it is determined that the most important term for instability is $\varepsilon^{(1)}_{xx}$. This is not surprising, because at these large values of $k_\perp$, coupling to the compressional wave is largely negligible. Upon examination of Eq. (4.66), it is apparent that the possibility of amplification is determined primarily by the sign of $P_{n=1}$, with the fundamental cyclotron frequency being the dominant contributor in this frequency range.

In order to make comparisons to the results of Lashmore-Davies and Russell [25], plasma parameters are chosen to correspond to $r = 50$ cm in Fig. 4.7: $B = 49.1$ kG, $n_e = 5.9 \times 10^{13}$ cm^{-3}, $T_e = 31.1$ keV, $T_D = T_T = 27.8$ keV, $T_{\perp\alpha} = 2$ MeV, $T_{||\alpha} = 1.5$ MeV, and $n_\alpha = 0.01 n_e$. The ion densities preserve quasi neutrality through the relation, $n_D = n_T = n_e/2 - n_\alpha$. Figure 4.11 explores the possibility of amplification for two values of

$k_\perp$. On the horizontal axis is the scaled frequency, ω/Ω_T, and on the vertical axis is the imaginary part, $\mathrm{Im}[k_{||}]$. The solid and dashed curves correspond to $k_\perp\rho_\alpha = 2.5$ and 4.5, $k_\perp\delta_e = 0.044$ and 0.080, $\lambda_\perp = 9$ and 5 cm, respectively. The local extrema of the curves immediately adjacent to the cutoff in Fig. 4.11 occur when $x_{1\alpha} \sim -1$, so that the alpha particle contribution possesses a significant imaginary part but the background deuterium is still far from cyclotron resonance, a conclusion which agrees with the work of Lashmore-Davies and Russell [25]. From the sign of P_1, the intervals of $k_\perp\rho_\alpha$ which correspond to instability can be determined. These fall between the peak and successive zero of the Bessel function, J_1. The first two intervals are $k_\perp\rho_\alpha \in (1.84, 3.83)$ and $k_\perp\rho_\alpha \in (5.33, 7.02)$. It is seen from Fig. 4.11 that the value of $k_\perp\rho_\alpha$ which is within the first interval corresponds to strong instability, i.e., the curve falls below the y-axis for a portion of the frequency domain. The value of $k_\perp\rho_\alpha$ that falls outside these two intervals is damped. The second interval of $k_\perp\rho_\alpha$ for which $J_1 < 0$ exhibits much weaker instability with $\mathrm{Im}[k_{||}]$ reaching a minimum negative value roughly an order of magnitude less than the solid line in Fig. 4.11. This is because of the larger cyclotron damping that occurs in the background plasma at smaller perpendicular wavelengths.

A critical density for these two intervals of $k_\perp\rho_\alpha$ can now be determined using the condition for marginal stability, $\mathrm{Im}[k_{||}^{(0)} + k_{||}^{(1)}] = 0$, where $k_{||}^{(1)}$ is assumed to be at the critical density, $n_{\alpha c}$. So long as the perturbative model is valid, $k_{||}^{(1)}$ is linear in n_α. Thus, the marginal stability condition can be rewritten as

$$\mathrm{Im}\left[k_{||}^{(0)} + k_{||}^{(1)}(n_\alpha)\frac{n_{\alpha c}}{n_\alpha}\right] = 0. \tag{4.77}$$

This condition is scanned in frequency to determine the smallest critical density, while choosing the value of $k_\perp$ for which P_1 is most negative within the interval of interest. This procedure results in the critical densities $n_\alpha/n_e = 7.3 \times 10^{-5}$ for the first interval, and $n_\alpha/n_e = 3.6 \times 10^{-3}$ for the second, but it should be emphasized that these densities are obtained at $r = 50$ cm, and these values will vary with radius.

A simple analytic estimate for the critical density can be obtained in the following approximations: coupling to the compressional wave is negligible, cyclotron damping on the

background ions is negligible, and the electrons are inertial but experience Landau damping. These approximations are valid for perpendicular wavelengths much larger than the ion skin-depth and for waves with frequency close to the cutoff. In these approximations, the dispersion relation is given by $D = D_S$. Expanding in the alpha density as before, the dispersion relation to first order is given by Eq. (4.59). From the zeroth order equation, it is determined that

$$k_{||}^{(0)} = k_0^2 \varepsilon_{xx}^{(0)} \left(1 + k_\perp^2 \delta_e^2\right), \tag{4.78}$$

where $\delta_e = c/\omega_{pe}$ is the electron skin depth. In the above expression, the fact the electrons are inertial to zeroth order has been used. Asymptotically expanding the plasma dispersion function that appears in the electron term in Eq. (4.38) for large argument gives the first order term,

$$\varepsilon_{||}^{(1)} = \sqrt{2\pi} i \frac{\omega_{pe}^2}{\omega^2} \frac{\omega^3}{k_{||}^3 \bar{v}_e^3} \exp\left(-\frac{\omega^2}{2k_{||}^2 \bar{v}_e^2}\right), \tag{4.79}$$

where the superscript of $k_{||}^{(0)}$ is dropped on the right hand side of the equation for simplicity of expression. For the first order term, $\varepsilon_{xx}^{(1)}$, only the drive of the alpha particles is considered because cyclotron damping has been neglected. Further, only the dominant term proportional to P_1 is included. This leads to the expression,

$$\varepsilon_{xx}^{(1)} = \frac{\omega_{p\alpha}^2}{\omega^2} \left[-1 + \frac{\Omega_\alpha}{\sqrt{2} k_{||} \bar{v}_{||\alpha}} Z(x_{1\alpha})\right] P_1. \tag{4.80}$$

Substituting these expressions into Eq. (4.64) results in

$$\begin{aligned} \text{Im } k_{||} = \text{Im } k_{||}^{(1)} &= \sqrt{\frac{\pi}{2}} \frac{k_\perp^2 \delta_e^2}{1 + k_\perp^2 \delta_e^2} \frac{\omega^3}{k_{||}^2 \bar{v}_e^3} \exp\left(-\frac{\omega^2}{2k_{||}^2 \bar{v}_e^2}\right) \\ &+ \frac{\omega_{p\alpha}^2}{2\sqrt{2} k_{||} c^2} \frac{\Omega_\alpha}{k_{||} \bar{v}_{||\alpha}} (1 + k_\perp^2 \delta_e^2) P_1 \text{ Im}\left[Z(x_{1\alpha})\right]. \end{aligned} \tag{4.81}$$

In our approximations, $k_{||}^{(0)}$ is completely real. For this reason, the imaginary part of $Z(x_{1\alpha})$ is $\sqrt{\pi}\exp(-x_{1\alpha}^2)$. Making this substitution and using the marginal stability condition, it can be determined that

$$\frac{\omega_{p\alpha}^2}{\omega^2} = -\frac{\omega}{2\Omega_\alpha} \frac{c^2 \bar{v}_{||\alpha}}{\bar{v}_e^3} \frac{k_\perp^2 \delta_e^2}{\left(1 + k_\perp^2 \delta_e^2\right)^2} P_1 \exp\left[\frac{(\omega - \Omega_\alpha)^2}{2k_{||}^2 \bar{v}_{||\alpha}^2} - \frac{\omega^2}{2k_{||}^2 \bar{v}_e^2}\right]. \tag{4.82}$$

This equation can be minimized with respect to frequency to obtain an approximate critical density. For the same conditions used in the preceding paragraph, this formula yields a critical density of $n_\alpha/n_e = 3.2 \times 10^{-5}$ and $n_\alpha/n_e = 8.3 \times 10^{-4}$ for the first and second unstable intervals of $k_\perp$, respectively. This under predicts the critical density by a factor of two and four, compared to the more accurate calculation performed previously. This is not surprising because cyclotron damping was not included in the derived, analytic formula. However, this provides a quick way of getting an estimate of the density of energetic particles required to drive the instability. Further, it should be noted that simulations of expected conditions for burning plasma in ITER predict that the alpha density will be 0.85% of the electron density on the magnetic axis [66]. This justifies the use of the alpha density as an expansion parameter in all of the previous work. In the analysis that follows, values of $k_\perp$ are chosen that fall in the interval of largest instability.

Next, the results of the stability analysis are related to the ion-ion hybrid resonator in ITER. An amplification factor is defined as,

$$A = -\int_{s_0}^{s_0} \mathrm{Im}[k_{||}]\mathrm{d}s, \tag{4.83}$$

indicating the exponential factor that a wave grows (or damps) during a single pass through a resonator of length $2s_0$. If $A > 0$, this indicates that the drive of the alpha particles is greater than the damping on the background plasma. In Fig. 4.12, the imaginary part of $k_{||}$ is displayed for five resonator modes at a radial position of $r = 50$ cm, where the profiles specified in Fig. 4.6 are used. This corresponds to the parameters, $n_e = 5.95 \times 10^{13}$ cm^{-3}, $T_e = 31.1$ keV, and $T_i = 27.8$ keV. The magnetic field on the outboard side of the flux surface is $B = 49.1$ kG. For the alpha particles, the same parameters are used as in Fig. 4.11. The perpendicular wavelength is chosen to maximize instability drive, minimizing P_1. The horizontal axis corresponds to the distance spanned by the mode along a field line, and the vertical axis to the imaginary part of $k_{||}$ with both the zeroth order term and first order correction included. The dashed, solid, and dashed-dotted curves correspond to three different trapped modes, $n = 7$, 17, and 27 with amplification factors, $A = 2.6$, 3.1, and 2.6, respectively. At this position, the $n = 2 - 34$ modes have positive amplification factors and

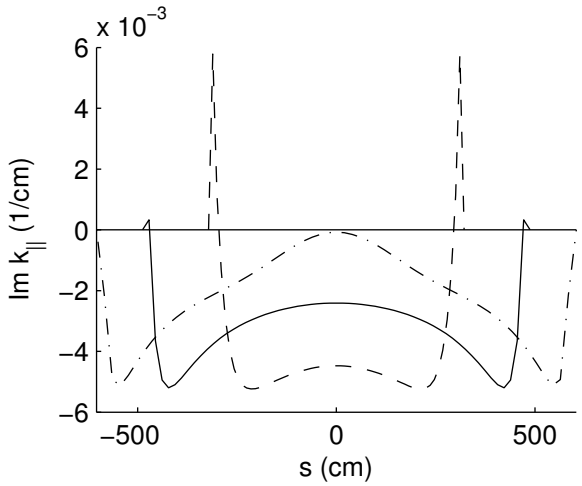

Figure 4.12: Imaginary part of $k_{||}$ for different resonator modes within one well. The background plasma parameters are the same as in Fig. 4.7 evaluated at $r = 50$ cm, and the alpha distribution parameters are those used in Fig. 4.11. The horizontal axis corresponds to distance along a field line, and the vertical axis, to the imaginary part of $k_{||}$. The dashed, solid, and dashed-dotted curves correspond to the mode numbers, $n = 7$, 17, and 27 with amplification factors, $A = 2.6$, 3.1, and 2.6, respectively. The mode with largest amplification is $n = 17$. For higher mode numbers, damping towards the center limits the growth, and at lower mode numbers, the well decreases in length, limiting total amplification.

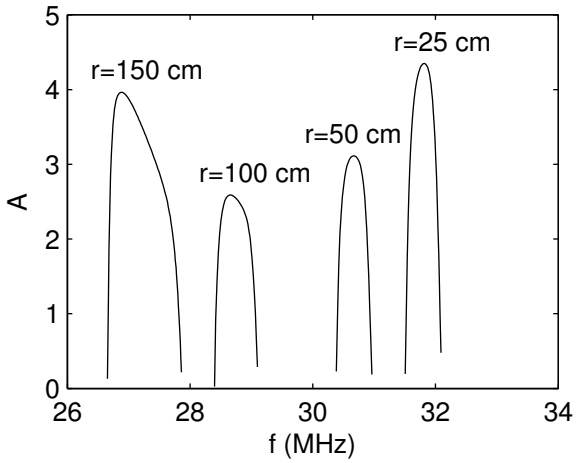

Figure 4.13: Amplification factors at different radii. The background plasma parameters are the same as in Fig. 4.7 evaluated at $r = 50$ cm, and the alpha distribution parameters are those used in Fig. 4.11. On the horizontal axis is the frequency range of the amplified modes in MHz, and on the vertical axis, the amplification factor. The individual curves correspond to $r = 25$, 50, 100, and 150 cm, and are labeled accordingly. The continuous decrease in the frequency band results in a spread of several MHz over which the resonator can be amplified across the plasma. The increase in A towards the magnetic axis is a geometrical effect, which lengthens the well. The increase towards the edge is due to the colder background plasma. In reality, this increase will be offset by a decrease in alpha particle density towards the edge.

exhibit a narrow frequency range of $f = 30.38 - 30.96$ MHz, with $n = 17$ the most unstable. The spatial undulations of the growth coefficient seen in Fig. 4.12 arise due to the lengthening of the resonator, maximizing cyclotron resonance with the alpha particles, and minimizing cyclotron damping on the background plasma. At small n numbers, cyclotron resonance with the alpha particles is not possible because $k_{||}$ is too small over the resonator region. Thus, the first unstable mode appears at $n = 2$. As the mode number increases, the mode comes into cyclotron resonance with the alpha particles and the resonator-length increases, leading to maximum amplification at $n = 17$. As the mode number increases beyond this value, cyclotron damping on the background ions becomes dominant and inhibits amplification of the resonator modes.

In order to illustrate the frequency bandwidth of amplified resonator modes at different radii, Fig. 4.13 displays the amplification factor, A, versus frequency at four different radii. The four solid curves correspond to $r = 25$, 50, 100, and 150 cm, and are labeled accordingly. At each radius, the bandwidth of the amplified modes is roughly 600 kHz, with the frequency of greatest amplification shifting to lower frequencies at larger radii, as expected from the eigenfrequency outline in Fig. 4.7(a). Amplification of the modes is seen to increase towards the core and the edge. The increase towards the core is a geometrical effect, which lengthens the resonator. The increase towards the edge is because of decreased damping due to the lower temperatures; however, the density of the fusion-born alpha population should significantly decrease at these larger radii, likely limiting the amplification experienced by the modes. Finally, it should be mentioned that while the amplified frequencies are shown only at four different radii, the radius of the flux surface is a continuous variable. For this reason, the eigenfrequencies of the resonator become a continuous function of radius, and amplified frequencies for the entire plasma column can vary over several MHz.

4.5 Influence of shear

To explore the effects of magnetic field shear, an attempt is made to determine the structure of the eigenmodes in the global geometry of the tokamak. To do so, an eikonal form for the wave field is assumed, similar to that which is commonly used in ballooning-mode analysis. This takes the form

$$\mathbf{E} = \mathbf{E}_S e^{i\psi}, \tag{4.84}$$

where ψ is the rapidly varying eikonal and $\mathbf{E}_S$ is the eigenvector which corresponds to the shear Alfvén wave root. The amplitude of the eigenvector, $\mathbf{E}_S$, is assumed to vary much slower than ψ. In this approximation, the wave number is related to the eikonal through $\mathbf{k} = \nabla\psi$. The poloidal coordinates are defined in the cylindrical approximation as in section 4.3 to be (r, θ). The toroidal angle is taken to be ϕ. This allows for the eikonal to be written as

$$\psi = \int k_{||}(r, s)\mathrm{d}s + m\left[\phi - q(r)(\theta - \theta_0)\right] + k_r r, \tag{4.85}$$

where m corresponds to a Fourier decomposition of the modes in the toroidal coordinate. This is done because azimuthal symmetry of the equilibrium profile is assumed. Further, k_r is assumed constant, corresponding to the radial wave number, and s is a coordinate, which measures the relative distance along a respective field line. Coordinate surfaces are defined in a similar manner to nonlinear simulations of tokamak turbulence using flux tubes [67]. The orthogonal coordinate surfaces are described by the variables, r, corresponding to a unique flux surface, $\alpha = \phi - q(r)(\theta - \theta_0)$, which, for constant r, uniquely specifies a field line, and s, defined to be orthogonal to the other coordinate surfaces; $s = 0$ is chosen to correspond to the outboard side of the tokamak. An approximate form for s is given in Eq. (4.48). From this form, it is apparent that if a Fourier decomposition of Eq. (4.85) is performed in poloidal angle through the basis functions, $\exp(il\theta)$, the result would contain many values of l because the modes are poloidally localized to the outboard side. The quantity $k_{||}$ is independent of α, because, for fixed r and s, the dispersion relation is invariant with respect to the field line chosen. With Eq. (4.85), the wave vector is determined to be,

$$\mathbf{k} = k_{||}\hat{\mathbf{b}} + k_t\hat{\mathbf{t}} + k_n\hat{\mathbf{r}}, \tag{4.86}$$

$$k_t = m\frac{B}{RB_p} \approx m\frac{q(r)}{r}, \tag{4.87}$$

$$k_n = \frac{\partial}{\partial r}\left[\int k_{||}\mathrm{d}s\right] - mq'(r)(\theta - \theta_0) + k_r, \tag{4.88}$$

where the unit vectors are $\hat{\mathbf{r}}$, normal to the flux surfaces, $\hat{\mathbf{t}} = \hat{\boldsymbol{\phi}}B_p/B - \hat{\boldsymbol{\theta}}B_t/B$, lying in the geodesic direction, and $\hat{\mathbf{b}} = \hat{\boldsymbol{\phi}}B_t/B + \hat{\boldsymbol{\theta}}B_p/B$, lying parallel to the magnetic field. The perpendicular wave number, $k_\perp = \sqrt{k_t^2 + k_n^2}$, is now seen to vary with position. It should be mentioned that since $\hat{\mathbf{t}}$ lies predominantly in the $\hat{\boldsymbol{\theta}}$ direction, k_t can be approximately interpreted as the poloidal wave number. Further, choosing m to be an integer preserves periodicity in the toroidal direction. Subtle issues involving periodicity requirements for the poloidal angle are unimportant to the trapped modes examined here, because they exhibit strong localization in the poloidal direction.

To apply this method, an iterative process is used in which the variable, s, is first discretized. The outboard location, $s = 0$, is chosen as a starting point at which the value of k_n is specified. The new value of k_n is computed at the adjacent grid point using the value

of $k_{||}$ at the initial point. This new value of k_n is then used to compute $k_{||}$ at the new point, thus the method resembles a finite difference scheme. Using Eq. (4.48) to express Eq. (4.88) as a function of s yields

$$k_n = \frac{\partial}{\partial r}\left[\int k_{||}\mathrm{d}s\right] - \frac{mq'(r)}{Rq(r)}(s - s_0) + k_r. \tag{4.89}$$

With this form, the difference scheme becomes

$$k_n^{(j+1)} = k_n^{(j)} + \left[\frac{\partial k_{||}^{(j)}}{\partial r} - \frac{mq'(r)}{RQ(r)}\right]\mathrm{d}s. \tag{4.90}$$

For definiteness, θ_0 and k_r are defined to vanish at the outboard location. This is done to minimize radial propagation of the mode so that perpendicular propagation initially occurs solely in the geodesic direction. As the wave evolves, it develops a nonzero component of k_r, which causes the energy to travel radially because of the non-ideal feature of the shear Alfvén waves in this regime.

First, to provide insight into the role of magnetic shear, the methodology is applied to an idealized cold plasma. Figure 4.14 illustrates the calculated parallel and perpendicular wave numbers as a function of the variable, s. The magnetic well is examined at the radius, $r = 50$ cm, with electron density, $n_e = 5.9 \times 10^{13}$ cm^{-3}, and safety factor, $q = 1.45$. The frequency of the wave is chosen to be $\omega = 1.01\omega_{ii}$, where ω_{ii} is given by Eq. (1.2) with cyclotron frequencies evaluated at $s = 0$. The solid, dashed, and dash-dotted curves in the top and bottom panels correspond to the m-numbers, $m = 4$, 8, and 12. The choice of m results in a minimum value for the absolute magnitude of $k_\perp$ because k_t is unaffected by the magnetic shear, as seen in Eq. (4.87). Increasing m causes the wave to begin with a larger initial $k_\perp$, thus, minimizing coupling to the compressional wave. In the top panel, Fig. 4.14(a), the vertical axis corresponds to $k_{||}^2$, and in the bottom panel, Fig. 4.14(b), the vertical axis corresponds to the scaled perpendicular wave number, $k_\perp\delta_e$. It is seen from the top panel that there is little variation in the cutoff point for the three cases. This arises because, in the cold plasma case, variations in the cutoff position are caused by coupling to the compressional mode. At the cutoff location, the effect of magnetic shear increases the value of $k_\perp$ sufficiently that the coupling is weak. The degree to which the value of $k_\perp\delta_e$

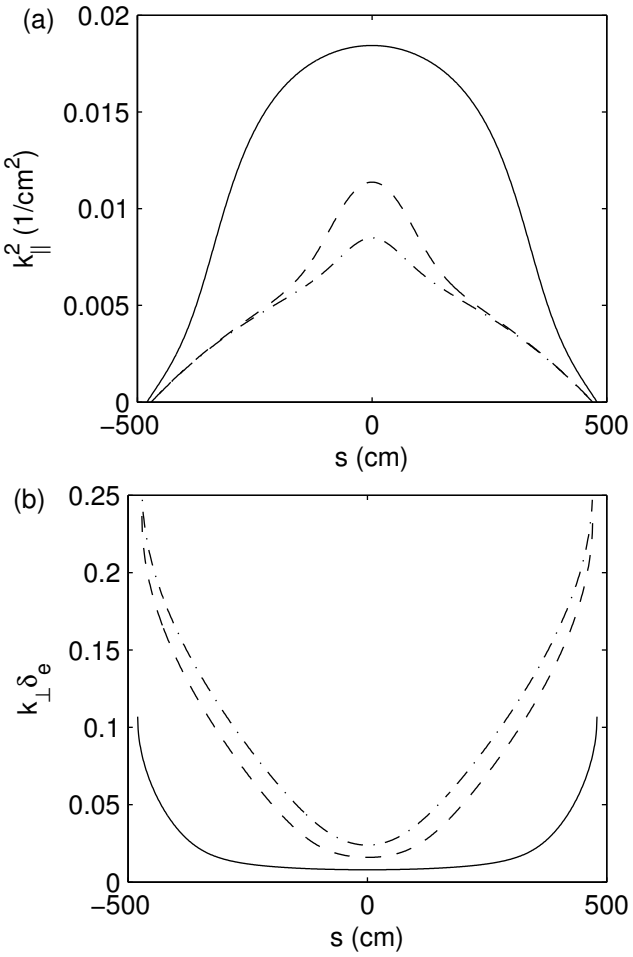

Figure 4.14: Effects of magnetic shear on resonator modes in a cold plasma. The background plasma parameters are as in Fig. 4.7 evaluated at $r = 50$ cm, except that the plasma temperature is artificially set to zero. The frequency of the wave is $\omega = 1.01\omega_{ii}$, where ω_{ii} is given by Eq. (1.2), with the cyclotron frequencies evaluated at the outboard side. The horizontal axes correspond to distance along a field line, s. The solid, dashed and dash-dotted lines correspond to $m = 4$, 8, and 12. (a) Dependence of $k_{||}^2$. (b) Dependence of $k_\perp \delta_e$. Both panels show that the reflection point is largely independent of $k_\perp$. As m increases, the magnetic shear more effectively changes the value of $k_\perp$, resulting in a distorted profile for $k_{||}^2$.

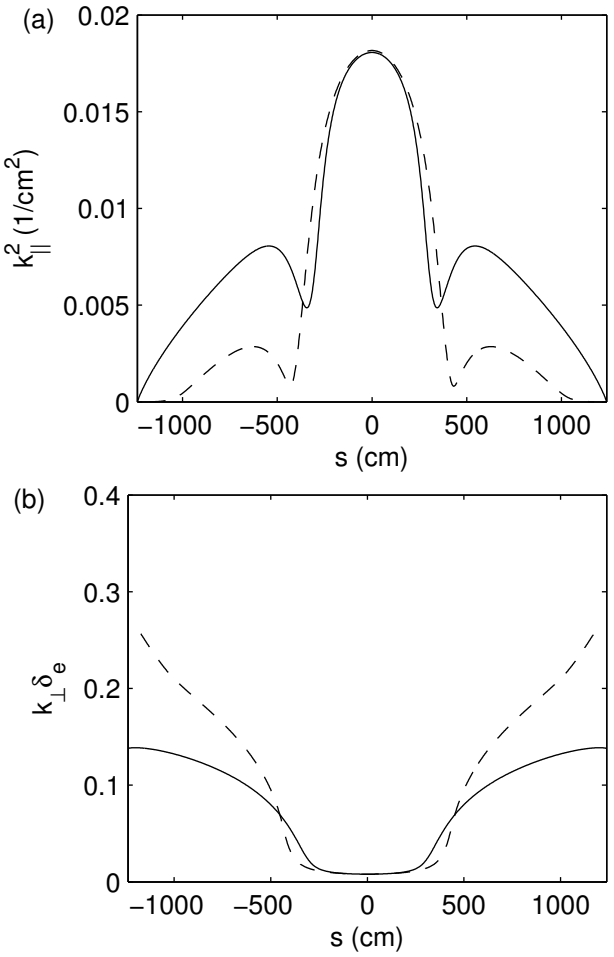

Figure 4.15: Effects of magnetic shear on resonator modes in a hot plasma. The background plasma parameters are as given in Fig. 4.7, evaluated at $r = 50$ cm, with $m = 4$ and the ion temperatures set to 27.8 keV and 7.0 keV for the solid and dashed lines, respectively. The frequency of the wave is $\omega = 1.005\omega_{ii}$. (a) Dependence of $k_{||}^2$. (b) Dependence of $k_\perp \delta_e$. The difference in cut-off points between the solid and dashed lines is attributed to the reduction in the Larmor radius. If the temperature is further decreases, the result approaches the cold plasma behavior shown in Fig. 4.14.

changes is largely determined by the first term on the right-hand side of Eq. (4.89), because, from Fig. 4.6(a), it can be seen that the derivative, $q'(r)$, is very small at the flux surface being examined. The behavior illustrated by Fig. 4.14 indicates that resonator modes can clearly exist for cold plasma conditions.

Next, the effects of finite ion temperature in the presence of magnetic shear are considered. Figure 4.15 is the analog of Fig. 4.14, but at a slightly lower frequency, $\omega = 1.005\omega_{ii}$, and with ion temperature included. For this case, $m = 4$ is chosen for both displays. The ion temperature at this flux surface is $T_i = 27.8$ keV, and corresponds to the solid line in both panels. For the dashed line, the ion temperature is artificially lowered to $T_i = 7.0$ keV, to provide a comparison. It is found that for temperatures below $T_i = 2.8$ keV the cold plasma result shown in Fig. 4.14 is recovered, but it is not shown. The top panel, Fig. 4.15(a), illustrates coupling to an IBW, as evidenced by the lobes that appear in the display. The appearance of these lobes causes an increase of both the length of the resonator and of the area under the curves shown in this panel. When magnetic shear and FLR effects are included, the quantization condition, Eq. (4.50), causes the value of the eigenfrequency to decrease for a given n. The bottom panel, Fig. 4.15(b), illustrates the corresponding increase in the value of $k_\perp$. The variations in $k_\perp$ have two significant consequences. First, the damping of the wave increases with increased $k_\perp$. Second, the instability driven by the alpha particles can be tuned and detuned depending on the local value of $k_\perp$. Such a spatial variation is expected to reduce the amplification factors reported in section 4.4. However, many different modes can be amplified at each poloidal position, and subsequently carry the energy to other locations.

4.6 Discussion

In this chapter, an analytical study has been performed to explore how the challenging environment of burning plasmas modifies the properties of the ion-ion hybrid resonator. First, a one-dimensional WKB model was developed considering both inertial and adiabatic electrons. Then, a detailed study of the kinetic dispersion relation for shear Alfvén waves, in-

cluding coupling to the compressional mode, has been made for the relevant burning plasma conditions. It is identified that the high ion temperatures introduce a variation of the reflection points of the resonator modes with perpendicular wave number. The one-dimensional WKB model was then extended to include kinetic effects in the calculation of the eigenfrequencies of the trapped modes. It is found that ion cyclotron damping limits the possible resonator modes to a narrow bandwidth (on the order of 500 kHz) above the local ion-ion hybrid frequency on the outboard side of a given magnetic surface. Within this bandwidth several weakly damped resonator modes can be found. The modes experience strong poloidal localization (ranging from 10 to 50 degrees) about the midplane. The spatial amplification of resonator modes driven by energetic, fusion-born alpha particles has been considered. The alpha particles are modeled using a ring distribution, which is relevant to the post-birth phase of the alpha particles before collisional relaxation occurs. It is determined that such a ring distribution can effectively couple energy into shear Alfvén modes, resulting in roughly three e-foldings of amplification in one pass through the resonator.

A preliminary assessment of the effects caused by magnetic shear has been made The primary effect is the increase in the value of the perpendicular wave number as the shear Alfvén wave propagates along the resonator. Under cold plasma conditions, this effect prevents energy transfer to the compressional mode, and, in a sense, provides for a more robust resonator. But it is found that such behavior pertains to ion temperatures below 2.8 keV. For larger ion temperatures, the magnetic shear causes the Alfvén wave to couple to an ion-Bernstein mode. This in turn lengthens the resonator and reduces the reflection efficiency. The increase in the value of $k_\perp$ also can increase the damping along the propagation path, although this effect may be offset somewhat by the decrease of $k_{||}$ as the wave approaches the cut-off point. The instability drive by the alpha particles can also be affected by the variations in $k_\perp$. This can lead to spatial tuning and detuning of the wave resonance with the alpha particle population, possibly reducing the amplification factors reported.

In summary, the presence of an ion-ion hybrid Alfvén resonator has unique signatures that may be sampled in future burning plasma experiments. The results of this investigation provide clear guidelines for comprehensive studies of related phenomena (e.g., plasma

rotation, alpha channeling) that should be based on advance computational techniques that expand on the present frontier RF codes such as AORSA [21] and TORIC [68].

CHAPTER 5

Cherenkov radiation of shear waves

The excitation of shear Alfvén waves by energetic particles is a phenomenon that can occur naturally in space plasmas as well as in magnetically confined fusion devices. It has been shown that fast electron bursts occurring in the auroral ionosphere can be generated by interactions with time-varying, localized potential structures [69]. Further, fast particle bursts have been measured in the magnetosphere even during magnetically quiet periods [70]. In a tokamak environment, the fusion process produces energetic alpha particles. In each of these cases, the fast particles can directly radiate energy in the form Alfvén waves through the Cherenkov process. This mechanism enhances the level of the ambient magnetic fluctuations and contributes to the slowing down of the fast particles. In basic laboratory experiments, energetic particle bursts can be generated by the ablation of solid targets with powerful laser pulses [71] and the ensuing emission of waves can be investigated. The controlled injection of ion beams into tokamaks and basic magnetized devices [72] can also result in Cherenkov radiation of shear Alfvén waves.

A previous theoretical investigation [50] evaluated the emission of shear Alfvén waves in a single species plasma. That earlier study was motivated by a basic laboratory experiment [73] in which an electron burst arises from the nonlinear absorption [74] of a powerful pulse of high frequency electromagnetic waves. In those studies, it is found that, in the inertial regime of wave propagation, the wake pattern of the resulting Cherenkov radiation exhibits an inverted V-shape due to the backward-propagating nature of the shear Alfvén waves, i.e., the perpendicular group velocity is in the opposite direction to the perpendicular phase velocity of the wave. Another predicted feature is the clustering of the radiation around the ion-cyclotron frequency. Further, no radiation is emitted for particles moving faster than the

Alfvén speed. In the kinetic regime, the wake exhibits the familiar Cherenkov cone pattern so long as the particles do not travel faster than the Alfvén speed. However, when the particles exceed the Alfvén speed, field-aligned current channels develop in the wake. This is largely due to the natural exclusion of low perpendicular wave numbers from the radiated signal.

The work presented here differs from these previous studies in that a second ion species is included in the model. This introduces an upper frequency propagation band, as discussed previously, as well as the presence of the ion-ion hybrid frequency. With the inclusion of a second ion species, the lower branch exhibits all of the same characteristics determined by the prior single species studies. The upper branch, however, differs in that it always allows for the Cherenkov condition to be met. This allows for radiation in the inertial regime even when the particle exceeds the Alfvén speed. Further, when considering the kinetic regime, the current filaments present in the lower branch signal due to a particle exceeding the Alfvén speed are overwhelmed by the signal radiated in the upper branch.

This chapter is organized as follows. Section 5.1 summarizes the previous model [50] of Cherenkov emission by a field-aligned, charged particle burst. It is reproduced here for logical continuity and convenience as the details are especially relevant to the remainder of this chapter. Section 5.2 illustrates the properties of the waves in the inertial regime, and section 5.3 illustrates the properties in the adiabatic regime. Displays are made for conditions relevant to LAPD to assist in the interpretation of possible future experiments. Section 5.4 gives the results of radiation for a point particle for parameters relevant to LAPD in the inertial regime and relevant to ITER in the adiabatic regime. A discussion of the results from this chapter is presented in section 5.5.

5.1 Formulation

Although this formulation has been presented elsewhere [50], the details are especially pertinent to the results in the remainder of the Chapter. In this formulation, the plasma is considered to be spatially uniform and infinite in extent. The confining magnetic field is

placed along the z-axis of a Cartesian coordinate system (x, y, z). A charged particle burst is modeled as an external source, removing any feedback of the plasma on the particle burst. The burst is taken to travel predominantly along the z-axis so that it couples most strongly to the shear wave. The burst is assumed to travel with sufficient speed that collisions with the background plasma are negligible, and for this reason, the speed of the burst is taken to be constant. In reality, the burst will lose energy due to a radiative reaction, but such effects should be small, and could, in principle, be treated perturbatively. With these assumptions in mind, the charged particle burst is modeled as

$$\mathbf{j}_S = vqN_b \frac{1}{\pi d_\perp^2} \exp\left(-\frac{x^2+y^2}{d_\perp^2}\right) \delta\left(z - vt\right) \hat{\mathbf{z}}. \tag{5.1}$$

Here, v is the speed of the burst, q is the charge of an individual particle, and N_b is the number of particles associated with the burst. A Gaussian spatial profile with spread $d_\perp$ is specified in the transverse direction in order that the burst be spatially localized and for theoretical simplification. A delta function is used to specify the z dependence in order to ensure that all of the charges travel at the same speed. This results in spatial and temporal coherence of the emitted radiation. The formulation could be extended to include the possibility of a distribution of charged particles, with variation both in momentum and position. This would result in loss of coherence in the resulting signals and would have direct relevance to noise levels in a burning plasma, but this calculation is not performed here.

To find the resulting radiation, Maxwell's equations must be solved with the source current given in Eq. (5.1). This is most easily done through the use of Fourier transforms. For a generic quantity, $f(\mathbf{r}, t)$, the relation to its transform is

$$\tilde{f}(\mathbf{k}, \omega) = \int f(\mathbf{r}, t) e^{-i(\mathbf{k}\cdot\mathbf{r} - \omega t)} d\mathbf{r} dt, \tag{5.2}$$

$$f(\mathbf{r}, t) = \int \tilde{f}(\mathbf{k}, \omega) e^{i(\mathbf{k}\cdot\mathbf{r} - \omega t)} \frac{d\mathbf{k} d\omega}{(2\pi)^4}. \tag{5.3}$$

In this Fourier representation, the plasma current density response due to the source is included in the dielectric tensor, and upon solving for the electric field in Maxwell's equations, the following equation results

$$(k_i k_j - k^2 \delta_{ij} + k_0^2 \varepsilon_{ij}) \tilde{E}_j = -\frac{4\pi i \omega}{c^2} (\tilde{\mathbf{j}}_S)_i. \tag{5.4}$$

Here, as before, $k_0 = \omega/c$ and ε_{ij} is the ij component of the plasma dielectric tensor. The Fourier transform of the source current is given by

$$\tilde{\mathbf{j}}_S = 2\pi v q N_b e^{-\frac{k_\perp^2 d_\perp^2}{4}} \delta(\omega - k_{||} v - i\nu)\hat{z}. \tag{5.5}$$

A small imaginary part has been included in the argument of the delta function. This implies that the fields vanish as $t \to -\infty$. This ensures that causality is not violated and yields convergent integrals when inverting the Fourier transform. In performing contour integrals later, $\nu \to 0$ so that the final result is independent of this parameter. The wave vector is decomposed into components parallel to the confining magnetic field, $k_{||} = k_z$, and perpendicular to the magnetic field, $k_\perp = \sqrt{k_x^2 + k_y^2}$. Solving Eq. (5.4) requires inversion of the operator acting on $\tilde{\mathbf{E}}$ and inverting the Fourier transform by performing the necessary integrations. As will be shown, two integrals can be performed analytically with the remaining integral performed numerically.

In order to proceed, it is necessary to specify the precise form of the dielectric tensor. Since the focus is on shear Alfvén waves, the off-diagonal component, ε_{xy} is neglected. With this choice, upon solving for the Fourier amplitude of the electric field,

$$\tilde{\mathbf{E}} = -\frac{4\pi i\omega}{c^2}\frac{k_{||}}{D(\mathbf{k},\omega)}\mathbf{h}, \tag{5.6}$$

$$\mathbf{h} = \begin{pmatrix} k_x \\ k_y \\ (k_{||}^2 - k_0^2\varepsilon_\perp)/k_{||} \end{pmatrix}, \tag{5.7}$$

$$D(\mathbf{k},\omega) = -k_0^2\left(k_0^2\varepsilon_\perp\varepsilon_{||} - k_\perp^2\varepsilon_\perp - k_{||}^2\varepsilon_{||}\right). \tag{5.8}$$

From Faraday's law, the Fourier amplitude of the magnetic field is

$$\tilde{\mathbf{B}} = -\frac{4\pi i}{c}\frac{\varepsilon_\perp}{k_0^2\varepsilon_\perp\varepsilon_{||} - k_\perp^2\varepsilon_\perp - k_{||}^2\varepsilon_{||}}\tilde{j}_{S,z}\mathbf{k}\times\hat{\mathbf{z}}. \tag{5.9}$$

Because of the azimuthal symmetry of the field-aligned source given by Eq. (5.1), the source only excites the azimuthal component of the magnetic field, B_ϕ with B_r and B_z vanishing. For this reason, it is useful to express the magnetic field in terms of cylindrical coordinates, (r,ϕ,z). In the cylindrical representation, $\tilde{B}_x = \tilde{B}_r$ and $\tilde{B}_y = \tilde{B}_\phi$ when $y = 0$, and since the

radial and azimuthal components of the wave magnetic field are independent of the azimuthal angle, the variable x can be replaced by r in the resulting expressions. Representing the wave vector in cylindrical coordinates yields, $k_x = k_\perp \cos\alpha$ and $k_y = k_\perp \sin\alpha$ where α is the azimuthal angle of the wave vector. When inverting the Fourier transform, the integral over α can be performed independently of either the form of the dielectric tensor, or the specific type of source. This property leads to the following integral over α which is readily evaluated to

$$\int_0^{2\pi} e^{ik_\perp r\cos\alpha} \begin{pmatrix} \sin\alpha \\ \cos\alpha \end{pmatrix} d\alpha = 2\pi i \begin{pmatrix} 0 \\ 1 \end{pmatrix} J_1(k_\perp r). \tag{5.10}$$

Performing this integral leads to the following expression for B_ϕ

$$B_\phi = -\frac{1}{2\pi^2 c}\int k_\perp^2 dk_\perp dk_{||} d\omega \frac{\varepsilon_\perp J_1(k_\perp r) e^{i(k_{||}z-\omega t)}}{k_0^2\varepsilon_\perp\varepsilon_{||} - k_\perp^2\varepsilon_\perp - k_{||}^2\varepsilon_{||}} \tilde{j}_{S,z}. \tag{5.11}$$

Since in the sections that follow, the plasma wake is displayed through contour plots of the z-component of the plasma current density, an expression for this quantity is obtained through Ampère's law. The displacement current is negligible for the frequencies of interest. For this reason, in regions away from the source current, the plasma current density can be expressed as

$$\mathbf{j}_p = \frac{c}{4\pi}\nabla \times \mathbf{B}. \tag{5.12}$$

Substituting the result of Eq. (5.11) into the above expression results in

$$j_z = -\frac{1}{8\pi^3}\int k_\perp^3 dk_\perp dk_{||} d\omega \frac{\varepsilon_\perp J_0(k_\perp r) e^{i(k_{||}z-\omega t)}}{k_0^2\varepsilon_\perp\varepsilon_{||} - k_\perp^2\varepsilon_\perp - k_{||}^2\varepsilon_{||}} \tilde{j}_{S,z}. \tag{5.13}$$

5.2 Inertial Regime

The electrons are in the inertial regime if $\omega/k_{||} \gg \bar{v}_e$ where $\bar{v}_e$ is the electron thermal speed. Due to the presence of the delta function Eq. (5.5), this condition is met if the burst speed is much larger than the electron thermal speed, $v \gg \bar{v}_e$. In this limit, the parallel component of the dielectric tensor can be approximated by Eq. (2.18), and for the case of relatively cold ions, the perpendicular dielectric can be approximate by Eq. (1.1). Without loss of generality, the frequency ordering is assumed to be $\Omega_2 > \Omega_1$ or $m_2 < m_1$. Further,

the plasma density and magnetic field are assumed to be large enough that the following frequency ordering is assumed to hold: $\omega < \Omega_2 \ll \omega_{pi} \ll \omega_{pe}, \Omega_e$.

It is useful to introduce the following dimensionless quantities: $w = \omega/\Omega_1$, $a = k_\perp \delta_e$, $\kappa = k_{||} v_A/\Omega_1$, $\mu = \Omega_2/\Omega_1$, $\sigma = \omega_{ii}/\Omega_1$, $t' = \Omega_1 t$, $z' = \Omega_1 z/v_A$, $r' = r/\delta_e$, and $u = v/v_A$, where $\delta_e = c/\omega_{pe}$. Upon substitution of these definitions into Eq. (5.11),

$$B_\phi = -\frac{\Omega_1^2}{2\pi^2 c\delta_e v_A}\int da d\kappa dw\, a^2 \frac{\left(1-\frac{w^2}{\sigma^2}\right) J_1(ar') e^{i(\kappa z' - wt')}}{\frac{\kappa^2}{w^2}(1-w^2)\left(1-\frac{w^2}{\mu^2}\right) - (1+a^2)\left(1-\frac{w^2}{\sigma^2}\right)} \tilde{j}_{S,z}, \tag{5.14}$$

$$\tilde{j}_{S,z} = 2\pi \frac{v_A q N_b}{\Omega_1} u e^{-\frac{a^2 d_\perp^2}{4\delta_e^2}} \delta(w - \kappa u - i\nu'). \tag{5.15}$$

Before evaluating the integrals, it is useful to first understand the poles of the integrand, which are associated with the dispersion relation of the waves. From Eq. (5.14), it is seen that the values of w and κ must simultaneously satisfy the relations

$$\frac{w}{\kappa} = u, \tag{5.16}$$

$$\frac{\kappa^2}{w^2}(1-w^2)\left(1-\frac{w^2}{\mu^2}\right) - (1+a^2)\left(1-\frac{w^2}{\sigma^2}\right) = 0. \tag{5.17}$$

Solving this system of equations for κ yields two solutions. One solution corresponds to a propagating wave with frequency smaller than Ω_1, while the other is in the frequency range $\omega_{ii} < \omega < \Omega_2$. The solutions are

$$\kappa_\pm^2 = \frac{1}{2}\left(\beta_s \pm |\beta_s|\sqrt{1+\frac{4\beta_0}{\beta_s^2}}\right), \tag{5.18}$$

with

$$\beta_s = \frac{1}{u^2}(\mu^2+1) - \frac{\mu^2}{\sigma^2}(1+a^2), \tag{5.19}$$

$$\beta_0 = \frac{\mu^2}{u^2}(1+a^2) - \frac{\mu^2}{u^4}. \tag{5.20}$$

It can be shown algebraically that since $1 < \sigma < \mu$, the discriminant is always positive. Further, it can be shown that κ_+^2 is always positive and that κ_-^2 is positive provided that

$$a < a_M = \mathrm{Re}\sqrt{\frac{1}{u^2} - 1}. \tag{5.21}$$

These proofs are outlined in Sec. 5.3 for the adiabatic regime, and a similar proof is applicable here. Figure 5.1 illustrates the physical meaning of the two solutions for helium-hydrogen mixture and parameters typical of experiments that can be performed in the LAPD. The vertical and horizontal axes correspond to κ and w, respectively. The solid straight line represents Eq. (5.16) for $u = 0.5$; it corresponds to the Cherenkov condition that the phase velocity of the wave match the speed of the burst. The single dashed curves correspond to Eq. (5.17) for a value of "a" that satisfies the condition of Eq. (5.21). It is seen that there are two intersections between these curves and the solid straight line. These intersections are the two values represented in Eq. (5.18); the negative root corresponds to intersection at a smaller scaled frequency, and the positive root, to a larger scaled frequency. The dot-dashed curves are, again, Eq. (5.18), but now for a value of the parameter "a" that violates Eq. (5.21). Here, the intersection at higher frequency is seen, but the intersection at lower frequency is not possible. A solution exists for which κ_- is purely imaginary, but this corresponds to an evanescent signal and would not exhibit Cherenkov radiation.

Figure 5.2 complements Fig. 5.1 by illustrating possible solutions for various burst velocities in the range $0.3 \leq u \leq 0.7$. As u decreases, it is apparent that the solutions move closer to the respective cyclotron frequencies, especially for the smaller values of "a" (which is expected due to the radial envelope of the source). For $u = 0.3$, a clustering of the radiated frequencies occurs near the cyclotron frequencies of both species; the signal generated exhibits beating between these two freqeucneis, as shown below. If the source is sharply peaked radially, then large values of "a" admit Cherenkov solutions with frequencies close to the ion-ion hybrid frequency. This is explored in Sec. 5.4, where the wake due to a single alpha particle for conditions anticipated in the ITER device is considered.

With the understanding of the expected properties of the wave features, Eq. (5.14) can be evaluated. The integral over frequency is easily performed due to the delta function, with the imaginary part in the argument of the delta function considered to be vanishingly small at this stage. The finite imaginary part causes the poles to move away from the real axis in such a manner as to preserve causality. Upon performing the frequency integral, the

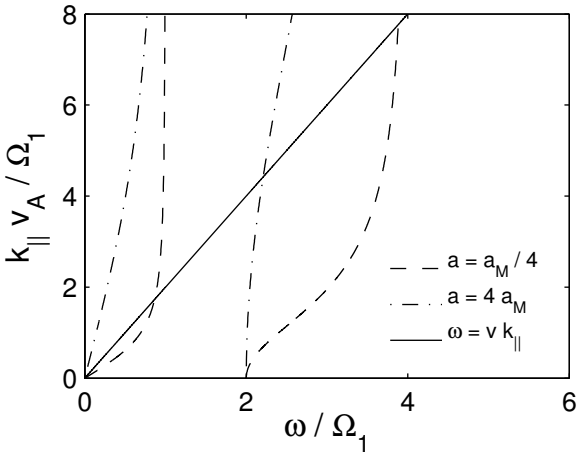

Figure 5.1: Constraints on Cherenkov radiation in the inertial regime. Vertical axis is the scaled wave number, κ, and horizontal axis, the scaled frequency, w as defined above Eq. (5.14). The solid, straight line corresponds to Eq. (5.16) and reflects the wave-particle resonance condition for a value of $v/v_A = 0.5$. The broken curves correspond to the two branches of the dispersion relation of the inertial mode in Eq. (5.17) for a 50% H+, 50% He+ plasma, for two values of the transverse width "a." The upper frequency branch always possesses a real solution, but the lower branch only yields a real solution if $a < a_M = \sqrt{1/u^2 - 1}$. $\omega/\Omega_1 = 1$ is the helium cyclotron frequency, $\omega/\Omega_1 = 2$, the ion-ion hybrid frequency, and $\omega/\Omega_1 = 4$, the hydrogen cyclotron frequency.

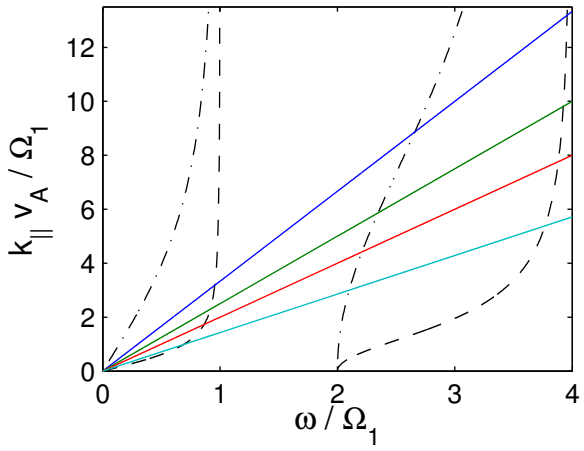

Figure 5.2: Range of intercepts leading to Cherenkov radiation. The blue line is for $u = 0.3$, green $u = 0.4$, red $u = 0.5$, and cyan $u = 0.7$. The black curves are the same as in Fig. 5.1. As u decreases and at smaller perpendicular wave numbers, the radiative solutions cluster around the individual cyclotron frequencies.

expression for the magnetic field becomes

$$B_\phi = -\frac{qN_b\Omega_1}{\pi c\delta_e}\frac{\mu^2}{u}\int da d\kappa\, a^2 \frac{\left(1-\frac{\kappa^2u^2}{\sigma^2}\right)J_1(ar')e^{-\frac{a^2d_\perp^2}{4\delta_e^2}}e^{i\kappa(z'-ut')}}{(\kappa^2-\kappa_+^2)(\kappa^2-\kappa_-^2)} \tag{5.22}$$

Next, the integral over κ is performed. This can be done by contour integration. A distinction must be made between the two cases, $z' - ut' < 0$ and $z' - ut' > 0$. For the former case, the contour is closed below the real axis, and for the latter case, above. Causality dictates that the pole due to κ_+ be treated as if it lies below the real axis. It only contributes to the integral when $z' - ut' < 0$, or for times after which the burst has passed the axial position considered. For times such that $z' - ut' > 0$, the pole is not enclosed by the contour, and thus, it does not contribute to the integral. The second root, κ_-, has the same properties for values of "a" that satisfy Eq. (5.21). For $a > a_M$, κ_- is purely imaginary and makes a contribution regardless of which direction the contour is closed. Upon completion of the

integral over κ, the magnetic field becomes

$$B_\phi = -2\frac{qN_b\Omega_1}{c\delta_e}\frac{\mu^2}{u}\left[\int_0^\infty da\, a^2 e^{-\frac{a^2 d_\perp^2}{4\delta_e^2}}\frac{\left(1-\frac{\kappa_+^2 u^2}{\sigma^2}\right)J_1(ar')\sin\left(\kappa_+(z'-ut')\right)}{\kappa_+\left(\kappa_+^2-\kappa_-^2\right)}\right.$$
$$+\int_0^{a_M} da\, a^2 e^{-\frac{a^2 d_\perp^2}{4\delta_e^2}}\frac{\left(1-\frac{\kappa_-^2 u^2}{\sigma^2}\right)J_1(ar')\sin\left(\kappa_-(z'-ut')\right)}{\kappa_-\left(\kappa_-^2-\kappa_+^2\right)} \tag{5.23}$$
$$\left.+\frac{1}{2}\int_{a_M}^\infty da a^2 e^{-\frac{a^2 d_\perp^2}{4\delta_e^2}}\frac{\left(1-\frac{\kappa_-^2 u^2}{\sigma^2}\right)J_1(ar')e^{|\kappa_-|(z'-ut')}}{\kappa_-\left(\kappa_-^2-\kappa_+^2\right)}\right], \qquad z'-ut'<0,$$

and

$$B_\phi = -\frac{qN_b\Omega_1}{c\delta_e}\frac{\mu^2}{u}\int_{a_M}^\infty da\, a^2 e^{-\frac{a^2 d_\perp^2}{4\delta_e^2}}\frac{\left(1-\frac{\kappa_-^2 u^2}{\sigma^2}\right)J_1(ar')e^{-|\kappa_-|(z'-ut')}}{\kappa_-\left(\kappa_-^2-\kappa_+^2\right)}, \qquad z'-ut'>0, \tag{5.24}$$

where the evanescent part of the response is included for completeness. This component of the signal has been previously examined [50], and it can be thought of as the magnetic analog of Debye shielding. Because the primary interest of this investigation is in the radiated signal, the evanescent portion is neglected in what follows.

In describing the wake pattern, it is illuminating to display the z-component of the plasma current density. This is given by Eq. (5.13), and its calculation is equivalent to replacing the Bessel function, $J_1(ar')$, in the magnetic response with the quantity, $J_0(ar')ac/4\pi\delta_e$. Figure 5.3 illustrates the wake found by numerical integration, for the values, $d_\perp/\delta_e = 3$, $u = 0.5$, $\sigma = 2$, and $\mu = 4$, corresponding to a hydrogen-helium plasma in LAPD. The color scale in the contour displays is normalized to the maximum amplitude of the signal. The charge burst is located at the origin and is moving upward at speed, v. The pattern is computed at $t = 0$, and for $t \neq 0$, the pattern simply translates with the charge. In addition to exhibiting the inverted-V pattern, as in the single species case, it is clear that two distinct waves are propagating and interfering with each other. Further, in addition to having different wavelengths and frequencies, the Cherenkov cone angle is different for each of the waves that make up the total signal. This is understood by examining the group velocity for shear Alfvén waves. The angle at which the group velocity propagates is given by $\tan\theta = v_{g\perp}/v_{g||} = -\partial k_{||}/\partial k_\perp$. This quantity can be evaluated from the dispersion relation

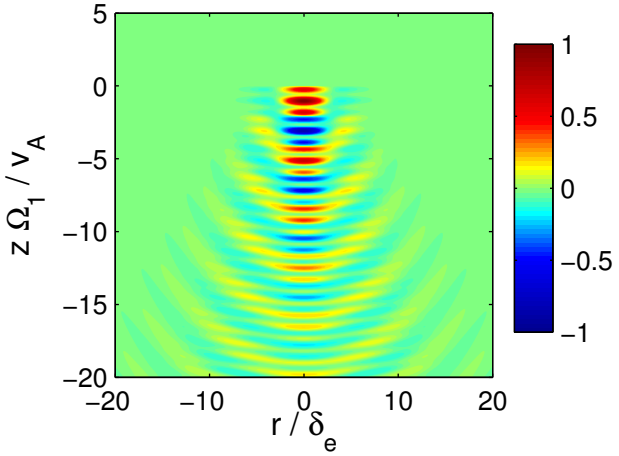

Figure 5.3: Wake radiated by a particle burst in the inertial regime. Spatial pattern of parallel current density $j_z/|j_z|_{\mathrm{Max}}$ for $d_\perp/\delta_e = 3$, $u = 0.5$, $\sigma = 2$, and $\mu = 4$. Color contours represent the current wake at $t = 0$ with the charge burst centered at the origin and moving upwards. Two separate patterns are clearly visible. The broader, longer wavelength pattern corresponds to the lower frequency branch and the narrower, shorter wavelength pattern, to the upper branch.

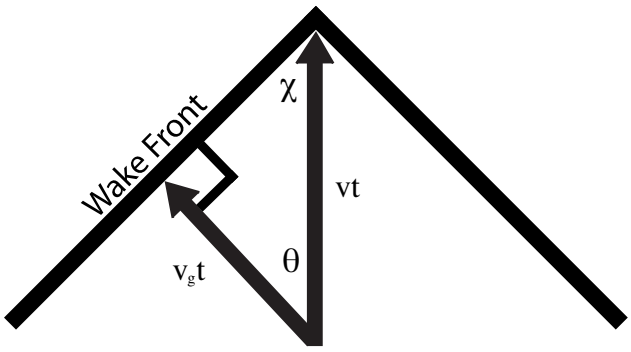

Figure 5.4: Relationship between angle formed by group velocity, θ, and the cone angle of the Cherenkov emission, χ. A signal is excited in the plasma after the charge passes by. As θ increases, χ decreases. This explains the two cone angles visible in Fig. 5.3.

in Eq. (5.8). In the inertial regime, the corresponding angle is given by

$$\tan\theta = -\frac{k_\perp k_{||}\delta_e^2}{1+k_\perp^2\delta_e^2}, \tag{5.25}$$

or in terms of scaled quantities,

$$\tan\theta' = \frac{v_A}{\delta_e\Omega_1}\tan\theta = -\frac{a\kappa}{1+a^2}. \tag{5.26}$$

From Fig. 5.1 and Eq. (5.18), it is clear that $\kappa_+ > \kappa_-$ for a given value of "a." This implies that the group velocity angle is much larger for the higher frequency band than for the lower one. Schematically, the resulting situation is illustrated in Fig. 5.4. Geometrically, the cone angle of the radiation, χ, is related to the angle formed by the group velocity by $\chi = \pi/2 - \theta$. Thus, for a larger angle, θ, the cone angle, χ, is smaller as shown in Fig. 5.3.

The temporal signature of the radiated magnetic field shown in Fig. 5.3, obtained by evaluating Eq. (5.23) at a fixed spatial position, is shown in Fig. 5.5(a). Time, $t = 0$, corresponds to the burst being located at the same axial position at which the field is sampled. The radial position is $r' = 10$, chosen to allow for sufficient temporal separation between the two components of the signal. The displayed signal is normalized to its peak value. It is seen from Fig. 5.5(a) that the lower frequency component arrives first and the larger frequency component arrives later. This feature is primarily due to the larger cone angle exhibited by the lower frequency propagation band. Figure 5.5(b) displays the power

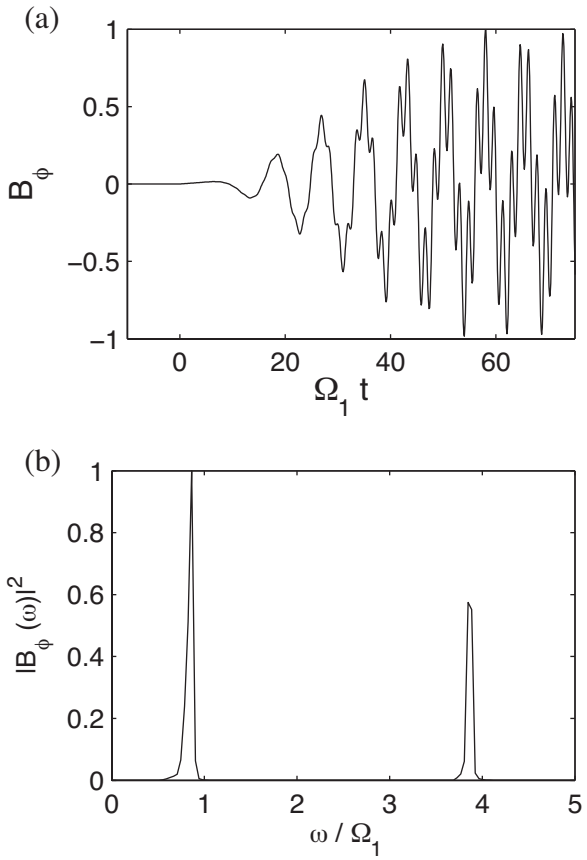

Figure 5.5: Temporal signature of the magnetic field corresponding to the wake pattern of Fig. 5.3 at a fixed radial position, $r/\delta_e = 10$. (a) Time dependence of the magnetic field normalized to its peak value. The arrival of the source at the same axial position of the location sampled corresponds to $t = 0$. The lower frequency arrives sooner than the upper frequency due to the difference in cone angles, as illustrated in Fig. 5.4. (b) Power spectrum normalized to the peak value. Two frequency bands are clearly visible just below the individual cyclotron frequencies.

spectrum of the time signal in Fig. 5.5(a), again normalized to its peak value. The radiated frequencies are clustered close to the cyclotron frequencies of the individual ion species. This is due to the associated increase in traverse group velocity as the cyclotron frequency is approached, in accordance with Eq. (5.25). The relative amplitude of the power that appears into the lower and higher frequency components, however, depends on the radial position sampled. At small radial positions, the higher frequency spectral peak is dominant.

5.3 Adiabatic Regime

In the extreme kinetic regime, the burst speed is considered to be much smaller than the electron thermal speed, $v \ll \bar{v}_e$, while all other assumptions made in the analysis of the inertial regime are presumed to remain valid. In this limit, the parallel dielectric coefficient is approximated by

$$\varepsilon_{||} \Rightarrow \frac{\omega_{pe}^2}{k_{||}^2 \bar{v}_e^2}, \tag{5.27}$$

while the perpendicular dielectric coefficient, $\varepsilon_\perp$, remains as in Eq. (1.1) (i.e. kinetic effects are negligible for the ions). The cold ion contribution is neglected in Eq. (5.27), which eliminates the ion-acoustic wave from the dispersion relation. This is a valid approximation when the speed of the source is much greater than the ion-acoustic speed, c_s. Further, to neglect the coupling between the Alfvén and acoustic modes, it is assumed that $v_A \gg c_s$ which is appropriate for low-beta plasmas. If either of these conditions is violated, the ion contribution must be retained in Eq. (5.27) in order to properly include the ion-acoustic wave in the formulation.

The same methodology used in the inertial case, given in Sec. 5.2, applies here. All quantities are scaled as before with the exception of the radial variable. Here, the relevant radial scale is the ion-sound gyro radius, $\rho_s = c\bar{v}_e/v_A\omega_{pe}$. Accordingly, the scaled transverse direction becomes $r' = r/\rho_s$ and $b = k_\perp \rho_s$. With these scaled quantities and the adiabatic

expression for the parallel dielectric, Eqs. (5.5) and (5.11) become

$$B_\phi = -\frac{\Omega_1^2}{2\pi^2 c\rho_s v_A}\int dbd\kappa dw\, b^2 \frac{\left(1-\frac{w^2}{\sigma^2}\right)J_1(br')e^{i(\kappa z'-wt')}}{\left(\frac{w^2}{\kappa^2}-b^2\right)\left(1-\frac{w^2}{\sigma^2}\right)-(1-w^2)\left(1-\frac{w^2}{\mu^2}\right)}\tilde{j}_{S,z}, \tag{5.28}$$

$$\tilde{j}_{S,z} = 2\pi\frac{v_A q N_b}{\Omega_1} u e^{-\frac{b^2 d_\perp^2}{4\rho_s^2}}\delta(w-\kappa u - i\nu'). \tag{5.29}$$

As before, the solution is determined by the poles associated with the dispersion relation. In analogy with Eqs. (5.16) and (5.17), the poles are now determined by the relations

$$\frac{w}{\kappa} = u, \tag{5.30}$$

$$\left(\frac{w^2}{\kappa^2}-b^2\right)\left(1-\frac{w^2}{\sigma^2}\right)-\left(1-w^2\right)\left(1-\frac{w^2}{\mu^2}\right)=0, \tag{5.31}$$

which yield two solutions, $\kappa_\pm$, that take the same form as Eq. (5.18), but with the new definitions for β_s and β_0,

$$\beta_s = \frac{1}{u^2}\left(1+\mu^2-\frac{\mu^2}{\sigma^2}\left(u^2-b^2\right)\right), \tag{5.32}$$

$$\beta_0 = \frac{\mu^2}{u^4}\left(u^2-1-b^2\right). \tag{5.33}$$

As in the inertial case, the discriminant is always positive. To prove this, first observe that the discriminant can only be negative if $\beta_0 < 0$. With this restricting in mind, and recalling that $1 < \sigma < \mu$

$$\beta_s^2 = \frac{1}{u^4}\left(1+\mu^2-\frac{\mu^4}{\sigma^2}\beta_0-\frac{\mu^2}{\sigma^2}\right)^2, \tag{5.34}$$

$$\beta_s^2 > \frac{1}{u^4}\left(1-\frac{u^4}{\sigma^2}\beta_0\right)^2 > \frac{1}{u^4}\left(1-u^4\beta_0\right)^2. \tag{5.35}$$

With this relation, it can be shown that $\beta_s^2+4\beta_0>0$ by the following inequalities,

$$\beta_s^2+4\beta_0 > \frac{1}{u^4}\left[\left(1-u^4\beta_0\right)^2+4u^4\beta_0\right] = \frac{1}{u^4}\left(1+u^4\beta_0\right)^2 > 0. \tag{5.36}$$

Next, it can be shown that κ_+ is always real. This can be seen by showing that if $\beta_s < 0$, then $\beta_0 > 0$. The former condition implies that $b^2 < u^2-(1+\mu^2)\,\sigma^2/\mu^2$. This relation leads to the condition that $\beta_0 > [(1+\mu^2)\,\sigma^2/\mu^2-1]\,\mu^2/u^4 > 1/u^4$, where the condition that $\sigma > 4$ has been used.

Examining next the condition on κ_-, it is seen that if $\beta_s < 0$, then κ_- is imaginary. If instead it is assumed that $\beta_s > 0$, then the condition that κ_- be real is equivalent to $\beta_0 < 0$. This leads to the condition that

$$b > b_M = \mathrm{Re}\sqrt{u^2 - 1}, \tag{5.37}$$

which is the same condition obtained for a single species plasma.

With an understanding of the poles in the integrand, the frequency integration in Eq. (5.28) yields

$$B_\phi = \frac{qN_b\Omega_1}{\pi c\rho_s}\frac{\mu^2}{u^3}\int dbd\kappa\, b^2 \frac{\left(1-\frac{\kappa^2u^2}{\sigma^2}\right)J_1(br')e^{-\frac{b^2d_\perp^2}{4\rho_s^2}}e^{i\kappa(z'-ut')}}{(\kappa^2-\kappa_+^2)(\kappa^2-\kappa_-^2)}. \tag{5.38}$$

The integrations over κ are next performed in the same manner as in Sec. 5.2 for the inertial regime to obtain

$$\begin{aligned} B_\phi = 2\frac{qN_b\Omega_1}{c\rho_s}\frac{\mu^2}{u^3}\Bigg[&\int_0^\infty db\, b^2 e^{-\frac{b^2d_\perp^2}{4\rho_s^2}}\frac{\left(1-\frac{\kappa_+^2u^2}{\sigma^2}\right)J_1(br')\sin\left(\kappa_+(z'-ut')\right)}{\kappa_+\left(\kappa_+^2-\kappa_-^2\right)} \\ &+\int_{b_M}^\infty db\, b^2 e^{-\frac{b^2d_\perp^2}{4\rho_s^2}}\frac{\left(1-\frac{\kappa_-^2u^2}{\sigma^2}\right)J_1(br')\sin\left(\kappa_-(z'-ut')\right)}{\kappa_-\left(\kappa_-^2-\kappa_+^2\right)}\Bigg], \qquad z'-ut'<0, \end{aligned} \tag{5.39}$$

in which the evanescent fields have been neglected. If included, they result in a form similar to those found in the inertial regime, shown in Eqs. (5.23) and (5.24). The remaining integrals are evaluated by numerical integration.

The wake patterns associated with the z-component of the plasma current density are illustrated in Fig. 5.6 for values of $u = 0.5$, 1.0, 1.5, and 2.0. The parameters are $\mu = 4$, $\sigma = 2$, and $d_\perp/\rho_s = 3$, corresponding to LAPD conditions. In each panel, the current density is normalized to the maximum amplitude in the contour. As before, the charge is located at the origin and is traveling upward with velocity, v. Figures 5.6(a) and 5.6(b) not only display, overall, the characteristic Cherenkov radiation pattern but also exhibit spatial interference between two modes with different wavelengths, corresponding to simultaneous excitation of the two propagation bands. Figure 5.6(c) shows that as the velocity of the burst increases beyond $u = 1$, a periodic array of field-aligned current filaments develops from the

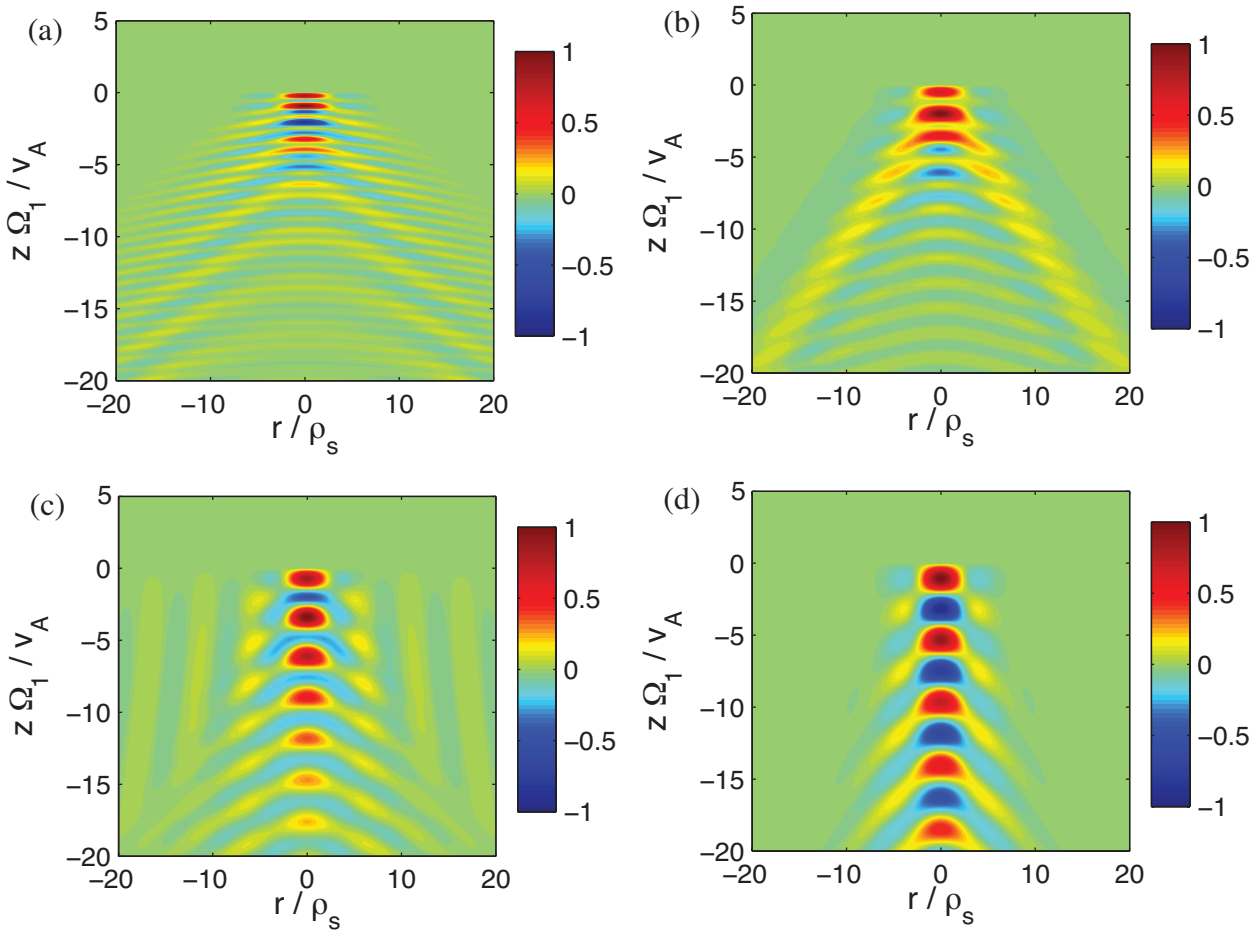

Figure 5.6: Wake radiated by a burst in the adiabatic regime. Spatial pattern of parallel current density $j_z/|j_z|_{\mathrm{Max}}$ for $d_\perp/\rho_s = 3$, $\sigma = 2$, and $\mu = 4$. From top to bottom, $u = 0.5$, 1.0, 1.5, and 2.0. The pattern of the lower branch transitions into the vertical pattern as u increases above one. This is most apparent in (c) for the $u = 1.5$ case. In (d), $u = 2.0$, the upper branch is dominant. The upper branch does not develop the current filament structure because it has no lower limit on the integral over $k_\perp$.

magnetic structure associated with the second integral in Eq. (5.39). This behavior is in agreement with the single-species result found previously [50]. The effect can be understood from Eq. (5.37), which reflects the fact that as u increases, the lower-branch is dominated by short perpendicular wavelengths. Also, when the limit of large u is considered, $\kappa_- \sim 2\sigma^2/u^2$, indicating that the parallel wavelength becomes large. However, the limiting spectral decrease in the source current, due to the assumed Gaussian radial shape of the burst, causes the signals with large values of "b" to become less significant, until the pattern becomes dominated by the first integral in Eq. (5.39). This is the reason why the field-aligned currents are no longer visible in Fig. 5.6(d) for $u = 2.0$, since the display format is normalized to the peak value. At these higher speeds, the pattern is dominated by the radiation of the higher frequency band, which does not develop filamentary structures.

5.4 Wake due to a point particle

To illustrate the Alfvénic wake produced by a point particle, two situations are considered; a fast particle propagating in LAPD with inertial electron response, and a fusion-born alpha particle propagating in ITER-like conditions for which the electrons exhibit an adiabatic response. In evaluating these two situations, all of the previously discussed concepts are appropriate. However, in this context the moving source (i.e. the fast particle) must be considered as a point source, and this can be modeled by taking $d_\perp \to 0$, in which the transverse Gaussian profile approaches a delta function. In this limit, care must be taken to ensure numerical convergence of the resulting integrals.

To illustrate the limiting pattern, the inertial regime is first considered. The z-component of the wave current becomes

$$j_{pz} = -\frac{qN_b\Omega_1}{2\pi\delta_e^2}\frac{\mu^2}{u}\left[\int_0^\infty da\, a^3 \frac{\left(1-\frac{\kappa_+^2u^2}{\sigma^2}\right)J_0(ar')\sin\left(\kappa_+(z'-ut')\right)}{\kappa_+ + (\kappa_+^2-\kappa_-^2)}\right.$$
$$\left. + \int_0^{a_M} da\, a^3 \frac{\left(1-\frac{\kappa_-^2u^2}{\sigma^2}\right)J_0(ar')\sin\left(\kappa_-(z'-ut')\right)}{\kappa_- + (\kappa_-^2-\kappa_+^2)}\right], \qquad z'-ut' < 0. \tag{5.40}$$

The second integral is easily performed numerically. To perform the first integral, the asymp-

totic form of the integrand must be examined. In the limit of large "a",

$$\kappa_-^2 \sim -\frac{\mu^2}{\sigma^2}a^2, \tag{5.41}$$

$$\kappa_+^2 \sim \frac{\sigma^2}{u^2} - \frac{\sigma^2}{u^4}\left(1 + \frac{\sigma^2}{4\mu^2}\left(\sigma^2 - 4\mu^2 - 4\right)\right)\frac{1}{a^2}. \tag{5.42}$$

If the numerically evaluated portion of the first integral in Eq. (5.40) is truncated at a value, $a_{\rm Max}$, that satisfies both $a_{\rm Max} \gg 1$ and $a_{\rm Max}r' \gg 1$, then for the asymptotic contribution, the Bessel function can also be replaced by its asymptotic form. In this case, the asymptotic portion of the first integral is proportional to

$$\begin{aligned}\int_{a_{\rm Max}}^{\infty} \frac{\cos(ar' - \pi/4)}{a^{3/2}}\,da = &-\frac{2\cos(a_{\rm Max}r' - \pi/4)}{\sqrt{a_{\rm Max}}} \\ &+ 2\sqrt{\pi r'}\left[S\left(\sqrt{\frac{2a_{\rm Max}r'}{\pi}}\right) - C\left(\sqrt{\frac{2a_{\rm Max}r'}{\pi}}\right)\right],\end{aligned} \tag{5.43}$$

where the functions, $C(x)$ and $S(x)$ are the Fresnel integrals

$$C(x) = \int_0^x \cos\left(\frac{\pi u^2}{2}\right)\,du, \qquad S(x) = \int_0^x \sin\left(\frac{\pi u^2}{2}\right)\,du. \tag{5.44}$$

Upon expanding the Fresnel integrals for large argument, Eq. (5.43) becomes

$$\int_{a_{\rm Max}}^{\infty} \frac{\cos(ar' - \pi/4)}{a^{3/2}}\,da \approx \frac{4\cos(a_{\rm Max}r' - \pi/4)}{\sqrt{a_{\rm Max}}} + O\left(\frac{1}{a_{\rm Max}^{3/2}}\right). \tag{5.45}$$

Thus, if $a_{\rm Max}$ is chosen such that the integrand (including the Bessel functions) is asymptotic and the leading order term in Eq. (5.45) vanishes, then the integral converges relatively quickly and the oscillatory part of the integral at infinity can be neglected. Similar results hold for the magnetic field with the leading order term of the asymptotic portion being proportional to $\cos(a_{\rm Max}r' - 3\pi/4)/a_{\rm Max}^{3/2}$.

Figure 5.7(a) illustrates the Cherenkov wake pattern for the single particle case in the inertial limit for a H-He mixture of equal concentrations, as can be realized in LAPD experiments. The general features seen earlier in Fig. 5.3 are present: there are two distinct patterns and the lower branch has a larger Cherenkov angle than the upper branch. However, Fig. 5.7(a) differs from Fig. 5.3 in that the wake pattern is dominated by the contributions from the upper frequency branch with the lower branch only barely visible just outside the

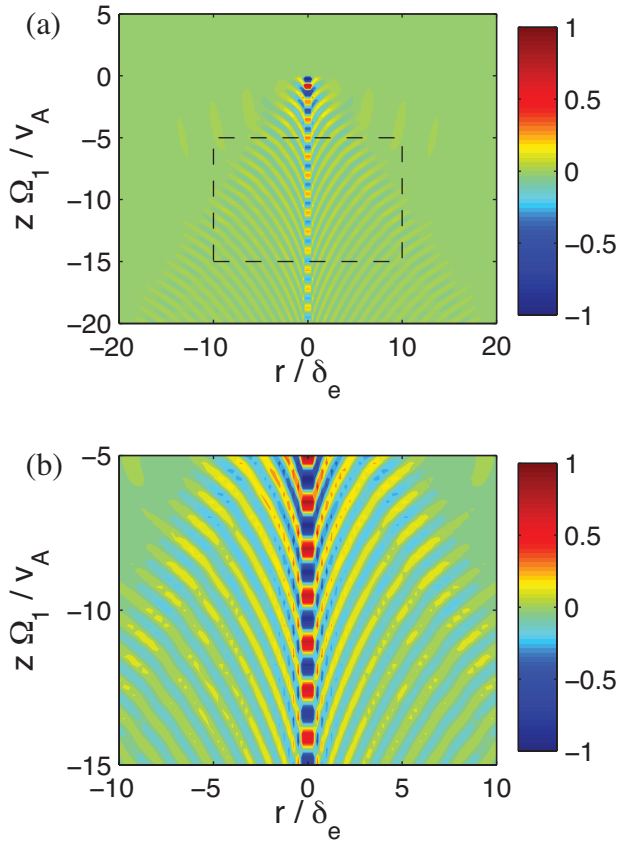

Figure 5.7: (a) Wake pattern in the inertial regime due to a single particle traveling at $u = 0.5$ in a background plasma of equal concentrations of hydrogen and helium. The dominant signal possesses a narrower cone angle and corresponds to the upper branch. The longer wavelength pattern with a larger Cherenkov cone angle corresponds to the lower branch and is barely visible. (b) Expanded view of region within dashed-line rectangle in (a).

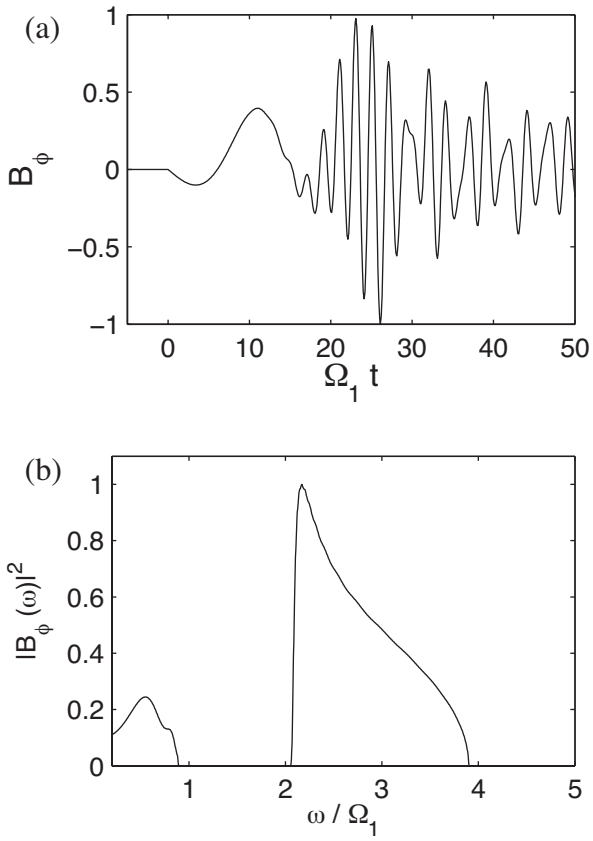

Figure 5.8: Temporal signature of the wake pattern of Fig. 5.7 at a fixed radial position, $r/\delta_e = 10$. (a) Magnetic field. (b) Power spectrum. The lower-branch signal arrives first, followed by the upper-branch, which starts around $t' = 15$. $\omega/\Omega_1 = 1$ is the helium cyclotron frequency, $\omega/\Omega_1 - 2$, the ion-ion hybrid frequency and $\omega/\Omega_1 = 4$, the hydrogen cyclotron frequency. A clear frequency separation between the upper and lower band is apparent.

cone of the upper branch, as seen in Fig. 5.7(b), which is a blow-up of the region bounded by the dashed rectangle in Fig. 5.7(a), and locally normalized to the peak value. To further illustrate these differences, Fig. 5.8 shows the temporal evolution of the magnetic field at radial position $r' = 10$, readily comparable to Fig. 5.5. In the top panel, the signal is again normalized to the peak value, and in the bottom panel, the frequency spectrum is normalized to the peak value in the upper frequency branch. From Fig. 5.8(a), it is apparent that the upper branch does not arrive until roughly $t' \approx 15$. Although not evident from the figure, the signal associated with the upper band chirps, wherein the signal starts at a frequency close to the hydrogen cyclotron frequency, and gradually approaches the ion-ion hybrid; this is due to the narrowing of the Cherenkov cone-angle at frequencies close to the ion-ion hybrid frequency. In Fig. 5.8(b) it is seen that there is a much larger frequency spread than in Fig. 5.5. This effect is mainly caused by the contribution of larger transverse wave numbers, which allows solutions to the Cherenkov matching condition at frequencies away from the cyclotron frequencies. The clustering of the spectrum around the cyclotron frequency is less apparent for the lower branch than it is for the Gaussian beam case. For the upper branch, the radiated signals now extend from the ion-ion hybrid frequency to the ion cyclotron frequency.

Next, it is useful to illustrate the Cherenkov radiation by fusion-born alpha particles in ITER. In the fusion environment expected for ITER, the thermal speed of 10 keV electrons is $\bar{v}_e = 4 \times 10^9$ cm/s, and the initial speed of a 3.5 MeV alpha particle, $v_\alpha = 1.3 \times 10^9$ cm/s. The Cherenkov condition is that the parallel phase velocity of the wave be equal to the velocity of the particle considered. With these conditions, the kinetic, parallel dielectric is

$$\epsilon_{||} \approx -\frac{\omega_{pe}^2}{2\bar{v}_e^2} Z' \left(\frac{v_\alpha}{\sqrt{2}\bar{v}_e k_{||}^2} \right), \tag{5.46}$$

where $Z'(x)$ is the derivative of the plasma dispersion function. For relevant parameters, the argument of the plasma dispersion function is on the order of 0.1, placing the electron response in the adiabatic regime, i.e., $Z' \sim -2$. Furthermore, as the alpha particle slows down, the adiabatic approximation is better satisfied.

Taking the same point-charge limit as in the inertial regime, the wave current is described by the relation,

$$j_{pz} = \frac{qN_b\Omega_1}{2\pi\rho_s^2}\frac{\mu^2}{u^3}\left[\int_0^\infty db\, b^3 \frac{\left(1-\frac{\kappa_+^2u^2}{\sigma^2}\right)J_0(br')\sin\left(\kappa_+(z'-ut')\right)}{\kappa_+\left(\kappa_+^2-\kappa_-^2\right)}\right.$$
$$\left. + \int_{b_M}^\infty db\, b^3 \frac{\left(1-\frac{\kappa_-^2u^2}{\sigma^2}\right)J_0(br')\sin\left(\kappa_-(z'-ut')\right)}{\kappa_-\left(\kappa_-^2-\kappa_+^2\right)}\right], \qquad z'-ut'<0. \tag{5.47}$$

Again, the asymptotic regime of the integral is considered. In the limit of large "b",

$$\kappa_+^2 \sim \frac{\mu^2}{u^2\sigma^2}b^2, \tag{5.48}$$

$$\kappa_-^2 \sim \frac{\sigma^2}{u^2} - \frac{\sigma^4}{\mu^2u^2}\left(1+\mu^2-\frac{\mu^2}{\sigma^2}u^2-\sigma^2\right)\frac{1}{b^2}. \tag{5.49}$$

The second integral is amenable to the same type of analysis as done in the inertial regime, and the same results apply. The first integral is more problematic. The asymptotic form of this integral is proportional to

$$\int_{b_{\rm Max}}^\infty b^{3/2}\cos\left(br'-\pi/4\right)\sin\left(\frac{\mu}{u\sigma}\left(z'-ut'\right)b\right)db. \tag{5.50}$$

From the form of this integral, it is clear that it is not convergent. From Eq. (5.50), it is apparent that the frequencies of the waves associated with the divergence are, $w=\mu b/\sigma$, which increase without limit. This is unphysical and reflects the neglect of the displacement current in the expression for the perpendicular dielectric. The equivalent expression in the analysis for the one-species plasma [50] shares this same divergent property, which shows that it is not a multi-ion effect. The breakdown in the formulation results from trying to extend the integration to frequencies above the cyclotron frequency of the lighter ion species. At these higher frequencies the dispersion relation used to explicitly isolate the shear Alfvén mode (i.e., Eq. (5.8)) is not valid. To rectify this limitation, a low-pass filter function is introduced that isolates the contribution from shear Alfvén waves in the integration over "b" in Eq. (5.47). A filter function possessing the desired properties is

$$f(b) = \frac{1}{1+\exp\left(\frac{b-\zeta}{\xi}\right)}. \tag{5.51}$$

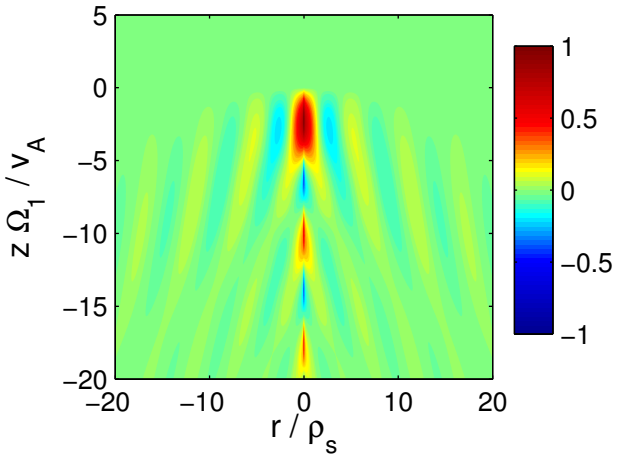

Figure 5.9: Wake pattern in the adiabatic regime due to a single charge traveling at 1.5 times the Alfvén speed. Background plasma consists of equal concentrations of deuterium and tritium, a situation analogous to a fusion-born alpha particle traveling parallel to the magnetic field in ITER. The parallel wave current along the field line is shown, normalized to its peak value. The pattern exhibits the type of filamentary structure shown in Fig. 5.6(c) for a charge burst.

Here, ζ is the value of "b" that satisfies the equation, $\kappa_+ u = \mu$, which corresponds to the frequency at which $\omega = \Omega_2$. Also, the parameter, ξ, determines the sharpness of the filter. In order to have a reasonably sharp filter, the value $\xi = 0.01$ is used in performing the numerical integration.

Figure 5.9 displays the wave current along the confinement magnetic field for a background plasma of equal D-T concentration, corresponding to $\mu = 1.5$ and $\sigma = \sqrt{1.5} \approx 1.22$. The source particle is traveling at 1.5 times the Alfvén speed. The wake pattern displays the type of current filaments seen earlier in Fig. 5.6(c); this is a consequence of the lower cutoff of the lower band. The contribution from the upper frequency band results in a slight bending of the current filaments.

Figure 5.10 shows the corresponding temporal evolution of the magnetic field at a position $r/\rho_s = 10$ from the trajectory of the particle. Time $t = 0$ corresponds to the particle passing the axial position of this location. The signal in Fig. 5.10(a) is normalized to its peak

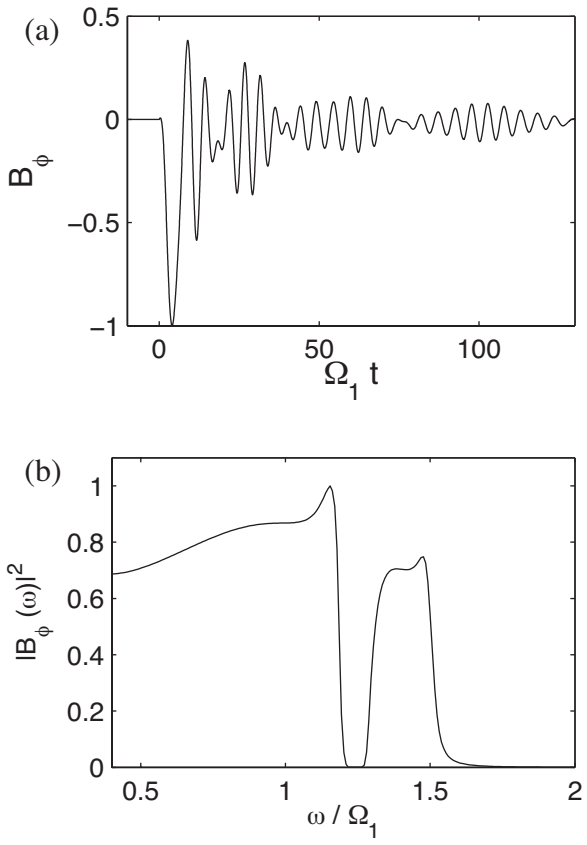

Figure 5.10: Temporal signal corresponding to the wake pattern of Fig. 5.9 at a fixed radial position, $r/\rho_s = 10$. (a) Temporal dependence of the magnetic field normalized to its peak value. Time $t = 0$ corresponds to the arrival of the source at the same axial position of the location sampled. (b) Power spectrum, normalized to the peak value. $\omega/\Omega_1 = 1$ corresponds to the tritium cyclotron frequency, $\omega/\Omega_1 \approx 1.22$, the ion-ion hybrid frequency, and $\omega/\Omega_1 = 1.5$, the deuterium frequency. The propagation seen above the individual cyclotron frequencies is a feature of the adiabatic approximation for shear waves.

value, while the power spectrum shown in Fig. 5.10(b) is normalized to the peak below the ion-ion hybrid frequency. Figure 5.10(a) shows a large signal detected around $t' = 0$ which corresponds to the leading edge of the current filament at that position. The power spectrum exhibits a frequency gap below the ion-ion hybrid frequency (i.e., $\omega \approx 1.22$) and peaks at a frequency that is up-shifted from the cyclotron frequency. This shift is a consequence of the adiabatic approximation for shear Alfvén waves and is also present in single species plasmas; it is caused by coupling to the ion-acoustic wave.

5.5 Discussion

This theoretical investigation has extended the results of a previous study [50] of Cherenkov radiation of shear Alfvén waves by a burst of charged particles, in magnetized plasmas with a single charge species, to the more general case where two ion species are present. By taking the limit of vanishing transverse dimension of the burst, the Alfvénic wake of a point-charge has been obtained for the inertial and adiabatic regimes of wave propagation. The methodology has been used to illustrate the properties of the magnetic perturbations associated with fusion-born alpha particles for conditions expected in ITER.

The essential physics arising from the presence of two ion species is that Alfvén waves propagate within two different frequency bands separated by a gap determined by the value of the ion-ion hybrid frequency. In the inertial regime one band is restricted to frequencies below the cyclotron frequency of the heavier species, and the other to frequencies between the ion-ion hybrid frequency, and the cyclotron frequency of the lighter species. In the adiabatic regime, the frequency bands extend slightly beyond the individual cyclotron frequencies for large perpendicular wave numbers. The Cherenkov radiation pattern in the lower frequency band is found to exhibit essentially the same properties reported in the previous single species study. However, the upper frequency band differs from the lower one in that the Cherenkov radiation condition can be satisfied for all particle velocities.

The observable consequences of the simultaneous excitation of two different propagation bands are that a mixture of spatial patterns arises in the wake, and that the temporal signal

exhibits beats. Typically, at a fixed spatial location the frequencies corresponding to the lower frequency band arrive earlier and those in the higher band, later. This arises because each band propagates along a different cone angle. In the inertial regime, two separate spatial patterns arise. A broader, longer wavelength pattern corresponds to the lower branch and a narrower, shorter wavelength pattern, to the upper band. The pattern for the adiabatic regime is significantly altered by the presence of two ion species. The development of a periodic array of filamentary currents seen in Fig. 10 of Ref. 5, for super-Alfvénic bursts in a single species plasma, is tempered by the stronger excitation of the upper frequency band, as shown in Fig. 5.6.

In summary, intrinsic features associated with the presence of two ion species have been identified in the process of Cherenkov radiation of shear Alfvén waves in magnetized plasmas. This information should be useful in interpreting observations in space, laboratory, and fusion plasmas where such ion populations are present. The gap structure in the frequency spectrum may provide a useful diagnostic signature in fusion environments.

CHAPTER 6

Ballooning mode in a divertor

In a tokamak, the core plasma is confined to a region of closed field lines. The scrape-off-layer (SOL) possesses open field lines which intersect the divertor plates, and the SOL is separated from the core plasma by a separatrix. The change in magnetic topology between the plasma core and the SOL requires the presence of a poloidal field null, which is created through the use of external, poloidal field coils. The region in the vicinity of this null is referred to as the "divertor". During tokamak operation in the H-mode, the plasma routinely experiences instability of edge-localized modes (ELMs) which deliver a large amount of particle and heat flux into the SOL. The resulting plasma is transported along the field lines towards the divertor region where the heat and particle fluxes are ultimately deposited on the divertor plates. This geometry is schematically shown in Fig. 6.1(a). The machine center is represented by the dashed black line, the divertor plates, by the thick green line segments, and the separatrix by the thick black curve. The null point occurs at the point where the separatrix crosses itself and forms the characteristic "x" point.

In extrapolating the current heat loads deposited on the divertor plates in existing devices towards future fusion devices, the heat loads are expected to be greater than current materials can endure. For this reason, much research is being devoted to find novel methods to reduce the heat loads on the divertor plates. One such idea is the snowflake divertor [34, 35], shown schematically in Fig. 6.1(b). In this configuration, the magnitude of the poloidal field increases quadratically with distance from the null point. This gives the flux surfaces a characteristic hexagonal structure in the vicinity of the null point, which resembles a snowflake. The quadratic dependence of the poloidal field strength leads to an increased flux expansion at the target plates, increased shear in the pedestal region, and stronger squeezing

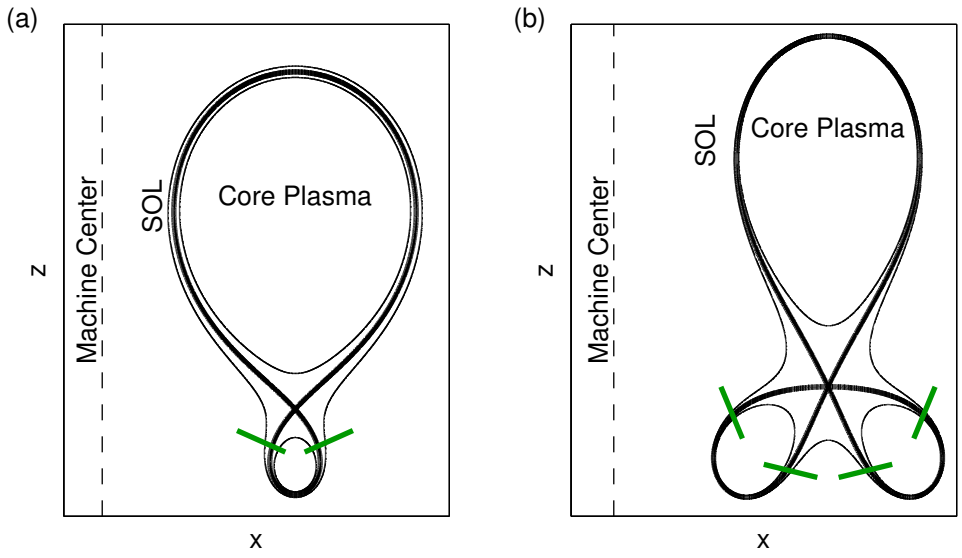

Figure 6.1: Schematic of flux surfaces in the presence of a divertor. Dashed line is machine center, thick black curve is the separatrix, thin black curves are flux surfaces and thick green lines are the divertor plates.The poloidal null occurs where the separatrix forms the characteristic "x" point near the divertor plates. (a) Standard divertor. (b) Snowflake divertor.

of magnetic flux-tubes passing near the null-point [36]. The flux expansion reduces heat loads directly by increasing the area over which the heat is deposited. The increased shear and stronger squeezing of magnetic flux-tubes impact plasma instabilities common to the edge region: edge-localized modes (ELMs) and blobs. Further theoretical investigation concluded that the magnetic geometry of the snowflake divertor leads to increased divertor radiation leading to plasma detachment from the divertor plates, alleviation of the divertor target heat load, and better control of ELMs [37].

The snowflake divertor has been realized on three different tokamaks: NSTX [38, 39], TCV [40, 41, 42], and DIII-D [43]. The experiments on TCV are of particular interest because they observed heat flux deposited on the two strike points in the private flux region [44], i.e., the two strike points that are disjoint from the SOL. Further, numerical simulations under-predict the amount of expected heat flux on these strike points by two orders of magnitude

[45]. This suggests that some mechanism drives convective transport in the vicinity of the null point, enhancing transport across the separatrices. One possibility is the presence of plasma instability due to the small poloidal field strength in the vicinity of the null point.

The parameters characterizing the plasma in the divertor region are machine specific. For an idealized device, the density and temperature at the divertor plates is on the order of $n \sim 10^{12}$ cm^{-3} and $T \sim 10$ eV during inter-ELM operation [75]. The plasma density typically decays exponentially away from the separatrix with a length scale on the order of centimeters, and the ion Larmor radius is on the order of 100 μm. For such a plasma, ideal MHD is a valid approximation when considering a zeroth order description of the system. It is the aim of this and the following chapter to apply MHD stability to the divertor region to determine whether MHD instabilities can account for the convective transport in the vicinity of the null point. In this chapter, ballooning instability is considered, and in the following chapter, the instability of an axisymmetric, quasi-flute mode is considered.

In describing the equilibrium about which instability is to be examined, the Grad-Shafranov equation [76] is a useful starting point. First, magnetic flux coordinates are employed, with the flux surface labeled by ψ, the generalized poloidal coordinate, χ, and the toroidal coordinate, ζ. In this coordinate system, the magnetic field can be expressed as

$$\mathbf{B} = I(\psi)\nabla\zeta + \nabla\psi \times \nabla\zeta, \tag{6.1}$$

where the toroidal field is $B_t = I(\psi)/r$ with r, the radial distance from the major axis and $I(\psi)$, a general function of the flux coordinate, and the poloidal field, $\mathbf{B}_p = \nabla\psi \times \nabla\zeta$. The Grad-Shafranov equation is

$$\Delta^*\psi = -4\pi r^2 p'(\psi) - I(\psi)I'(\psi), \tag{6.2}$$

where a prime denotes a derivative with respect to ψ. The operator, Δ^* is defined in a cylindrical coordinate system, (r, ζ, z), with r and ζ defined as before, and z defined to be orthogonal to the other two coordinates,

$$\Delta^* = r\frac{\partial}{\partial r}\left(\frac{1}{r}\frac{\partial}{\partial r}\right) + \frac{\partial^2}{\partial z^2}. \tag{6.3}$$

Further, the toroidal and poloidal current densities are given by,

$$\frac{4\pi j_t}{c} = -\frac{1}{r}\Delta^*\psi, \tag{6.4}$$

$$\frac{4\pi j_p}{c} = I'(\psi)B_p. \tag{6.5}$$

In describing the geometry of the flux surfaces in the vicinity of the null point, it is a standard approximation to assume that the poloidal field, $\mathbf{B}_p$, is curl free [34, 35], which implies that the toroidal current density, j_t, is negligible. This condition amounts to considering equilibria for which $\Delta^*\psi = 0$, with the plasma equilibrium provided by the interaction of the poloidal current with the toroidal magnetic field. Additionally, the plasma pressure, p, is much weaker than the magnetic pressure in the divertor, and for this reason, $\beta_t = 8\pi p/B_t^2 \ll 1$. These properties of the plasma in the vicinity of the poloidal null allow for a zeroth order approximation of the Grad-Shafranov equation, $I'(\psi) = 0$. Reformulating this statement in terms of the toroidal field, it is equivalent to saying that the toroidal field is well described by its vacuum value, the plasma not possessing enough pressure to disturb the toroidal field.

Further simplifications exist when the spatial orderings of the problem are observed. First, it is assumed that the distances from the null point, d, are much smaller than the minor radius of the plasma, a. This allows for a local expansion of the flux function where the lowest order term is retained as described in section 6.1. Further, because the major radius, R, is larger than the minor radius, a cylindrical approximation can be made in which toroidicity effects are neglected. In investigating MHD stability in the vicinity of the null point, these geometrical approximations are made for a flux geometry applicable to both the standard and snowflake divertors.

In this chapter, a ballooning instability is considered. For such an instability, the perturbation varies rapidly transverse to the magnetic field, but slowly in the direction of the field lines. In this case, the energy of bending the magnetic field is offset by the slow variation of the perturbation along the field line. The theory of ballooning modes was first fully developed for the ideal MHD equations for closed magnetic field lines by Connor, Hastie, and Taylor [77]. Since then, many papers have been published about ballooning modes, and the theory is found in various reviews and textbooks, e.g., [76]. In considering ballooning modes

in the divertor region, the biggest difference is that the field lines are now open and intersect the conducting end plates. Many papers have been published considering the effects of the boundary conditions [78, 79, 80, 81]. In the present analysis, the shear of the magnetic field acts as an effective boundary, causing the modes to rapidly decay away from the null point. For this reason, the perturbations considered are well localized near the null point and are negligibly small at the divertor plates. Thus, the divertor plates can be neglected. Because the modes considered are a special class of perturbation, the resulting instability condition is less strict than theories which describe the core plasma and include the x-point in the analysis, for example, Webster and Gimblett's analysis of peeling modes near the separatrix [82]. The modes considered here have different consequences, being responsible for dynamics isolated to the null point.

The outline of this chapter is as follows. In section 6.1, the geometry of the flux surfaces for both the standard and snowflake divertors is presented. In section 6.2, the ballooning mode formalism is summarized and applied to both the standard and snowflake divertors. In section 6.3, a test function is used in the energy principle to derive an instability threshold. The resulting threshold for the ballooning instability is then applied to experimental parameters in section 6.4.

6.1 Geometry of standard and snowflake divertors

In describing the divertor geometry, the emphasis is in the vicinity of the null point of the poloidal field. All equilibrium quantities are assumed to be independent of the toroidal coordinate, ζ. In describing the poloidal plane, two coordinate systems are used, and relations between the two are given later in this section. The first is a Cartesian coordinate system, (x, z), defined such that the origin is located at the null point. Since the analysis corresponds to the vicinity of the null, the ordering of spatial scales is $|x|, |z| \ll a < R$, where a and R are the minor and major radii, respectively. With these assumptions, $\nabla\zeta = \hat{\boldsymbol{\zeta}}/R$. Flux coordinates are also used because they allow for a simple form for the equations governing the ballooning mode. Thus, the flux surface and generalized poloidal angle are denoted by

ψ and χ, respectively. Because of the spatial orderings, the straight, cylindrical approximation is made in both coordinate systems, but the use of flux coordinates allows for the accurate description of the complicated magnetic geometry in the vicinity of the null point. As mentioned in Chapter 7, in flux coordinates, the poloidal field can be written as

$$\mathbf{B}_p = \nabla\psi \times \nabla\zeta. \tag{6.6}$$

The standard assumption that $\mathbf{B}_p$ is curl free results in the equation,

$$\nabla \times \mathbf{B}_p = -\nabla\zeta\nabla^2\psi = 0. \tag{6.7}$$

The Laplacian which acts on ψ can be simplified if the torus is treated in the straight-cylindrical approximation. In this case, the equation reduces to

$$\left(\frac{\partial^2}{\partial x^2} + \frac{\partial^2}{\partial z^2}\right)\psi = \left[\frac{1}{r}\frac{\partial}{\partial r}\left(r\frac{\partial}{\partial r}\right) + \frac{1}{r^2}\frac{\partial^2}{\partial\theta^2}\right]\psi = 0, \tag{6.8}$$

where in this chapter $r = \sqrt{x^2 + z^2}$ and $\theta = \tan^{-1}(x/z)$ are the familiar polar coordinates. From here, it is clear that the solutions can be expanded in terms of sinusoidal harmonics each with their own radial dependence. Additionally, since the fields must be bounded at the origin, the flux function can be written as

$$\psi = \sum_{m=0}^{\infty}\left(\frac{r}{a}\right)^m \left(A_m\cos(m\theta) + B_m\sin(m\theta)\right), \tag{6.9}$$

with A_m and B_m being constants that determine the specific expansion of the flux function about the origin. The constant term, $m = 0$, does not appear in the poloidal field as $\mathbf{B}_p$ is related to ψ through a derivative. The $m = 1$ term corresponds to a non-vanishing field at the origin. Such a field is relevant to the model geometry considered in section A.2. Here, the $m = 1$ term is discarded. The $m = 2$ term is the dominant term for the standard divertor in the vicinity of the null, the $m = 3$ term for the snowflake, and the $m = 4$ term for the cloverleaf[83] which possesses a third order null. For this reason, the flux function for the standard divertor is approximated in the vicinity of the null point as

$$\psi = C\frac{B_{pM}Ra}{2}\left(\frac{r}{a}\right)^2\cos(2\theta) = CB_{pM}Ra\left(\frac{x^2 - z^2}{2a^2}\right), \tag{6.10}$$

and for the snowflake divertor,

$$\psi = C\frac{B_{pM}Ra}{3}\left(\frac{r}{a}\right)^3\cos(3\theta) = CB_{pM}Ra\left(\frac{x^3-3xz^2}{3a^3}\right). \tag{6.11}$$

In these expressions, the constant has been determined by considering the asymptotic value of the flux function as $r \sim a$. In this limit, $B_p = |\nabla\psi|/R \sim B_{pM}$, the strength of the poloidal field in the midplane. The specific choice of a cosine represents a specific orientation of the flux surfaces. To retain generality in this formulation, the major radius is assumed to form an angle, α, with the x-axis. It is true that higher order terms in the expansion may contribute at distances from the origin that are on the order of the minor radius, but here the surfaces are approximated to lowest, non-vanishing order, consistent with the length scales in the problem. Additionally, the lowest order terms given are proportional to a constant of order unity, C, which depends on the specific global geometry of the problem. These constants of order unity can be determined by considering the global geometry for a specific device.

In determining the generalized poloidal coordinate for this geometry, a degree of freedom exists. For convenience, choose $|\nabla\chi| = |\nabla\psi|$. This choice causes χ to be harmonically conjugate to ψ. The form of χ for the standard divertor is

$$\chi = C\frac{B_{pM}Ra}{2}\left(\frac{r}{a}\right)^2\sin(2\theta) = CB_{pM}Ra\left(\frac{xz}{a^2}\right), \tag{6.12}$$

and for the snowflake divertor

$$\chi = C\frac{B_{pM}Ra}{3}\left(\frac{r}{a}\right)^3\sin(3\theta) = CB_{pM}Ra\left(\frac{3x^2z-z^3}{3a^3}\right). \tag{6.13}$$

A complex flux function can be defined in this case to be

$$\eta = \psi + i\chi = C\frac{B_{pM}Ra}{m}\left(\frac{r}{a}\right)^m\exp(im\theta) = C\frac{B_{pM}Ra}{m}\left(\frac{x+iz}{a}\right)^m, \tag{6.14}$$

where $m = 2$ corresponds to the standard divertor and $m = 3$ to the snowflake. The form of this function is convenient because it can be inverted so that the coordinates, (x, z), are expressed analytically in terms of their counterparts, (ψ, χ). This would not be the case if higher order terms were present in the expansions or if a toroidal current were present in the vicinity of the null, causing ψ to no longer be a harmonic function.

The Jacobian of the flux coordinate system can be determined from the relation

$$\frac{1}{J} = \nabla\chi \cdot (\nabla\psi \times \nabla\zeta)\,. \tag{6.15}$$

This is done for arbitrary m using Eq. (6.14) to compute the necessary gradients to obtain

$$\frac{1}{J} = C^2 R B_{pM}^2 \left(\frac{x^2+z^2}{a^2}\right)^{m-1} = C^2 R B_{pM}^2 \left(\frac{m^2(\psi^2+\chi^2)}{C^2 B_{pM}^2 R^2 a^2}\right)^{\frac{m-1}{m}}. \tag{6.16}$$

Setting $m = 2$ gives the following result for the standard divertor,

$$\frac{1}{J} = C^2 R B_{pM}^2 \left(\frac{x^2+z^2}{a^2}\right) = 2C^2 R B_{pM}^2 \left(\frac{\psi^2+\chi^2}{C^2 R^2 a^2 B_{pM}^2}\right)^{1/2}, \tag{6.17}$$

and $m = 3$ for the snowflake divertor gives,

$$\frac{1}{J} = C^2 R B_{pM}^2 \left(\frac{x^2+z^2}{a^2}\right)^2 = 3^{4/3} C^2 R B_{pM}^2 \left(\frac{\psi^2+\chi^2}{C^2 R^2 a^2 B_{pM}^2}\right)^{2/3}. \tag{6.18}$$

Because of the choice that $|\nabla\chi| = |\nabla\psi|$, a useful relation between the Jacobian, the magnitude of the poloidal field, and the major radius is

$$B_p^2 R J = 1. \tag{6.19}$$

This relation is used later to simplify various expressions.

Figure 6.2 shows the flux surface geometry both in the standard and snowflake divertors. The surfaces of constant ψ are shown as black curves, and the surfaces of constant χ as dashed red curves. The separatrices are represented by the straight black lines. The upper panel shows the characteristic 'X' shape of the separatrix present in the standard divertor, and the poloidal plane is divided into four disjoint regions in which the magnetic field lines are separated from the other regions. The lower panel shows the characteristic hexagonal shape of a pure snowflake divertor. In both panels, a second set of axes, (x', z'), is illustrated by the thick blue lines. This reflects the arbitrary direction of the major radius which is taken to form the angle, α, with the x-axis.

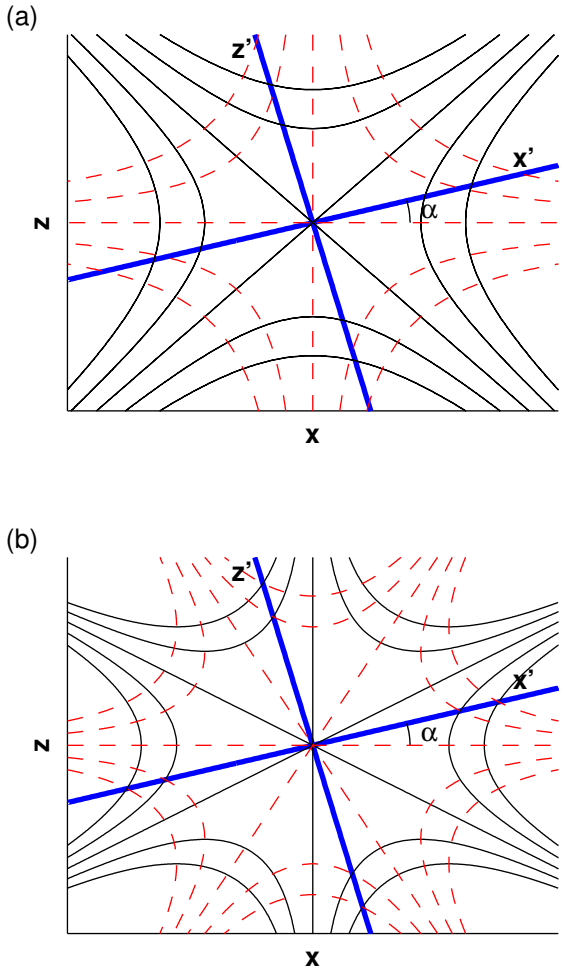

Figure 6.2: Geometry of flux surfaces in the vicinity of the poloidal null. (a) Standard divertor, (b) snowflake divertor. Solid black lines are surfaces of constant ψ and dashed red lines are surfaces of constant χ. The thick blue lines indicate an alternate choice of (x, z) axes in which the flux surfaces are rotated through an angle, α. Here, it is assumed that the machine center and the toroidal curvature lies in the $-x'$ direction. The toroidal direction is out of the page.

6.2 Ballooning mode equations

The ballooning mode formalism has been discussed in many studies, e.g. [77, 76, 79, 80, 81]. As mentioned previously, the mode is assumed to be localized to the null point. As will

be shown later, this is valid because of the large shear between the null and the divertor plates. For this reason, the form of the boundary conditions at the plates is unimportant. Because of this effect, the component of the plasma displacement, $\boldsymbol{\xi}$, parallel to the magnetic field decouples from the perpendicular motion when minimizing the energy to find the most unstable mode. As a result, the differential equations reduce to a single, uncoupled equation for the perpendicular plasma displacement when the parallel displacement is chosen to minimize the energy.

Adopting the method used by Freidberg[76], an eikonal approximation is first made for the plasma displacement which takes the form

$$\boldsymbol{\xi} = \boldsymbol{\eta} e^{in\left(\zeta - \int_{\chi_0}^{\chi} \nu \, d\chi'\right)}, \tag{6.20}$$

where n corresponds to the toroidal mode number. The quantity ν is chosen so that the phase in the exponential is constant along a field line and is expressed as $\nu = B_t J/R$, where B_t is the toroidal field strength. The perpendicular wave vector can be found by taking the gradient of the eikonal,

$$\mathbf{k}_\perp = -n \left(\int_{\chi_0}^{\chi} \frac{\partial \nu}{\partial \psi} \, d\chi' \right) \nabla\psi + n \left(\nabla\zeta - \nu \nabla\chi \right), \tag{6.21}$$

$$= k_n \hat{\boldsymbol{\psi}} + k_t \hat{\mathbf{t}}, \tag{6.22}$$

where the wave vector is resolved into two components: k_n, the portion normal to the flux surfaces; and k_t, lying orthogonal to both the normal to the flux surfaces and the magnetic field, parallel to the vector $\hat{\mathbf{t}} = \hat{\boldsymbol{\zeta}} B_p/B - \hat{\boldsymbol{\chi}} B_t/B$. From Eqs. (6.6) it can be shown that $|\nabla\psi| = B_p R$. Further, since $|\nabla\psi| = |\nabla\chi|$, k_n and k_t can be written as

$$k_n = -nRB_p \int_{\chi_0}^{\chi} \frac{\partial \nu}{\partial \psi} \, d\chi', \tag{6.23}$$

$$k_t = n \frac{B}{RB_p}. \tag{6.24}$$

To minimize the energy, $\boldsymbol{\eta}_\perp$ is to lowest order,

$$\boldsymbol{\eta}_\perp = \frac{X}{nB} \hat{\mathbf{b}} \times \mathbf{k}_\perp. \tag{6.25}$$

Here, B is the total magnetic field strength, and $\hat{\mathbf{b}}$ is a unit vector in the direction of the magnetic field. The n in the denominator is introduced to keep the perturbed energies and fields of order unity. With these definitions, the energy principle for the ballooning mode is given by

$$\omega^2 = \frac{W}{K}, \tag{6.26}$$

$$W = \frac{1}{4}\int d\psi\, W(\psi), \tag{6.27}$$

$$W(\psi) = \frac{1}{n^2}\int J d\chi \left[\frac{1}{J^2B^2}\left(k_n^2 + k_t^2\right)\left|\frac{\partial X}{\partial \chi}\right|^2 - \frac{8\pi R B_p}{B^2}\frac{dp}{d\psi}\left(k_t^2\kappa_n - k_t k_n \kappa_t\right)|X|^2\right], \tag{6.28}$$

$$K = \frac{\pi}{n^2}\int J d\psi d\chi \frac{\rho(k_n^2 + k_t^2)}{B^2}|X|^2, \tag{6.29}$$

where the plasma displacement is assumed to have harmonic time dependence, $\exp(-i\omega t)$. If $\omega^2 < 0$, this corresponds to instability and exponential growth of the perturbation. The quantity, $-\omega^2 K$, corresponds to the perpendicular kinetic energy with the parallel kinetic energy neglected. This is done as in the original paper by Connor, et al.[77] in order to simplify the resulting equations. This simplification does not alter the resulting instability thresholds derived, though it may overestimate the predicted growth rates. The potential energy change caused by the perturbation is given by W. As expressed in the equations, the integrand only depends on ψ as a parameter, and as a result, the analysis can be performed on each flux surface independently of the other flux surfaces, reflecting the one-dimensional property that occurs when the ballooning limit is taken. The quantities, ρ and p represent the plasma mass density and pressure, respectively, and $\boldsymbol{\kappa}$ corresponds to the curvature of the magnetic field. The magnetic curvature is resolved into two components, $\boldsymbol{\kappa} = \kappa_n\hat{\boldsymbol{\psi}} + \kappa_t\hat{\mathbf{t}}$, just as $\mathbf{k}_\perp$ is. The magnetic curvature is defined to be $\boldsymbol{\kappa} = \hat{\mathbf{b}}\cdot\nabla\hat{\mathbf{b}}$. From this definition and the plasma equilibrium, it can be shown that

$$\boldsymbol{\kappa} = -\frac{4\pi}{B^2}\hat{\mathbf{b}}\times\left[\hat{\mathbf{b}}\times\nabla\left(p + \frac{B^2}{8\pi}\right)\right], \tag{6.30}$$

$$= \frac{4\pi}{B^2}\left[\frac{1}{JB_p}\frac{\partial}{\partial\psi}\left(p + \frac{B^2}{8\pi}\right)\hat{\boldsymbol{\psi}} - \frac{1}{JB_p}\frac{\partial}{\partial\chi}\left(\frac{B^2}{8\pi}\right)\frac{B_t}{B}\hat{\mathbf{t}}\right]. \tag{6.31}$$

In this expression, it is convenient to remove all dependence on the plasma pressure. To do this, the Grad-Shafranov equation is used but with the toroidal current set to zero in

agreement with the earlier assumptions. The components of the curvature vector are found to be

$$\kappa_t = \boldsymbol{\kappa} \cdot \hat{\mathbf{t}} = -\frac{1}{2}\frac{B_t}{JB_pB^3}\frac{\partial B^2}{\partial \chi}, \tag{6.32}$$

$$\kappa_n = -\frac{RB_p}{2}\left[\frac{B_t^2}{B^2}\frac{\partial \log R^2}{\partial \psi} + \frac{B_p^2}{B^2}\frac{\partial \log J}{\partial \psi}\right]. \tag{6.33}$$

Substituting all of these expressions into the potential energy and kinetic energy, Eqs. (6.28) and (6.29) become

$$\begin{aligned} W(\psi) = \int J d\chi \Bigg\{ & \frac{1}{J^2R^2B_p^2}\left[1 + \left(\frac{R^2B_p^2}{B}\int_{\chi_0}^{\chi}\frac{\partial \nu}{\partial \psi}d\chi'\right)^2\right]\left|\frac{\partial X}{\partial \chi}\right|^2 \\ & + 4\pi\frac{dp}{d\psi}\left[\frac{B_t^2}{B^2}\frac{\partial \log R^2}{\partial \psi} + \frac{B_p^2}{B^2}\frac{\partial \log J}{\partial \psi} + \frac{RB_t}{JB^2}\left(\int_{\chi_0}^{\chi}\frac{\partial \nu}{\partial \psi}d\chi'\right)\frac{\partial \log B^2}{\partial \chi}\right]|X|^2\Bigg\}, \end{aligned} \tag{6.34}$$

$$K = \pi\int d\psi d\chi \, \frac{J\rho}{R^2B_p^2}\left[1 + \left(\frac{R^2B_p^2}{B}\int_{\chi_0}^{\chi}\frac{\partial \nu}{\partial \psi}d\chi'\right)^2\right]|X|^2, \tag{6.35}$$

Further, from the energy principle, an Euler equation can be derived. The result is

$$\begin{aligned} 0 = & \frac{1}{J}\frac{\partial}{\partial \chi}\left\{\frac{1}{JB_p^2R^2}\left[1 + \left(\frac{R^2B_p^2}{B}\int_{\chi_0}^{\chi}\frac{\partial \nu}{\partial \psi}d\chi'\right)^2\right]\frac{\partial X}{\partial \chi}\right\} \\ & + \left\{\omega^2\frac{4\pi\rho}{R^2B_p^2}\left[1 + \left(\frac{R^2B_p^2}{B}\int_{\chi_0}^{\chi}\frac{\partial \nu}{\partial \psi}d\chi'\right)^2\right]\right. \\ & \left. - 4\pi\frac{dp}{d\psi}\left[\frac{B_t^2}{B^2}\frac{\partial \log R^2}{\partial \psi} + \frac{B_p^2}{B^2}\frac{\partial \log J}{\partial \psi} + \frac{RB_t}{JB^2}\left(\int_{\chi_0}^{\chi}\frac{\partial \nu}{\partial \psi}d\chi'\right)\frac{\partial \log B^2}{\partial \chi}\right]\right\}X. \end{aligned} \tag{6.36}$$

Substantial simplifications can be made if the orderings of the physical problem are observed. First, expand R in the vicinity of the null. If R_0 is the major radius of the null-point, then from Fig. 6.2, it is clear that

$$R = R_0 + x' = R_0 + \cos(\alpha)x + \sin(\alpha)z. \tag{6.37}$$

Further, because $R_0 \gg |x|, |z|$,

$$\frac{\partial \log R^2}{\partial \psi} \ll \frac{\partial \log J}{\partial \psi}. \tag{6.38}$$

At the same time, the toroidal field in the vicinity of the null is much larger than the poloidal field, $B_t \gg B_p$. Using these relations, consider the expression, $\partial\nu/\partial\psi$. As in Chapter 7, it

is again assumed that the toroidal field is well-approximated by its vacuum solution. This implies that the quantity $B_t R$ is constant. Combining all of this,

$$\frac{\partial \nu}{\partial \psi} = B_t R \frac{\partial}{\partial \psi}\left(\frac{J}{R^2}\right) \approx \frac{B_0}{R_0}\frac{\partial J}{\partial \psi}, \tag{6.39}$$

where the toroidal field and major radius have been approximated by their values at the null-point, B_0 and R_0, respectively. Further, using Eq. (6.19) and $B \approx B_t \approx B_0$,

$$\frac{R^2 B_p^2}{B}\int_{\chi_0}^{\chi} \frac{\partial \nu}{\partial \psi} d\chi' \approx \frac{1}{J}\int_{\chi_0}^{\chi} \frac{\partial J}{\partial \psi} d\chi' \equiv s. \tag{6.40}$$

In this context, s corresponds to the shear in the magnetic field integrated along the poloidal coordinate, as is shown later in this section. In the quantity, $\partial B^2/\partial \chi$, the same approximations can be applied to yield

$$\frac{\partial \log B^2}{\partial \chi} \approx -\frac{\partial \log R^2}{\partial \chi} - \frac{B_p^2}{B_0^2}\frac{\partial \log J}{\partial \chi}. \tag{6.41}$$

Using these results and the orderings previously mentioned, Eq. (6.36) simplifies to

$$\begin{aligned} 0 = \frac{1}{RJ}\frac{\partial}{\partial \chi}\left[\left(1+s^2\right)\frac{\partial X}{\partial \chi}\right] + \Bigg\{ \omega^2 \frac{4\pi\rho}{R^2 B_p^2}\left(1+s^2\right) \\ -4\pi \frac{dp}{d\psi}\left[\left(\frac{\partial \log R^2}{\partial \psi} + \frac{B_p^2}{B_0^2}\frac{\partial \log J}{\partial \psi}\right) - \left(\frac{\partial \log R^2}{\partial \chi} + \frac{B_p^2}{B_0^2}\frac{\partial \log J}{\partial \chi}\right) s\right]\Bigg\} X. \end{aligned} \tag{6.42}$$

It is important to understand the meaning of the physical constant, χ_0, present in the definition of s. Hameiri made the observation that χ_0 corresponds to the polarization of the electric field [81]. This is easily seen from Ohm's law in the form

$$\mathbf{E} = \frac{i\omega}{c}\boldsymbol{\xi} \times \mathbf{B} = \frac{i\omega}{c} X \frac{\mathbf{k}_\perp}{n}, \tag{6.43}$$

$$= \frac{i\omega}{c} X \frac{B}{R B_p}\left[\hat{\mathbf{t}} - \frac{1}{J}\int_{\chi_0}^{\chi} \frac{\partial J}{\partial \psi} d\chi' \hat{\boldsymbol{\psi}}\right]. \tag{6.44}$$

From this expression and Eq. (6.25), it is seen that χ_0 corresponds to the point at which the electric field is oriented completely in the geodesic direction and the plasma displacement is normal to the flux surface. Further, at points along the field line away from χ_0, the normal component of the electric field grows relative to the geodesic component and a geodesic component of the plasma displacement begins to shear the perturbations. Thus, an initial perturbation is distorted in the geodesic direction as it moves along the field line away from

the point, χ_0. In the absence of shear, the electric field would lie solely in the geodesic direction and all plasma displacements would be normal to the flux surface.

Next, the differential equation is applied to the specific geometries of the standard and snowflake divertors. First consider the derivatives, $\partial \log R^2/\partial\psi$ and $\partial \log R^2/\partial\chi$, which can be computed as follows. From Eq. (6.14), $x+iz$ can be expressed in terms of η, resulting in

$$x + iz = am^{1/m}\left(\frac{\eta}{CB_{pM}Ra}\right)^{1/m}. \tag{6.45}$$

The desired derivatives can be computed by differentiating Eq. (6.37) consistent with the large R_0 approximation to yield

$$\frac{\partial \log R^2}{\partial\psi} = \frac{2}{R_0}\mathrm{Re}\left[\frac{d(x+iz)}{d\eta}e^{-i\alpha}\right], \tag{6.46}$$

$$\frac{\partial \log R^2}{\partial\chi} = -\frac{2}{R_0}\mathrm{Im}\left[\frac{d(x+iz)}{d\eta}e^{-i\alpha}\right], \tag{6.47}$$

The derivatives are

$$\frac{\partial \log R^2}{\partial\psi} = \frac{2}{CR_0^2B_{pM}}\left(\frac{m^2(\psi^2+\chi^2)}{C^2R_0^2a^2B_{pM}^2}\right)^{\frac{1-m}{2m}}\cos(\alpha+\delta), \tag{6.48}$$

$$\frac{\partial \log R^2}{\partial\chi} = \frac{2}{CR_0^2B_{pM}}\left(\frac{m^2(\psi^2+\chi^2)}{C^2R_0^2a^2B_{pM}^2}\right)^{\frac{1-m}{2m}}\sin(\alpha+\delta), \tag{6.49}$$

Here, δ represents the angle a vector normal to a flux surface forms with the x-axis. Thus, in the above expressions, the sum of the angles, $\alpha+\delta$, represents the projection of the normal to the flux surface onto the x' axis shown in Fig. 6.2. The angle δ is expressed as

$$\delta = \frac{m-1}{m}\tan^{-1}\left(\frac{\chi}{\psi}\right) + 2\pi j/m. \tag{6.50}$$

The parameter j represents a branch cut, and can take values, $j = 0, 1, 2, ..., m-1$, corresponding to the disjoint regions in Fig. 6.2. Since the specific orientation of the flux surfaces is captured by the parameter α, we set $j = 0$ without loss of generality. This focuses the analysis on the flux surfaces bounded by the separatrix and enclosing the positive x-axis in Fig. 6.2, while allowing the orientation with respect to the major radius through the angle, α, to be varied choosing $m = 2$ for the standard divertor and $m = 3$ for the snowflake as mentioned in Section 6.1.

The derivatives, $\partial \log J/\partial\psi$ and $\partial \log J/\partial\chi$ are given for general m by

$$\frac{\partial \log J}{\partial \psi} = -\left(\frac{m-1}{m}\right)\frac{2\psi}{\psi^2+\chi^2}, \tag{6.51}$$

$$\frac{\partial \log J}{\partial \chi} = -\left(\frac{m-1}{m}\right)\frac{2\chi}{\psi^2+\chi^2}. \tag{6.52}$$

Further, using the relation for the Jacobian, the shear, s, can be computed. This gives the integral relation,

$$s = -2\left(\frac{m-1}{m}\right)\left(1+\frac{\chi^2}{\psi^2}\right)^{\frac{m-1}{m}}\int_{\chi_0/\psi}^{\chi/\psi}\frac{dx}{(1+x^2)^{\frac{2m-1}{m}}}. \tag{6.53}$$

This integral can be evaluated for general m through the use of hypergeometric functions. For the standard divertor, the integral is

$$s = -\frac{\chi}{\psi} + \frac{\chi_0}{\psi}\sqrt{\frac{1+(\chi/\psi)^2}{1+(\chi_0/\psi)^2}}, \tag{6.54}$$

but in the case of the snowflake divertor, no expression in terms of elementary functions exists. Thus, in evaluating s for the snowflake, the integral needs to be performed numerically for arbitrary χ_0. For $\chi_0 = 0$, the two asymptotic forms can be used to obtain an approximate form for s that agrees well over the range of x,

$$s \sim -2\left(\frac{m-1}{m}\right)\frac{\chi}{\psi}, \qquad \frac{\chi}{\psi} \ll 1, \tag{6.55}$$

$$s \sim -2\left(\frac{m-1}{m}\right)\left[\int_0^\infty \frac{dx}{(1+x^2)^{\frac{2m-1}{m}}}\right]\left(\frac{\chi}{\psi}\right)^{\frac{2(m-1)}{m}}, \qquad \frac{\chi}{\psi} \gg 1. \tag{6.56}$$

Thus, for the snowflake, the function s can be well approximated by

$$s \approx -\frac{4}{3}\frac{\chi}{\psi}\left(1+0.7554\left|\frac{\chi}{\psi}\right|\right)^{1/3}, \tag{6.57}$$

with the constant, 0.7554, found by numerically performing the integral in Eq. (6.56).

Finally, Eq. (6.19) allows an expression for B_p^2 to be found. With these expressions, the differential equation modeling ballooning modes can be written specifically for the two divertor configurations. It is useful to scale the equations so that the dimensionless parameters are clearly apparent,

$$\psi \to CR_0 a B_{pM}\psi, \tag{6.58}$$

$$\chi \to CR_0 a B_{pM}\chi. \tag{6.59}$$

Further, it is convenient to replace the variable χ with $x = \chi/\psi$ as this is the natural scaling for the poloidal coordinate. The differential equation for the standard divertor becomes

$$-\frac{\partial}{\partial x}\left[(1+s^2)\frac{\partial X}{\partial x}\right] + \beta_{pM}\frac{d\log p}{d\log\psi}\left[\frac{a}{2\sqrt{2}C^2R_0\psi^{1/2}}\frac{\cos(\alpha+\delta)-s\sin(\alpha+\delta)}{(1+x^2)^{3/4}} - \frac{B_{pM}^2}{2B_0^2}\frac{1-sx}{1+x^2}\right]X = \frac{\omega^2a^2}{4C^2v_{AM}^2}\frac{1+s^2}{1+x^2}X, \tag{6.60}$$

where $\beta_{pM} = 8\pi p/B_{pM}^2$ and $v_{AM}^2 = B_{pM}^2/4\pi\rho$. For the snowflake divertor the result is

$$-\frac{\partial}{\partial x}\left[(1+s^2)\frac{\partial X}{\partial x}\right] + \beta_{pM}\frac{d\log p}{d\log\psi}\left[\frac{a}{18C^2R_0\psi}\frac{\cos(\alpha+\delta)-s\sin(\alpha+\delta)}{1+x^2} - \frac{B_{pM}^2}{3B_0^2}\frac{1-sx}{1+x^2}\right]X = \frac{\omega^2a^2}{3^{8/3}C^2v_{AM}^2\psi^{2/3}}\frac{1+s^2}{(1+x^2)^{4/3}}X. \tag{6.61}$$

To evaluate the derivative $d\log p/d\log\psi$, it is assumed that the full pressure drops over the width between the flux surfaces, $\psi = 0$ and $\psi = \Delta_M/a$. The latter flux surface corresponds to the flux surface at the edge of the SOL. Thus, the derivative becomes

$$\frac{d\log p}{d\log\psi} \approx \frac{\Delta p/p}{\Delta\psi/\psi} \approx -1. \tag{6.62}$$

If the distance from the null to the plates along the separatrix is L, this translates to a value of $x = \pm L^2/2\Delta_M a$ for the standard divertor and $x = \pm L^3/3\Delta_M a^2$ for the snowflake divertor. Typically, these values of x are much greater than unity, and this combined with the large value of s which develops over this distance, justifies the neglect of the precise boundary conditions at the divertor plates.

This section closes with a discussion on shear. Analysis of shear in the snowflake divertor has been performed elsewhere [36]. In what follows, a slightly different presentation is given in order to elucidate the relevance of the shear to the problem considered here. The relative strength of the shear in the snowflake as compared to the standard divertor is somewhat misleading from the form of Eqs. (6.54) and (6.57). The fact that s grows faster in the snowflake than in the standard divertor as a function of χ/ψ reflects the fact that for a given poloidal distance traversed, s is larger in the snowflake case. However, because of the smaller poloidal field in the snowflake, this corresponds to many more toroidal transits and a much larger distance along the field line is traversed. To see this more clearly, first find the position

of a field line poloidally as it moves toroidally around the device. In what follows, set $C = 1$ as its precise value is unimportant for this discussion. Starting at the point $x = x_0$, $z = 0$, since the field lines are confined to surfaces of constant ψ, this gives a relation between x and z along the field line's trajectory. For the standard divertor, the trajectory of the rays is governed by

$$\frac{dx}{z} = \frac{dz}{x} = \frac{d\zeta}{q^*}, \tag{6.63}$$

where $q^* = aB_0/RB_{pM}$. Further, constant ψ requires that $x_0^2 = x^2 - z^2$ to obtain

$$x = x_0 \cosh\left(\frac{\zeta - \zeta_0}{q^*}\right), \tag{6.64}$$

$$z = x_0 \sinh\left(\frac{\zeta - \zeta_0}{q^*}\right). \tag{6.65}$$

Substituting these results into Eq. (6.54) with $\chi_0 = 0$ results in

$$s = -\sinh\left(\frac{2\,(\zeta - \zeta_0)}{q^*}\right) \approx -\frac{2\,(\zeta - \zeta_0)}{q^*}, \tag{6.66}$$

where the approximate form is for small argument. Doing the same procedure for the snowflake,

$$\frac{dx}{2xz} = \frac{dz}{x^2 - z^2} = \frac{d\zeta}{aq^*}. \tag{6.67}$$

Constant ψ requires that $x_0^3 = x^3 - 3xz^2$. Solving for z and substituting into the previous equation results in

$$\int_{x_0}^{x} \frac{1}{2}\sqrt{\frac{3}{x'(x'^3 - x_0^3)}}dx' = \frac{\zeta - \zeta_0}{aq^*}. \tag{6.68}$$

This integral can be approximated for values of x close to x_0 to obtain

$$x = x_0 + x_0^3\left(\frac{\zeta - \zeta_0}{aq^*}\right)^2, \tag{6.69}$$

$$z = x_0^2\left(\frac{\zeta - \zeta_0}{aq^*}\right). \tag{6.70}$$

Plugging this into the asymptotic expression for s for $\chi/\psi \ll 1$, results in

$$s = -4\frac{x_0}{a}\frac{\zeta - \zeta_0}{q^*}. \tag{6.71}$$

From here, it is apparent that the shear is smaller for a given toroidal distance travelled in the snowflake by a factor of x_0/a. For a given SOL width in the midplane, Δ_M, the distance

closest to the null is $x_0/a = (3\Delta_M/a)^{1/3}$. This is typically a small factor (about 0.25 for DIII-D parameters), though the greater fanning of the flux surfaces near the null results in the exponent 1/3, which can make the shear comparable for the two divertor configurations.

6.3 Instability threshold

The next step is to determine the thresholds for instability for Eqs. (6.60) and (6.61). This amounts to determining the value of β_{pM} for which $\omega^2 = 0$. Further, for a given value of β_{pM}, the parameter, $\Gamma = \omega^2 a^2/v_{AM}^2$ can be found. This is done by employing a variational approach in which a test function approximates the fundamental mode of the differential equation. For this reason, the thresholds reported are sufficient conditions for instability, but they are not necessary. Setting $\chi_0 = 0$ specializes to modes which are unstable in the vicinity of the null point where the poloidal field is small. A more detailed numerical analysis could be performed in which different values of χ_0 are explored, but this is more appropriate for future applications to specific experimental devices. It should be mentioned that in choosing values of χ_0, it is important that the spatial positions still satisfy the length scales of the problem, i.e. that $r/a \ll 1$. If this assumption is violated, the mode is no longer localized to the null point, and the boundary effects of the divertor plates must be modeled more carefully.

First consider the standard divertor. In this case, the choice of $\chi_0 = 0$ greatly simplifies the differential equation into the form

$$-\frac{\partial}{\partial x}\left[(1+x^2)\frac{\partial X}{\partial x}\right] - \beta_{pM}\left[\frac{a}{2\sqrt{2}C^2R_0\psi^{1/2}}\frac{\cos(\alpha+\delta)+x\sin(\alpha+\delta)}{(1+x^2)^{3/4}} - \frac{B_{pM}^2}{2B_0^2}\right]X = \frac{\omega^2 a^2}{4C^2 v_{AM}^2}X. \tag{6.72}$$

Casting the equation into a variational form is easily done by multiplying by X and then integrating over the domain. The trial function chosen is

$$X = \sqrt{\frac{1}{\pi\,(1+x^2)}}. \tag{6.73}$$

This choice enables most of the integrals to be performed analytically. Further, because $|X|^2$

converges to zero as $1/x^2$, the conducting planes can be neglected as these conditions are enforced at large values of x as mentioned in Section 6.2. Performing the resulting integrals,

$$\int_{-\infty}^{\infty} \left(1+x^2\right) \left|\frac{\partial X}{\partial x}\right|^2 \, dx = \frac{1}{2}, \tag{6.74}$$

$$\int_{-\infty}^{\infty} \frac{\cos(\alpha+\delta)+x\sin(\alpha+\delta)}{(1+x^2)^{3/4}} \left|X\right|^2 \, dx \approx \frac{1}{\sqrt{2}}\cos\alpha, \tag{6.75}$$

$$\int_{-\infty}^{\infty} \left|X\right|^2 \, dx = 1. \tag{6.76}$$

In evaluating Eq. (6.75), the odd portion of the integrand vanishes. For nonzero values of χ_0, this would not be the case, and an additional term proportional to $\sin\alpha$ would appear. This would have the effect of shifting the argument of the cosine on the right hand side of Eq. (6.75) by some angle, and it would change the the numerical coefficient. Both of these effects would display a complicated dependency on the value of χ_0. In the present case, the resulting integral is performed numerically due to the factors of $\cos\delta$ and $\sin\delta$ that appear. The resulting numeric integral is close to the factor $1/\sqrt{2}$. Upon performing the integrals, the following equation results,

$$1-\beta_{pM}\left(\frac{a}{2C^2R_0}\left(\frac{a}{\Delta_M}\right)^{1/2}\cos\alpha-\frac{B_{pM}^2}{B_0^2}\right)=\frac{\omega^2}{2C^2a^2v_{AM}^2}, \tag{6.77}$$

where the choice $\psi=\Delta_M/a$ has been made, consistent with earlier approximations. Factoring B_{pM}^2/B_0^2 out and with the definition

$$\cos\alpha_c = 2C^2\frac{R_0}{a}\frac{B_{pM}^2}{B_0^2}\left(\frac{\Delta_M}{a}\right)^{1/2} = \frac{2C^2}{q^{*2}}\frac{(\Delta_M a)^{1/2}}{R}, \tag{6.78}$$

with $q^*=aB_0/RB_{pM}$, and defining $\Gamma=\omega^2a^2/v_{AM}^2$ results in

$$\Gamma = -2C^2\left[\beta_t\left(\frac{\cos\alpha}{\cos\alpha_c}-1\right)-1\right], \tag{6.79}$$

and the instability threshold becomes

$$\beta_{pM} > \frac{2C^2\frac{R}{a}\left(\frac{\Delta_M}{a}\right)^{1/2}}{\cos\alpha-\cos\alpha_c}. \tag{6.80}$$

The presence of a critical angle introduces an additional constraint that must also be satisfied, namely that $\cos\alpha_c < 1$, in order for the expression to be valid.

Using the same procedure, the ballooning instability is examined in a snowflake divertor for which it is appropriate to use a more rapidly converging test function, because of the decreased shear present in the snowflake. It is also important that the test function not converge too rapidly as this would maximize the energy created by line-bending in the differential equation, resulting in robust stability. This motivates the test function

$$X = \sqrt{\frac{3}{8\pi}} \frac{1}{1+x^2}. \tag{6.81}$$

Higher powers of $1/(1+x^2)^n$ have also been considered, but this choice gives the lowest instability threshold. For the shear, the approximation given by Eq. (6.57) is used. Because of the complicated form of s, all integrals are performed numerically. Using the same procedure as in the standard divertor case results in the equations

$$\Gamma = -\left(\frac{\Delta_M}{a}\right)^{2/3} C^2 \left[\frac{I_3}{I_4}\beta_t \frac{a}{\Delta_M}\left(\frac{\cos\alpha}{\cos\alpha_c} - 1\right) - \frac{I_1}{I_4}\right], \tag{6.82}$$

$$\cos\alpha_c = \frac{I_3}{I_2}\frac{aC^2}{Rq^{*2}}, \tag{6.83}$$

$$\beta_{pM} > C^2 \frac{I_1}{I_2} \frac{\frac{R\Delta_M}{a^2}}{\cos\alpha - \cos\alpha_c}. \tag{6.84}$$

where the values of I_j are given by

$$I_1 = \int_{-\infty}^{\infty} (1+s^2) \left|\frac{\partial X}{\partial x}\right|^2 dx, \tag{6.85}$$

$$I_2 = \frac{1}{18}\int_{-\infty}^{\infty} \frac{\cos\delta - s\sin\delta}{1+x^2} |X|^2 \, dx, \tag{6.86}$$

$$I_3 = \frac{1}{3}\int_{-\infty}^{\infty} \frac{1-xs}{1+x^2} |X|^2 \, dx, \tag{6.87}$$

$$I_4 = \frac{1}{3^{8/3}}\int_{-\infty}^{\infty} \frac{1+s^2}{(1+x^2)^{4/3}} |X|^2 \, dx, \tag{6.88}$$

and the expressions become

$$\Gamma = -\left(\frac{\Delta_M}{a}\right)^{2/3} C^2 \left[6.04\,\beta_t \frac{a}{\Delta_M}\left(\frac{\cos\alpha}{\cos\alpha_c} - 1\right) - 31.5\right], \tag{6.89}$$

$$\cos\alpha_c = 8.3\, C^2 \frac{a}{Rq^{*2}}, \tag{6.90}$$

$$\beta_{pM} > 43.2\, C^2 \frac{\frac{R\Delta_M}{a^2}}{\cos\alpha - \cos\alpha_c}. \tag{6.91}$$

Relating the distance of closest approach of the flux surface to the null point, d, the width of the SOL in the midplane, the equation, $d^3 = 3\Delta_M a^2$ results. Rewriting the instability threshold for β_t, we see that it scales as

$$\beta_t > 14.4\, C^2 \frac{\frac{d^3}{Ra^2 q^{*2}}}{\cos\alpha - \cos\alpha_c}. \tag{6.92}$$

If $\alpha = 0$ and the critical angle is set to $\pi/2$, this result agrees with the simple scalings first reported by Ryutov et al.[46]. The critical angle, which can be traced to terms proportional to derivatives of the Jacobian, is an effect due to the convergence of the field lines away from the null point and could not be captured by the simple arguments previously reported.

6.4 Application to various devices

In the preceding sections, instability thresholds for the ballooning mode have been derived which show the scalings and the dependence on the relevant parameters in both the standard and snowflake divertor configurations. The presence of a critical angle introduces an additional requirement for instability. This has been shown to be caused by the variation of the Jacobian with spatial position and is a geometrical effect due to the field-line topologies encountered in the presence of a poloidal field null. In addition, there is the well-known requirement that unfavorable curvature be present along the flux surface. A ballooning mode instability in a standard divertor could be important if it leads to heat flux broadening. At a more fundamental level, this theory places a limit on the steepness of the pressure gradient and would place a lower limit on the characteristic width of the plasma in the private flux region. This feature is also present in the snowflake divertor, with the addition that new strike points can be activated through turbulent mixing caused by the nonlinear evolution of the ballooning mode [46].

Table 6.1 sumarrizes the predicted limits for the following tokamaks: NSTX, DIII-D, TCV, and an ITER-like device. Characteristic values for q^*, a/R, and Δ_M/R are given, and C is set to unity. From these values, the instability thresholds are computed for both the standard and snowflake divertor configurations. The instability thresholds are given in the

Table 6.1: Ballooning Instability threshold applied to various tokamaks

				Standard divertor		Snowflake divertor	
Tokamak	q^*	a/R	Δ_M/R	α_c	$\beta_{pM,c}$	α_c	$\beta_{pM,c}$
NSTX[39, 85, 86]	1.60	0.80	7.1×10^{-3}	86.6°	0.24	$\cos\alpha_c > 1$	N/A
DIII-D[86]	3.17	0.40	2.1×10^{-3}	89.7°	0.36	70.7°	0.56
TCV[44, 85, 87]	2.03	0.28	9.1×10^{-3}	88.6°	1.3	55.7°	5.0
ITER[84]	3	0.32	1.6×10^{-4}	89.9°	0.14	72.8°	6.8×10^{-2}

form

$$\beta_{pM} > \frac{\beta_{pM,c}}{\cos\alpha - \cos\alpha_c}, \tag{6.93}$$

with α_c and $\beta_{pM,c}$ given in the table. For NSTX in the snowflake case, the modes are robustly stable. Even in the standard case, the threshold is large enough that instability would not occur except during a large ELM event. For TCV, instability is, in principle, possible in the snowflake case. However, the resulting threshold is too large to be realistic. From this table, it is concluded that ballooning instability is not the cause of the large heat flux events observed at the additional strike points in TCV. Considering DIII-D parameters results in a slightly lower instability threshold due to a smaller SOL width, but the threshold found is still too high to be of experimental relevance. For conditions relevant to ITER, the thresholds are lower than for the existing devices both for the standard divertor and snowflake. This is largely due to the much lower value of Δ_M/R. The smaller SOL width used for ITER is projected from a theory developed by Goldston and Eich [84] which scales well with existing devices, while a generic value of q^* is used.

This theory can also be applied in the private flux region in order to ascertain whether these modes could be responsible for the observed heat flux width in this region. To make comparisons, set $\cos\alpha = 1$ and assume $\cos\alpha_c \ll 1$. The resulting values of Δ_M justify the latter assumption. Further, the quantity, Δ_M/a is now replaced with the dimensionless flux function, ψ. The resulting flux function can then be expressed in terms of the distance from the null point, d, which is unstable, $\psi = d^2/2a^2$ for the standard divertor and $\psi = d^3/3a^3$ for the snowflake. The pressure drive is assumed to be provided by plasma transported from the

Table 6.2: Lower bound of flux width in private flux region during Inter-ELM operation

			Standard divertor		Snowflake divertor	
Tokamak	a/R	β_{pM} (Inter-ELM)	μ	d (cm)	μ	d (cm)
NSTX	0.80	$> 6 \times 10^{-3}$	5×10^{-4}	0.2	1×10^{-2}	5
DIII-D	0.40	$> 3.5 \times 10^{-3}$	1×10^{-4}	7×10^{-2}	1×10^{-2}	3
TCV	0.28	$\sim 6 \times 10^{-3}$	2×10^{-5}	3×10^{-2}	1×10^{-3}	1

SOL towards the divertor region, so characteristic values for β_{pM} are used. The instability thresholds then become

$$\psi_c = \frac{d^2}{2a^2} < \frac{1}{4}\frac{a^2}{R^2}\beta_{pM}^2, \tag{6.94}$$

for the standard divertor and

$$\psi_c = \frac{d^3}{3a^3} < \frac{1}{43.2}\frac{a}{R}\beta_{pM}, \tag{6.95}$$

for the snowflake. A ratio can then be defined of the unstable flux to the flux that characterizes the SOL, i.e., $\mu = \psi_c/(\Delta_M/a)$. This parameter is given so that as the field lines converge away from the null point, a meaningful width near the divertor plates can be determined. Again, attempting to select parameters relevant to existing devices, Table 6.2 presents both the ratio, μ, and the distance from the null point, d, that would be unstable in the private flux region. The results found are likely too small to be of consequence to the SOL in the absence of ELMDS. During an ELM, however, the value of β_{pM} can increase by a factor of $10 - 30$. In this case, the values of μ for which instability occurs are greater than those reported in Table 6.2 by factor of $100 - 900$ for the standard divertor and $10 - 30$ for the snowflake. These results supply a lower limit to the observed widths of the heat flux in the private flux region during an ELM event. To determine if this mechanism is indeed responsible, the theory would need to compared in more detail with experimental data for a given device. It would be necessary to account for the contraction of the flux as it moves from the null point towards the divertor plates.

CHAPTER 7

Axisymmetric instability in a divertor

A well known feature of the flute instability is that it can develop in strongly magnetized plasmas [88]. This instability is well studied and its details are reported in various reviews, e.g., [89, 76]. If the poloidal field vanishes identically everywhere, then the plasma is unstable with respect to the toroidally symmetric ($n = 0$) flute mode because of the unfavorable toroidal curvature present. Plasma convection in the form of toroidally symmetric "rolls" would then ensue. If a small poloidal field is included, anchored to the conducting divertor plates, stabilization will occur due to the bending of the respective field lines. Eventually, at strong enough poloidal field, the plasma is stabilized. An analysis of the linear stage of this convection in a model geometry is given in the Appendix in section A.3 with the linear stage of the convection shown in Fig. A.4. This instability is similar to the Rayleigh-Taylor instability and would ultimately lead to mixing of the plasma. In this chapter, this axisymmetric mode is considered using the geometry of a standard and snowflake divertor as described in section 6.1.

The present chapter is outlined as follows. In Sec. 7.1, a form for the axisymmetric perturbation is given, and the MHD energy principle is simplified by observing the spatial orderings relevant to the problem. Sec. 7.2 presents instability thresholds for the two geometries, and a brief discussion is given at the conclusion of the section.

7.1 Energy principle

In performing stability analysis, the ideal MHD energy principle [90] is employed in the form

$$\omega^2 = \frac{W_F}{K}, \tag{7.1}$$

$$K = \frac{1}{2}\int \rho \left|\boldsymbol{\xi}\right|^2 \, \mathrm{d}V, \tag{7.2}$$

$$W_F = \frac{1}{2}\int \left[\gamma p \left(\nabla\cdot\boldsymbol{\xi}\right)^2 + \left(\nabla\cdot\boldsymbol{\xi}\right)\left(\boldsymbol{\xi}\cdot\nabla p\right) - \frac{\mathbf{j}}{c}\cdot\left(\mathbf{Q}\times\boldsymbol{\xi}\right) + \frac{Q^2}{4\pi}\right] \, \mathrm{d}V, \tag{7.3}$$

In the above expressions, $\boldsymbol{\xi}$ represents the plasma displacement from equilibrium and is assumed to have harmonic time dependence with frequency ω. The kinetic energy is equal to $-\omega^2 K$, and the potential energy is comprised solely of a fluid term, W_F. The mass density is defined by ρ, γ is the ratio of specific heats, p is the pressure, $\mathbf{j}$ is the equilibrium current density, $\mathbf{Q} = \nabla\times\left(\boldsymbol{\xi}\times\mathbf{B}\right)$ is the perturbed magnetic field, and $\mathbf{B}$ is the equilibrium magnetic field. As in the preceding chapter, the perturbation is assumed to be localized to the vicinity of the null point, and the boundary conditions at the conducting plates are unimportant. The localization for the axisymmetric mode considered here occurs because of the increase in the magnitude of the poloidal field away from the null point and is not due to the large shear adjacent to the null that localizes the ballooning modes. At marginal stability, the potential energy will satisfy the relation $W_F = 0$.

Perturbations are considered which are of the form,

$$\boldsymbol{\xi}\times B_t\hat{\boldsymbol{\zeta}} = \nabla\Phi. \tag{7.4}$$

Using the same geometrical description given in section 6.1, ξ_ζ is not related to Φ and is left as a free parameter. However, in the situation considered, the plasma motion in the toroidal direction decouples from the motion in the poloidal plane and represents a stable, torque mode. For this reason, $\xi_\zeta = 0$ is chosen. With this choice and the previous relation, the toroidal field remains unperturbed. This is necessary because it is energetically unfavorable to perturb the toroidal field, which implies that the instability threshold is independent of B_t. Further, the analysis specializes to modes that are axisymmetric. From the previous expression, it is clear that Φ cannot depend on ζ, and with the choice that $\xi_\zeta = 0$, convection

occurs only in the poloidal plane. This choice of perturbations automatically excludes other possible unstable modes, leading the final instability threshold to be a sufficient but not a necessary condition. Substituting Eq. (7.4) into Ohm's law,

$$\mathbf{E} = \frac{i\omega}{c}\left[\nabla\Phi + \boldsymbol{\xi}\times\mathbf{B}_p\right]. \tag{7.5}$$

Because axisymmetric displacements are considered and $\xi_\zeta = 0$ is chosen, the two terms in Eq. (7.5) are orthogonal. From these conclusions, the physical interpretation of Φ becomes clear: it is proportional to that portion of the electrostatic potential that gives rise to electric fields perpendicular to the toroidal field.

From Eq. (7.4), the potential energy can be computed. To do so, the divergence of the plasma displacement, the destabilizing pressure drive, and the perturbed magnetic field are computed using the assumption that the toroidal field is well approximated by its vacuum field. These quantities become

$$\begin{aligned}
\nabla\cdot\boldsymbol{\xi} &= \nabla\left(\frac{R}{B_t}\right)\cdot\left(\nabla\zeta\times\nabla\Phi\right), && (7.6)\\
&= \left[\frac{\partial}{\partial\psi}\left(\frac{R}{B_t}\right)\nabla\psi + \frac{\partial}{\partial\chi}\left(\frac{R}{B_t}\right)\nabla\chi\right]\cdot\left[\nabla\zeta\times\left(\frac{\partial\Phi}{\partial\psi}\nabla\psi + \frac{\partial\Phi}{\partial\chi}\nabla\chi\right)\right], && (7.7)\\
&= \frac{1}{J}\left[\frac{\partial}{\partial\psi}\left(\frac{R}{B_t}\right)\frac{\partial\Phi}{\partial\chi} - \frac{\partial}{\partial\chi}\left(\frac{R}{B_t}\right)\frac{\partial\Phi}{\partial\psi}\right], && (7.8)\\
&= \frac{1}{B_tRJ}\left[\frac{\partial R^2}{\partial\psi}\frac{\partial\Phi}{\partial\chi} - \frac{\partial R^2}{\partial\chi}\frac{\partial\Phi}{\partial\psi}\right], && (7.9)
\end{aligned}$$

where the fact that B_tR is constant in this approximation has been used. The destabilizing pressure term is given by

$$\boldsymbol{\xi}\cdot\nabla p = \frac{R}{JB_t}\frac{\mathrm{d}p}{\mathrm{d}\psi}\frac{\partial\Phi}{\partial\chi}, \tag{7.10}$$

and the perturbed magnetic field by

$$\begin{aligned}
\mathbf{Q} &= \nabla\times\left(\nabla\Phi + \frac{R}{B_t}\left(\nabla\zeta\times\nabla\Phi\right)\times\left(\nabla\psi\times\nabla\zeta\right)\right), && (7.11)\\
&= \nabla\zeta\times\nabla\left[\frac{R}{B_tJ}\frac{\partial\Phi}{\partial\chi}\right], && (7.12)\\
&= \nabla\zeta\times\left[\frac{\partial}{\partial\psi}\left(\frac{R}{B_tJ}\frac{\partial\Phi}{\partial\chi}\right)\nabla\psi + \frac{\partial}{\partial\chi}\left(\frac{R}{B_tJ}\frac{\partial\Phi}{\partial\chi}\right)\nabla\chi\right], && (7.13)\\
&= \frac{1}{B_tR}\nabla\zeta\times\left[\frac{\partial}{\partial\psi}\left(\frac{R^2}{J}\frac{\partial\Phi}{\partial\chi}\right)\nabla\psi + \frac{\partial}{\partial\chi}\left(\frac{R^2}{J}\frac{\partial\Phi}{\partial\chi}\right)\nabla\chi\right], && (7.14)
\end{aligned}$$

The quantity $\mathbf{Q} \times \boldsymbol{\xi}$ is found to lie in the toroidal direction. Since there is no toroidal current, the current drive term in the potential energy vanishes. Observing the same spatial orderings as before, $|\nabla \log p| \gg |\nabla \log R^2|$, which implies that the plasma compression term, $\gamma p \left(\nabla \cdot \xi\right)^2$, can be neglected. With these simplifications, Eq. (7.3) becomes,

$$\begin{aligned} W_F = \frac{1}{2} \int J \mathrm{d}\psi \mathrm{d}\chi \mathrm{d}\zeta \, \frac{1}{R^2 B_t^2} \Bigg\{ & \frac{R^2}{J^2} \frac{\mathrm{d}p}{\mathrm{d}\psi} \left[\frac{\partial R^2}{\partial \psi} \frac{\partial \Phi}{\partial \chi} - \frac{\partial R^2}{\partial \chi} \frac{\partial \Phi}{\partial \psi} \right] \frac{\partial \Phi}{\partial \chi} \\ & + \frac{1}{4\pi R^2} \left[\left(\frac{\partial}{\partial \psi} \left(\frac{R^2}{J} \frac{\partial \Phi}{\partial \chi} \right) \right)^2 |\nabla \psi|^2 + \left(\frac{\partial}{\partial \chi} \left(\frac{R^2}{J} \frac{\partial \Phi}{\partial \chi} \right) \right)^2 |\nabla \chi|^2 \right] \Bigg\}. \end{aligned} \tag{7.15}$$

Further simplification exists if the ordering in Eq. (6.38) is observed. As before, χ is chosen to be harmonically conjugate to ψ so that $|\nabla \psi| = |\nabla \chi|$. Recalling Eqs. (6.15) and (6.19), leads to the relation that $|\nabla \psi|^2 = |\nabla \chi|^2 = R/J$. Thus, the potential energy becomes

$$\begin{aligned} W_F = \frac{1}{2} \int J \mathrm{d}\psi \mathrm{d}\chi \mathrm{d}\zeta \, \frac{1}{R^2 B_t^2} \Bigg\{ & \frac{R^2}{J^2} \frac{\mathrm{d}p}{\mathrm{d}\psi} \left[\frac{\partial R^2}{\partial \psi} \frac{\partial \Phi}{\partial \chi} - \frac{\partial R^2}{\partial \chi} \frac{\partial \Phi}{\partial \psi} \right] \frac{\partial \Phi}{\partial \chi} \\ & + \frac{R^3}{4\pi J} \left[\left(\frac{\partial}{\partial \psi} \left(\frac{1}{J} \frac{\partial \Phi}{\partial \chi} \right) \right)^2 + \left(\frac{\partial}{\partial \chi} \left(\frac{1}{J} \frac{\partial \Phi}{\partial \chi} \right) \right)^2 \right] \Bigg\}. \end{aligned} \tag{7.16}$$

Next, the energy principle is cast in a scaled form using the same transformations given in section 6.2, i.e., $\psi \to CRaB_{pM}\psi$ and $\chi \to CRaB_{pM}\chi$. The Jacobian is also transformed to a dimensionless form and becomes $1/J \to RB_{pM}^2/J$ to yield

$$\begin{aligned} W_F = \frac{1}{2} \int \mathrm{d}\psi \mathrm{d}\chi \mathrm{d}\zeta \, \frac{RC^2 B_{pM}^2}{4\pi a^2 B_t^2} \Bigg\{ & \frac{1}{J} \frac{4\pi}{C^2 B_{pM}^2} \frac{\mathrm{d}p}{\mathrm{d}\psi} \left[\frac{\partial \log R^2}{\partial \psi} \frac{\partial \Phi}{\partial \chi} - \frac{\partial \log R^2}{\partial \chi} \frac{\partial \Phi}{\partial \psi} \right] \frac{\partial \Phi}{\partial \chi} \\ & + \left[\left(\frac{\partial}{\partial \psi} \left(\frac{1}{J} \frac{\partial \Phi}{\partial \chi} \right) \right)^2 + \left(\frac{\partial}{\partial \chi} \left(\frac{1}{J} \frac{\partial \Phi}{\partial \chi} \right) \right)^2 \right] \Bigg\}. \end{aligned} \tag{7.17}$$

It now remains to apply the precise geometry of the standard and snowflake divertors to Eq. (7.17) using a scaled form of Eqs. (6.48), (6.49), (6.51), and (6.52). After these substitutions, the potential energy for the standard divertor reduces to

$$\begin{aligned} W_F = \frac{1}{2} \int \mathrm{d}\psi \mathrm{d}\chi \mathrm{d}\zeta \, & \frac{RC^2 B_{pM}^2}{4\pi a^2 B_t^2} \times \\ & \Bigg\{ \frac{8\pi}{B_{pM}^2} \frac{\mathrm{d}p}{\mathrm{d}\psi} \frac{\sqrt{2}a}{C^2 R_0} \left(\psi^2 + \chi^2\right)^{1/4} \left[\cos(\alpha + \delta) \frac{\partial \Phi}{\partial \chi} - \sin(\alpha + \delta) \frac{\partial \Phi}{\partial \psi} \right] \frac{\partial \Phi}{\partial \chi} \\ & + 4(\psi^2 + \chi^2) \left[\left(\frac{\partial^2 \Phi}{\partial \psi \partial \chi} + \frac{\psi}{\psi^2 + \chi^2} \frac{\partial \Phi}{\partial \chi} \right)^2 + \left(\frac{\partial^2 \Phi}{\partial \chi^2} + \frac{\chi}{\psi^2 + \chi^2} \frac{\partial \Phi}{\partial \chi} \right)^2 \right] \Bigg\}, \end{aligned} \tag{7.18}$$

where δ is given by Eq. (6.50) with $m = 2$. Choosing $m = 3$, the same expressions can be substituted for the snowflake which leads to,

$$W_F = \frac{1}{2}\int \mathrm{d}\psi \mathrm{d}\chi \mathrm{d}\zeta \, \frac{RC^2 B_{pM}^2}{4\pi a^2 B_t^2} \times \\ \left\{ \frac{8\pi}{B_{pM}^2}\frac{\mathrm{d}p}{\mathrm{d}\psi}\frac{3^{2/3}a}{C^2 R_0}\left(\psi^2+\chi^2\right)^{1/3}\left[\cos(\alpha+\delta)\frac{\partial\Phi}{\partial\chi} - \sin(\alpha+\delta)\frac{\partial\Phi}{\partial\psi}\right]\frac{\partial\Phi}{\partial\chi} \right. \\ \left. +3^{8/3}(\psi^2+\chi^2)^{4/3}\left[\left(\frac{\partial^2\Phi}{\partial\psi\partial\chi}+\frac{4}{3}\frac{\psi}{\psi^2+\chi^2}\frac{\partial\Phi}{\partial\chi}\right)^2 + \left(\frac{\partial^2\Phi}{\partial\chi^2}+\frac{4}{3}\frac{\chi}{\psi^2+\chi^2}\frac{\partial\Phi}{\partial\chi}\right)^2\right]\right\}. \tag{7.19}$$

7.2 Instability threshold

In order to determine a meaningful instability threshold, the pressure gradient is specified to be

$$\frac{\mathrm{d}p}{\mathrm{d}\psi} = -p_0\delta(\psi-\psi_0), \tag{7.20}$$

with $\psi_0 = \Delta_M/a$ as before. This allows for the integral over ψ to be performed for terms proportional to the pressure. Using this property, an instability threshold can be determined for both the standard and snowflake divertors for an arbitrary test function, Φ. These thresholds are

$$\beta_{pM} > \frac{2\sqrt{2}C^2R_0}{a}\frac{\int \mathrm{d}\chi\mathrm{d}\psi\,(\psi^2+\chi^2)\left[\left(\frac{\partial^2\Phi}{\partial\psi\partial\chi}+\frac{\psi}{\psi^2+\chi^2}\frac{\partial\Phi}{\partial\chi}\right)^2+\left(\frac{\partial^2\Phi}{\partial\chi^2}+\frac{\chi}{\psi^2+\chi^2}\frac{\partial\Phi}{\partial\chi}\right)^2\right]}{\int \mathrm{d}\chi\,\left(\psi_0^2+\chi^2\right)^{1/4}\left[\cos(\alpha+\delta)\frac{\partial\Phi}{\partial\chi}-\sin(\alpha+\delta)\frac{\partial\Phi}{\partial\psi}\right]\Big|_{\psi_0}\left.\frac{\partial\Phi}{\partial\chi}\right|_{\psi_0}}, \tag{7.21}$$

for the standard divertor, and

$$\beta_{pM} > \frac{9C^2R_0}{a}\frac{\int \mathrm{d}\chi\mathrm{d}\psi\,(\psi^2+\chi^2)^{4/3}\left[\left(\frac{\partial^2\Phi}{\partial\psi\partial\chi}+\frac{4}{3}\frac{\psi}{\psi^2+\chi^2}\frac{\partial\Phi}{\partial\chi}\right)^2+\left(\frac{\partial^2\Phi}{\partial\chi^2}+\frac{4}{3}\frac{\chi}{\psi^2+\chi^2}\frac{\partial\Phi}{\partial\chi}\right)^2\right]}{\int \mathrm{d}\chi\,\left(\psi_0^2+\chi^2\right)^{1/3}\left[\cos(\alpha+\delta)\frac{\partial\Phi}{\partial\chi}-\sin(\alpha+\delta)\frac{\partial\Phi}{\partial\psi}\right]\Big|_{\psi_0}\left.\frac{\partial\Phi}{\partial\chi}\right|_{\psi_0}}, \tag{7.22}$$

for the snowflake.

A trial function must now be chosen subject to the localization condition. In the poloidal direction, the mode is assumed to be localized over some distance d from the null point. This position corresponds to the poloidal coordinate through the relation $\chi = \pm\chi_0$ where $\chi_0 = d^2/2a^2$ for the standard divertor and $\chi_0 = d^3/3a^3$ for the snowflake. With this orientation,

it is required that both Φ and its first derivative with respect to χ vanish at $\chi = \pm\chi_0$ and that Φ vanish as $\psi \to \pm\infty$ in order to prevent complications arising from branch cuts. To motivate the form of the trial function, it is important to observe that if $\partial\Phi/\partial\chi = J$, then the magnetic compression term vanishes, and the system is unstable for any nontrivial value of β_{pM}. For this reason, a trial function is chosen such that $\partial\Phi/\partial\chi$ is the Jacobian multiplied by another function which allows the boundary conditions to be satisfied. This other function is chosen to be similar to the form of the eigenfunction found in the model problem and given by Eq. (A.33).

Considering first the standard divertor, the trial function is

$$\Phi = \int_{-\chi_0}^{\chi} \mathrm{d}\chi' \, \frac{f(\chi', \psi)}{(\chi'^2 + \psi^2)^{1/2}}, \tag{7.23}$$

where

$$f(\chi, \psi) = \sin\left(\frac{\pi\chi}{\chi_0}\right) \exp\left(-\frac{\pi\,|\psi - \psi_0|}{\chi_0}\right). \tag{7.24}$$

This trial function and its first derivative with respect to χ vanish at $-\chi_0$. At $\chi = \chi_0$, Φ vanishes because the integrand is odd, and $\partial\Phi/\partial\chi$ vanishes because $f(\chi_0, \psi) = 0$ by design. Substituting the previous equation into the instability threshold given in Eq. (7.21) and performing the necessary derivatives, the numerator is vastly simplified and the integrations can be performed analytically, while the denominator must be evaluated numerically. To obtain a qualitative estimate, $\alpha = 0$ is chosen to maximize the instability drive. Upon performing these substitutions and scaling the poloidal integration variable in the denominator through the relation, $x = \chi/\chi_0$, it can be shown that the instability threshold reduces to

$$\beta_{pM} > \frac{4\sqrt{2}\pi C^2}{\mu^{1/2} I_{Sd}} \frac{R_0}{a} \left(\frac{\Delta_M}{a}\right)^{1/2}, \tag{7.25}$$

where

$$\begin{aligned} I_{Sd} = &\int_{-1}^{1} \frac{\cos\left(\frac{1}{2}\tan^{-1}(x/\mu)\right) \sin^2 \pi x}{(x^2 + \mu^2)^{3/4}} \, \mathrm{d}x \\ &+ \int_{-1}^{1} \left[\frac{\sin\left(\frac{1}{2}\tan^{-1}(x/\mu)\right) \sin \pi x}{(x^2 + \mu^2)^{1/4}} \left(\int_{-1}^{x} \frac{\mu \sin \pi y}{(y^2 + \mu^2)^{3/2}} \, \mathrm{d}y \right) \right] \mathrm{d}x, \end{aligned} \tag{7.26}$$

where I_{Sd} depends on a single parameter, $\mu = \psi_0/\chi_0 = 2\Delta_M a/d^2$. For $\mu = 0.333$, the

instability threshold has a minimum of

$$\beta_{pM} > 19\ C^2 \frac{R_0}{a} \left(\frac{\Delta_M}{a} \right)^{1/2}, \tag{7.27}$$

which implies that the mode has a poloidal extent of $d/a = 2.5\ (\Delta_M/a)^{1/2}$.

Applying the same procedure to the snowflake divertor, and choosing the trial function to be

$$\Phi = \int_{-\chi_0}^{\chi} \mathrm{d}\chi' \, \frac{f(\chi', \psi)}{(\psi^2 + \chi'^2)^{2/3}}, \tag{7.28}$$

with f defined as before in Eq. (7.24) leads to

$$\beta_{pM} > \frac{18\pi C^2}{\mu I_{Sf}} \frac{R_0 \Delta_M}{a^2}, \tag{7.29}$$

where

$$\begin{aligned} I_{Sf} = & \int_{-1}^{1} \frac{\cos\left(\frac{2}{3}\tan^{-1}(x/\mu)\right) \sin^2 \pi x}{x^2 + \mu^2} \, \mathrm{d}x \\ & + \frac{4}{3}\mu \int_{-1}^{1} \left[\frac{\sin\left(\frac{2}{3}\tan^{-1}(x/\mu)\right) \sin \pi x}{(x^2 + \mu^2)^{1/3}} \left(\int_{-1}^{x} \frac{\sin \pi y}{(y^2 + \mu^2)^{5/3}} \, \mathrm{d}y \right) \right] \, \mathrm{d}x. \end{aligned} \tag{7.30}$$

For the snowflake divertor, the parameter, μ, relates to physical scales through the relation $\mu = \psi_0/\chi_0 = 3a^2\Delta_M/d^3$. For $\mu = 0.100$, the instability threshold has a minimum of

$$\beta_{pM} > 170\ C^2 \frac{R_0 \Delta_M}{a^2}, \tag{7.31}$$

which implies that the mode has a poloidal extent of $d/a = 3.1\ (\Delta_M/a)^{1/3}$.

If comparison between the instability thresholds for the axisymmetric mode, Eqs. (7.27) and (7.31), and that of the ballooning instability, Eqs. (6.80) and (6.91), it is seen that the instability thresholds scale with device parameters in the same manner. The dimensionless, numerical coefficient in the instability threshold for the ballooning mode is lower than that derived for the axisymmetric mode. For this reason, the instability threshold for the axisymmetric mode is also not satisfied for the machine parameters outlined in section 6.4, and the ballooning mode is more likely to exhibit instability in a given device. This analysis suggests that MHD instability is unlikely to account for the convective mixing observed on TCV [44].

CHAPTER 8

Conclusions

Experimental results from the investigation of the ion-ion hybrid resonator in the Large Plasma Device (LAPD) at UCLA are analyzed. Long-lived modes are found with quality factors of roughly 20. A full-wave description that models the cold plasma response but neglects coupling to the compressional wave, finite ion temperature effects, and radial gradients in the plasma, predicts the observed resonant frequencies and is consistent with the measured radial shape of the resonator modes. Dissipation due to electron collisions is included in the model, and the predicted quality factors are an order of magnitude larger than those found experimentally. An assessment of radial convection of the wave energy due to finite ion temperature effects and coupling to the compressional mode is made using a ray-tracing approach. The rays are shown to experience a radial reflection as they approach the parallel reflection point. At small values of $k_\perp$, those least affected by electron collisions, the perpendicular refraction in the reflection layer is pronounced, and the wave energy convects towards the edge of the plasma. An estimate of the dissipation due to radial convection shows that the quality factors are too large by a factor of 5. Ion-neutral collisions, ion-cyclotron damping, and electron Landau damping are all unlikely to explain the observed dissipation. Further investigation should consider the inclusion of radial gradients coupled with mode-conversion to ion-Bernsten waves as a possible explanation. Another possibility is transit-time acceleration experienced by electrons in the reflection region.

Ray-tracing studies are also performed for a pure toroidal field relevant to the Enormous Toroidal Plasma Device (ETPD). It has been demonstrated that for rays propagating along a curved field line, field-line curvature effects preferentially increase the component of the wave vector in the direction opposite to the curvature of the field line. This effect coupled

with a zero in the perpendicular group velocity leads to radial focusing. The radial focusing of the wave enhances energy trapping in resonators that exist along a field line where the curvature is predominantly in one direction. These effects are present for both a cold plasma and for finite ion-temperature. The introduction of finite ion temperature complicates this picture by introducing additional radial reflections in the perpendicular group velocity. As $k_\perp$ evolves along the ray trajectory, a single ray can experience each of these reflections.

When ion temperature effects are negligible in a tokamak fusion device, as may be the case for edge conditions, the ray tracing studies show that a resonator can exist. The effects of field line curvature cause the ray to be focused radially allowing for many reflections which largely retrace each other. However, when ion temperature effects are included, this picture is altered, because the parallel reflection point now becomes a function of $k_\perp$. From a one-dimensional WKB formulation, it is seen that magnetic shear and curvature cause coupling to the ion-Bernstein wave. This causes the size of the well to increase for a given frequency, and the eigenfrequencies of a given mode shift to lower frequency as the ion temperature increases.

The one-dimensional WKB model is also used to assess kinetic damping and possible instability due to interaction with fusion-born alpha particles in a tokamak fusion device. It is determined that roughly 20 modes are weakly damped over the radial extent of the plasma with frequencies lying in a narrow bandwidth just above the local ion-ion hybrid frequency on the outboard side. These modes are largely limited by electron Landau damping. For mode numbers roughly greater than 20, ion cyclotron damping causes the modes to be heavily damped, preventing the formation of a resonator mode. It is determined that the resonator modes are confined poloidally to the outboard side, spanning a poloidal angle of 10-50 degrees. Instability by fusion-born alpha particles can result in roughly three e-foldings of amplitude increase in one pass through the resonant cavity and occurs for a bandwidth of roughly 600 kHz above the local ion-ion hybrid frequency on the outboard side. If the effects of shear and magnetic curvature are included, detuning from the drive provided by the alpha particles can occur. Further investigation of these effects with the use of state of the art codes is warranted.

Cherenkov radiation by a charged particle burst in a two ion species plasma is also considered. The wake pattern is obtained for the inertial and kinetic regimes of wave propagation. Due to the presence of two ion-species, the Alfvén waves propagate within two different frequency bands separated by a gap. One band is restricted to frequencies below the cyclotron frequency of the heavier species and the other to frequencies between the ion-ion hybrid frequency and the cyclotron frequency of the lighter species. The radiation pattern in the lower frequency band is found to exhibit essentially the same properties reported in a previous study [50] of a single species plasma. However, the upper frequency band differs from the lower one in that it always allows for the Cherenkov radiation condition to be met. The methodology is extended to examine the Alfvénic wake of point-charges in the inertial and adiabatic regimes. The adiabatic regime is illustrated for conditions applicable to fusion-born alpha particles in ITER.

In considering MHD stability in the plasma in the divertor of a tokamak, sufficient instability thresholds for both ballooning modes and axisymmetric, quasi-flute modes are determined. The resulting thresholds are applied for the parameters of three tokamaks: NSTX, DIII-D, and TCV. It is determined that these modes should be stable in these three devices. From this stability, it is concluded that MHD instability is unlikely to explain recent experimental results [44] which suggest that convection is occurring close to the null point of the divertor. This suggests that MHD theory is unable to account for this transport provided the assumptions made in the analysis are correct. The precise form of the pressure distribution in the vicinity of the null point is unknown. One weakness of MHD is in the assumption of an equilibrium in which the pressure is assumed to be constant on a flux surface. In the divertor region, pressure gradients exist between the plasma in the scrape-off-layer in the midplane and the plasma adjacent to the divertor plates. These gradients coupled with the weak poloidal field present in the vicinity of the null may make it impossible to describe the plasma equilibrium, if it exists at all, in the framework of MHD theory. Even if the pressure distribution could be described as a flux function, the precise pressure distributions assumed in the analysis may also not be correct. Specifically, a nonzero pressure gradient present on the separatrix (and on the null point) may drastically alter the results reported

here. However, the analysis provides a framework in which future work can be performed. From the discrepancy between theory and experiment, it is determined that the underlying assumption of a valid plasma equilibrium is likely not valid, and future work should be concentrated in this area.

APPENDIX A

MHD Stability in a model geometry

A.1 Model geometry and correspondence to divertor

The geometry of the flux surfaces present in a snowflake divertor is shown in Fig. A.1. The horizontal axis is the radial coordinate and is expressed in terms of x where $r = R + x$, R being the major radius of the $B_p = 0$ circle and r, the radial distance from the major axis. The vertical axis, z, runs parallel to the major axis, though the divertor could be rotated through an arbitrary angle. The toroidal coordinate lies into the page. The black and red lines represent the nested magnetic flux surfaces with the thicker black lines representing the separatrices. The thick green segments are representative of the divertor plates upon which heat is deposited due to the streaming of the plasma along the field lines. The core plasma is contained in the top sextant with the two adjacent sextants containing the scrape off layer (SOL). The three remaining sextants in the lower half plane are private flux regions and are largely isolated from the remainder of the plasma in the absence of instability. With the orientation shown in the figure, private flux regions 1, 2, and 3 have portions of the flux surface which experience unfavorable curvature, and as a result, these flux surfaces could be unstable.

A somewhat simpler geometrical description can be adopted as a model problem to examine the features relevant to stability. This geometry is shown in Fig. A.2. The horizontal axis is the radial distance from the major axis of the device, and the vertical axis lies along the major axis, represented by the dashed-dotted line, which is defined to be the z direction. The plasma is shown as the gray shaded region. In the figure, the toroidal field, B_t, is into the page and indicated by the blue "x"es, and the poloidal field, B_p, is vertical and

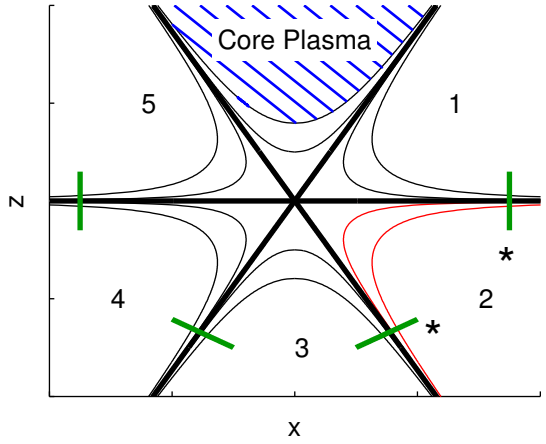

Figure A.1: Flux surfaces of snowflake divertor. Horizontal axis is radial distance from the null point. Green segments represent divertor plates, thicker black lines are separatrices, and thin curves are flux surfaces. If red lines are stretched vertically and the divertor plates marked by asterisks are reoriented, the geometry reduces to Fig. A.2 which is possibly unstable. We specialize to sextant 2. Sextants 1 and 3 may also be unstable.

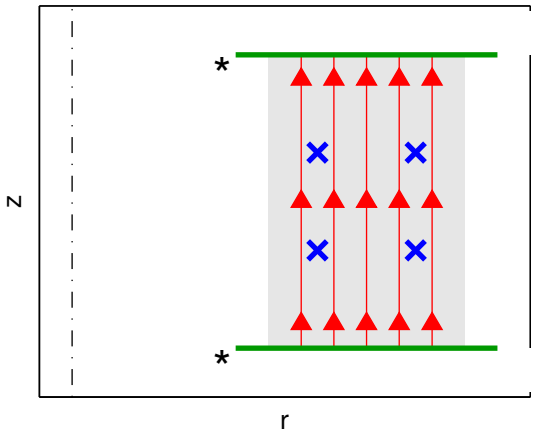

Figure A.2: A simplified geometry of Fig. A.1. Vertical axis is major axis, indicated by the dashed-dotted line, and the horizontal axis is radial distance from the major axis. Shaded, gray region is an annulus of plasma. Blue "x"es represent the toroidal field that points into the page. Poloidal field is represented by the red lines. Conducting plates are represented by the thick green segments. The plasma stability is determined by the value of β_p and distance between plates. Asterisks are used to make connection to Fig. A.1.

indicated by the red lines. In the vertical direction, the plasma is limited by conducting plates, illustrated by the green segments. In the presence of a vertical field, the line-tying boundary conditions can stabilize the plasma. To make connection between the general divertor geometry and the simplified geometry, two divertor plates have been marked by an asterisk in both Figs. A.1 and Fig. A.2. Focus is given to the private flux region in Fig. A.1 that has red lines with the other private flux regions ignored. If the orientations of the two plates in Fig. A.1 are changed such that they are parallel to each other and the connecting flux surfaces are rectified, Fig. A.1 is transformed into Fig. A.2 with the asterisks marking the position to which the plates have shifted. In making the transformation, the orientation of the coordinates is chosen such that the vector $\hat{\mathbf{z}}$ points in the vertical direction, the vector $\hat{\mathbf{r}}$ points to the right, and the toroidal direction, $\hat{\boldsymbol{\phi}}$, points into the board. The divertor plates exist as planes located at $z = 0,\ L$, at which the appropriate boundary conditions must be imposed. This is in contrast to the instabilities considered in Chapters 6 and 7 where localization of the mode occurred as a simple consequence of either the shear near the null or the rapid increase in the poloidal field strength. In the model geometry, the boundary conditions at the divertor plates are necessary to stabilize the system.

In the simplified geometry, a general equilibrium presents no great complication. For this reason, an equilibrium is considered in which both a toroidal and poloidal current density are present. In this case, the equilibrium is now defined by

$$\frac{\mathrm{d}p}{\mathrm{d}r} = \frac{j_t B_p}{c} - \frac{j_p B_t}{c}. \tag{A.1}$$

This allows the pressure to be partitioned into two functions, p_p and p_t, satisfying $\mathrm{d}p_p/\mathrm{d}r = j_t B_p/c$ and $\mathrm{d}p_t/\mathrm{d}r = -j_p B_t/c$. Using Ampère's law and solving for the fields leads to

$$B_p^2(r) = B_{p0}^2 - 8\pi p_p(r), \tag{A.2}$$

$$B_t^2(r) = B_{t0}^2 \left(\frac{r_0}{r}\right)^2 - 8\pi \int_{r_0}^{r} \frac{\mathrm{d}p_t}{\mathrm{d}r'} \left(\frac{r'}{r}\right)^2 \mathrm{d}r', \tag{A.3}$$

where now, the poloidal field is no longer curl free. It is still assumed that $\beta_t \ll 1$, which allows the toroidal fields to be approximated by their vacuum case and the integral in Eq. (A.3) to be neglected.

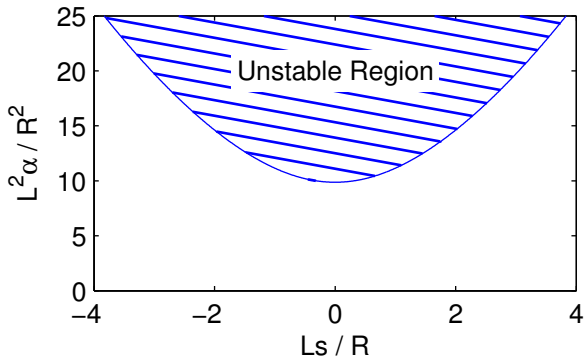

Figure A.3: Instability threshold for ballooning modes with a vertical poloidal field and azimuthal toroidal field. Horizontal axis is the product of the shear, s, given by Eq. (A.8) with the distance between conducting planes, L, divided by the major radius, R. The vertical axis gives the instability threshold for the parameter, α, given by Eq. (A.9) multiplied by L^2/R^2. Instability exists when parameters fall above the curve.

A.2 Ballooning instability in model geometry

Consider now the case of a straight poloidal field with no null, i.e., the $m = 1$ case in Section 6.1. Instead of the designation that $|\nabla\psi| = |\nabla\chi|$, choose that $\psi = \int_0^x RB_p\, dx'$ and $\chi = z$. The Jacobian is $J = 1/B_p$. In order to have a valid equilibrium, R must be aligned with the x-axis and $\alpha = 0$. Computing first the gradient of the eikonal, it can be shown that

$$k_t = n\frac{1}{R}\frac{B}{B_p}, \tag{A.4}$$

$$k_n = -n\frac{\partial}{\partial x}\left[\frac{B_t}{RB_p}\right](z - z_0). \tag{A.5}$$

Since the curvature is solely in the normal direction with no geodesic curvature present,

$$\boldsymbol{\kappa} = -\frac{B_t^2}{RB^2}\hat{\mathbf{x}}. \tag{A.6}$$

Substituting these expressions into Eq. (6.28) gives

$$W(\psi) = \int \frac{dz}{R^2 B_p}\left[\left(1 + \left(\frac{B_t}{B}\frac{\nu'}{\nu}(z - z_0)\right)^2\right)\left|\frac{\partial X}{\partial z}\right|^2 + \frac{8\pi p}{B^2}\frac{B_t^2}{B_p^2}\frac{p'}{pR}|X|^2\right], \tag{A.7}$$

where, in this case, $\nu = B_t/RB_p$ and a prime denotes a derivative with respect to R which

is equivalent to a derivative with respect to x. Defining the following parameters,

$$s = \frac{B_t}{B}\frac{d\log\nu}{d\log R}, \tag{A.8}$$

$$\alpha = \beta_p \frac{B_t^2}{B^2}\left|\frac{d\log p}{d\log R}\right|, \tag{A.9}$$

and scaling the z coordinate to the distance between the plates, L, by making the transformation, $z' = z/L$, the potential energy can be rewritten as

$$W(\psi) = \int \frac{dz}{R^2 L^2 B_p}\left[\left(1+\left(\frac{sL}{R}(z'-z_0')\right)^2\right)\left|\frac{\partial X}{\partial z'}\right|^2 - \frac{L^2}{R^2}\alpha\left|X\right|^2\right]. \tag{A.10}$$

Again, a differential equation can be found which governs the eigenfunctions that exist at marginal stability,

$$\frac{\partial}{\partial z'}\left[\left(1+\left(\frac{sL(z'-z_0')}{R}\right)^2\right)\frac{\partial X}{\partial z'}\right] + \frac{L^2}{R^2}\alpha X = 0, \tag{A.11}$$

with X on the domain, $z' \in (-1/2, 1/2)$. From the potential energy formulation, the shear term is to be minimized, so $z_0' = 0$ is chosen. If the shear is negligible, the most unstable mode is given by

$$X = C\cos\left(\pi z'\right), \tag{A.12}$$

and results in the instability threshold that

$$\alpha > \frac{\pi^2 R^2}{L^2}. \tag{A.13}$$

Figure A.3 displays the instability threshold as a function of shear. It is assumed that the poloidal field is constant with radius, that the poloidal field is small relative to the toroidal field so that $B_t \approx B$, and that the toroidal field is well approximated by its vacuum solution, i.e. that $\beta_t \ll 1$, then $s = -2$. To arrive at a numerical estimate, take $R/L = 5$. This gives the instability threshold of $\alpha > 252$. The derivative, $|d\log p/d\log R| = R/L_p$, where L_p is the characteristic length scale over which the pressure gradient drops. Taking this to be the width of the SOL in TCV, 8 mm, the instability threshold results in $\beta_p > 2.3$.

A.3 Axisymmetric mode in model geometry

As mentioned previously, in considering the axisymmetric mode in this model geometry, the boundary conditions at the divertor plates are important. The divertor plates are assumed to be perfect conductors, and so, line-tying boundary conditions are appropriate. From Ohm's law, it can be shown that this requires

$$\xi_r|_{z=0,L} = 0, \qquad \xi_z|_{z=0,L} = 0, \tag{A.14}$$

$$\left.\frac{\partial\Phi}{\partial r}\right|_{z=0,L} = 0, \qquad \left.\frac{\partial\Phi}{\partial z}\right|_{z=0,L} = 0, \tag{A.15}$$

where the conducting plates are located at positions, $z = 0$ and L. Equation (7.4) relates the components of $\boldsymbol{\xi}$ to the function, Φ.

From Eq. (7.3), the potential energy can be computed. To do so, the perturbed magnetic field and the divergence of the plasma displacement are computed using the assumption that the toroidal field is well approximated by its vacuum field. These quantities become

$$\nabla\cdot\boldsymbol{\xi} = \frac{2}{rB_t}\frac{\partial\Phi}{\partial z} = \frac{2}{r}\xi_r, \tag{A.16}$$

$$\mathbf{Q} = \hat{\mathbf{r}}\frac{B_p}{B_t}\frac{\partial^2\Phi}{\partial z^2} - \hat{\mathbf{z}}\frac{1}{r}\frac{\partial}{\partial r}\left(\frac{rB_p}{B_t}\frac{\partial\Phi}{\partial z}\right) = \hat{\mathbf{r}}B_p\frac{\partial\xi_r}{\partial z} - \hat{\mathbf{z}}\frac{1}{r}\frac{\partial}{\partial r}\left(rB_p\xi_r\right). \tag{A.17}$$

These expressions are then combined with the equilibrium current distribution

$$\frac{4\pi\mathbf{j}}{c} = \hat{\mathbf{z}}\frac{1}{r}\frac{\mathrm{d}}{\mathrm{d}r}\left(rB_t\right) - \hat{\phi}\frac{\mathrm{d}B_p}{\mathrm{d}r}, \tag{A.18}$$

where the general equilibrium given in section A.1 is assumed. Substituting the previous relations into the energy principle gives rise to the following equation for the potential energy

$$W_F = \int\left[\frac{2\gamma p\xi_r^2}{r^2} + \frac{\xi_r^2}{r}\frac{\mathrm{d}p_t}{\mathrm{d}r} + \frac{B_p^2}{8\pi}\left(\left(\frac{\partial\xi_r}{\partial z}\right)^2 + \left(\frac{1}{r}\frac{\partial(r\xi_r)}{\partial r}\right)^2\right)\right]\mathrm{d}V, \tag{A.19}$$

where the pressure partition made in Sec. A.1 is used to reduce the quantity, $\mathrm{d}(p+B_p^2/8\pi)/\mathrm{d}r$ to $\mathrm{d}p_t/\mathrm{d}r$, where p_t is that portion of the plasma pressure which is confined by the toroidal field. The boundary condition that $\xi_z = 0$ at the divertor plates and the relation in Eq. (A.16) coupled with integration by parts have been used to obtain the form shown in Eq. (A.19). At this point, further simplification can be made if it is assumed that the perturbations are

localized at a radius much larger than any other scale length in the problem. This is valid because the pressure variation in the divertor region is very rapid compared to R. This assumption allows the first term in Eq. (A.19) to be neglected in favor of the second term and to expand derivatives in r using the relation $r = R + x$ to lowest order in $1/R$. If this is done, Eq. (A.19) becomes

$$W_F = \int \left[\frac{\xi_r^2}{R} \frac{\mathrm{d}p_t}{\mathrm{d}x} + \frac{B_p^2}{8\pi} \left(\left(\frac{\partial \xi_r}{\partial z} \right)^2 + \left(\frac{\partial \xi_r}{\partial x} \right)^2 \right) \right] \mathrm{d}V. \tag{A.20}$$

The first term in the integrand above is the source of free energy which drives the instability.

Next, it is useful to consider the resulting Euler equation associated with the energy principle. This can be done either from the energy principle or directly from the equations of motion from which the energy principle is derived. Either way, the same equation results, and it is more easily expressed in terms of the function, Φ, than in terms of ξ_r. The resulting differential equation is

$$\nabla \cdot \left[\frac{\rho\omega^2}{2} \nabla\Phi \right] + \frac{\partial^2}{\partial z^2} \left[-\frac{1}{R} \frac{\mathrm{d}p_t}{\mathrm{d}x} \Phi + \frac{B_p^2}{8\pi} \nabla^2 \Phi + \frac{\mathrm{d}}{\mathrm{d}x} \left(\frac{B_p^2}{8\pi} \right) \frac{\partial \Phi}{\partial x} \right] = 0, \tag{A.21}$$

where $\nabla = \hat{\mathbf{x}}\partial/\partial x + \hat{\mathbf{z}}\partial/\partial z$. This equation is inseparable in general, i.e., the solution cannot be written as a product of a function of x and a function of z. This makes it difficult to obtain the normal modes when not at marginal stability. Semi-analytic methods exist to solve non-separable problems [91], however, since this is a model problem, such a sophisticated treatment is unwarranted.

The problem is separable if the conducting plates are removed and the plasma is assumed to be of infinite extent. A Fourier decomposition can then be performed in the z direction so that $\xi_r \propto \exp(ikz)$. For this case, Eq. (A.21) becomes

$$\frac{\partial}{\partial x} \left[\left(\frac{\rho\omega^2}{2k^2} - \frac{B_p^2}{8\pi} \right) \frac{\partial \Phi}{\partial x} \right] + \left[\frac{1}{R} \frac{\mathrm{d}p_t}{\mathrm{d}x} - k^2 \left(\frac{\rho\omega^2}{2k^2} - \frac{B_p^2}{8\pi} \right) \right] \Phi = 0. \tag{A.22}$$

For Fourier harmonics that satisfy $\omega^2/k^2 \gg B_p^2/4\pi\rho$, the terms proportional to B_p^2 can be neglected. Recasting in a variational form,

$$\omega^2 = \frac{\int \frac{1}{R} \frac{\mathrm{d}p_t}{\mathrm{d}x} |\Phi|^2 \, \mathrm{d}x}{\int \frac{\rho}{2k^2} \left[\left| \frac{\partial \Phi}{\partial x} \right|^2 + k^2 |\Phi|^2 \right] \mathrm{d}x}, \tag{A.23}$$

where the denominator is positive definite, because it relates to the kinetic energy contained in the perturbation. The numerator can be made negative so long as Φ is localized to a region for which $\mathrm{d}p_t/\mathrm{d}x$ is negative. From this, it is concluded that without the stabilization of the conducting end plates, this situation is unstable to modes of long wavelength in the direction of the poloidal field.

If the plates are included, the problem is also separable if marginal stability is considered. To illustrate this, a rapid pressure drop is assumed which can be approximated by a delta-function pressure gradient. When this choice is made, Eq. (A.21) is separable at marginal stability and can be solved exactly. Here, the poloidal field is allowed to vary and $p_t \neq p$. Thus, the pressure gradient is

$$-\frac{\mathrm{d}p_t}{\mathrm{d}x} = p_{t0}\delta(x). \tag{A.24}$$

$$B_p = \begin{cases} B_{pi}, & x < 0 \\ B_{p0}, & x > 0 \end{cases}, \tag{A.25}$$

where p_{t0} now represents the amount of plasma pressure confined by the toroidal field, and B_{pi} and B_{p0} are the values of the poloidal field on each side of the pressure drop. The problem is reduced to solving the equation

$$\frac{\partial^2}{\partial z^2}\left[\frac{p_{t0}}{R}\delta(x)\Phi + \frac{B_p^2}{8\pi}\nabla^2\Phi + \frac{\mathrm{d}}{\mathrm{d}x}\left(\frac{B_p^2}{8\pi}\right)\frac{\partial\Phi}{\partial x}\right] = 0, \tag{A.26}$$

subject to the boundary conditions in Eq. (A.15). The delta-function gives a jump condition for Φ which must be satisfied by connecting the two solutions on either side of the discontinuity. Away from the gradient, the equation reduces to Laplace's equation for the second order derivative of Φ with respect to z. The solutions are easily written as

$$\frac{\partial^2\Phi}{\partial z^2} = -k^2 f_1(x)\cos(kz) - k^2 f_2(x)\sin(kz), \tag{A.27}$$

$$\frac{\partial\Phi}{\partial z} = -k f_1(x)\sin(kz) + k f_2(x)\cos(kz) + k f_3(x), \tag{A.28}$$

$$\Phi = f_1(x)\cos(kz) + f_2(x)\sin(kz) + f_3(x)kz + f_4(x). \tag{A.29}$$

Applying the boundary conditions leads to the solution

$$\Phi = f(x)\left[(kL - \sin kL)(1 - \cos kz) - (1 - \cos kL)(kz - \sin kz)\right], \tag{A.30}$$

where $f(x)$ is defined later, and k is determined by the condition that $\partial\Phi/\partial z$ must vanish at $z = L$. This gives two different quantization conditions for k which depend on whether Φ is even or odd about $z = L/2$. The quantization conditions for k are

$$\sin\frac{kL}{2} = 0 \quad \text{(even)}, \tag{A.31}$$

$$\tan\frac{kL}{2} = \frac{kL}{2} \quad \text{(odd)}. \tag{A.32}$$

The most restrictive condition is given by the longest wavelength. For the even mode, the longest wavelength solution is $kL = 2\pi$, and for the odd mode, $kL = 2.86\ \pi$. Thus, the most restrictive instability threshold is given by an even mode, and $kL = 2\pi$ is assumed in the analysis that follows. Further, from the differential equation and the requirement that the plasma displacement is radially localized, the function, $f(x)$, must be a decaying exponential, $\exp(-k|x|)$. Having determined $f(x)$, the form of Φ at marginal stability is

$$\Phi = \Phi_0 e^{-k|x|}\left(1 - \cos kz\right). \tag{A.33}$$

Finally, the jump condition is determined by integrating Eq. (A.26) on the interval $(-\epsilon, \epsilon)$ and taking the limit as $\epsilon \to 0$. This gives the condition that

$$\frac{p_{t0}}{R}\left.\frac{\partial^2\Phi}{\partial z^2}\right|_{x=0} + \Delta\left(\frac{B_p^2}{8\pi}\frac{\partial^3\Phi}{\partial z^2\partial x}\right) = 0, \tag{A.34}$$

where Δ denotes the difference in the limit of the function as $x = 0$ is approached from both the right and the left. Substituting in the form of Φ results in

$$\frac{8\pi p_{t0}}{B_{p0}^2} > kR\left(1 + \frac{B_{pi}^2}{B_{p0}^2}\right), \tag{A.35}$$

where the inequality is added at this point as a sufficient condition for instability. It is clear that if $L \to \infty$, $k \to 0$, and the plasma is inherently unstable, as is expected. If $B_{pi} = B_{p0}$, then p_{t0} can be replaced with p_0 with all of the pressure being confined by the toroidal field, and this reduces to

$$\frac{8\pi p_0}{B_{p0}^2} > 2kR. \tag{A.36}$$

If, on the other hand, the poloidal field is confining as much of the plasma pressure as it possibly can, $B_{pi}/B_{p0} \ll 1$. Recalling the pressure partition of Sec. A.1, $p_{t0} = p_0 - p_{p0}$. In

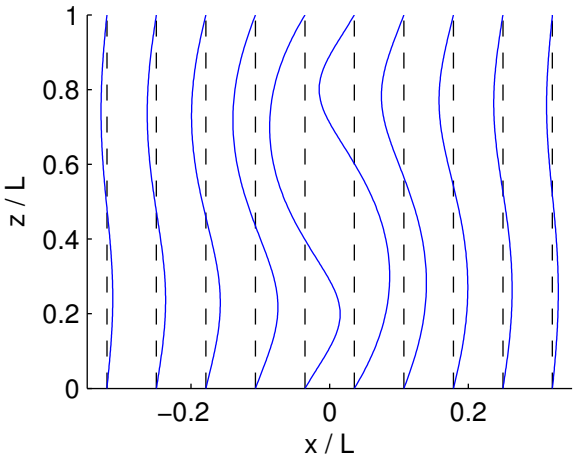

Figure A.4: Perturbed plasma surfaces of most unstable, axisymmetric mode at marginal stability. Vertical axis is z-coordinate scaled to distance between plates, L. Horizontal axis is the distance from the peak in pressure gradient scaled to distance between plates. Dashed black lines are the equilibrium plasma position, and solid blue lines are the perturbed plasma displacement as given in Eqs. (A.38) and (A.39). Scale of horizontal plasma displacement is exaggerated for visibility. In the nonlinear stage, mode drives poloidal convection and would lead to transport of heat flux.

this limit, $8\pi p_p/B_{p0}^2 = 1$. If this is the case, the instability limit becomes

$$\frac{8\pi p_0}{B_{p0}^2} > kR + 1 \approx kR, \tag{A.37}$$

where in the approximate expression, it is assumed that $R \gg L$.

From Φ, the functions ξ_r and ξ_z can be computed and are

$$\xi_r = \frac{k}{B_t}\Phi_0 e^{-k|x|}\sin kz, \tag{A.38}$$

$$\xi_z = -\frac{\mathrm{sgn}(x)k}{B_t}\Phi_0 e^{-k|x|}\left(1-\cos kz\right), \tag{A.39}$$

where

$$\mathrm{sgn}(x) = \frac{x}{|x|}. \tag{A.40}$$

The discontinuity in ξ_z at $x = 0$ is characteristic of the Rayleigh-Taylor instability. Figure A.4 shows the displacement that occurs in the linear stage of the instability. The black dashed

lines represent equilibrium plasma surfaces, and the solid blue curves show how the plasma is displaced as the instability grows. The conducting planes are placed at $z = 0$ and $z = L$. The instability decays away from the pressure gradient in the x-direction as can be seen in the figure. It is obvious from this picture that this instability will lead to convective mixing of the plasma and increased transport across field lines.

Using the same parameters as in the previous section, i.e., $R/L = 5$, the most restrictive instability condition is given by $\beta_p = 8\pi p_0/B_{p0}^2 \approx 30$, much greater than that derived for the ballooning instability. Finally, a comparison of the present analysis to the gravitational instability is warranted. Previous work examined convection in a plasma in the presence of a horizontal magnetic field and a vertical gravitational force in order to model the Rayleigh-Taylor instability for a magnetized fluid. Newcomb [92] has shown that the Schwarzschild criterion for convection in a compressible, ideal fluid holds even for an electrically conducting fluid in the presence of a horizontal magnetic field. The irrelevance of the strength of the magnetic field to the convection criterion reflects the fact that flute modes are driving the convection. The gravitational force in that problem plays the role of the toroidal curvature pressure term that appears in the analysis presented here. Zweibel and Bruhwiler [93] extended these ideas by performing the calculation within a vertical slot with line-tying boundary conditions enforced at the two planes. Their work most closely resembles the work presented here. The difference is that they consider a situation where there is no component of the magnetic field parallel to the plates, only the normal component. With the inclusion of a strong horizontal field oriented parallel to the plates, a correspondence can be shown between their work and the analysis in this section. The presence of a strong guide field serves to make the plasma incompressible, leading to stronger plasma stability.

References

[1] S. J. Buchsbaum, Phys. Fluids **3**, 418 (1960).

[2] R. L. Smith and N. Brice, J. Geophys. Res. **69**, 5029 (1964).

[3] M. Ono, Phys. Rev. Lett. **42**, 1267 (1979).

[4] G. J. Morales, R. S. Loritsch, and J. E. Maggs, Phys. Plasmas **1**, 3765 (1994).

[5] G. J. Morales and J. E. Maggs, Phys. Plasmas **4**, 4118 (1997).

[6] F. S. Tsung, J. W. Tonge, and G. J. Morales, Phys. Plasmas **12**, (2005).

[7] D. T. Young, S. Perraut, A. Roux, C. de Villedary, R. Gendrin, A. Korth, G. Kremser, and D. Jones, J. Geophys. Res. **86**, 6755 (1981).

[8] J. L. Rauch and A. Roux, J. Geophys. Res. **87**, 8191 (1982).

[9] S. Perraut, R. Gendrin, A. Roux, and C. de Villedary, J. Geophys. Res. **89**, 195 (1984).

[10] M. Temerin and R. L. Lysak, J. Geophys. Res. **89**, 2849 (1984).

[11] A. V. Guglielmi, A. S. Potapov, and C. T. Russell, JETP Lett. **72**, 298 (2000).

[12] M. Mithaiwala, L. Rudakov, and G. Ganguli, J. Geophys. Res. **112**, n/a (2007).

[13] J. M. Cornwall and M. Schulz, J. Geophys. Res. **76**, 7791 (1971).

[14] N. P. Meredith, R. M. Thorne, R. B. Horne, D. Summers, B. J. Fraser, and R. R. Anderson, J. Geophys. Res. **108** (2003).

[15] S. T. Vincena, G. J. Morales, and J. E. Maggs, Phys. Plasmas **17**, 052106 (2010).

[16] G. G. Borg and R. C. Cross, Plasma Phys. Contr. Fusion **29**, 681 (1987).

[17] T. Intrator, M. Vukovic, A. Elfimov, P. H. Probert, and G. Winz, Phys. Plasmas **3**, 1054 (1996).

[18] J. Jacquinot, B. D. McVey, and J. E. Scharer, Phys. Rev. Lett. **39**, 88 (1977).

[19] F. W. Perkins, Nucl. Fusion **17**, 1197 (1977).

[20] R. Majeski, C. K. Phillips, and J. R. Wilson, Phys. Rev. Lett. **73**, 2204 (1994).

[21] E. F. Jaeger, L. A. Berry, E. F. D'Azevedo, R. F. Barrett, S. D. Ahern, D. W. Swain, D. B. Batchelor, R. W. Harvey, J. R. Myra, D. D. D'Ippolito, C. K. Phillips, E. Valeo, D. N. Smithe, P. T. Bonoli, J. C. Wright, and M. Choi, Phys. Plasmas **15**, 072513 (2008).

[22] C. Castaldo and A. Cardinali, Phys. Plasmas **17**, 072513 (2010).

[23] P. Lee, R. Taylor, W. Peebles, H. Park, C. Yu, Y. Xu, N. Luhmann Jr, and S. Jin, Phys. Rev. Lett. **49**, 205 (1982).

[24] Y. Lin, J. E. Rice, S. J. Wukitch, M. J. Greenwald, A. E. Hubbard, A. Ince-Cushman, L. Lin, E. S. Marmar, M. Porkolab, M. L. Reinke, N. Tsujii, J. C. Wright, et al., Phys. Plasmas **16**, 056102 (2009).

[25] C. N. Lashmore-Davies and D. A. Russell, Phys. Plasmas **4**, 369 (1997).

[26] L. Chen and F. Zonca, Physica Scripta **T60**, 81 (1995).

[27] W. W. Heidbrink, E. J. Strait, E. Doyle, G. Sager, and R. T. Snider, Nucl. Fusion **31**, 1635 (1991).

[28] B. N. Breizman, H. L. Berk, and H. Ye, Phys. Fluids B **5**, 3217 (1993).

[29] V. E. Moiseenko and E. Tennfors, Plasma Phys. Contr. Fusion **38**, 2133 (1996).

[30] N. J. Fisch and J.-M. Rax, Phys. Rev. Lett. **69**, 612 (1992).

[31] D. S. Darrow, S. J. Zweben, S. Batha, R. V. Budny, C. E. Bush, Z. Chang, C. Z. Cheng, H. H. Duong, J. Fang, N. J. Fisch, R. Fischer, E. D. Fredrickson, G. Y. Fu, R. F. Heeter, W. W. Heidbrink, H. W. Herrmann, M. C. Herrmann, K. Hill, E. F. Jaeger, R. James, R. Majeski, S. S. Medley, M. Murakami, M. Petrov, C. K. Phillips, M. H. Redi, E. Ruskov, D. A. Spong, E. J. Strait, G. Taylor, R. B. White, J. R. Wilson, K. Wong, and M. C. Zarnstorff, Phys. Plasmas **3**, 1875 (1996).

[32] D. S. Darrow, R. Majeski, N. J. Fisch, R. F. Heeter, H. W. Herrmann, M. C. Herrmann, M. C. Zarnstorff, and S. J. Zweben, Nucl. Fusion **36**, 509 (1996).

[33] D. S. Clark and N. J. Fisch, Phys. Plasmas **7**, 2923 (2000).

[34] D. D. Ryutov, Phys. Plasmas **14**, 064502 (2007).

[35] D. D. Ryutov, M. A. Makowski, and M. V. Umansky, Plasma Phys. Contr. Fusion **52**, 105001 (2010).

[36] D. D. Ryutov, R. H. Cohen, T. D. Rognlien, and M. V. Umansky, Phys. Plasmas **15**, 092501 (2008).

[37] M. V. Umansky, T. D. Rognlien, D. D. Ryutov, and P. B. Snyder, Contrib. Plasma Phys. **50**, 350 (2010).

[38] V. A. Soukhanovskii, J.-W. Ahn, R. E. Bell, D. A. Gates, S. Gerhardt, R. Kaita, E. Kolemen, B. P. LeBlanc, R. Maingi, M. Makowski, R. Maqueda, A. G. McLean, J. E. Menard, D. Mueller, S. F. Paul, R. Raman, A. L. Roquemore, D. D. Ryutov, S. A. Sabbagh, and H. A. Scott, Nucl. Fusion **51**, 012001 (2011).

[39] V. A. Soukhanovskii, R. E. Bell, A. Diallo, S. Gerhardt, S. Kaye, E. Kolemen, B. P. LeBlanc, A. G. McLean, J. E. Menard, S. F. Paul, M. Podesta, R. Raman, T. D. Rognlien, A. L. Roquemore, D. D. Ryutov, F. Scotti, M. V. Umansky, D. Battaglia, M. G. Bell, D. A. Gates, R. Kaita, R. Maingi, D. Mueller, and S. A. Sabbagh, Phys. Plasmas **19**, 082504 (2012).

[40] F. Piras, S. Coda, I. Furno, J.-M. Moret, R. A. Pitts, O. Sauter, B. Tal, G. Turri, A. Bencze, B. P. Duval, F. Felici, A. Pochelon, and C. Zucca, Plasma Phys. Contr. Fusion **51**, 055009 (2009).

[41] F. Piras, S. Coda, B. P. Duval, B. Labit, J. Marki, S. Y. Medvedev, J.-M. Moret, A. Pitzschke, O. Sauter, et al., Plasma Phys. Contr. Fusion **52**, 124010 (2010).

[42] F. Piras, S. Coda, B. P. Duval, B. Labit, J. Marki, S. Y. Medvedev, J.-M. Moret, A. Pitzschke, O. Sauter, et al., Phys. Rev. Lett. **105**, 155003 (2010).

[43] S. L. Allen, T. H. Osborne, E. Kolemen, J. Boedo, N. Brooks, M. Fenstermacher, R. Groebner, D. N. Hill, A. Hyatt, C. Lasnier, A. Leonard, M. Makowski, W. H. Meyer, A. McLean, T. Petrie, D. Ryutov, and J. Watkins, Initial snowflake divertor physics studies on diii-d, in *Proc. 24th Int. Conf. on Fusion Energy*, p. PD 1/2, San Diego, CA, 2012.

[44] H. Reimerdes, G. P. Canal, B. P. Duval, B. Labit, T. Lunt, W. A. J. Vijvers, S. Coda, G. De Temmerman, T. W. Morgan, F. Nespoli, B. Tal, et al., Plasma Phys. Contr. Fusion **55**, 124027 (2013).

[45] T. Lunt, G. P. Canal, Y. Feng, H. Reimerdes, B. P. Duval, B. Labit, W. A. J. Vijvers, D. Coster, K. Lackner, and M. Wischmeier, Plasma Phys. Contr. Fusion **56**, 035009 (2014).

[46] D. D. Ryutov, R. H. Cohen, E. Kolemen, L. LoDestro, M. Makowski, J. Menard, T. D. Rognlien, V. A. Soukhanovskii, M. V. Umansky, and X. Q. Xu, Theory and simulations of elm control with a snowflake divertor, in *Proc. 24th Int. Conf. on Fusion Energy*, pp. P 4–18, San Diego, CA, 2012.

[47] D. D. Ryutov, R. H. Cohen, T. D. Rognlien, and M. V. Umansky, Plasma Phys. Contr. Fusion **54**, 124050 (2012).

[48] D. D. Ryutov, R. H. Cohen, T. D. Rognlien, and M. V. Umansky, Contrib. Plasma Phys. **52**, 539 (2012).

[49] C. Gormezano, A. C. C. Sips, T. C. Luce, S. Ide, A. Becoulet, X. Litaudon, A. Isayama, J. Hobirk, M. R. Wade, T. Oikawa, R. Prater, A. Zvonkov, B. Lloyd, T. Suzuki, E. Barbato, P. Bonoli, C. K. Phillips, V. Vdovin, E. Joffrin, T. Casper, J. Ferron, D. Mazon, D. Moreau, R. Bundy, C. Kessel, A. Fukuyama, N. Hayashi, F. Imbeaux, M. Murakami, A. R. Polevoi, and H. E. St John, Nucl. Fusion **47**, S285 (2007).

[50] B. Van Compernolle, G. J. Morales, and W. Gekelman, Phys. Plasmas **15**, 082101 (2008).

[51] W. Gekelman, H. Pfister, Z. Lucky, J. Bamber, D. Leneman, and J. Maggs, Rev. Sci. Instr. **62**, 2875 (1991).

[52] J. D. Huba, NRL plasma formulary, Technical Report NRL/PU/6790–09-523, Naval Research Laboratory, Washington, DC, 2009.

[53] C. Torrence and G. P. Compo, Bull. Amer. Meteor. Soc. **79**, 61 (1998).

[54] S. I. Braginskii, in *Reviews of Plasma Physics Vol. 1*, edited by M. A. Leontovich, Consultants Bureau, New York, 1965, pp. 205–311.

[55] M. Opher, G. J. Morales, and J. N. Leboeuf, Phys. Rev. E **66**, 016407 (2002).

[56] A. I. Zhmoginov and N. J. Fisch, Phys. Plasmas **16**, 112511 (2009).

[57] A. I. Zhmoginov and N. J. Fisch, Phys. Plasmas **19**, 055702 (2012).

[58] C. M. Cooper and W. Gekelman, Phys. Rev. Lett. **110**, 265001 (2013).

[59] I. B. Bernstein, Phys. Fluids **18**, 320 (1975).

[60] J. Haselgrove, in *Report of Physics Society Conference on Physics of the Ionosphere*, Cambridge Univ., Cambridge, 1954, pp. 355–364.

[61] I. Yabroff, J. Res. Natl. Bur. Stand. Sect. D **65 D(5)**, 485 (1961).

[62] R. Aymar, P. Barabaschi, and Y. Shimomura, Plasma Phys. Contr. Fusion **44**, 519 (2002).

[63] D. J. Griffiths, *Introduction to Quantum Mechanics, 2nd ed.*, Pearson Prentice Hall, Upper Saddle River, 2005.

[64] M. Brambilla, *Kinetic Theory of Plasma Waves: Homogeneous Plasmas*, Oxford University Press, New York, 1998.

[65] J. A. C. Weideman, SIAM J. Numer. Anal. **31**, 1497 (1994).

[66] R. V. Budny, Nucl. Fusion **42**, 1383 (2002).

[67] M. A. Beer, S. C. Cowley, and G. W. Hammett, Phys. Plasmas **2**, 2687 (1995).

[68] J. C. Wright, P. T. Bonoli, M. Brambilla, F. Meo, E. DAzevedo, D. B. Batchelor, E. F. Jaeger, L. A. Berry, C. K. Phillips, and A. Pletzer, Phys. Plasmas **11**, 2473 (2004).

[69] R. L. Arnoldy, K. A. Lynch, J. B. Austin, and P. M. Kintner, J. Geophys. Res. **104**, 22613 (1999).

[70] V. A. Sergeev, A. G. Yahnin, R. A. Rakhmatulin, S. I. Solovjev, F. S. Mozer, D. J. Williams, and C. T. Russell, Planet. Space Sci. **34**, 1169 (1986).

[71] W. Gekelman, M. Van Zeeland, S. Vincena, and P. Pribyl, J. Geophys. Res. **108** (2003).

[72] H. Boehmer, D. Edrich, W. W. Heidbrink, R. McWilliams, L. Zhao, and D. Leneman, Rev. Sci. Instrum. **75**, 1013 (2004).

[73] B. Van Compernolle, W. Gekelman, and P. Pribyl, Phys. Plasmas **13**, 092112 (2006).

[74] F. S. Tsung, G. J. Morales, and J. Tonge, Phys. Plasmas **14**, 042101 (2007).

[75] P. C. Stangeby, *The Plasma Boundary of Magnetic Fusion Devices*, Taylor & Francis Group, LLC, New York, 2000.

[76] J. P. Freidberg, *Ideal Magnetohydrodynamics*, Plenum Press, New York, 1987.

[77] J. W. Connor, R. J. Hastie, and J. B. Taylor, Proc. R. Soc. Lond. A **365**, 1 (1979).

[78] W. B. Kunkel and J. U. Guillory, in *Proceedings of the 7th International Conference on Phenomena in Ionized Gases*, edited by B. Perovic and D. Tosic, Gradevinska Knjiga Publishing House, 1966, volume II, p. 702.

[79] J. R. Myra, D. A. DIppolito, and J. P. Goedbloed, Phys. Plasmas **4**, 1330 (1997).

[80] F. D. Halpern, S. Jolliet, J. Loizu, A. Mosetto, and P. Ricci, Phys. Plasmas **20**, 052306 (2013).

[81] E. Hameiri, Phys. Plasmas **6**, 674 (1999).

[82] A. J. Webster and C. G. Gimblett, Phys. Rev. Lett. **102**, 035003 (2009).

[83] D. D. Ryutov and M. V. Umansky, Phys. Plasmas **20**, 092509 (2013).

[84] R. J. Goldston and T. Eich, Drift-based model for power-scrape-off width in low-gas-puff h-mode tokamak plasmas: Comparison with experiment and implications, in *Proc. 24th Int. Conf. on Fusion Energy*, pp. TH/P4–19, San Diego, CA, 2012.

[85] V. A. Soukhanovskii, R. E. Bell, A. Diallo, S. Gerhardt, S. Kaye, E. Kolemen, B. P. LeBlanc, A. McLean, J. E. Menard, S. F. Paul, M. Podesta, R. Raman, D. D. Ryutov, F. Scotti, R. Kaita, R. Maingi, D. M. Mueller, A. L. Roquemore, H. Reimerdes, G. P. Canal, B. Labit, W. Vijvers, S. Coda, B. P. Duval, T. Morgan, J. Zielinski, G. D. Temmerman, and B. Tal, J. Nucl. Matt. **438**, S96 (2013).

[86] V. A. Soukhanovskii, private communication, 2014.

[87] W. A. J. Vijvers, private communication, 2014.

[88] M. N. Rosenbluth and C. L. Longmire, Ann. Phys. **1**, 120 (1957).

[89] B. B. Kadomtsev, in *Reviews of Plasma Physics Vol. 2*, edited by M. A. Leontovich, Consultants Bureau, New York, 1966, pp. 153–199.

[90] I. B. Bernstein, E. A. Frieman, M. D. Kruskal, and R. M. Kulsrud, Proc. R, Soc. London, Ser. A **244**, 17 (1958).

[91] E. G. Evstatiev, G. L. Delzanno, and J. M. Finn, Phys. Plasmas **13**, 072902 (2006).

[92] W. A. Newcomb, Phys. Fluids **4**, 391 (1961).

[93] E. G. Zweibel and D. L. Bruhwiler, Astrophys. J. **399**, 318 (1992).